Primordial non-Gaussianity in the cosmic microwave background and in the large-scale structure

Thomas Montandon

To cite this version:

Thomas Montandon. Primordial non-Gaussianity in the cosmic microwave background and in the large-scale structure. Other. Université Paris Cité, 2021. English. NNT : 2021UNIP7185 . tel-03937509

HAL Id: tel-03937509
https://theses.hal.science/tel-03937509

Submitted on 13 Jan 2023

Université de Paris

Ecole doctorale: Sciences de la Terre et de l'Environnement et Physique de l'Univers
Laboratoires: AstroParticule et Cosmologie et Laboratoire Irène Joliot-Curie

Primordial non-Gaussianity in the cosmic microwave background and in the large-scale structure

Par Thomas Montandon

Thèse de doctorat de Physique de l'Univers

Dirigée par Guillaume Patanchon
et par Bartjan van Tent

Présentée et soutenue publiquement le 8 Novembre 2021

Devant le jury composé de:

Karim Benabed	Astronome	Sorbonne Université	Président et Rapporteur
Ruth Durrer	Professeure	Université de Genève	Rapporteur
Michele Liguori	Maitre de conférence	Université de Padoue	Examinateur
James Bartlett	Professeur	Université de Paris	Examinateur
Guillaume Patanchon	Maitre de conférence	Université de Paris	Directeur de thèse
Bartjan van Tent	Maitre de conférence	Université Paris-Saclay	Directeur de thèse

À Vincent Coutellier

Contents

Acknowledgments

Je commencerai tout naturellement par remercier mes deux directeurs de thèse, pour tout ce qu'ils m'ont appris et leur soutien constant. D'abord, merci à Guillaume Patanchon, à qui j'ai fait confiance pour qu'il finisse son HDR pour que je puisse, à quelque jour près, commencer ma thèse. Merci ensuite à mon deuxième directeur de thèse, Bartjan van Tent, pour ta forte implication dans nos projets, tes déplacements à l'APC qui ont fait vivre notre collaboration à trois et pour ton aide à remettre les "s" aux bons endroits dans ma thèse.

Je remercie ensuite Clément Stahl, pour m'avoir guidé dans mon deuxième projet de thèse, pour ces interminables discussions au tableau dans ton bureau et pour m'avoir permis de rencontrer les trois prochaines personnes que je dois ici remercier. Tout d'abord Jorge Noreña, qui m'a énormément appris pendant presque deux années de skype (heureusement que tu as fini par mettre ta caméra au bout d'un an de skype, sinon tu ne serais encore aujourd'hui que ta photo de profil pour moi). Ensuite, merci à Juan Calles, pour son implication dans notre projet et pour son aide pour débugger mes codes. Merci à Julian Adamek, qui a fait passer notre projet à la vitesse supérieure et qui m'a permis de faire ma première conférence (sur une ile paradisiaque en plus) ainsi que mon premier déplacement de ma thèse en m'invitant à Zurich.

Je remercie également mes deux laboratoires: l'APC et le LPT. Je remercie Yannick Giraud-Héraud, pour son aide précieuse dans les moments difficiles de ma thèse. Je remercie Ken Ganga ainsi que tous mes collègues de bureau. Merci à mon ami Calum Murray, pour tous les concerts de jazz et pour avoir supporté mon mauvais francais. Merci à Louise Mousset, Guillaume Stankowiak, Bastien Arcelin, Tuan van Bui et Batiste Jost pour tous les bons moments que j'ai passés à l'APC. Merci à Tim Anson, Martin Novoa Brunet, Florian Nortier et Giulia Isabella pour de magnifiques moments passés à Orsay, des milliers de bières et bien sur, le meilleur voyage de ma vie! Finalement, merci à tous mes amis du NPAC.

Merci à toute ma famille. Mes parents et ma grand-mère pour leur soutien durant toute ma vie qui m'a permis d'en arriver à devenir docteur. Merci à mon frère pour son soutien, mais aussi pour tous les bons moments que j'ai réussi à t'imposer dans Paris et pour les dizaines de films et pizzas.

Finalement, merci à Dounia Hélis, pour ton soutien, ta bonne humeur, pour tous les merveilleux moments, pour avoir rythmé mes journées pendant les confinements, pour m'avoir supporté pendant la rédaction de cette thèse, jour et nuit.

Abstract

Inflation is the oldest period in the history of our universe corroborated by observations. The simplest model consists of a phase during which the universe was dominated by a single scalar field producing accelerated expansion. This dynamics explains the homogeneity, isotropy and flatness of our universe. Inflation also generates small adiabatic and quasi-Gaussian fluctuations. Adiabaticity means that no fluctuation in composition or relative velocity, called isocurvature modes, can be generated. A natural extension of the single-field model is to consider additional fields: this is the so-called multi-field inflation. In these models, it is possible to generate isocurvature modes, as well as measurable non-Gaussianities. A specific signature of the non-Gaussianities of multi-field inflation, called local PNG, is a large coupling in the squeezed limit, i.e. a coupling between the large and the small scales.

The cosmic microwave background (CMB) is a radiation that was emitted 380,000 years after inflation. The observation of the temperature and polarization anisotropies of the CMB makes it possible to constrain the Gaussianity and the adiabaticity of the initial conditions. The Planck collaboration gave the strongest constraints, showing that the initial conditions are compatible with a purely adiabatic and Gaussian universe.

In this thesis, we propose the first joint analysis of the power spectrum and the bispectrum of the CMB for isocurvature modes in the framework of a generic two-field inflation model. In general, the lack of detection in the Planck data prevents the constraints from being improved for isocurvature modes. On the other hand, for subclasses of models, the constraints can be improved and we give the conditions under which this is possible. Then, we produce forecast constraints for the future CMB missions: LiteBIRD and CMB-S4. We show that the improvement of the constraints can give rise to the detection of isocurvature modes and their non-Gaussianities. Under conditions that we specify, the joint analysis for these future missions can greatly improve the error bars on isocurvature modes.

Another complementary observable is the large-scale structure (LSS). Future galaxy surveys should greatly improve the constraints on PNG. To get an accurate measurement in the squeezed limit, we need a high accuracy for very large scales as well as small, which makes this measurement extremely difficult. At large scales, relativistic effects (RE) become important and at small scales, non-linearities become very large and the perturbations theory breaks down. Second-order calculations show that RE are degenerated with local PNG and have the same time dependency. Because of this time dependency, RE cannot be neglected in the initial conditions of N-body simulations.

In the last part of this thesis, we describe the code we have developed: RELIC. This code produces relativistic initial conditions up to the second order for N-body simulations. By neglecting the couplings between small scales, RELIC can generate the initial conditions for large simulations in a reasonable time. The theory of perturbations then allows us to calculate all the fields useful to initialize the N-body simulation code gevolution. The analysis of the initial conditions generated by RELIC and reconstructed by gevolution shows good agreement at large scales and in the squeezed limit. We have thus built a pipeline, taking into account RE and non-linearities up to second order, essential to quantify the local PNG contaminations that RE generates.

Key words: Inflation, non-Gaussianities, Adiabatic, Isocurvature modes, joint analysis, relativistic effects, initial conditions

Résumé

L'inflation est la plus ancienne période de l'histoire de notre univers corroborée par les observations. Le modèle le plus simple consiste en une phase durant laquelle l'univers a été dominé par un unique champ scalaire produisant une expansion accélérée. La dynamique de l'inflation permet d'expliquer l'homogénéité, l'isotropie et la platitude de notre univers. L'inflation permet aussi de générer des petites perturbations adiabatiques et quasi-gaussiennes. L'adiabaticité signifie qu'aucune fluctuation de composition ou de vitesse relative, appelée modes isocourbure, ne peut être générée. Une extension naturelle du modèle à un champ est de considérer plusieurs champs: l'inflation multi-champs. Dans ces modèles, il est possible de générer des modes isocourbure, ainsi que des non-gaussianités mesurables. Une signature caractéristique des non-gaussianités de l'inflation multi-champs, appelées PNG locales, est un grand couplage entre les grandes et les petites échelles, appelé limite squeezed.

Le fond diffus cosmologique (CMB) est un rayonnement qui a été émis 380 000 ans après l'inflation. L'observation des anisotropies de température et de polarisation du CMB permettent de poser de fortes contraintes sur la gaussianité et l'adiabaticité des conditions initiales. La collaboration Planck a ainsi donné les plus fortes contraintes, montrant que les conditions initiales sont compatibles avec un univers purement adiabatique et gaussien.

Dans cette thèse, nous proposons la première analyse jointe du spectre de puissance et du bispectre du CMB pour les modes isocourbure dans le cadre d'un modèle générique d'inflation à deux champs. Dans le cadre général, l'absence de détection dans les données Planck empêche les contraintes d'être améliorées pour les modes isocourbure. En revanche, pour des sous-classes de modèles, les contraintes peuvent être améliorées et nous donnons les conditions dans lesquelles c'est possible. Ensuite, nous produisons des contraintes prévisionnelles pour les futures missions CMB LiteBIRD et CMB-S4. Nous montrons que l'amélioration des contraintes pourra donner lieu à une détection de modes isocourbure et de leurs non-gaussianités. Dans des conditions que nous spécifions, l'analyse jointe pour ces futures missions pourra améliorer grandement les barres d'erreur sur les modes isocourbure.

Une autre observable complémentaire est la structure à grandes échelles (large-scale structure LSS). Les futures relevés de galaxies devraient grandement améliorer les contraintes sur les PNG. Pour obtenir une mesure de précision dans la limite squeezed, nous avons besoin d'une grande précision pour les très grandes échelles tout comme les petites, ce qui rend cette mesure extrêmement difficile. Aux grandes échelles, les effets relativistes (RE) deviennent importants et aux petites échelles, les non-linéarités deviennent très grandes. Les calculs au deuxième ordre montrent que les RE sont dégénérés avec les PNG locales et qu'ils possèdent la même dépendance temporelle. A cause de cette dépendance temporelle, les RE ne peuvent pas être négligés dans les conditions initiales des simulations à N-corps.

Dans la dernière partie de cette thèse, nous décrivons le code que nous avons développé:

RELIC. Ce code permet de générer des conditions initiales relativistes jusqu'au deuxième ordre pour les simulations à N-corps. En négligeant les couplages entre les petites échelles, RELIC peut générer les conditions initiales pour de grandes simulations en un temps raisonnable. La théorie des perturbations nous permet ensuite de calculer tous les champs utiles pour initialiser la simulation à N-corps gevolution. L'analyse des conditions initiales générées par RELIC et reconstruites par gevolution montrent un bon accord à grandes échelles et dans la limite squeezed. Nous avons ainsi construit une pipeline, prenant en compte les RE et les non-linéarités, essentielle pour quantifier les contaminations des PNG locales qu'ils génèrent.

Mots clés: Inflation, non-gaussianités, mode adiabatique et isocourbure, analyse jointe, effets relativistes, conditions initiales

Extended Summary

Dans cette thèses, nous proposons deux contributions pour la recherche de non-gaussianités primordiales, en particulier dans le cadre des modèles d'inflation. L'inflation est un mécanisme causal qui peut expliquer la planéité, l'homogénéité et l'isotropie de l'univers. Ces modèles fournissent un mécanisme pour générer de petites perturbations adiabatiques et quasi-gaussiennes qui sont les germes de la formation de structures à grande échelle. L'adiabaticité signifie qu'aucune fluctuation de composition ou de vitesse relative, appelée modes isocourbure, ne peut être générée. Une extension naturelle du modèle à un champ est de considérer plusieurs champs: l'inflation multi-champs. Dans ces modèles, il est possible de générer des modes isocourbure, ainsi que des non-gaussianités mesurables. Une signature caractéristique des non-gaussianités de l'inflation multi-champs, appelées PNG locales, est un grand couplage entre les grandes et les petites échelles, appelé limite squeezed.

Pour la première analyse, nous nous concentrons sur le fond diffus cosmologique (CMB). L'observation des anisotropies de température et de polarisation du CMB permettent de poser de fortes contraintes sur la gaussianité et l'adiabaticité des conditions initiales. La présence de modes d'isocourbure (en plus du mode adiabatique dominant) dans le CMB serait une preuve directe que les perturbations cosmologiques sont produites par au moins deux degrés de liberté primordiaux, qui dans le contexte du paradigme inflationniste signifierait une inflation multi-champs. Ceci écarterait donc l'inflation à un champ, qui pour l'instant est compatible avec toutes les observations. Étant donné le contenu en matière de l'univers, nous avons trois modes isocourbure possibles: le mode de densité de matière noire (CDM), le mode densité des neutrinos et le mode de vitesse des neutrinos. L'analyse du spectre de puissance de Planck n'a trouvé aucun signe de ces modes isocourbure et a posé de fortes contraintes sur leurs amplitudes. De la même manière, l'analyse du bispectre de Planck n'a détecté aucune non-gaussianité adiabatique et isocourbure mais a posé des contraintes. Nous avons réalisé une analyse jointe du spectre de puissance et du bispectre des fluctuations de température et de polarisation du CMB afin d'améliorer les contraintes sur les modes isocourbure. Pour ce faire, nous devons supposer un modèle qui nous permet de lier les paramètres observables du spectre de puissance et du bispectre. Nous avons dû faire un compromis entre, d'une part, garder le modèle aussi général que possible afin que notre analyse s'applique à une classe de modèles d'inflation aussi large que possible, et d'autre part, garder limité le nombre de paramètres libres supplémentaires. Ce compromis nous a conduit à ne considérer que des modèles d'inflation à deux champs, avec un seul mode isocourbure en plus du mode adiabatique. En plus, nous avons supposé que l'un des champs domine à la fois le mode isocourbure linéaire et les parties de second ordre du mode adiabatique et du mode isocourbure. Pour le reste, ce modèle reste général. Il possède cinq paramètres libres, dont l'un est fixé par l'amplitude adiabatique du spectre de puissance. Par conséquent, notre modèle a quatres paramètres supplémentaires par rapport à la cosmologie ΛCDM standard, qui sont l'amplitude d'isocourbure du spectre de puissance β_{iso}, la corrélation linéaire entre le mode adiabatique et le mode d'isocourbure $\cos\Delta$ et les amplitudes bispectrales adiabatique et d'isocourbure κ_ζ et κ_S respectivement. Le spectre de puissance ne dépend que des deux premiers. Dans une telle configuration, il y a six paramètres f_{NL} différents que l'on peut extraire du bispectre, bien que les relations imposées par le modèle signifient que seulement trois d'entre eux sont indépendants.

Nous avons d'abord appliqué notre méthodologie aux données de Planck. Nous avons construit une vraisemblance jointe du spectre de puissance et des f_{NL}, qui est simplement le produit des deux vraisemblances car la statistique à deux points et à trois points peuvent être considérées comme statistiquement indépendantes. Nous avons utilisé la vraisemblance de Planck 2018 pour le spectre de puissance. Comme une vraisemblance bispectre complète ne peut pas être calculée, nous considérons une vraisemblance sur les f_{NL}, beaucoup plus simple et rapide, basée sur la matrice de Fisher. Dans le cas général où les quatre paramètres supplémentaires sont laissés libres, l'analyse jointe ne donne pas de meilleures contraintes que le spectre de puissance seul. Nous avons également donné un argument théorique pour expliquer pourquoi cela doit être ainsi sans détection de modes isocourbure dans le spectre de puissance et sans détection de non-gaussianité.

Cependant, si nous considérons une classe de modèles plus restreinte où soit $\cos\Delta$ soit les κ sont fixés à une valeur spécifique non nulle, alors l'analyse jointe peut améliorer les contraintes dans le cas de Planck. En particulier, nous avons montré que pour $|\kappa| > 10^3$ fixé, l'analyse jointe donnera de meilleures contraintes sur $\beta_{\rm iso}$ et $\cos\Delta$ que le spectre de puissance seul. De même, pour une valeur fixe de $|\cos\Delta| \leq 0.1$ l'analyse jointe améliore les contraintes sur β_{iso}. Remarquablement, pour de telles valeurs de $\cos\Delta$ dans le cas du mode isocourbure de la vitesse des neutrinos, l'analyse jointe semble même indiquer une détection de β_{iso} à un niveau de 3-4σ. Cependant, pour différentes raisons nous considérons qu'il s'agit d'une fluctuation statistique.

Pour les futures expériences comme LiteBIRD et CMB-S4, nous utilisons un modèle simplifié des observations sans avant-plan et une vraisemblance du spectre de puissance simplifiée. Notre évaluation théorique a montré que dans le cas général l'analyse jointe peut améliorer les contraintes si deux conditions sont satisfaites. Premièrement, l'amplitude du mode isocourbure β_{iso} doit être détectée dans le spectre de puissance, sinon l'espace des paramètres à échantillonner est infini et fortement dégénéré. Deuxièmement, l'un des deux κ_I doit être détecté. Nous avons construit une vraisemblance combiné du spectre de puissance et des f_{NL} pour LiteBIRD et CMB-S4 et étudié dans quelle région de l'espace des paramètre $(\beta_{iso}, \cos\Delta)$ compatible avec les résultats de Planck, ces conditions sont satisfaites, étant donné également les valeurs de référence pour les paramètres κ compatibles avec Planck à 1σ. Dans tous nos résultats, nous avons constaté que LiteBIRD est le principal moteur des améliorations par rapport à Planck, alors que CMB-S4 n'apportant qu'une amélioration marginale.

Pour le mode isocourbure CDM nous avons constaté que, compte tenu des contraintes de Planck actuelles, la probabilité d'une détection par LiteBIRD+CMB-S4 est assez faible. Nous avons dû choisir un couple relativement improbable de valeurs fiduciaires β_{iso} et $\cos\Delta$, qui ne sont compatibles qu'à 2σ avec Planck. Dans ce cas seulement, l'analyse jointe améliore de manière très significative les contraintes sur β_{iso} et $\cos\Delta$.

Pour les modes isocourbure des neutrinos, la situation est plus encourageante. Nous pouvons facilement trouver des valeurs fiduciaires pour β_{iso} et $\cos\Delta$ dans les contours de Planck 1σ où les conditions ci-dessus sont satisfaites. Pour le mode de vitesse des neutrinos, environ la moitié de la région à l'intérieur du contour de Planck 1σ satisfait à ces conditions. Nos valeurs fiduciaires choisies signifient que β_{iso} serait détecté par LiteBIRD+CMB-S4 dans le spectre de puissance avec 5σ et 7σ pour la densité et la vitesse des neutrinos, respectivement. L'analyse jointe apporte alors des améliorations très significatives sur les barres d'erreur de $\cos\Delta$ par rapport au spectre de puissance seul. Pour donner un exemple pour le mode isocourbure de la vitesse des neutrinos, pour nos valeurs fiduciaire choisies, la barre d'erreur de $\cos\Delta$ s'améliore de 67%, conduisant à une détection hautement significative à 12σ.

Dans la deuxième analyse de cette thèse, nous nous sommes concentré sur les grandes structures de l'univers (LSS). Répétons ici que la limite squeezed du bispectre est un outil puissant pour contraindre les PNG. En particulier, la détection d'un signal limite squeezed avec une amplitude $f_{NL} \gtrsim 0,1$ éliminerait définitivement tous les modèles d'inflation à un champ. La mission Euclid devrait contraindre f_{NL} avec un écart type $\sigma_{f_{NL}} \sim 1$ alors que des mission comme SPHEREx et SKA pourraient atteindre $\sigma_{f_{NL}} \sim 0.1$. Cependant, la modélisation de la limite squeezed dans le LSS est très difficile. En effet, la limite squeezed est un couplage entre les grandes et les petites échelles où la physique est très différente. Aux grandes échelles, les effets relativistes deviennent importants à mesure que l'on approche de l'horizon. Aux petites échelles, les calculs analytiques deviennent impossibles et il faut des simulations numériques.

Les effets relativistes qui nous intéressent dans cette thèse apparaissent dans la dynamique cosmologique des perturbations. Dans la limite sous-horizon, ils peuvent être négligés et la dynamique newtonienne est suffisante. Lorsque nous approchons de l'horizon, ces corrections ne peuvent plus être négligées. De nombreuses études ont été réalisées au cours des 30 dernières années pour rendre compte de ces effets jusqu'au second ordre. L'une des principales conclusions de ces travaux est que les effets relativistes dynamiques sont dégénérés avec PNG dans l'espace des moments et dans l'espace de redshift. Leur modélisation précise est donc cruciale pour la contrainte des PNG. Des codes numériques résolvant les équations d'Einstein-Boltzmann et tenant compte des effets non linéaires jusqu'au second ordre ont été développés; nous utilisons dans cette thèse le code SONG.

Les calculs analytiques sont précis lorsque la théorie des perturbations est toujours valable. Dans la limite squeezed, les grandes échelles influencées par les effets relativistes sont mélangées aux petites échelles où la théorie des perturbations ne marche plus. Pour étudier ces échelles, les simulations numériques sont un outil très puissant. Par conséquent, le code à N-corps entièrement relativiste gevolution est l'outil parfait pour tester la précision des calculs analytiques. Dans son implémentation actuelle, gevolution utilise des conditions initiales gaussiennes, calculées en propageant linéairement les conditions initiales gaussiennes. Cependant, certains effets relativistes du second ordre proviennent des conditions initiales de la simulation et se développent comme les perturbations linéaires.

Afin de tenir pleinement compte des effets relativistes, nous devons construire les conditions initiales de la simulation jusqu'au second ordre. Dans la dernière partie de cette thèse, nous présentons le générateur de conditions initiales relativistes de second ordre RELIC. En général, générer des conditions initiales au second ordre est en dehors des capacités numériques actuelles pour une simulation raisonnablement grande. En nous concentrant sur les effets relativistes et la contamination des PNG dans la limite squeezed, nous avons construit une approximation qui consiste à ne calculer que les couplages de modes qui nous intéressent, c'est à dire le couplage grande-grande échelle et le couplage grande-petite échelles. Ce faisant, nous négligeons le couplage entre les petites échelles, qui est dominé par les non-linéarités newtoniennes générées par la simulation. Grâce à cette approximation, la complexité du code passe de N^6 à N^3 où N est le nombre de modes considérés.

Les mesures du spectre de puissance et du bispectre du champ de densité CDM résultant montrent en général un bon accord avec les prédictions théoriques. Nous avons montré deux limites à la précision. Premièrement, la prédiction théorique du spectre de puissance du second ordre est difficile à calculer à cause d'une intégrale lentement convergente qui, de plus, dépend des bornes d'intégration. Pour résoudre ce problème, nous devons utiliser une taille plus physique de la boîte, et placer la fréquence maximale bien après l'échelle de l'égalité rayonnement-matière. La seconde limitation est due au binning du spectre de puissance et de l'estimateur bispectre que nous utilisons. Cela n'affecte que les deux ou trois premiers points. Afin d'avoir une comparaison précise, en particulier pour construire un estimateur f_{NL}, nous devons utiliser soit une boîte plus grande que nécessaire et ensuite rejeter les premiers points, soit binner la prédiction théorique de la même manière que les mesures. En dehors de ces problèmes, les mesures du bispectre dans la limite équilatérale et dans la limite squeezed ont montré un très bon accord tant que l'on considère les modes inférieurs à la coupure entre les grandes et les petites échelles utilisées.

Enfin, nous avons présenté une vérification de cohérence non triviale en cours d'étude de notre pipeline relativiste. Nous avons calculé de deux manières très différentes les champs de densité CDM. De manière directe, en utilisant le noyau renvoyé par SONG, nous avons calculé le spectre de puissance du champ de densité tel que calculé par RELIC. Ensuite, nous avons donné à gevolution le champ de déplacement, que nous avons calculé au second ordre, ainsi que la vitesse et le potentiel. A partir de ces champs, gevolution génère un maillage de particules à partir duquel il peut, de manière non perturbative, recalculer le champ de densité. La comparaison du spectre de puissance des deux champs de densité a montré une forte discordance. Ce problème a été résolu très récemment. Nous pouvons tirer parti du générateur de conditions initiales de premier ordre de gevolution pour générer de manière itérative un champ de déplacement de second ordre qui, étant donné un opérateur laplacien discret, reproduit exactement le champ de densité de second ordre calculé par RELIC.

Part I

An introduction to cosmological science

Chapter 1

Historical overview

In this chapter, we propose a historical review to introduce modern cosmology. We will start with the pre-relativistic era of cosmology, in section 1.1, when the total universe could be considered as the Milky Way. We will introduce the fundamental observations that have completely changed our conception of the universe. In section 1.2, we will introduce the theory of general relativity and its first application to cosmology as well as the first observations of a dynamical universe. Finally, in section 1.4, we will introduce the observations that led to the standard model of cosmology, the so-called ΛCDM model. This section will be finished by introducing the period of inflation which is one of the main motivations of the two works of this thesis. Note that, in this chapter, the formulas and the measurements results are given in their original form. They are not meant to properly define the quantities for this thesis. This will be done in chapter 2.

1.1 Pre-relativistic cosmology

1.1.1 Stellar parallax

In 1847, Wilhelm Struve wrote the Etudes d'Astronomie Stellaire [2] where he describes the state of the art of the astronomy of the Milky Way, see also [3]. It describes and actualizes the massive work done by John and Caroline Herschel based on a count of stars to map the sky. This work was suggested that the Milky Way is composed of a layer of stars as drawn in figure 1.1, with the sun around the center of the system. Nevertheless,

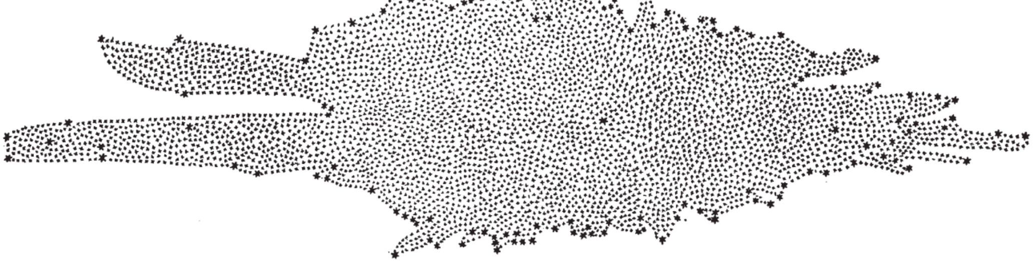

Figure 1.1: Original map of the Milky way done by John and Caroline Herschel in [1]

John Herschel could not conclude about the size of the “stellar system” surrounding us because no distances could be measured outside our solar system.

Edmond Halley had already noticed in a paper in 1718 that some stars’ positions had changed since the measurement by the Greek astronomer Hipparchus (190-120 BC) [4]. After this, the tangential proper motions of stars were measured this indicating which stars were the closest. One of the closest stars seemed to be 61 Cygni. The measurement of its parallax was performed by Friedrich Bessel in 1838 [5] which gave a distance of 3 pc. At the time of [2], 35 star distances were known. Using these measurements and the assumption that all stars have the same brightness, Wilhelm Struve estimated the size of the Milky Way, about 4 kpc. The parallax measurement was fastidious and limited to a few hundred parsecs.

1.1.2 Spectroscopy

In the 19th century, scientists started to use spectroscopy in astronomy, initialized by Joseph von Fraunhofer. Apart from important discoveries concerning the composition of the stars, spectroscopy brought essential information on the radial movement of these stars which was still inaccessible. In 1868, William Huggins and William Allen Miller started to measure in 1868 the shift in the spectrum of different stars [6] and gave the corresponding radial velocities, about 20 to 200 km/s. In the same year, Huggins published a paper in which he described the observed spectrum of Andromeda. He wrote: *The spectrum* [is] *similar to that of an ordinary star* [7]. This result was a strong argument in the old debate on the “island universe” which we shall introduce later.

1.1.3 Mean parallax

At the beginning of the 20th century, Jacobus Kapteyn came with a new distance measurement technique called the mean parallax based on a correlation between parallax and proper motion. Indeed, as mentioned in section 1.1.1 for 61 Cygni, the fact that this star has a large proper motion was a hint of its proximity. The same reasoning holds for the magnitude and the proximity. Based on a catalog of 133 stars with known parallax, proper motion, and magnitude and under the assumption that the motion of stars is random, Jacobus Kapteyn established a relation between all these quantities [8]. This relation allowed us to compute the expected parallax (and then its distance) of a star by knowing its magnitude and proper motion. Although this method was theoretically able to estimate the distances of objects up to 10 times farther away, we know today that the stars turn around the center of the Milky Way such that the assumption of random velocity was false. As nicely explained in [3]: *Kapteyn was in the habit of visualizing his data by plotting points or drawing vectors with white chalk on globes covered with blackboard material, and when he did this with the velocities of the stars in his study, he saw a distinct pattern emerging on the celestial sphere.* His tentative to measure distances then turned to evidence for a global flow of the stars.

1.1.4 Cepheids

In 1908, Henrietta Swan Leavitt published a catalog of 1777 Cepheid variables in the Magellanic clouds [10]. These types of stars have variable magnitudes and have been observed at least since the 18th century [11]. Table VI of [10], 16 Cepheid variables with

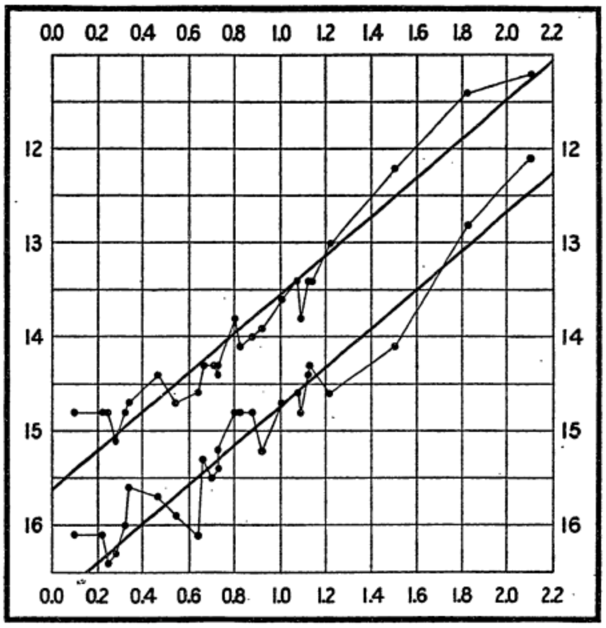

Figure 1.2: Original plot published by Henrietta Swan Leavitt in [9]. On the y-axis, the maximum and minimum observed magnitudes for the upper and the lower curves. The x-axis shows the logarithm of the periods.

their maximum and minimum magnitudes and periods are summarized. It is mentioned for the first time that a relation between the brightness and the period could exist. She wrote: *it is worthy of notice that in Table VI, the brighter variables have the longer periods.* However, the number of measured periods was too small to conclude. In 1912, Leavitt published the relation that will be used in future discoveries in cosmology [9]. Strictly speaking, the relation established in figure 1.2 shows that the observed magnitude M_{obs} is related to the period following a power law:

$$M_{obs} = a\,(\log_{10} P - 1) + b_1 \tag{1.1}$$

The observed and intrinsic magnitudes, M_{obs} and M, are related:

$$M_{obs} - M = 5\,(\log_{10} d - 1) \tag{1.2}$$

where d is the distance. The 25 Cepheids studied are all contained in the Magellanic cloud so that their distances from the Earth are assumed to be nearly the same so that $M_{obs} = M$+constant. Thus, Leavitt could concluded that:

$$M = a\,(\log_{10} P - 1) + b_2 \tag{1.3}$$

Furthermore, she measured the slope $a \simeq -2$. The first calibration, *i.e.* measurement of b_2, of the relation was performed by Ejnar Hertzsprung in 1913 [12], by measuring the distances of close Cepheids using the parallax. One of the last measurements was performed in 2007 [13] using the Hubble space telescope and gave $a = -2.43 \pm 0.12$ and $b_2 = -4.05 \pm 0.02$. Leavitt's law was used intensively because, once it is calibrated, we can use it to compute maximum (or minimum) intrinsic magnitude from the period, which is easily measurable. Then, knowing the observed luminosity, which is also easily measurable, we can use the relation (1.2) to find the distance d. This way, Ejnar Hertzsprung was able to determine the distance of the Small Magellanic cloud [12] and give a value of 1 kpc. It turned later out to be underestimated. However, it shows the great potential of the Cepheids. Until then, the largest distance measured could not exceed 30 pc using the geometric parallax method so that the measurable universe was confined to our galaxy.

1.1.5 Globular clusters

Starting from 1914, Harlow Shapley studied globular clusters. Today, we know that these objects contain 10^5 to 10^7 stars. Shapley believed they could be similar in size as the Milky Way, *i.e.* of the order of 3 kpc as it was believed at that time. In 1915 already, he found Cepheid variables in the Hercules cluster and gave a distance of 30 kpc [14] and also re-measured the distance to the Small Magellanic cloud and found 20 kpc. One of the main contributions of Harlow Shapley to our vision of the universe came in 1918 when he determined the position of all the 69 known globular clusters of this time using 3 methods to estimate the distances. For the clusters in which a Cepheid was observed, he used Leavitt's law. He assumed that the brightest stars were as bright as the brightest stars in other globular clusters for the clusters without Cepheids. Finally, for the clusters that were so far away that even the brightest stars could not be seen, he assumed shape similarities [15, 16]. He remarkably noticed that the globular clusters are "subordinate to the general galactic system" since their position indicates they are outside the galactic disk. Moreover, he noticed that the geometrical center of the system consisting of all globular clusters coincides with the highest density of stars of the Milky Way. He interprets this center as the center of the galactic system.

1.1.6 Galaxies

Galaxies, known today as being galactic systems like our Milky Way, can contain about 10^{11} stars, have been observed at least since the 10th century, the date of the earliest known observation of the Andromeda galaxy by Al-Sufi. Until the 20th century, the difference between nebulas, globular clusters, and galaxies was unknown. For John Herschel, the fact that he could see a cluster of stars with his powerful telescope instead of a nebula without stars, as described in previous observations, was an indication that any nebula was, in fact, an island universe similar to our Milky Way with the "nebulosity" indicating how far away the system is [3].

In addition to the previous spectral observations done by Huggins, see 1.1.2, in 1915 Vesto Slipher came up with more spiral nebula spectra and noticed that except for Andromeda and its neighbor M32, all the spirals have a redshift in the spectrum that indicated that these galaxies are moving away from us.

Thanks to the observations of William Parsons around 1860, astronomers believed that the spiral shape of some nebulas was due to a rotation, see for example [17]. The actual evidence of rotation was performed by Adriaan van Maanen in 1916 [18]. It turned out later that Van Maanen was biased by systematic effects that explained all observations.

One year later, Heber Curtis published a note on the "new stars" appearing in spiral nebulas [19]. First, he argued that if we observe a similar number of novas in a spiral nebula that should mean that it contains the same number of stars as the Milky Way since we also observe such few even in it. Secondly, he pointed out that 27 similar new stars had been observed in the Milky Way with a magnitude of about 5. Assuming these events should have a similar intrinsic magnitude, he concluded that the spiral nebulas

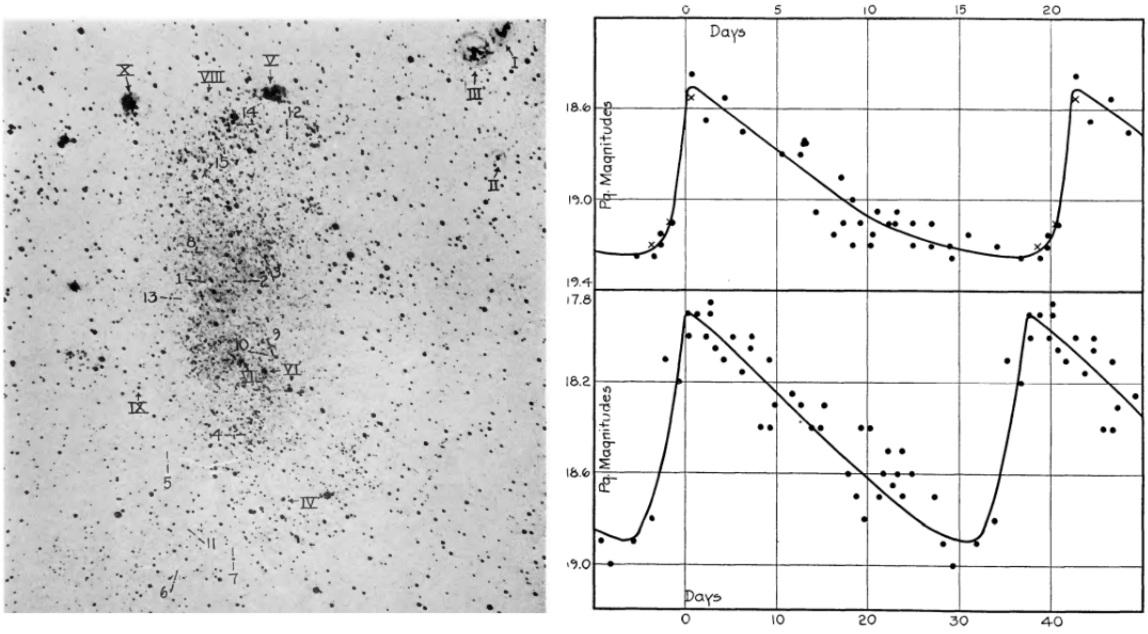

Figure 1.3: On the left, the negative of the plate of N.G.C. 6822. The Arabic numbers designate the variables or suspected variables. No variables are found outside the system so that those observed are considered as being part of N.G.C. 6822. The Roman numerals designate supposedly non-galactic nebulae. On the right, the light curves of two Cepheids (number 6 above and 2 below). Credit [21]

should lie at a distance of 6 Mpc. Moreover, if we assume such a distance, given the apparent size of the spiral nebulas, we can show that their intrinsic size should be similar to what it was believed for the Milky Way at that time. The same conclusion was reached by Harlow Shapley around the same time [20]. However, as discussed in 1.1.5, one year after, Shapley showed that the globular clusters, which were also believed to be island universes, form a system gravitationally bound to the Milky Way.

Also, in the novas analyzed by Curtis, he voluntarily dropped one nova, S Andromedae, which was the first discovered outside our galaxy in 1885. Indeed, its magnitude was 2 times smaller than all the other ones and hence not representative. For Shapley, if the distance of this event was of the order 300 kpc, thus the intrinsic luminosity would be crazy. He wrote: *a luminosity nearly a hundred million times that of our sun, the equivalent of light emission of a million stars of zero magnitudes, and probably, therefore, much greater than the total light of all the stars seen with the naked eye* [20]. Finally, the discovery of the rotation of spiral nebulas by Van Maanen would imply with such a distance a rotational speed larger than the speed of light. These ideas were those exposed in 1921 during the "great debate" opposing Shapley and Curtis on the nature of the spiral nebulas. Today, we know that S Andromedae was indeed not comparable with the usual novas. It was a supernova; 10000 times brighter than the novas, which explains why it was only two times less bright than the Milky Way novas while it lies in Andromeda.

The question of the island universes was finally answered by Edwin Hubble in 1925 when he found Cepheid variables in N.G.C. 6822, the Andromeda, and the triangle nebula. In the figure 1.3, we can see one of the original plates of N.G.C. 6822. The variables are indicated with Arabic numbers and eleven of them (1 to 11) are confirmed and used for the measurement. Two of the light curves are shown on the right panel of figure 1.3. The estimated distance of N.G.C. 6822 was 210 kpc which makes this small galaxy, similar in size to the Magellanic clouds *the first object definitely assigned to a region outside the galactic system* [21], *i.e.* not gravitationally bound to the Milky Way. Andromeda was the third after N.G.C. 6822 and the triangle galaxy whose distance was estimated one years later at 260 kpc [22]. Andromeda came in 1929 [23] with an estimated distance of 270 kpc. All these distances were underestimated; the most recent values, in the same order are 500 ± 10 kpc, 847 ± 60 kpc, 778 ± 17 kpc.

1.2 General Relativity

Our conception of the universe has been boosted by the theory of general relativity (GR). Today, it is a very successful theory and our complete understanding of the universe's history depends on it. To understand how it came up, we have to return to the 19th century.

1.2.1 Electromagnetism

The work of Thomas Young and Augustin-Jean Fresnel at the beginning of the 19th century showed that light was acting like a transverse wave. It was supposed that this nature came from the oscillation of an elastic medium called aether. When James Maxwell formulated the theory of electromagnetism in 1864, he found propagating wave equations for the electric and magnetic fields [24]. This equation says that the waves propagate with an invariant speed determined by the property of the propagating medium: $v^2 = 1/\varepsilon\mu$ where μ is the permeability and ε the permittivity of the medium. He noticed that from electromagnetic experiments, the value obtained for v was very similar to the light speed measurement. He wrote: *The agreement of the results seems to show that light and magnetism are affections of the same substance, and that light is an electromagnetic disturbance propagated through the field according to electromagnetic laws.* At the end of the 19th century, the theory of James Maxwell was well accepted and experimentally tested, but the invariance of the speed of light that had been confirmed by the famous Michelson–Morley experiment in 1887 was not well understood.

1.2.2 Special relativity

The last try based on a motionless aether was the theory of Hendrik Lorentz [25]. In this theory, he notably introduced as an additional assumption the so-called Lorentz transformations implying length contraction to explain the experimental results. At the same time, Henri Poincaré was trying to build a theory based on the principle of relativity discussed in [26, 27]. A few days before the famous publication of special relativity by Albert Einstein, Poincaré generalized the recent development made by Lorentz, *i.e.* the electromagnetic field equations are invariant under his Lorentz transformation, and derives the relativistic velocity addition law [28, 29]. He also noted that the Newtonian gravitational law does not satisfy this invariance and supposed that if it would, then gravity would propagate at the speed of light in the form of *gravity waves*. Poincaré and Lorentz anticipated many results and principles used by Einstein but both of them always interpreted their results as artifacts of our motion in aether. The first complete and coherent formulation of special relativity was published by Einstein in [30]. It is based on the principle of relativity and on the fact that the speed of light is invariant without needing any additional aether.

1.2.3 General relativity

Albert Einstein then came to the question of changing the classical theory of gravity to make it compatible with its theory of special relativity. With the equivalence principle as a starting point, he found that the Lorentz transformation would be violated and that a relativistic theory of gravitation has to use non-Euclidean geometry as developed by the mathematicians Riemann Ricci and Levi-Civita. With Marcel Grossmann, he introduced in 1913 this formalism to describe gravity [31]. The final step to build the correct equation is accomplished simultaneously by Einstein, and David Hilbert in 1915 [32, 33]. The original form of the equation in Einstein's article was:

$$G_{im} = -\kappa \left(T_{im} - \frac{1}{2} g_{im} T \right) \tag{1.4}$$

where G is the Ricci tensor, T_{im} is the stress-energy tensor, T is the trace of T_{im}, g_{im} is the metric and κ a constant factor.

The first important result of GR came immediately in the same article [32] where it is shown that it predicts a precession of the perihelium of Mercury of $43''$ per century. This experimental result was determined in 1859 by Urbain Le Verrier. After removing the influence of every known planet of the solar system, he concluded that either the mass of Venus should be larger or there should be another unknown planet or group of small planets [34].

It is worth noting that a similar orbit perturbation was observed for Uranus. It led to the discovery of Neptune thanks to the computation of Le Verrier and the observations of Johann Gottfried Galle in 1846. However, in the case of Mercury, no extra planets have ever been discovered to explain the orbit of Mercury. But, the theory of GR produced the same shift without any additional planet.

The second test was performed by Dyson, Eddington, and Davidson, thanks to a solar eclipse in 1919. Indeed, as they explain in [35], the eclipse is an occasion to look at stars close to the sun. There are 3 possibilities:

- The path is not influenced by gravitation, and the positions of nearby stars are unchanged.
- Light is subject to gravitation and follows the Newtonian law strictly; this leads to an apparent displacement of a star close to the sun by an angle 0".87.
- Light is following Einstein's generalized relativity theory, which leads to an apparent displacement of a star by an angle 1".75, *i.e.* two times the angle obtained with Newtonian theory.

The measurements led to the second great success of GR. They conclude: *Thus the results of the expeditions to Sobral and Principe can leave little doubt that a deflection of light takes place in the neighborhood of the sun and that it is of the amount demanded by Einstein's generalized theory of relativity, as attributable to the sun's gravitational field* [35].

Therefore the two similar problems, the orbits of Uranus and Mercury, led to two opposite solutions. In the case of Uranus, the discovery of Neptune remarkably confirmed

Newton's theory of gravitation. For what concerns Mercury, it led to the confirmation of GR, thus excluding the theory of Newton.

1.3 Relativistic cosmology

1.3.1 The universes of Einstein and de Sitter

The first relativistic model of cosmology using GR came in an article of 1917 by Einstein himself [36]. The Einstein equation (1.4) needs boundary conditions at infinity. Assuming the Mach assumptions, which suppose that distant objects cause inertia of bodies, Einstein came up with two unsatisfactory solutions; either we require a suitable choice of the reference frame at infinity, and the metric there is the Minkowski metric, or we claim no general validity, and we have to choose the boundary condition in each case. This second possibility is for Einstein equivalent to giving up. However, the first possibility breaks the relativity principle as it prefers some coordinate system and would also be in contradiction with the Mach principle. Indeed in this option, material points alone in the universe would have inertia almost as large as in a universe full of matter. Einstein supposed a finite and closed universe to overcome this boundary condition problem: a hypersphere of radius R independent of time. Next, he supposed the *cosmological principle* defined as follows: *But if we are concerned with the structure only on a large scale, we may represent the matter to ourselves as being uniformly distributed over enormous spaces* [36] However, to preserve a static universe, he modified (1.4) by including an additional term $-\lambda g_{\mu\nu}$ on the right-hand side by arguing that it does not destroy the general covariance. He then solves the equation and concludes that it is satisfied if:

$$\lambda = \frac{\kappa\rho}{2} = \frac{1}{R^2} \tag{1.5}$$

where ρ is the mean density of matter and R the radius. He arrived at this conclusion because of the assumption of a static universe and did not see that this solution was unstable. This constant λ is called today the cosmological constant, has led to much discussion for at least four reasons:

- Albert Einstein could have predicted the expansion/contraction of the universe with or without λ and even with the very fine-tuned value because that solution is unstable. Einstein called this constant the biggest blunder of his life after discovering the universe's expansion.

- There has been much discussion on whether he introduced this term only to preserve a static universe or if he knew about this term before, see for example [37]. In an earlier work in 1916 [38], Albert Einstein derived the vacuum equation $R_{\mu\nu} = 0$ where $R_{\mu\nu}$ is the modern notation of the Ricci tensor. In a footnote, he noted that the general equation is actually $R_{\mu\nu} + \lambda g_{\mu\nu}(g^{\alpha\beta}R_{\alpha\beta}) = 0$ which reduces to the previous one. In the original version of the article, the Ricci tensor was noted by $B_{\mu\nu}$, and in the English translation, it became G, the latter being also used for the Einstein tensor that is defined with respect to the Ricci tensor R as $G_{\mu\nu} = R_{\mu\nu} - 1/2 g_{\mu\nu}R$. By reading the English version ($G_{\mu\nu} + \lambda g_{\mu\nu}(g^{\alpha\beta}G_{\alpha\beta}) = 0$), we can then easily be confused and think that already in 1916, Albert Einstein knew about the cosmological constant. As we said, this second term Einstein had in his paper from 1916 is the trace part in the Einstein tensor, $1/2 g_{\mu\nu}R$, where he wrote a more general constant λ instead of $1/2$.

- As we will see later, the discovery of the acceleration of the universe's expansion in 1998 made the cosmological constant one of the central parts of the modern standard model of cosmology.
- Quantum field theory predicts a vacuum energy that could act as a cosmological constant, but a naive computation differs from the cosmological measurement by 120 orders of magnitude, often called the worst prediction of physics.

The Einstein universe is often summarized as this blunder. However, we must underline that this work is a first demonstration of the abilities of GR to describe the universe using the cosmological principle, and it opens up the question of the global geometry of the universe, if it is finite or not, that was previously only a philosophical question.

Willem de Sitter, in 1917, tried to give an estimate of R based on the current observational data [39]. Based on different reasoning regarding the mean density of the center of our galaxy estimated by Kapteyn and regarding the found distances of spiral nebulas assuming they are objects similar to our galactic system, he found $R \sim 3$ Mpc.

In the same paper, de Sitter found another solution of the Einstein equation, assuming that the metric tends to zero at infinity. Contrary to Einstein, he supposed that the effect of matter induces deviations from the boundary conditions according to his equation, and then if all the coefficients of the metric tend to zero at infinity, the whole inertia and gravitation will be determined by the local matter. The solution he found is the one of an empty universe dominated by the cosmological constant [39]:

$$\rho = 0, \qquad \lambda = \frac{1}{R^2} \tag{1.6}$$

This universe has a positive and constant curvature and is stationary because there exist coordinates where all the metric coefficients are constant. De Sitter found that coordinate system, the so-called comoving coordinates. In this universe, the frequency of propagating light decreases with distance, systematically giving a redshift in the spectrum of distant galaxies. Slipher had provided such observations, but their number was not large enough to conclude. De Sitter then concluded by noting that if future observations were to measure more redshifts, it would corroborate his hypothesis and rule out the one of Einstein. Based on Slipher's observations and assuming their distance was about 0.1 Mpc, he found $R = 0.3$ Mpc.

The precise linear relation between the recession velocity and the distance of objects in this universe (we speak here about test particles since the universe is empty) was found by George Lemaître in 1926 [40]. He noted that the coordinates of de Sitter in which the universe is static introduce an artificial center. He then gave new coordinates to solve this problem, in which the lines of constant space are also geodesics. In these new coordinates, he found that de Sitter's universe is not static anymore; an exponentially time-dependent spatial scale factor appears explicitly in the metric. He derived the linear relation in these new coordinates and concluded that this provides a possible explanation for Slipher's observations. However, he also found that this universe has a vanishing constant curvature. At that time, as we explained for Einstein, the idea of an infinite universe was not physically imaginable. For this reason, Einstein assumed a closed universe and Lemaître rejected the de Sitter universe. He wrote explicitly as a conclusion: *De Sitter's solution has to be abandoned, not because it is non-static, but because it does not give a finite space without introducing an impossible boundary* [40]. In his article in 1927 [41], he nicely explains the dilemma between the Einstein and the de Sitter universe:

- The De Sitter universe ignores the presence of matter but can explain the recession speed of the nebulas observed by Slipher.
- The Einstein universe takes into account matter but is static.

This dilemma will be resolved first by Friedmann and then independently by Lemaître.

1.3.2 The Friedmann Universe

In 1922, Alexander Friedmann published his first fundamental paper about cosmology [42]. He started from two classes of assumptions. First, he assumed, as Einstein and De Sitter, that the metric satisfies the Einstein equation (1.4), including the cosmological constant, and that matter has a low speed with respect to the speed of light. Thus, he only included non-relativistic matter, which has a vanishing pressure term. Secondly, he wrote the line element ds^2 as follows:

$$ds^2 = R^2(x_4)\left(dx_1^2 + \sin^2(x_1)dx_2^2 + \sin^2(x_2)dx_3^2\right) + M^2 dx_4^2 \tag{1.7}$$

He considered a closed universe and included the Einstein and de Sitter universes with a special value of M and R^2. Of course, the crucial thing here is that the curvature may depend on the time, denoted here as x_4. Then, he solved the Einstein equations and found two cases; either the time derivative of the curvature is zero or the spatial derivative of M is zero. Assuming the first case, *i.e.* a static universe, he derived the two only solutions: the Einstein and De Sitter solutions. In the second case, he opened the question of the universe's history by deriving the so-called Friedmann equations (for a positive curvature universe and not including the pressure term). It is a system of two differential equations:

$$\begin{aligned}&\left(\frac{R'}{R}\right)^2 + \frac{2RR''}{R^2} + \frac{c^2}{R^2} - \lambda = 0\\&\left(\frac{3R'}{R}\right)^2 + \frac{3c^2}{R^2} - \lambda = \kappa c^2 \rho\end{aligned} \tag{1.8}$$

These equations do not give a specific value for λ. Considering it is an arbitrary value, he found an infinite number of solutions, depending on the choice of λ, leading to a monotonic or a periodic dynamics. GR became, in these articles, a theory conceptualizing a history of the universe that depends on its contents and this constant λ. He computed as an illustrative example the age of a universe where $\lambda = 0$ and with a mass 5×10^{21} solar masses: 10 billion years which, almost one century later, sounds like a remarkable intuition. In 1924, he gave the equivalent of (1.8), but for a constant negative curvature [43], *i.e.* the same equations as (1.8) with the opposite sign for the $1/R^2$ terms, and he also discussed the equivalent of a static De Sitter universe. The universe with constant positive curvature studied before has a finite volume, but the field equation also allows constant negative curvature with infinite volume. Thus, Friedmann concluded: *the universe equations alone are not enough to conclude on the finiteness of the universe.* A few years later, in 1927, Lemaître independently re-discovered the results of Friedmann, *i.e.* equation (1.8) but including, in addition, a pressure term [41]. He understood that it can describe the radiation pressure and wrote that even though it is very weak, it could be important when considering the whole universe.

1.3.3 Galactic redshift

The observation made by Slipher in 1915, see 1.1.6, that most of the galaxies are moving away was the first evidence of the expansion of the universe. Gustaf Stromberg extended this observation in 1925 when he published a complete catalog of radial velocities of galaxies [44]. Using this catalog, he determined the velocity of the sun with respect to the galaxies. In 1926, Hubble published a classification of the extra-galactic objects depending on their apparent shape (elliptic, spiral, or irregular) [45]. He established an empirical relation between the intrinsic magnitude and the maximum diameter for each type of shape. Then, using the distance of galaxies already known, he established a relation between the distance and the intrinsic magnitude:

$$\log D = 4.04 + 0.2M \tag{1.9}$$

where D is the distance and M the intrinsic magnitude. In the same paper, Hubble noted that his observation seems consistent with a uniform density of space. He then measured the density of nebulas and thus derived the density of matter in the universe. Knowing the density of the universe, he re-estimated the radius of the closed Einstein universe: 27 Gpc, which represents about 600 times the distance measured for the farthest spiral nebula known at that time.

In 1928, Lemaître, after having re-discovered the Friedmann equations, established in a non-static universe of constant positive curvature the relation between the recession velocity and the distance [41]:

$$\frac{v}{c} = \frac{R'}{R} D \tag{1.10}$$

where v is the radial velocity, R the curvature, and D again the distance (this relation is the equivalent of the one he found in the De Sitter universe [40]). Using the empirical law found by Hubble (1.9) and the velocities given by Stromberg and Slipher gave the first estimation of the Hubble constant $R'/R = H_0 = 625$ km/s/Mpc [41].

More robust evidence of the so-called Hubble's law, *i.e.* equation (1.10), came two years later, in 1929 [23]. At this time, 46 extra-galactic velocities were known, but only 24 distances had been determined by using Cepheid stars or by supposing the magnitude of the brightest stars to be similar. Assuming the velocity varied linearly with the distance, Hubble found $H_0 = 500$ km/s/Mpc. He did not mention the work of Lemaître and Friedmann and thus only interpreted his result as evidence for the de Sitter cosmology. In addition to discovering the universe's expansion, the redshift measurements, together with Hubble's law, provide a new way to measure distances. Galaxy's redshift measurement provides its distance once the law is calibrated.

The article [41] was written in French. Arthur Eddington translated this article but, as asked by Lemaître, without the part containing the derivation of (1.10) and the estimation of H_0. On the other hand, Hubble measured in a more direct a precise way H_0 (without using the empirical law (1.9)). For this reason, the law (1.10) and the quantity H_0 are referred to as Hubble's law and Hubble's factor.

1.3.4 The Lemaître Universe

In 1931, Lemaître developed a model of the universe in which he tried to take into account the formation of the nebulas and the observed speed of the expansion of the universe [46, 47]. The expansion rate measured by Hubble, around $H_0 = 500$ km/s/Mpc, was quite large and would imply an age of the universe of 2 billion years, while the estimate of the age of the Earth with uranium was about 4 billion years. Hence, the cosmological constant was fundamental to accelerating the universe's expansion to the large observed value.

A more structured version is published in 1933 [48]. In particular, he developed the idea of a cyclic universe, also called the Phoenix-universe. This kind of universe is one of the solutions found by Friedmann, *i.e.* the periodic one. It starts with a singularity, expands until a maximum size, and then re-collapses into a singularity. He showed that we cannot avoid the appearance of a singularity even with exotic equations of state.

1.4 Foundation of the standard model

The discovery of Hubble and Lemaître was strong evidence for an expanding universe that ruled out both the universes of Einstein and De Sitter. In 1932, Einstein and de Sitter published a concise paper introducing a very "minimal" model of an expanding universe: a universe with no pressure, no curvature, and no cosmological constant. This model lasted for decades as a reference and is still an accurate approximation of the universe in the so-called matter domination era. We will use in the second and the third part of this thesis this Einstein-de Sitter (EdS) model. However, and in parallel, Lemaître elaborated a much more complicated model trying to fit observations and, more importantly, trying to figure out the primordial universe.

1.4.1 The cosmic microwave background (CMB)

From 1931, Lemaître started to develop a very early model of the primordial universe. Since the universe is expanding, if we go back in time, the size of the universe has to decrease and the energy density to increase. Inspired by the new quantum theory, he imagined that the universe originates from a single primordial atom that decays [49, 50]. He thought that the cosmic rays could have for origin the decay of this primordial quantum. This theory suffered from a lack of observational data.

Later, in 1946, George Gamow took up the idea of an expanding dense early universe to explain the origin of the abundance of chemical elements [51]. With his Ph.D. student Ralph Alpher, they developed this idea and were able to predict the abundance of light elements. After these first steps regarding Big Bang nucleosynthesis, the first computation of cosmological black-body radiation was performed by Alpher and Robert Herman in [52]. This article was published in the journal Nature and corrected some errors of a previous article of Gamow, also published in Nature [53]. Having fixed the mistakes, they extended the computation and found that, long after nucleosynthesis, the universe became transparent. The residual temperature of the black-body emission that should be emitted at this "recombination time" should be 5K today. This computation was improved afterward and until 1965, many different estimations were computed. Because of the overestimation of the Hubble factor and the use of the wrong EdS universe, the CMB emission was estimated to happen 30 million years after the Big Bang instead of the 380 000 years that we now know to be the correct result [54].

The first measurement of the CMB temperature was performed by chance in 1964-1965 by two engineers: Arno Penzias and Robert Wilson. They were working on an ultra-sensitive cryogenic microwave antenna for radio astronomy. By testing their antenna, they observed a noise that they could not explain. They concluded in their article

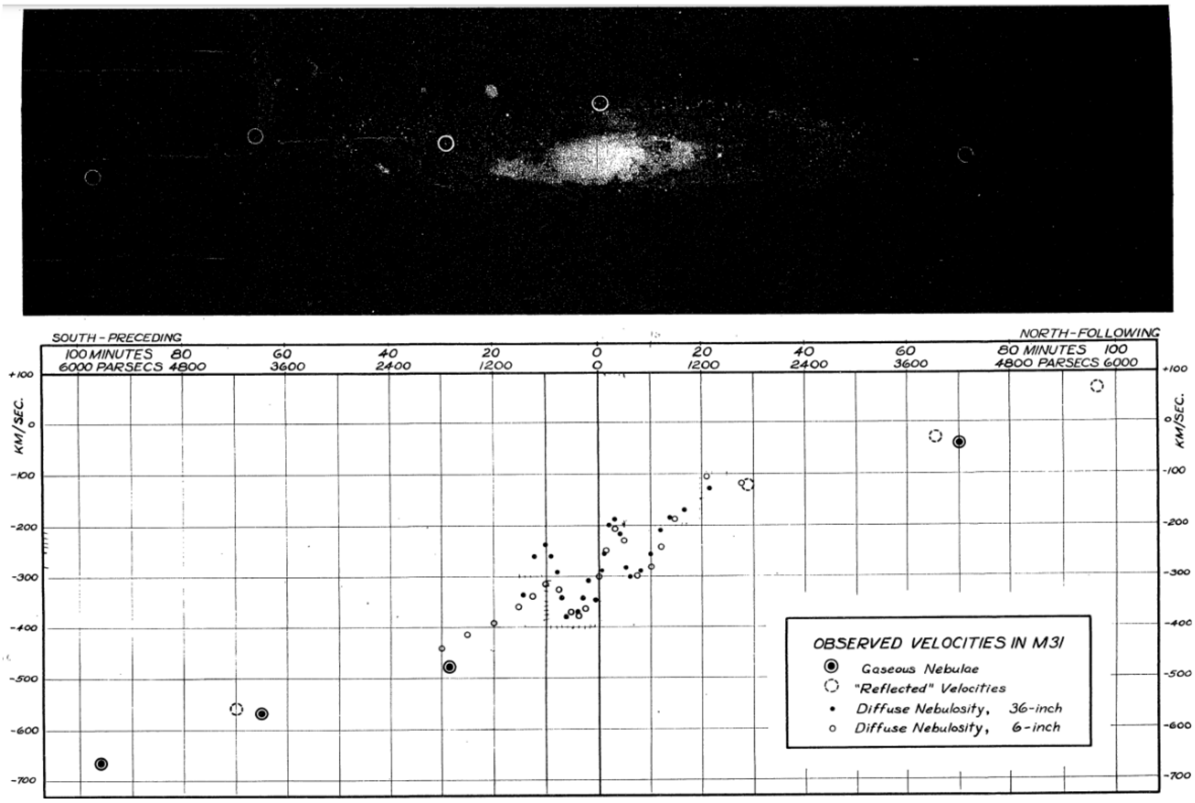

Figure 1.4: Top: the photographic plate of the Andromeda galaxy used for the measurement of the velocities. Bottom, the velocity measurement of for different type of object, as indicated in the legend. The x-axis of the top and bottom panel are the same. Taken from [58]

[55]: *This excess temperature is, within the limits of our observations, isotropic, unpolarized, and free from seasonal variations.* They measured a temperature of 3.5K. The theoretical interpretation was done in a companion paper written by Dicke, Peebles, Roll, and Wilkinson [56]. This team was working on the Phoenix universe and noted that the entropy production could lead to a relic thermal cosmological background. They were building their antenna to measure the CMB and were finally “scooped” by Penzias and Wilson.

This measurement was the first in a long series that is still ongoing. The discovery of the temperature fluctuations and the most precise frequency spectrum was made by the satellite COBE in 1992, see the last release [57]. Then the ground mission DASI discovered in 2002 that the CMB is polarized at a level of 10% and finally, the most precise measurements of the temperature and polarization fluctuations were performed by the satellites WMAP (2001-2012) and Planck (2009-2018). In this thesis, we will use the Planck data to constrain a class of models of the early universe.

1.4.2 Dark matter

One of the fundamental components of our cosmological model is the so-called *dark matter*. Originally, this name encompassed all forms of matter that do not emit light. For instance, it could be composed of planets, gas, or neutrinos, *i.e.* well-known objects that cannot be detected as simply as the stars. Already in 1922, Kapteyn used this denomination and explained that, if our cosmological model is correct: *it may be possible to determine the amount of dark matter from its gravitational effect* [59]. Of course, at that time, the cosmological model refers to the Milky Way model.

The first measurement of a large discrepancy between the observed mass and the gravitational mass is attributed to Fritz Zwicky. Indeed, in [60], he determined the velocity of the Coma cluster galaxies using the Doppler effect. He found a medium-sized Doppler effect of 1000 km/s. Supposing that the cluster is stationary, he used the Virial theorem to determine the mean velocity from the observed mass of the system. He found 80 km/s. One of the explanations he explored is that the gravitational mass of the cluster might be 400 times larger than the luminous mass.

Further measurements came a few years later with the measurement of the rotation curve of the Andromeda galaxy by Horace Babcock. He measured the rotation speed of different objects as a function of the distance to the center of the host galaxy. He found that the velocity tends to increase for increasing distance to the center, with the angular velocity tending to a constant [58]. This can be seen in the original figure 1.4. This would mean that the matter density increases with the radius and in particular, a large part of the mass should be located in the outer part of the galaxy. The ratio of the gravitational mass to the luminous mass is found to be 50. This work was confirmed during the 1970s by the work of Vera Rubin, Kent Ford, and Ken Freeman who presented strong evidence for dark matter in, *e.g.* [61].

Strong evidence for the existence of a dark matter component of our universe, such as the rotation curves, the structure formation, the CMB, the lensing, makes it one of the main ingredients of the current standard model of cosmology. However, none of the particle accelerators or low-energy experiments have been able to find a particle compatible with the observed dark matter yet. In this thesis, the dark matter component is central. In the second part, we will constrain the variation of the composition of the dark matter. In the third part, dark matter is assumed to be the only component of the universe in our simulations.

1.4.3 Inflation

The model developed first by Lemaître, Gamow, Alpher, and Herman is called the *Hot Big Bang* model. To summarize, it supposes that the universe is expanding and was a long time ago in a dense and hot state. This model can predict the abundance of light elements thanks to the mechanism of nucleosynthesis and an early radiation emission called the CMB which has been detected by Penzias and Wilson. However, this model suffers from at least 4 theoretical problems.

The *horizon problem*

The first one is the *horizon problem.* In cosmology, we generally define two kinds of horizon: the *event horizon* and the *particle horizon.* These definitions have been clarified in [62]. The horizon problem concerns the *particle horizon* (the *event horizon* will be described in section 3.1). The particle horizon *is a surface in the instantaneous 3-space* $t = t_0$*, which divides all fundamental events into two non-empty classes: those that have already been observable by* A *at time* t_0 *and those that have not.* Note that if one of these two classes is empty, then the horizon does not exist.

In the Hot Big Bang, one can calculate that the particle horizon at the time of the CMB emission should have an angular appearance size of a few degrees [63]. This means that two regions further apart than this angular size had never interacted at the time of the CMB emission. Hence, the CMB should be anisotropic on scales larger than this horizon, which is in contradiction with the observations. We even have stronger constraints from nucleosynthesis which happens a few minutes after the Big Bang and from which we know that the observable universe should already be homogeneous at that time. Hence, it seems that the particle horizon is much larger than the theoretical prediction, this is the horizon problem.

The *flatness problem*

The second is the *flatness problem*. It was pointed out by Robert Dicke in [64]. The point is that, as we will see in the following chapter, one can define a critical density ρ_{cr} which corresponds to the density of a universe with no curvature. If the actual density of the universe is $\rho > \rho_{cr}$ ($\rho < \rho_{cr}$), that means that we live in a closed (open) universe. The quantity $\rho/\rho_{cr} - 1$ represents the curvature of the universe. The problem originates from the fact that the point $\rho = \rho_{cr}$ is unstable in the "standard" universe. The evolution time scale of the density is $\sqrt{\kappa} \sim 10^{-44}s$ where κ is given in equation (1.8). For instance, a closed universe will reach its maximum size and an open universe would be diluted in this time scale [65]. We know that the universe is $\sim 10^{10}$ years old and we also know that $\rho/\rho_{cr} = 0.9993 \pm 0.0037$ [66]. Hence, for the universe to reach $\rho/\rho_{cr} \sim 1$ after $\sim 10^{10}$ years, the initial value of the curvature $\rho/\rho_{cr} - 1$ should be of order 10^{-60}.

The *inhomogeneity problem*

As explained in the horizon problem section, the universe is observed to be homogeneous at large scales. The deviations from homogeneity and isotropy are observed to be of order 10^{-5}. As we shall see in the third part of this thesis, the density inhomogeneities tend to grow with time by gravitational collapse. To explain the observations, the initial conditions should be extremely close to homogeneity. This is again a fine-tuning problem. Moreover, where do these very small inhomogeneities come from? Without these, no galaxies or any small structure could form.

The *monopole problem*

This problem arises in grand unified theories of elementary particle physics. These theories are based on a simple gauge group with symmetries valid at the highest energies of the theory. When the energy decreases, spontaneous symmetries breakings take place at different energy scales to give the known gauge groups of the three fundamental forces: electromagnetism and the weak and strong nuclear interactions. During this process, stable particles carrying a monopole charge, which we do not observe, are produced with other topological defects [65].

One single solution: *Inflation*

These problems were discussed in the literature for a long time. The Phoenix universe was thought to be a possible solution for the horizon problem [67]. Indeed, the whole universe could have first collapsed into a singularity where the particle horizon would vanish. However, this model suffers from the entropic production problem [68]. The start of a solution was pointed out in [69], where Demosthenes Kazanas remarks that a nearly exponential expansion can *lead to a horizon-free universe which might, in turn, be isotropic*. This can be used as a definition of inflation: a period where the expansion is nearly exponential which corresponds to a nearly-de Sitter universe. A formal definition will be discussed in detail in the next chapter 2.

As for most discoveries, precursor studies were performed regarding inflation. We have cited the work of Kazanas [69]. We should also point out the work of Starobinsky [70] who noted that supergravity corrections of the form R^2 which R the Ricci scalar could become important in the early universe, leading to a de Sitter expansion. We can refer to [67] for a very complete bibliography on the precursors of inflation.

The first complete picture of inflation is generally accepted to be the one developed in 1981 by Alan Guth [65]. In fact, Guth was a particle physicist and the original motivation for his research was *the monopole problem*. If the particles carrying a monopole were produced in the early universe, they could be diluted by a phase of inflation. If inflation occurred at an energy lower than the mass of these particles, the problem would be solved.

After the first formulation of an inflationary period [65], many others have followed, see [71] for a very complete review of the historical models of inflation. We simply point out here that the standard model of inflation, *i.e.* the slow-roll inflation that will be described in this thesis, has been developed by Andrei Linde, Andreas Albrecht and Paul Steinhardt in three articles [72–74].

Finally, the most remarkable prediction of an inflationary period is the generation of tiny fluctuations of density originating from the quantum fluctuations of the scalar field. These fluctuations explain the origin of the density perturbations that have collapsed to form the structure that we observe today. The first computations of the generation of the perturbations were elaborated during the Nuffield Workshop on the very early universe at Cambridge University by Stephen Hawking, Alexei Starobinsky, Alan Guth and So-Young Pi, James Bardeen, Paul Steinhardt, and Michael Turner [75–78]. A similar computation was performed first by Mukhanov and Chibisov in the context of the Starobinsky model [79]. The computation in the context of inflation will be presented in section 3.1 and more generally, this thesis is a small part of a vast project aiming to constrain the inflation models.

1.4.4 The cosmological constant

We cannot finish this historical review without mentioning the last major discovery which definitely rules out the Einstein-de Sitter universe. Two independent teams, the supernova cosmology project led by Saul Perlmutter and the supernova search team led by Brian Schmidt and Adam Riess have shown that the deceleration parameter is negative at a confidence level of 2.8σ, *i.e.* $\Omega_\Lambda > 0$ [80, 81]. They both used a method to determine the luminosity distances of type Ia supernovae that employ relations between SN Ia luminosity and light curve shape. Today, the combination of Planck and baryonic acoustic oscillation measurements leads to $\Omega_\Lambda = 0.6889 \pm 0.0056$ [66] which means that the cosmological constant is the main constituent of today's universe. Many large-scale surveys are motivated by the study of the cosmological constant.

Chapter 2

Modern cosmology

The simplest model able to explain all the observations available is the so-called standard model or ΛCDM. It relies on several hypotheses based on observational facts. The ΛCDM model supposes a flat and expanding universe whose constituents are photons and neutrinos, baryons, and the speculative cold dark matter (CDM) that is however based on strong observational facts briefly exposed in section 1.4. Moreover, we have also explained that more recent observations prove that the late cosmology is dominated by the cosmological constant Λ. The evolution of the universe can be correctly described by general relativity with the so-called *cosmological principle*, *i.e.* a homogeneous and isotropic universe, with small perturbations that can be described using *perturbation theory*. The cosmological principle is today strongly corroborated by cosmological observations. The seeds of the perturbations on super-Hubble scales are supposed to be *adiabatic* and *Gaussian* fluctuations with a nearly scale-invariant spectrum. As we have seen in section 1.4, the flatness and the homogeneity can be obtained with causal dynamics by a period of early *inflation* which dispenses us to set arbitrary initial conditions. Inflation can also generate the adiabatic and Gaussian initial perturbations. A large part of cosmological research is focused on constraining inflation models and this thesis proposes two contributions to achieve this goal.

We will start by introducing general relativity and *perturbation theory*, *i.e.* we will expand the Einstein equations perturbatively around a flat Friedmann-Lemaître-Robertson-Walker universe. Then, we will introduce the statistical tools that are used to constrain the models, mostly the *power spectrum* and the *bispectrum*. Finally, we will present the main results of the simplest inflationary model and discuss one of its extensions which is central to this thesis: multi-field inflation.

2.1 General relativity

General relativity relies on the *equivalence principle*. Following [63], this principle rests on the equality of gravitational and inertial mass. As a consequence, there excits a free-falling coordinate system ξ^μ_X within which the physics is locally (near the point X) that of special relativity.

$$\frac{d^2\xi_X^\mu}{d\tau_p^2} = 0, \qquad d\tau_p^2 = -\eta_{\mu\nu} d\xi_X^\mu d\xi_X^\nu\,, \tag{2.1}$$

where we use the convention $c = 1$ and τ_p is the proper time of the observer and $\eta_{\mu\nu}$ is the usual Minkowsky metric diag$(-1, 1, 1, 1)$. Any coordinate transformation:

$$d\xi_X^\mu = \xi_{X,\nu}^\mu dx^\nu\,, \tag{2.2}$$

where we use the notation $A_{,\nu} = \partial A/\partial x^\nu$, transforms the first equation of (2.1) to the geodesic equation:

$$\frac{d^2x^\mu}{d\tau_p^2} + \Gamma^\mu_{\alpha\beta}\frac{dx^\alpha}{d\tau_p}\frac{dx^\beta}{d\tau_p} = 0, \qquad \Gamma^\mu_{\alpha\beta} = \frac{\partial x^\mu}{\partial \xi_X^\nu}\xi^\nu_{X,\alpha\beta}\,, \tag{2.3}$$

where $\Gamma^\mu_{\alpha\beta}$ is the Christoffel symbol and is not a tensor. The geodesic equation describes the motion of a particle in any gravitational field and coordinate system. The second equation of (2.1) transforms as the generic line element:

$$d\tau_p^2 = -g_{\mu\nu}dx^\mu dx^\mu, \qquad g_{\mu\nu} = \xi^\alpha_{X,\nu}\xi_{X,\mu}\eta_{\alpha\beta}\,. \tag{2.4}$$

The metric tensor $g_{\mu\nu}$ is the principal object that describes gravity by its non zero derivatives. It can be linked with the Christoffel symbol [63]:

$$\Gamma^\alpha_{\mu\nu} = \frac{1}{2}g^{\alpha\beta}\left(g_{\mu\beta,\nu} + g_{\nu\beta,\mu} - g_{\mu\nu,\beta}\right)\,, \tag{2.5}$$

where $g^{\alpha\beta}$ is the inverse of $g_{\alpha\beta}$ such that $g_{\alpha\mu}g^{\beta\mu} = \delta^\beta_\alpha$ with δ^α_β the Kronecker symbol. The equivalence principle states that we can locally cancel $\Gamma^\alpha_{\mu\nu}$, *i.e.* the first derivatives of the metric tensor. All the equations that do not involve ξ^μ_X, *i.e.* the geodesic equation (first equation of (2.3)), (2.5) and the first equation of (2.4) are true at any point.

By analogy with electromagnetism (EM), one can construct a stress-energy tensor that can be used to express the conservation of energy and momentum. In EM, one 4-vector, usually called j^μ, is used to express the conservation of charge: $\partial_\mu j^\mu = 0$. Since in mechanics we have 4 conserved quantities, the stress-energy tensor must be of rank 2 and the conservation should be something like $\partial_\nu T^{\mu\nu} = 0$. This stress-energy tensor sources the gravitational field that is described by the derivatives of the metric tensor $g_{\mu\nu}$. David Lovelock showed that, in 4 dimensions, the only possible form of a rank-2 tensor that is a function of the first derivatives and a linear function of the second derivatives of $g_{\mu\nu}$ is the Einstein tensor plus a cosmological constant [82, 83]:

$$G_{\mu\nu} + \Lambda g_{\mu\nu} = R_{\mu\nu} - \frac{1}{2}g_{\mu\nu}R + \Lambda g_{\mu\nu}\,, \tag{2.6}$$

where $R_{\mu\nu}$ and R are the Ricci tensor and scalar respectively. To link $R_{\mu\nu}$ and R with $g_{\mu\nu}$, we use equation (2.5) Since we work on a curved spacetime, one needs to construct the covariant derivative of the vector v^ν:

$$\nabla_\mu v^\nu = v^{\nu,\mu} + \Gamma^\nu_{\mu\alpha}v^\alpha\,. \tag{2.7}$$

From equation (2.7), we can construct the Riemann tensor which determines the spacetime curvature:

$$\left[\nabla_\alpha, \nabla_\beta\right] v^\mu = {R^\mu}_{\delta\alpha\beta}v^\delta\,. \tag{2.8}$$

The meaning of the Riemann tensor can be understood by looking at equation (2.8). If the spacetime is curved, the covariant derivatives along two different directions do not commute, *i.e.* differentiating along a direction α and then along β gives a different vector than differentiating first along β and then α. The Riemann tensor encodes this difference. We can find a relation between the Riemann tensor and the Christoffel symbol which is a function of first derivatives of $g_{\mu\nu}$:

$$R^{\delta}{}_{\alpha\beta\mu} = \Gamma^{\delta}_{\alpha\mu,\beta} - \Gamma^{\delta}_{\beta\mu,\alpha} + \Gamma^{\nu}_{\alpha\mu}\Gamma^{\delta}_{\beta\nu} - \Gamma^{\nu}_{\beta\mu}\Gamma^{\delta}_{\alpha\nu} \,. \tag{2.9}$$

The Ricci tensor and scalar of equation (2.6) are obtained by contracting the Riemann tensor:

$$R_{\alpha\beta} = R^{\mu}{}_{\alpha\mu\beta}, \qquad R = R^{\mu}{}_{\mu} \,. \tag{2.10}$$

Finally, the field equation describing gravitation can be written using the Einstein tensor (2.6) plus a cosmological constant and the stress-energy tensor:

$$G_{\mu\nu} + \Lambda g_{\mu\nu} = R_{\mu\nu} - \frac{1}{2} g_{\mu\nu} R + \Lambda g_{\mu\nu} = \kappa T_{\mu\nu} \,. \tag{2.11}$$

Using the limit of weak field and small velocity to recover the Newtonian equation, one can show that $\kappa = 8\pi G$. The first assumption of the ΛCDM model is that the gravitational field is well described by (2.11). Finally, the Bianchi identity ($\nabla_{\mu}(G_{\mu\nu} + \Lambda g_{\mu\nu}) = 0$) implies, as expected, the conservation of the stress-energy tensor

$$\nabla_{\mu} T^{\mu\nu} = 0 \,. \tag{2.12}$$

2.2 Perturbation

Perturbation theory starts with the *cosmological principle* which supposes that there exists a scale where the universe can be described as homogeneous and isotropic. The isotropy is strongly supported by the observations, in particular, of the CMB [84]. The homogeneity is more complicated to test. Indeed, the large-scale structure (LSS) surveys observe the galaxies on the light-cone. Moreover, the expected scale should be of order 100 h^{-1}Mpc, where $h = H_0/100$, which means that in order to properly test the homogeneity, the surveys should probe much larger scales. Within the last decade, this starts to become a reality, see for instance [85, 86].

In the ΛCDM model, the universe is supposed to be flat. As explained in section 1.4, this is again corroborated by the observation of the CMB [66]. The general coordinates used for such a universe is the flat Friedmann-Lemaitre-Robertson-Walker (FLRW) metric:

$$ds^2 = -dt^2 + a^2(t) \left(dr^2 + r^2 d\Omega^2 \right) \,, \tag{2.13}$$

where a is the scale factor, t the comoving time, *i.e.* the time of an observer following the expansion, and r and Ω are the usual radial and angular coordinates. The universe is not perfectly homogeneous. We observe structures, not to mention our proper existence, on very small scales there are the planets and the stars, on middle scales the galaxies and the galaxy clusters, and on large scales, we observe the large-scale structure. On these large scales, the gravitational potential and the density of matter fluctuations are of order 10^{-5}. The universe on large scales can therefore be described by a perturbed FLRW universe.

We will follow closely the review of perturbation theory [87, 88]. First of all, let us define the perturbation $\mathcal{I}$ of any field f:

$$\mathcal{I}(t,\mathbf{x}) = \delta f(t,\mathbf{x}) = f(t,\mathbf{x}) - \bar{f}(t)\,, \tag{2.14}$$

where $\bar{f}$ is the background value of the field that depends only on time. The perturbation can be decomposed at any order

$$\mathcal{I}(t,\mathbf{x}) = \sum_{i=1}^{\infty} \mathcal{I}^{(i)}(t,\mathbf{x})\,, \tag{2.15}$$

where the (i) means the ith order of the perturbation. The most general perturbed metric of a flat FLRW metric can be written:

$$ds^2 = g_{\mu\nu}dx^\mu dx^\nu = -e^{2\phi}dt^2 + 2aB_i dx^i dt + a^2 E_{ij} dx^i dx^j\,, \tag{2.16}$$

where we have introduced the perturbed potentials ϕ, B_i and E_{ij}. The time t is the proper time of an observer at rest with respect to the cosmological expansion. The time dependence of the distance has been factorized out into the function $a(t)$ which is normalized such that today at t_0 we have $a(t_0) = 1$. This choice is only possible because we are in a flat universe.

It is very useful to decompose each of the coefficients into *scalar*, *vector* and *tensor* perturbations. These different types of perturbations have different physical nature and we can show, see for example [89], that these perturbations are not coupled at the linear level. At higher order $n > 1$, the perturbations of the same order decouple but can be sourced by any lower-order perturbations. The SVT decomposition reads:

$$\begin{aligned} B_i &= B_{,i} - S_i, &&\text{with} \quad S_i^{,i} = 0\,, \\ E_{ij} &= e^{-2\psi}\delta_{ij} + 2E_{,ij} + 2F_{[i,j]} + h_{ij} &&\text{with} \quad F_i^{,i} = 0 \qquad \text{and}\,, \quad h_i^i = h_{ij}^{,i} = 0\,, \end{aligned} \tag{2.17}$$

where we use the notation $F_{[i,j]} = F_{i,j} - F_{j,i}$. Vector perturbations are not generated by inflation and would decay exponentially with the expansion of the universe. However, once we consider second-order (or higher) perturbations, vector perturbation can be sourced by the first-order scalar perturbations. We will have to deal with this in the third part of this thesis. We will also briefly mention tensor perturbations because they are one of the predictions of the simplest inflation model and they have not been detected yet. Therefore, it is one of the main focuses of cosmological research. Our main focus will be on scalar perturbations that are well detected.

We have now 4 scalars (ϕ, ψ, B, E), 2 divergence-free vectors S_i, F_i and one trace- and divergence-free symmetric tensor, *i.e.* respectively 4+4+2 = 10 degrees of freedom. Recall that there are 16 Einstein equations (2.11) (4 × 4). The Einstein tensor and the stress-energy tensor are both symmetric, hence there are in reality 10 independent equations. Among these 10 equations, 4 are related to the 4 scalar degrees of freedom:

- the 00 equation: $G_{00} = \kappa T_{00}$,
- the divergence of the $i0$ equation: $G_{0i}^{,i} = \kappa T_{i0}^{,i}$,
- the trace of the ij equation: $G_i^i = \kappa T_i^i$,
- the divergence of the traceless ij equation: $\left(G_i^j - \frac{1}{3}\delta_i^j G_k^k\right)_{,j}^{,i} = \kappa\left(T_i^j - \frac{1}{3}\delta_i^j T_k^k\right)_{,j}^{,i}$.

Moreover, recall that the physics should be independent of the coordinate system. That means that the Einstein equations are invariant under the transformation

$$x^\mu \to x^\mu + \xi^\mu \,, \tag{2.18}$$

where ξ^μ is called the *generating vector*. Similarly to B_i in (2.17), the spatial part ξ^i can be split into one scalar, usually called β and a divergence free vector. If we consider only the scalar degrees of freedom, the transformation (2.18) can be written [87]

$$\begin{aligned} t &\to t + \alpha \,, \\ x^i &\to x^i + \beta^{,i} \,. \end{aligned} \tag{2.19}$$

Therefore, we see in (2.19) that 2 scalar degrees of freedom are arbitrary, *i.e.* only due to the choice of coordinate also called *gauge*. To fix the gauge we can suppress 2 of the 4 scalar degrees of freedom.

2.2.1 The Poisson gauge

One of the most popular choices is to set $B = E = 0$. This is so-called *longitudinal gauge* which unfortunately has many various other names: *orthogonal zero-shear*, *conformal Newtonian* or *Poisson*. In this thesis, we will use the Poisson gauge to write down the Einstein equations. The line element (2.16) in longitudinal gauge reduces to:

$$ds^2 = g_{\mu\nu} dx^\mu dx^\nu = a^2 \left(-e^{2\phi} d\tau^2 - 2S_i dx^i d\tau + (e^{-2\psi}\delta_{ij} + h_{ij}) dx^i dx^j \right) \,, \tag{2.20}$$

where instead of the time coordinate of a comoving observer t, we have written the line element as a function of the conformal time τ, not to be confused with the proper time τ_p introduced in equation (2.1). The relation between the comoving time and t is straightforward:

$$a d\tau = dt \,. \tag{2.21}$$

From the metric, we can write down the different relevant components of the Einstein tensor defined in equation (2.6). Keeping only the scalars modes, it leads:

$$\begin{aligned} -\frac{a^2}{2} G^0_0 &= \frac{3}{2} e^{-2\phi} (\mathcal{H} - \psi')^2 + e^{2\psi} \left[\Delta\psi - \frac{1}{2} (\psi_{,i})^2 \right] \,, \\ \frac{a^2}{2} G^0_i &= e^{-\phi} \left(e^{-\phi} (\mathcal{H} - \psi') \right)_{,i} \,, \\ a^2 G^i_j &= e^{-2\phi} \left[-\mathcal{H}^2 - 2\mathcal{H}' - 2\phi'\psi' - 3(\psi')^2 + 2\mathcal{H}(\phi' + 2\psi') + 2\psi'' \right] \delta^j_i \,, \\ &\quad + e^{2\psi} \left[\left(\phi^2_{,k} - \Delta\chi \right) \delta^j_i + \psi^{,i}\psi_{,j} - \phi^{,i}\phi_{,j} - \phi^{,i}\psi_{,j} - \psi^{,i}\phi_{,j} + \chi^{,i}_{,j} \right] \,, \end{aligned} \tag{2.22}$$

where we define $\chi \equiv \psi - \phi$ and where the derivative w.r.t. the conformal time τ is noted with $'$. The conformal Hubble factor denoted $\mathcal{H}$ is defined w.r.t. the scale factor a:

$$\mathcal{H} = \frac{a'}{a} = aH \,, \tag{2.23}$$

where H is the Hubble factor defined w.r.t. to the comoving time coordinate t. The derivative w.r.t. to t is denoted with a dot so that $H = \dot{a}/a$.

Having defined the perturbed metric $g_{\mu\nu}$ we need to define the stress-energy tensor in order to solve the Einstein equations perturbatively. To this purpose, let us define the 4-velocity of matter

$$u^\mu = \frac{dx^\mu}{d\tau_p}\,. \tag{2.24}$$

By using the definition of the proper time in equation (2.16), it is easy to verify that the modulus of the 4-velocity verifies:

$$u^\mu u_\mu = -1\,. \tag{2.25}$$

We will also make use of the 4-velocity v^μ defined w.r.t. the conformal time τ. The spatial part of v^μ defines the 3-velocity of matter v^i used in equation (2.35). We can decompose v^i into a scalar part and a transverse vector or curl part:

$$v^i = \delta^{ij} v_{,j} + w^i \qquad w^i_{,i} = 0\,. \tag{2.26}$$

We can show that the 4-velocity u^μ is simply the normalized vector in the direction of v^μ, *i.e.*

$$u^\mu = \frac{v^\mu}{\sqrt{-v_\nu v^\nu}} = \frac{v^\mu e^{-\phi}}{a\sqrt{1-e^{-2\phi-2\psi}v^2}}\,, \tag{2.27}$$

where we mean $v^2 = \delta_{ij} v^i v^j$. From (2.25) we can express the time component of u^μ as a function of the spatial component:

$$u^0 = \frac{e^{-\phi}}{a}\sqrt{1+u^i u_i}\,. \tag{2.28}$$

Note that $u^i u_i$ can be expressed as a function of v^2 thanks to equation (2.27). The covariant 4-velocity takes the form:

$$u_\mu = a\left(-e^{\phi}\sqrt{1+u^i u_i}, \quad e^{-2\psi-\phi}\frac{v_i}{\sqrt{1-e^{-2\psi-2\phi}v^2}}\right)\,, \tag{2.29}$$

where we define $v_i = \delta_{ji} v^j$.

In cosmology, the different components of the universe, *i.e.* CDM, baryons, neutrinos, and photons are treated as fluids. The stress-energy tensor of a fluid can be defined by using the density, the pressure, and the 4-velocity (2.29) by:

$$T_{\mu\nu} = (\rho + p)\, u_\mu u_\nu + p g_{\mu\nu} + \pi_{\mu\nu}\,, \tag{2.30}$$

where $\pi_{\mu\nu}$ is the anisotropic stress and has for properties to be traceless and orthogonal to the 4-velocity ($\pi_{\mu\nu} u^\mu = 0$). We consider only the scalar perturbations so that will only keep its trace-free scalar part:

$$\pi_{ij} = a^2\left(\pi_{,ij} - \frac{1}{3}\Delta\pi\delta_{ij}\right)\,. \tag{2.31}$$

For a perfect fluid like the baryons and CDM, $\pi_{\mu\nu}$ vanishes. The photons and neutrinos can develop anisotropic stress if they are not coupled to matter. This is typically the case for neutrinos that decouple from the matter at a very early time. The components of the stress-energy tensor read:

$$\begin{aligned}
T^0_0 &= -(\rho+p)\left(1+u^i u_i\right) + p\,,\\
T^0_i &= (\rho+p) v_i e^{-2\psi-2\phi}\sqrt{\frac{1+u^i u_i}{1-e^{-2\phi-2\psi}v^2}}\,,\\
T^i_j &= (\rho+p) e^{-2\psi-2\phi}\frac{v^2}{1-e^{-2\phi-2\psi}v^2} + \delta^i_j p + \frac{e^{2\psi}}{a^2}\pi^i_j\,.
\end{aligned} \tag{2.32}$$

Now that we have computed the Einstein tensor (2.22) in the Poisson gauge whose line element is defined in equation (2.20) and the stress-energy tensor in equation (2.32), we can write down the Einstein equation (2.11) perturbatively:

$$ {}^{(i)}\delta G_{\mu\nu} = \kappa \, {}^{(i)}\delta T_{\mu\nu} \, . \tag{2.33}$$

2.2.2 Gauge invariant variables

Once we study perturbations, the choice of coordinates, or gauge, can be very important. In the homogeneous case, the existence of a coordinate system where the perfect fluid of the universe is homogeneous and isotropic makes the choice easy. When we add perturbations, the choice of coordinates can introduce artificial perturbations also called gauge modes. This can be clarified by looking at gauge-invariant quantities, first used in [90] where the so-called Bardeen's potentials have been introduced. At first order, the expression of these potentials is:

$$\begin{aligned} \Phi^{(1)} &= \phi^{(1)} + \mathcal{H}\left(B^{(1)} - E'_{(1)}\right) + \left(B^{(1)} - E'_{(1)}\right)' \, , \\ \Psi^{(1)} &= \psi^{(1)} - \mathcal{H}\left(B^{(1)} - E'_{(1)}\right) \, . \end{aligned} \tag{2.34}$$

In the Poisson gauge, we have $B = E = 0$ so that the Bardeen's potentials exactly match the two potentials $\phi^{(1)}$ and $\psi^{(1)}$. Another common gauge-invariant variable used is $\mathcal{R}$ which matches the curvature perturbation in the comoving/unitary gauge where $B_i = 0$ and where the fluid has a vanishing 3-velocity $v_i^{(1)} = 0$. This last gauge is then defined by:

$$\mathcal{R}^{(1)} = \psi^{(1)} - \mathcal{H}\left(v^{(1)} + B^{(1)}\right) \, , \tag{2.35}$$

where $v^{(1)}$, similarly to $B^{(1)}$ is the scalar part of the 3-velocity. A very well known invariant variable used is the so-called Sasaki-Mukhanov variable q. It can be expressed as a function of the first order perturbation of a single scalar field φ in the comoving gauge:

$$q^{(1)} = a\left(\varphi^{(1)} + \frac{\psi^{(1)}}{\mathcal{H}}\bar{\varphi}'\right) = aQ^{(1)} \, . \tag{2.36}$$

It has been particularly used by [91]. The variable that we will mainly use in this thesis is the so-called curvature perturbation on uniform-density hypersurface [92, 93]:

$$-\zeta^{(1)} = \psi^{(1)} + \mathcal{H}\frac{\rho^{(1)}}{\bar{\rho}'} \, , \tag{2.37}$$

which again matches the curvature perturbation $\psi^{(1)}$ if we choose a gauge where there is no perturbations in density $\rho^{(1)} = 0$.

2.3 Background

At leading order, we obtain a perfect FLRW metric defined in equation (2.13). For photons $ds = 0$ therefore we deduce that $dt/a(t) = dx$ which is an equality between quantities that do not depend on the same variables. Hence, $dt/a(t)$ is constant. By integrating and by defining the photon wave length $\lambda = 1/\Delta t$, one finds

$$\frac{\Delta t_0}{a(t_0)} = \frac{\Delta t_1}{a(t_1)} \, , \tag{2.38}$$

where the subscript 1 means the emission of the photon and 0 is today. By convention, we can impose $a(t_0) = 1$ (this choice is possible only because we consider a flat universe). The redshift z is then

$$1 + z = \frac{\lambda_0}{\lambda_1} = \frac{1}{a(t_1)} \,. \tag{2.39}$$

At leading order the Einstein equation (2.33) becomes the Friedmann equations:

$$\begin{aligned} 3\mathcal{H}^2 &= a^2\kappa\bar{\rho} + a^2\Lambda \,, \\ 2\mathcal{H}' &= -\frac{a^2\kappa}{3}\left(\bar{\rho} + 3\bar{p}\right) + a^2\Lambda \,. \end{aligned} \tag{2.40}$$

The quantities $\bar{\rho}$ and $\bar{p}$ are the spatially constant density and pressure background. The first Friedmann equation is obtained with the 00 component of the Einstein equation while the second can be obtained by mixing the 00 with the trace $G^i_i = \kappa T^i_i$. These equations tell us the background dynamics, not to be confused from the perturbation dynamics that will follow from a first and second-order expansion around the FLRW metric. One can combine the two Friedmann equations (2.40) to obtain the stress-energy conservation equation:

$$\dot{\bar{\rho}} + 3H\left(\bar{\rho} + \bar{p}\right) = 0 \,, \tag{2.41}$$

which also follows from the energy-momentum tensor conservation $\nabla_\beta T^{\alpha\beta} = 0$. This conservation is a consequence of general relativity. More precisely it follows from the Bianchi identity. However, if the universe if filled with different species of particles, the conservation of $T^{\alpha\beta}_{(\alpha)}$ still holds for the specific type (α) only if α is not interacting (apart from gravitational interaction). Otherwise, we have in general

$$\nabla_\beta T^{\alpha\beta}_{(\alpha)} = Q^\alpha_{(\alpha)} \,, \tag{2.42}$$

where $Q^\nu_{(\alpha)}$ is the energy transfer. Therefore, for a non-interacting fluid we have $Q^\nu_{(\alpha)} = 0$ and the sum over all types of particles filling the universe must give

$$\sum_{(\alpha)} Q^\alpha_{(\alpha)} = 0 \,. \tag{2.43}$$

The dynamics of the background universe depends on the density and the pressure of the different species filling the universe. The history of the universe is a succession of periods where a given type of particle dominates the energy density. Each species is characterized by its equation of state:

$$\bar{p} = \omega\bar{\rho} \,. \tag{2.44}$$

Injecting equation (2.44) in the conservation equation (2.41), we find the density as a function of the scale factor. Then by using the first Friedmann equation we find the scale factor as a function of the time t:

$$\rho \propto a^{-3(1+\omega)}, \qquad a \propto t^{\frac{2}{3(1+\omega)}} \,, \tag{2.45}$$

where we have assumed that $\omega \neq -1$. The case $\omega = -1$ will be treated later.

The energy density of photons can be written $\rho_r = 2\pi\nu/V$ where V is a volume and ν is the frequency of the photons (we have used $\hbar = 1$). We have seen that the photon frequency decreases as $1/a$ and the volume scales as a^3. Hence, the radiation energy

	$\bar{\rho}$	$a(t)$	H	$a(\tau)$	$\mathcal{H}$	ω
radiation	a^{-4}	$t^{1/2}$	t^{-1}	τ^{1}	τ^{-1}	$\frac{1}{3}$
matter	a^{-3}	$t^{2/3}$	t^{-1}	τ^{2}	τ^{-1}	0
inflation/Λ	a^{0}	e^{Ht}	1	τ^{-1}	$-\tau^{-1}$	-1

Table 2.1: Time scaling of the density, the scale factor and the Hubble factor during the radiation and the matter domination era. We also put the result obtained in section 3.1 for inflation (quasi-de Sitter universe) that also holds in the case of a universe dominated by Λ. The last column gives the corresponding ω defined in equation (2.44).

density scales like a^{-4}. The density of non-relativistic matter can be written $\rho_m = m/V$ with m the mass in the volume V. Since m does not change with the scale factor we find the density of matter scales like a^{-3}. Injecting these results in the solution of the Friedmann equations (2.45), we find the corresponding ω_i. These results are summarized in table 2.1.

By looking at the power of the scale factor in the different cases in table 2.1, we understand why radiation dominated first; it has the smallest power -4. Then, the radiation energy density decreases faster than the matter energy density so that at some point, the non-relativistic matter will dominate the energy density of the universe. This starts at radiation-matter equality. Finally, the matter energy density continues to decrease until it becomes smaller than the cosmological constant which has a constant energy density.

To quantify the amount of a given species of matter, we define the density parameter:

$$\Omega_i = \frac{\rho_i(t_0)}{\rho_{cr}(t_0)}, \qquad \rho_{cr} = \frac{3H^2}{\kappa}, \tag{2.46}$$

where we recall that ρ_{cr}, as explained in section 1.4, is the critical density, *i.e.* the density of a universe with no curvature. The second equation (2.46) comes from the first Friedmann equation (2.40) where we have defined $\rho_{cr} = \rho + \rho_\Lambda$ with $\rho_\Lambda = \Lambda/\kappa$.

2.4 Perturbations

The expansion of the Einstein equation up to order (n) can always be written as a "pure" (n)th order left-hand side, which has the same form as the first-order equation, and a source term Q on the right-hand side, which is in general composed of a sum of the products of lower order terms. This can be written as

$$\left(\hat{G} - \kappa\hat{T}\right)^{(n)} = Q^{(n)}, \tag{2.47}$$

where we mean by the hat the pure (n)th order terms. At the first order, the source term vanishes. At the second order, the left-hand side takes the same form as the first order just by replacing the $\mathcal{I}^{(1)}$ by $\mathcal{I}^{(2)}$. The source term on the right-hand side is then quadratic in first-order fields. Therefore, solving the Einstein equation for any order higher than one is like solving the first-order equation with a source term.

The Einstein equation thus reads

$$3\mathcal{H}\left(\psi'+\mathcal{H}\phi\right)-\Delta\psi+\frac{3}{2}\mathcal{H}^2\delta=Q_{TT}\,, \tag{2.48a}$$

$$\left(\mathcal{H}\phi+\psi'\right)_{,i}+\frac{a^2\kappa}{2}\left(\bar\rho+\bar p\right)v_i=Q_{TS,i}\,, \tag{2.48b}$$

$$\chi-a^2\kappa\pi=Q_{SS}\,, \tag{2.48c}$$

$$\psi''+2\mathcal{H}\psi'+\mathcal{H}\phi'+\left(2\mathcal{H}'+\mathcal{H}^2\right)\phi-\frac{\kappa a^2}{2}p=Q_{Tr}\,, \tag{2.48d}$$

where we dropped the (n) index for readability and where the subscript T stands for "time", S for "space" and Tr for "trace". We have also defined in the first equation of (2.48) the density contrast δ so that

$$\rho=\bar\rho(1+\delta)\,. \tag{2.49}$$

2.4.1 Fourier transform

It is very convenient to use the Fourier transform of any field $f(\tau,\mathbf{x})$:

$$f(\tau,\mathbf{x})=\int\frac{d^3k}{(2\pi)^3}f(\tau,\mathbf{k})e^{i\mathbf{kx}},\qquad f(\tau,\mathbf{k})=\int d^3x\;f(\tau,\mathbf{x})e^{-i\mathbf{kx}}\,. \tag{2.50}$$

Often the field $f(\tau,\mathbf{x})$ is real which imposes that in Fourier space $f(\tau,-\mathbf{k})=f^*(\tau,\mathbf{k})$. Therefore, if f is real, only half of the Fourier space matters. One of the most important properties of the Fourier transform is that the functions $f(\tau,\mathbf{k})$ are the eigenvectors of the spatial derivative with eigenvalues $-i\mathbf{k}$, *i.e.*

$$f_{,i}(\tau,\mathbf{k})=-i\mathbf{k}f(\tau,\mathbf{k}),\qquad \Delta f(\tau,\mathbf{k})=-k^2f(\tau,\mathbf{k})\,. \tag{2.51}$$

In particular, the Einstein equations (2.48) can be written in terms of the Fourier modes.

The mode k is associated with a scale d by the relation $k=2\pi/d$. As we will see, in the standard cosmology, there is a very specific mode k_H that splits the evolution equations into two different regimes: the super-Hubble and sub-Hubble regimes.

2.4.2 Horizons

A very important concept in cosmology is the horizon. We have discussed the particle horizon in section 1.4. Let us now introduce the event horizon and give the formal definitions of these two types of horizons following [94]. From equation (2.13), we can write down the largest distance that a photon can travel between the emission time t_0 and a reception time t_1 is:

$$x(t_0,t_1)=\Delta\tau=\int_{t_0}^{t_1}\frac{dt'}{a}=\int_{a_0}^{a_1}d(\ln a)\,\frac{1}{\mathcal{H}}\,. \tag{2.52}$$

The distance $\mathcal{H}^{-1}$ is called the Hubble radius.

The event horizon is defined in [62] as follows. For a given observer A, the event horizon *is a hypersurface in space-time that divides all events into two non-empty classes: those that have been, are, or will be observable by A, and those that are forever outside A's possible powers of observation.* Let us imagine a particle at a distance D from A

emitting at a time t_0 a photon toward A's direction. One can find a specific distance D_0 for which the photon reaches A at $t = \infty$. We suppose here that $D_0 < \infty$. This means that if $D > D_0$, the photon will never reach A, and if $D < D_0$, it will. The surface of the sphere in the observer's instantaneous 3-space $t = t_0$ with radius D_0 is called the spatial event horizon. If we now consider another emission time $t_1 > t_0$, the radius D_1 (if it exists) will be smaller than D_0. The equation of motion of the spatial event horizon can be computed, and it corresponds to the equation of motion of a photon traveling toward A. Hence, the event horizon is the aggregate of all spatial event horizons, forming a hypersurface in space-time [62].

Given this definition, the *spatial event horizon* x_{EH} is the maximum distance from which we can see an event occurring at t_0 at some place, *i.e.*

$$x_{EH}(t_0) = x(t_0, t_1 \to \infty) = \int_{t_0}^{\infty} \frac{dt'}{a} \,. \tag{2.53}$$

In a universe dominated by matter or radiation, we have $x_{EH} \to \infty$. This means that if we wait long enough, we can see every event in the universe, no matter how far it is. This is however not the case for a de Sitter universe.

On the contrary, the *particle horizon* x_{PH} is the maximum causal distance at time t_1, *i.e.* the distance that a photon has traveled during the whole history of the universe. This gives

$$x_{PH}(t_1) = x(t_0 \to 0, t_1) = \int_{0}^{t_1} \frac{dt'}{a} \,. \tag{2.54}$$

Again, if the integral (2.53) is divergent, this means that the whole universe has been in causal contact. In the standard cosmology, *i.e.* matter or radiation domination, this integral converges. If we impose $\tau(t \to 0) = 0$, then (3.1) can be written as

$$x_{PH}(\tau) = \tau \,. \tag{2.55}$$

We see in table 2.1 that in the radiation domination era $\tau = \mathcal{H}^{-1}$, so that the particle horizon exactly coincides with the Hubble radius. This is still true up to a factor 2 in the matter domination era. In a de Sitter universe, $\mathcal{H}^{-1} \propto -\tau$, which means that the Hubble distance decreases with time.

As anticipated in the previous section 2.4.1, the time τ is always associated to a scale k_H defined as

$$k_H = \mathcal{H} \,. \tag{2.56}$$

The Hubble radius today is about $3h^{-1}$Gpc, while in the standard cosmology, the particle horizon is about $10h^{-1}$Gpc.

As explained above, in the radiation or matter domination era we have $\tau \sim \mathcal{H}^{-1}$. Hence, the condition (2.56) can be written $k_H\tau \sim 1$. It turns out that this scale defined w.r.t. to $\mathcal{H}$, defines the limit between two different regimes. Because of the similarity of $\mathcal{H}^{-1}$ and τ, the scale k_H (or $\mathcal{H}^{-1}$) is often referred equivalently to the Hubble and the horizon scale. When we consider modes $k \ll k_H$ or equivalently $k \ll \mathcal{H}$, we speak about the super-Hubble/super-horizon limit. Typically, when we consider single-field inflation, the modes are "frozen" in this regime which means that they do not evolve. The limit $k \gg \mathcal{H}$ is the sub-Hubble or sub-horizon limit. When $k \sim \mathcal{H}$, we say "horizon crossing". As we will see, after inflation, all modes are considered as being outside of the horizon. Then, as time continues, the Hubble radius increases, and the modes progressively enter the horizon and become sub-horizon. The exact physics for these modes depends on during which period they enter the horizon: during radiation, matter, or Λ domination.

Strictly speaking, it is better to define these two regimes w.r.t. to the Hubble factor $k_H = \mathcal{H}$ and then only refer to super-Hubble and sub-Hubble regimes. Even if in particular cases we may have $x_{PH} = \mathcal{H}^{-1}$, this is not true in general. As explained in section 1.4.3, it is one of the purposes of inflation to break this equality. This will be discussed in more detail in section 3.1.1. In this thesis, we will mainly use both horizon (meaning particle horizon) and Hubble distance interchangeably except when the difference is relevant.

2.4.3 First order

The three first equations (2.48a), (2.48b) and (2.48c) are first order differential equations in time derivatives and are thus called the Einstein constraint equations. At first order all source terms vanish ($Q = 0$), we can rewrite (2.48a), (2.48b) as one equation linking the invariant $\Psi^{(1)}$, $\zeta^{(1)}$ and $\mathcal{R}^{(1)}$ defined in equations (2.34), (2.37) and (2.35) respectively [87, 95]:

$$\Delta\Psi = \left(-3\mathcal{H}' - \mathcal{H}^2\right)(\zeta + \mathcal{R}) \ . \tag{2.57}$$

For the rest of this section, we will drop the (1) since all results here are first order. From equation (2.57), we see that on the super-Hubble regime where $k^2 \ll \mathcal{H}^2$ we have $\zeta = -\mathcal{R}$. It is common to refer to these variables when we speak about inflation or initial conditions. As we will see, the initial conditions are imposed on super-Hubble scales, *i.e.* ζ and $\mathcal{R}$ can often be used interchangeably (up to the sign).

From equation (2.48c), we see that for a vanishing anisotropic stress, we have $\chi = 0$, *i.e.*

$$\psi = \phi \, . \tag{2.58}$$

We can split the first order pressure as an *adiabatic* and an *entropic* part [95] so that

$$p = c_s^2 \bar{\rho}\delta + p_{nad} \, , \tag{2.59}$$

where we have defined the adiabatic sound speed $c_s^2 = \partial p/\partial \rho$ and where p_{nad} stands for *non-adiabatic* pressure.

By using equations (2.58) and (2.59) as well as equation (2.48a), we can rewrite equation (2.48d) as a closed second order differential equation for ψ:

$$\psi'' + 3(1 + c_s^2)\mathcal{H}\psi' + \left[2\mathcal{H}' + (1 + 3c_s^2)\mathcal{H}^2 - c_s^2\Delta\right]\psi = \frac{a^2\kappa}{2} p_{nad} \, . \tag{2.60}$$

In the standard model of cosmology, the perturbations are purely adiabatic so that $p_{nad}^{(1)} = 0$. Therefore, in this case, assuming that the scale factor can be written as a power law $a \propto t^\alpha$, which is typically the case in the matter and radiation domination eras, the integration of (2.60) for large scales (Laplacian negligible) gives

$$\psi = \frac{A}{\alpha + 1} + B\alpha t^{-(\alpha+1)} \, , \tag{2.61}$$

with A and B integration constants. There are 2 solutions, one is constant in time and is called the growing mode (even though it is not growing), and the other one is decreasing with time and is called the decaying mode. The decaying mode is typically not considered because it becomes rapidly negligible. Thus, the potential can be considered as constant during a given period of either radiation of matter domination but it evolves during the transition periods and eventually on sub-Hubble scales. Let us consider a transition during a period where $a \propto t^\alpha$ and a second one where $a \propto t^\beta$. Note that from equation (2.45), the powers α and β depend on ω. The two asymptotic values of the potential can be related by

$$\psi_\alpha = \frac{\beta+1}{\alpha+1}\psi_\beta\,. \tag{2.62}$$

If we combine the definition of the ζ (2.37) and the 00 Einstein equation (2.48a), by using the fact that the potential is constant on super-horizon scales, we find a relation between ψ and ζ:

$$\zeta = \frac{5+3\omega}{3(1+\omega)}\psi\,. \tag{2.63}$$

As we shall see, this relation (2.63) is very useful to link the value of the potential with the initial condition.

From the Einstein equation, or more simply with the stress-energy tensor conservation equation, one can obtain the continuity and Euler equations which read

$$\rho' + 3\mathcal{H}(\rho+p) + (\bar\rho+\bar p)\left(\Delta v - 3\psi'\right) = 0\,, \tag{2.64a}$$

$$v' + (1-3c_s^2)\mathcal{H}v + \phi + \frac{1}{\bar\rho+\bar p}\left(p + \frac{2}{3}\Delta\pi\right) = 0\,. \tag{2.64b}$$

Equation (2.64a) shows that ζ is a conserved quantity for adiabatic perturbations on large scales [96]. Indeed, equation (2.64a) can be rewritten in terms of ζ

$$\zeta' = -\mathcal{H}\frac{p_{nad}}{\bar p+\bar\rho} - \frac{1}{3}\Delta v\,. \tag{2.65}$$

Therefore, from equation (2.65) we see that $\zeta_{(1)}$ reduces to $-1/3\Delta v$ which becomes $1/3k^2v$ in Fourier space for purely adiabatic perturbations. Hence, we see that on super-Hubble scales $k \ll \mathcal{H}$, the Laplacian of the scalar velocity is negligible, and therefore from equation (2.65) we find that in an adiabatic universe, the first-order curvature perturbation on uniform-density hypersurface is constant. Reminder that in this regime $\zeta = -\mathcal{R}$, so that the same conclusion holds for the first-order curvature perturbation in the comoving gauge. There is however a difference with the potential ψ. The last is constant in a given period of domination but is still a function of ω which is not the case for ζ and $\mathcal{R}$. For these reasons, it is very convenient to use either ζ or $\mathcal{R}$ to describe the perturbations in the standard model which is adiabatic, and particularly to link the initial conditions with inflation. However, if the universe contains entropic perturbations, we see from equation (2.65) that the perturbation will evolve even in the super-Hubble regime, and this evolution is precisely driven by the non-adiabatic pressure.

2.4.4 Adiabatic and isocurvature modes

The system of equations governing the dynamics (2.64) is second order in time derivatives. Therefore, we will have to impose two initial conditions for each species. The simplest models involving one scalar field during inflation, as we shall see in the next section, generate *adiabatic initial conditions* (ADI). Multi-field inflation on the other hand can generate additional *entropic* or *isocurvature initial conditions.* The first part of this thesis addresses the constraints on these isocurvature modes. Let us first specify what we mean by entropy.

Entropy

The second law of thermodynamics can be written as

$$dE = TdS - pdV\,, \tag{2.66}$$

where E, T, S, p and V are the energy, temperature, entropy, pressure and volume of a system. Let us define the entropy density $s = dS/dV$. Equation (2.66) can be rewritten as

$$s = \frac{1+\omega}{T}\rho\,. \tag{2.67}$$

The cosmic fluid is assumed to be in thermal equilibrium. Thus, the density can be obtained by integrating the Bose-Einstein or Fermi-Dirac distributions depending on the type of particle: bosons or fermions.

$$\begin{aligned}\rho = \frac{4\pi N}{(2\pi)^2}\int \frac{\mathrm{d}\vec{p}}{(2\pi)^3}\frac{|\vec{p}|}{e^{|\vec{p}|/T}\pm 1} &= \frac{\pi^2}{30}NT^4 \quad \text{for bosons}\,,\\ &= \frac{7}{8}\frac{\pi^2}{30}NT^4 \quad \text{for fermions}\,,\end{aligned} \tag{2.68}$$

where $\vec{p}$ is the momentum of the fluid (to avoid any confusion with the pressure p, we note the modulus of the momentum by $|\vec{p}|$). The factor N is the number of spin degrees of freedom. The results (2.68) is called Stefan-Boltzmann's law for bosons. To simplify, we shall just call it Stefan's law in any case since the important behavior here is the dependence in T^4. Similarly, one can compute the number density for each type of particles. It reads,

$$\begin{aligned}n \simeq& \frac{1.2}{\pi^2}NT^3 \quad \text{for bosons}\,,\\ \simeq& \frac{3}{4}\frac{1.2}{\pi^2}NT^3 \quad \text{for fermions}\,.\end{aligned} \tag{2.69}$$

Now using (2.67), (2.68) and (2.69), we find that the entropy for a given specie is proportional the number density:

$$\begin{aligned}s \simeq& 3.6n \quad \text{for bosons}\,,\\ \simeq& 4.2n \quad \text{for fermions}\,,\end{aligned} \tag{2.70}$$

where we have used $\omega = 1/3$ in both cases. It follows that the number density of a given particle is a measure of the entropy. For more details, see [97]. Note that the same conclusion holds for $\omega = 0$.

Multiple fluids

Let us follow [87, 88, 97, 98] and explain how we can treat the case of multiple fluids. The total perturbation can simply be computed by summing over all particles α

$$\rho = \sum_i \rho_i, \qquad p = \sum_i p_i, \qquad v = \sum_i \frac{\bar{\rho}_i + \bar{p}_i}{\bar{\rho}+\bar{p}}v_i\,. \tag{2.71}$$

One can also define the gauge-invariant perturbations on the uniform i-density hypersurface ζ_i similarly to (2.37). The total ζ can then be recovered by a weighted sum

$$\zeta = \sum_i \frac{\rho_i'}{\rho'}\zeta_i, \qquad \zeta_i = \psi + \frac{\mathcal{H}}{\bar{\rho}_i'}\rho_i\,. \tag{2.72}$$

By using its definition, the adiabatic sound speed can also be obtained by a weighted sum

$$c_s^2 = \sum_i \frac{\rho_i'}{\rho'} c_i^2 \,, \tag{2.73}$$

where c_i^2 is defined similarly to the adiabatic sound speed for for a given specie: $c_i^2 = \partial p_i / \partial \rho_i$. One defines a perturbed entropy ratio between two species i and j:

$$\mathcal{S}_{ij} = \frac{\delta(n_i/n_j)}{n_i/n_j} = \frac{\delta n_i}{n_i} - \frac{\delta n_j}{n_j} \,. \tag{2.74}$$

This last equation (2.83) is in fact true at any order. Then, we can use the fact that $\rho_i \propto n^{1+\omega_i}$, and expand at first order to find

$$\mathcal{S}_{ij} = \frac{\delta_i}{1+\omega_i} - \frac{\delta_j}{1+\omega_j} \,. \tag{2.75}$$

From the proportionality of the entropy and the number density that we found in equation (2.70), the $\mathcal{S}_{ij}$ measure directly the local variation of composition of the cosmic fluid. One can also give an invariant definition of $\mathcal{S}_{ij}$ by using the ζ_i:

$$\mathcal{S}_{ij} = 3(\zeta_i - \zeta_j) \,. \tag{2.76}$$

When we consider a mixture of different fluids, instead of specifying the perturbation of each species, we specify the total perturbation on the uniform density hypersurface and the relative variation of composition w.r.t. a reference fluid (usually the photon fluid, since photons are the dominant contribution to the total entropy).

In equation (2.59), we have defined the non-adiabatic pressure p_{nad} which turns out to be a source of evolution on super-Hubble scales of ζ, see equation (2.65). By using the definition of the total pressure in equation (2.71), one can write the total non-adiabatic pressure as a sum of two terms [97]:

$$p_{nad} = \sum_i p_{nad,i} + \sum_i (c_i^2 - c_s^2)\rho_i, \text{ where } \quad p_{nad,i} = p_i - c_i^2 \rho_i \,. \tag{2.77}$$

The first term is called intrinsic $p_{nad,intr}$ because it is a sum of the non-adiabatic pressures of each individual fluid $p_{nad,i}$. The intrinsic pressure of the fluid i defined in the second equation of (2.77) turns out to be the source of its uniform i-density hypersurface ζ_i defined in (2.72). This means that similarly to (2.65), we would have [87]

$$\zeta_i' = -\mathcal{H} \frac{p_{i,nad}}{\bar{p}_i + \bar{\rho}_i} - \frac{1}{3}\Delta v_i \,. \tag{2.78}$$

Since we will consider only fluids in thermal equilibrium, we will always set this term to 0. The second term in the first equation of (2.77) is a relative contribution $p_{nad,rel}$ and *does not vanish* even if we set $p_{nad,i} = 0$. It is due to the relative entropy perturbation $\mathcal{S}_{ij}$. To see this, let us use the relation (2.73). By also setting the intrinsic non-adiabatic pressure to zero we have [97]:

$$p_{nad} = \frac{1}{2} \sum_{ij} \frac{(1+\omega_i)(1+\omega_j)\bar{\rho}_i\bar{\rho}_j}{\rho + p} (c_i^2 - c_j^2)\mathcal{S}_{ij} \,. \tag{2.79}$$

From the continuity equation and the Euler equation (2.64) applied to each particle type, one can derive the evolution equation of $\mathcal{S}_{ij}$ (note that for simplicity here, we suppose that there are no perturbed energy and momentum transfer between the fluids, *i.e.* $\nabla_\mu T_i^{\mu\nu} = 0$). Hence, the evolution equation reads

$$\mathcal{S}'_{ij} = -\Delta\left(\mathcal{V}_{ij}\right) , \tag{2.80}$$

where $\mathcal{V}_{ij} = v_i - v_j$. The time derivative of the entropic mode is then sourced by the difference between the scalar velocities of two species. This is also a gauge invariant quantity. We can similarly obtain an evolution equation for $\mathcal{V}_{ij}$, see [97] for the result. Finally, by combining the equation (2.80) and the evolution of $\mathcal{V}_{ij}$, one can find a second-order equation for $\mathcal{S}_{ij}$. A simplified form of it for a mixture of two fields can be written as

$$S''_{ij} + \mathcal{H}S'_{ij} - \frac{\rho_i(1+\omega_i)c_j^2 + \rho_j(1+\omega_j)c_i^2}{\bar{\rho}+\bar{p}}\Delta S_{ij} = (c_i^2 - c_j^2)\frac{\Delta\delta}{1+\omega} . \tag{2.81}$$

It is interesting to note that the adiabatic mode is sourced by the entropic mode (2.65). On the other hand, the isocurvature mode is only sourced by the total matter fluctuation contrast δ if the two fluids do not have the same speed of sound. This source is suppressed on super-horizon scales by the Laplacian. Hence, a super-horizon evolution can only arise from a non-zero initial $\mathcal{V}_{ij}$.

2.4.5 Initial conditions

Let us now review the different possibilities of initial conditions for the system (2.64). They are set for super-Hubble modes, *i.e.* $k/\mathcal{H} \ll 1$. We finally list the different initial condition possibilities [97, 99]

Adiabatic IC (ADI) The adiabatic initial condition is defined by setting an initial curvature at some non-zero value and the entropic mode to 0:

$$\zeta = \zeta^0, \qquad \zeta' = 0, \qquad \mathcal{S}_{ij} = 0, \qquad (\mathcal{S}_{ij})' = 0 . \tag{2.82}$$

Using equation (2.63) in the radiation domination era and by using the Poisson equation (2.48a), and (2.82)

$$\psi = \frac{2}{3}\zeta^0, \qquad \delta = -\frac{4}{3}\zeta^0, \qquad \frac{\delta_i}{1+\omega_i} = \frac{\delta_j}{1+\omega_j} , \tag{2.83}$$

which means that there is initially no variation of composition in the fluid. Moreover, the $0i$ Einstein equation together with the vanishing time derivative of $\mathcal{S}_{ij}$ implies that

$$v_i = v_j = -\frac{4}{9\mathcal{H}}\zeta^0 , \tag{2.84}$$

where we have used the definition of the total velocity (2.71). Since we are in the super-Hubble regime $kv_i \ll 1$, we set it to 0 at first order.

Density isocurvature IC We mean by *isocurvature* the fact that initially there is no curvature perturbation, *i.e.* $\zeta = 0$. We see here that we have two different possibilities. The first one is to set initially a non-zero $\mathcal{S}_{ij}$:

$$\zeta = 0, \qquad \zeta' = 0, \qquad \mathcal{S}_{ij} = \mathcal{S}^0_{(1)}, \qquad (\mathcal{S}_{ij})' = 0\,. \tag{2.85}$$

From (2.63), the Poisson equation and the $0i$ Einstein equation, one find

$$\psi = 0, \qquad \delta = 0, \qquad \frac{\delta_i}{1+\omega_i} = \mathcal{S}^0 + \frac{\delta_j}{1+\omega_j}\,., \qquad v_i = v_j = 0 \tag{2.86}$$

Velocity isocurvature IC The second possible isocurvature mode is to set an initial $(\mathcal{S}_{ij})'$.

$$\zeta = 0, \qquad \zeta' = 0, \qquad \mathcal{S}_{ij} = 0, \qquad (\mathcal{S}_{ij})' = \mathcal{V}^0\,. \tag{2.87}$$

This mode is not properly speaking an entropic mode since initially $\mathcal{S}_{ij} = 0$ which means that there is no entropy fluctuation between the different fluids. However, isocurvature and entropic modes are often thought interchangeable so that we might see in the literature this confusion. In this thesis, we will always use the unambiguous term *isocurvature* to speak about density isocurvature IC and velocity isocurvature IC together. Finally, we have in this case:

$$\psi = \delta_i = \delta_j = 0, \qquad \sum_i \frac{\bar{\rho}_\alpha + \bar{p}_\alpha}{\bar{\rho} + \bar{p}} v_i = 0, \qquad v_i = \mathcal{V}^0_{(1)} + v_j\,. \tag{2.88}$$

2.5 Statistics

Cosmological science is mostly a classical field theory; quantum field theory only plays a role in the early universe. All the fundamental objects we use, *e.g.* the density ρ or the gravitational potentials, are classical and continuous fields defined at all times τ and positions $\mathbf{x}$. In this section, we first introduce some basic concepts, tools, and assumptions that allow us to do cosmology. Then, we explain what we mean by (non-)Gaussian fields, and finally, we will define the power spectrum and the bispectrum of a field.

2.5.1 Basics

Expectation value

A field f is associated with a probability density function (PDF). The functional $\mathcal{P}$ is the probability of occurrence of a given realization at a given position (we will drop the time dependence for simplicity). Therefore, one can define the expectation value, or 1-point correlation function, as

$$\langle f(\mathbf{x}) \rangle = \int \mathcal{D}f \; \mathcal{P}[f(\mathbf{x})] f(\mathbf{x})\,. \tag{2.89}$$

Unfortunately, we only have access to the single realization of the universe we are living in. The integral (2.90) is then impossible to compute. For this reason, the science of cosmology relies on a very important principle called the *fair sample* hypothesis. We can define the fair sample hypothesis as *the finite part of the universe accessible to observations is a fair sample of the whole, which is represented by a statistically homogeneous and isotropic ergodic field [94].* Given [94], a stochastic field is ergodic if *all information about its multi-point probability distributions can be obtained from a single realization of the field [94].* Hence, well-separated regions of the universe can be thought of as independent realizations. The *fair sample* hypothesis allows us to compute the ensemble expectation $\langle . \rangle$ by identifying it with a spatial average:

$$\langle f(\mathbf{x}) \rangle = \frac{1}{V} \int_V d^3x \; f(\mathbf{x}) \, , \tag{2.90}$$

where V is the volume. Thus, to access the statistical properties of a field at a given scale, one needs enough independent regions of the corresponding size. The fair sample hypothesis, in practice, induces a *cosmic variance* because of the finite size of the observable universe. This variance increases with the size of the considered region, *e.g.* for a region with a size of half of the observable universe, the statistical properties can only be computed with an average over 8 realizations. The fair sample hypothesis holds in general for the fields that we consider in cosmology, in particular for Gaussian random fields. It can however break for specific models, *e.g.* a universe with a non-trivial global topology [94].

Correlation functions

In general the n-point correlation function is defined to be the n-th order connected part [94], *i.e.*

$$\xi_n = \langle f_1 \; ... \; f_n \rangle_c = \langle f_1 \; ... \; f_n \rangle - \sum_{p \in \pi} \prod_{b \in p} \langle b \rangle_c \, , \tag{2.91}$$

where π is the ensemble of all partition of all possible products of $\{f_1, ..., f_n\}$ except the product of all elements and where we denote by $\langle . \rangle_c$ the connected part. The quantity f_i means $f(\mathbf{x}_i)$ for readability. For $n = 1$, we find the trivial result

$$\langle f_1 \rangle = \langle f_1 \rangle_c \, . \tag{2.92}$$

For $n = 2$ we have $\pi = \{\{f_1, f_2\}\}$ and hence p can only be $\{f_1, f_2\}$ which means that:

$$\xi_2 = \langle f_1 f_2 \rangle_c = \langle f_1 f_2 \rangle - \langle f_1 \rangle_c \langle f_2 \rangle_c \, . \tag{2.93}$$

If we use the trivial result (2.92), we find that the two-point correlation function ξ_2 is the covariance of f_1 and f_2. We will often deal with fluctuations $\mathcal{I}$ defined in (2.14), *i.e.* 0-mean fields. In this case, $n = 3$ is also quite simple and all results greatly simplify:

$$\begin{aligned} \xi_1 &= \langle \mathcal{I}_1 \rangle_c = \langle \mathcal{I}_1 \rangle = 0 \, , \\ \xi_2 &= \langle \mathcal{I}_1 \mathcal{I}_2 \rangle_c = \langle \mathcal{I}_1 \mathcal{I}_2 \rangle \, , \\ \xi_3 &= \langle \mathcal{I}_1 \mathcal{I}_2 \mathcal{I}_3 \rangle_c = \langle \mathcal{I}_1 \mathcal{I}_2 \mathcal{I}_3 \rangle \, . \end{aligned} \tag{2.94}$$

The highest correlator that we will use is for $n = 4$ and for perturbations $\mathcal{I}$. In that case

$$\pi = \{\{\mathcal{I}_1\mathcal{I}_2, \mathcal{I}_2\mathcal{I}_3\}, \{\mathcal{I}_1\mathcal{I}_3, \mathcal{I}_2\mathcal{I}_4\}, \{\mathcal{I}_1\mathcal{I}_4, \mathcal{I}_3\mathcal{I}_2\}, \{\mathcal{I}_1, \mathcal{I}_2, \mathcal{I}_1, \mathcal{I}_2\}\} \, , \tag{2.95}$$

where we have omitted all the elements like $\{\mathcal{I}_1\mathcal{I}_2\mathcal{I}_2, \mathcal{I}_3\}$ which vanish. Hence we can write the result in the following form:

$$\langle \mathcal{I}_1\mathcal{I}_2\mathcal{I}_3\mathcal{I}_4 \rangle = \langle \mathcal{I}_1\mathcal{I}_2\mathcal{I}_3\mathcal{I}_4 \rangle_c + \langle \mathcal{I}_1\mathcal{I}_2 \rangle \langle \mathcal{I}_3\mathcal{I}_4 \rangle + \langle \mathcal{I}_1\mathcal{I}_3 \rangle \langle \mathcal{I}_2\mathcal{I}_4 \rangle + \langle \mathcal{I}_1\mathcal{I}_4 \rangle \langle \mathcal{I}_2\mathcal{I}_3 \rangle \, . \tag{2.96}$$

where we have used equation (2.94).

Statistical homogeneity and isotropy

The fair sample hypothesis requires statistically homogeneous and isotropic fields. The homogeneity means invariance under translations so that a random field is statistically homogeneous if the joint probability distribution $\mathcal{P}(f(\mathbf{x}_1), ..., f(\mathbf{x}_n))$, is invariant under translations:

$$\mathcal{P}(f(\mathbf{x}_1), ..., f(\mathbf{x}_n)) = \mathcal{P}(f(\mathbf{x}_1 + \mathbf{y}), ..., f(\mathbf{x}_n + \mathbf{y}))\,. \tag{2.97}$$

The statistical homogeneity of the random field (2.97) translates into the fact that the correlation function does not depend on the origin. Thus, the 2-point correlation function satisfies $\xi(\mathbf{x}_1, \mathbf{x}_2) = \xi(\mathbf{x}_1 - \mathbf{x}_2)$. Similarly, statistical isotropy means that the joint probability distribution $\mathcal{P}(f(\mathbf{x}_1), ..., f(\mathbf{x}_n))$ is invariant under rotations. For the 2-point correlation function, homogeneity plus isotropy means:

$$\xi(\mathbf{x}_1, \mathbf{x}_2) = \xi(|\mathbf{x}_1 - \mathbf{x}_2|)\,. \tag{2.98}$$

Transfer functions

We have introduced in section 2.4.1 the Fourier transform and one of its fundamental properties (2.50). In section 2.2, we also explained that we can split the perturbations into scalar, vector, and tensor perturbations. One can show that these perturbations are decoupled at the linear level in Fourier space. This means that they can be treated independently at first order. A proof for this is given in [89] for the adiabatic case.

Before going further, we stress here that we should differentiate the linear level and the first order. For example, if we consider equation (2.48c) at the linear level and for $\pi = 0$, we have $\chi = 0$. This means that at the linear level we have $\chi^{(n)} = 0$ for all orders n. If we consider equation (2.48c) up to the quadratic level, the source term does not vanish: $\chi = Q_{SS}$. At first order, we still have $\chi^{(1)} = 0$ but now at second order, we have $\chi^{(2)} = Q^{(2)}_{SS}$. Having this difference in mind, we will expand the field into a linear and a quadratic level dynamics thanks to the transfer functions.

Let us first consider the linear level. The translation invariance of the linearized equation of motion in real space translates into the fact that in Fourier space, the modes are decoupled. This means that each mode k can be studied independently. A proof is also given in [89]. This translates into the fact that all equations at the linear level (Einstein and conservation equations for instance) can be written in a form that only involves one single mode k with the corresponding $\mathcal{I}(\mathbf{k})$. Thanks to this property, we can split any field into a stochastic field at a fixed time and a deterministic *transfer function* $\mathcal{T}^{(1)}(\tau, k)$. If we consider the full perturbed field $\mathcal{I}$ (we do not use (2.15) yet), then the linear dynamics reads:

$$\mathcal{I}(\tau, \mathbf{k}) = \mathcal{T}^{(1)}(\tau, k)\mathcal{I}(\tau_0, \mathbf{k})\,. \tag{2.99}$$

Note that the isotropy implies that $\mathcal{T}^{(1)}(\tau, k)$ only depends on the modulus of the mode k. The field $\mathcal{I}(\tau_0, \mathbf{k})$ is usually taken to be the initial conditions generated by inflation. Typically, the initial condition of all the observed fields are expressed as functions of the curvature perturbation in the comoving gauge $\mathcal{R}(\tau_0)$ (or equivalently $\zeta(\tau_0)$), the primordial entropy perturbation $\mathcal{S}(\tau_0)$ and the primordial relative velocity $\mathcal{V}(\tau_0)$. Therefore, we define the respective first-order transfer function $\mathcal{T}^{(1)}_{I,\mathcal{I}}$:

$$\mathcal{I}(\tau, \mathbf{k}) = \sum_I \mathcal{T}^{(1)}_{I,\mathcal{I}}(\tau, k) I(\mathbf{k})\,, \tag{2.100}$$

where $I \in \mathcal{R}, \mathcal{S}, \mathcal{V}$. In the following, we note $I = I(\tau_0)$. The functions $\mathcal{T}^{(1)}_{I,\mathcal{I}}(\tau, k)$ contain the linear evolution of the modes but also the conversion of I to $\mathcal{I}$.

Note that we have not expanded the field following (2.15). Hence, from (2.100), we see that the perturbations, at any order (n), are linearly propagated through the cosmological history. However, for the next to linear level, the decoupling of the modes and of the SVT is not true anymore. Hence, another term taking into account the non-linear propagation of the linear primordial fluctuations should be added. To understand how the non-linearities couple the modes, let us consider the expansion of the Einstein equations up to the quadratic level w.r.t. to the perturbed fields (2.48) for ADI. On the right-hand side, the source terms Q are quadratic in the perturbed fields. For example, it is straightforward to show that

$$Q^{(2)}_{TT} = 3\mathcal{H}^2\psi^2 - \frac{1}{2}\psi^{,i}\psi_{,i} + 2\psi\Delta\psi\,, \tag{2.101}$$

which in Fourier space and in the adiabatic case becomes

$$Q^{(2)}_{TT}(\mathbf{k}) = \int_{\mathbf{k_1 k_2}} \left(3\mathcal{H}^2 - \frac{1}{2}\mathbf{k_1}\cdot\mathbf{k_2} + (k_1^2 + k_2^2)\right) \mathcal{T}^{(1)}_{\psi}(k_1)\mathcal{T}^{(1)}_{\psi}(k_2)\mathcal{R}(\mathbf{k_1})\mathcal{R}(\mathbf{k_2})\,, \tag{2.102}$$

where the integral is defined as

$$\int_{\mathbf{k_1 k_2}} = \int \frac{d^3k_1 d^3k_2}{(2\pi)^2}\delta(\mathbf{k} - \mathbf{k_1} - \mathbf{k_2})\,. \tag{2.103}$$

Thanks to the δ-function, we have $\mathbf{k} = \mathbf{k_1} + \mathbf{k_2}$ which implies the relation

$$\mathbf{k_1}\cdot\mathbf{k_2} = \frac{k^2 - k_1^2 - k_2^2}{2}\,. \tag{2.104}$$

The variables k_1 and k_2 are both dummy variables while k is the modulus of the Fourier mode of the field that we are computing. In a quadratic term, *e.g.* $\psi\Delta\delta$, the choice of which dummy variable we use for δ and ψ is arbitrary and breaks the symmetry. To keep the symmetry apparent in the kernels expression, we always symmetrize the kernel, for example

$$\psi(\mathbf{x})\Delta\delta(\mathbf{x}) \xrightarrow{\mathcal{F}_k} -\frac{1}{2}\left(k_2^2\psi(\mathbf{k}_1)\delta(\mathbf{k}_2) + k_1^2\psi(\mathbf{k}_2)\delta(\mathbf{k}_1)\right)\,. \tag{2.105}$$

We used this symmetrization to compute (2.102).

At the next to linear level, the source terms are quadratic and can always be written as an integral of the form (2.102). Hence, we define:

$$\mathcal{I}(\tau, k) = \mathcal{T}^{(1)}_{\mathcal{I}}(\tau, k)\mathcal{R}(\mathbf{k}) + \int_{\mathbf{k_1 k_2}} \mathcal{T}^{(2)}_{\mathcal{I}}(\tau, k_1, k_2, k)\mathcal{R}(\mathbf{k}_1)\mathcal{R}(\mathbf{k}_2)\,, \tag{2.106}$$

where $\mathcal{T}^{(2)}_{\mathcal{I}}$ is the second-order transfer function of the variable $\mathcal{I}$ [100, 101]. The first term of equation (2.106) is the linear propagation of the initial condition while the second accounts for the non-linear evolution which couples the modes. We neglect all the terms of order larger than $\mathcal{R}^2$. If not, we would have an infinite number of terms where we could define the n-th order transfer function $\mathcal{T}^{(n)}$ using the same principle.

For the quadratic terms, the second-order transfer function is *separable*. This means that the second order transfer function can be decomposed into a sum of products of three functions that depend only on one variable $F_i(k)$, $G_i(k)$ and $H_i(k)$:

$$\mathcal{T}^{(2)}_{\mathcal{I}}(k_1, k_2, k) = \sum_i F_i(k_1)G_i(k_2)H_i(k)\,. \tag{2.107}$$

Then, we can absorb the stochastic fields in F_i and G_i, *e.g.* $\tilde{F}_i(\mathbf{k}) = F_i(\mathbf{k})\mathcal{R}(\mathbf{k})$. We can also integrate out $\mathbf{k}_2$ thanks to the δ-function; a generic quadratic term Q becomes

$$Q^{(2)}(\tau, k) = \sum_i H_i(k) \int_{\mathbf{k_1}} \tilde{F}_i(\mathbf{k}_1)\tilde{G}_i(\mathbf{k} - \mathbf{k_1})\,, \tag{2.108}$$

which is a sum of the convolutions $\tilde{F}_i * \tilde{G}_i$ with a constant factor $H_i(k)$. The Fourier transform (here an inverse Fourier transform) of a convolution becomes a simple product. A product in real space is equivalent to a separable kernel in Fourier space. This might be obvious for the quadratic terms. For the pure second-order terms ($\mathcal{I}^{(2)}$) however, in general, the kernels are not separable. The only exact way is to compute the full integral (2.106), which is the subject of the third part of this thesis.

To conclude, up to the quadratic level, our fields can be written for ADI in the form of equation (2.106). Now, if we expand the field following (2.15), we find that the first-order part of the field $\mathcal{I}^{(1)}$ reads:

$$\mathcal{I}^{(1)}(\tau, \mathbf{k}) = \mathcal{T}^{(1)}_{\mathcal{R},\mathcal{I}}(\tau, k)\mathcal{R}^{(1)}(\mathbf{k})\,, \tag{2.109}$$

and the second-order part reads:

$$\mathcal{I}^{(2)}(\tau, \mathbf{k}) = \mathcal{T}^{(1)}_{\mathcal{R},\mathcal{I}}(\tau, k)\mathcal{R}^{(2)}(\mathbf{k}) + \int_{\mathbf{k_1 k_2}} \mathcal{T}^{(2)}_{\mathcal{I}}(\tau, k_1, k_2, k)\mathcal{R}^{(1)}(\mathbf{k}_1)\mathcal{R}^{(1)}(\mathbf{k}_2)\,. \tag{2.110}$$

The linear level and first-order are often confused because equation (2.100) and (2.109) are similar. If we look at (2.110) however, we see that even at second order, there is a linear term (the first term of the right-hand side).

The generalization of the second-order to the isocurvature modes is straightforward and will not be treated here. In this thesis, we neglect any higher-order corrections.

2.5.2 (non-)Gaussian fields

Gaussian field

The primordial fields generated by inflation have the very important property to be Gaussian at first order because of their quantum origin. Let us split in Fourier space the field f into a real and an imaginary part:

$$f(\mathbf{k}) = a_{\mathbf{k}} + ib_{\mathbf{k}}\,. \tag{2.111}$$

The field f depends on two random variables $a_{\mathbf{k}}$ and $b_{\mathbf{k}}$. It is a Gaussian random field if $a_{\mathbf{k}}$ and $b_{\mathbf{k}}$ are mutually independent and if they have a Gaussian distribution:

$$\mathcal{P}\left(w_{\mathbf{k}}\right) = \frac{1}{\sqrt{2\pi}\sigma_k} \exp\left(-\frac{w_{\mathbf{k}}^2}{2\sigma_k^2}\right), \tag{2.112}$$

where w can be the real or the imaginary part and where $\sigma_{\mathbf{k}}$ is the variance. Equivalently, one can obtain (2.112) by assuming that the phases are mutually independent and uniformly distributed between 0 and 2π [102]. A demonstration can be found in [103] (Theorem 6-3). Note that the standard deviation σ_k depends on the modulus of k because of isotropy and is the same for $a_{\mathbf{k}}$ and $b_{\mathbf{k}}$. From the definition of a Gaussian field

(2.112), we can derive the PDF of the modulus $|f_{\mathbf{k}}|$ of f, we find a Rayleigh distribution [102]

$$\mathcal{P}\left(|f_{\mathbf{k}}|\right) = \frac{|f_{\mathbf{k}}|}{2\pi\sigma_k^2}\exp\left(-\frac{|f_{\mathbf{k}}|^2}{2\sigma_k^2}\right), \tag{2.113}$$

while the PDF of the phase is uniform between 0 and 2π. We can also show from (2.113) that in real space, the PDF of $f(\mathbf{x})$ is still a Gaussian. Note that the Gaussianity in real space (2.113) follows from (2.111) but is not equivalent since we have supposed in addition the independence of the real and imaginary parts.

Nearly-Gaussian fields

Deviations from Gaussianity can be generated by a non-linear evolution. We can see that by looking at the leading order non-Gaussian expression in (2.106); the product of two Gaussian fields is not a Gaussian. We call *primordial non-Gaussianity* (PNG) any NG generated during inflation (or alternative early universe models). They can come from the presence of multiple fields, interactions, or non-standard kinetic terms. See [104, 105] for a review. In addition, general relativity is a non-linear theory so that in general, even if the initial conditions are perfectly Gaussian, the evolution generates non-Gaussianities. We usually call this type of NG the *intrinsic non-Gaussianities*. Fortunately, we can use perturbation theory because the amplitude of the field perturbations is small: of order 10^{-5} for the gravitational potentials ϕ and ψ and hence at second order $\phi^{(2)} \sim \phi_{(1)}^2 \ll \phi_{(1)}$.

To treat NG in a perturbative way, we usually use the *Edgeworth expansion* as derived in [94]. This is an expansion around a Gaussian with expansion coefficient the real space standard deviation σ.

2.5.3 Power spectrum

The power spectrum is probably one of the most important objects of cosmology since it contains all the information of a Gaussian field as we will see. It is the Fourier counterpart of the 2-point correlation function defined in equation (2.93). Let us write (2.93) in Fourier space:

$$\langle f(\mathbf{k}_1)f(\mathbf{k}_2)\rangle = \int d^3x d^3r \ \langle f(\mathbf{x})f(\mathbf{x}+\mathbf{r})\rangle\, e^{-i(\mathbf{k}_1+\mathbf{k}_2)\mathbf{x}-i\mathbf{k}_2\mathbf{r}}\,. \tag{2.114}$$

By using (2.93) and integrating out $\mathbf{x}$, we define the power spectrum $P(k)$ as:

$$\begin{aligned}\langle f(\mathbf{k}_1)f(\mathbf{k}_2)\rangle =& (2\pi)^3\delta(\mathbf{k}_1+\mathbf{k}_2)\int d^3r \ \xi_2(r)e^{-i\mathbf{k}_2\mathbf{r}}\\ =& (2\pi)^3\delta(\mathbf{k}_1+\mathbf{k}_2)P(k_2)\,,\end{aligned} \tag{2.115}$$

where ξ_2 is the two point correlation function defined in equation (2.93).

Scale invariant spectra are of particular importance for cosmology. One very important property that will characterize the cosmological fluctuations is *scale invariance*. A scale invariant field is a field whose statistical properties (*i.e.* the correlation functions) are left unchanged under the rescaling transformation $\mathbf{x} \to \lambda\mathbf{x}$ where λ is any real number. For the 2-point correlation function, it reads

$$\langle f(\mathbf{x}_1)f(\mathbf{x}_2)\rangle = \langle f(\lambda\mathbf{x}_1)f(\lambda\mathbf{x}_2)\rangle\ . \tag{2.116}$$

If we go to Fourier space, use the Dirac-δ property $\delta(\lambda\mathbf{k}) = \lambda^{-3}\delta(\mathbf{k})$ and use the fact that the Fourier modes transforms like $f(\lambda\mathbf{k}) \to \lambda^{-3} f(\mathbf{k})$, one can show that the power spectrum of a scale invariant field scales like k^{-3}. Hence, we sometime define the dimensionless power spectrum $\Delta(k)$, *e.g.* in [89]

$$\Delta(k) = \frac{k^3}{2\pi^2} P(k)\,, \tag{2.117}$$

which is now independent of k in the case of scale invariance.

Let us now compute the power spectrum of a Gaussian field by using its definition (2.112). In the definition of the expectation value (2.89) we can replace $\mathcal{D}f \to \Pi_{\mathbf{k}} \int da_{\mathbf{k}} db_{\mathbf{k}}$. Then, by using the fact that the integrand is even under $a_{\mathbf{k}}$ and $b_{\mathbf{k}}$ we can show that:

$$\langle f(\mathbf{k}_1) f(\mathbf{k}_2)\rangle = \sigma_k^2 \delta(\mathbf{k}_1 + \mathbf{k}_2)\,. \tag{2.118}$$

For a Gaussian field, the power spectrum represents the standard deviation. According to the definition we find:

$$P(k) = \frac{\sigma_k^2}{(2\pi)^3}\,. \tag{2.119}$$

Therefore, in the Gaussian case and under the isotropy and homogeneity assumptions using in equation (2.115), the power spectrum fully describes the statistics of the perturbations and all higher order statistics either vanish or can be reduced to a function of the power spectrum. This is called Wick's theorem [94]:

$$\begin{aligned} \langle f(\mathbf{k}_1)\ \ldots\ f(\mathbf{k}_{2N+1})\rangle &= 0\,, \\ \langle f(\mathbf{k}_1)\ \ldots\ f(\mathbf{k}_{2N})\rangle &= \sum_b \prod_{i,j\in b} \langle f(\mathbf{k}_i) f(\mathbf{k}_j)\rangle\ , \end{aligned} \tag{2.120}$$

where b is the ensemble of all couples of $\{1, ..., N\}$. The first equality is a consequence of the fact that a Gaussian is an even function. One can show that a field whose PDF follows an Edgeworth expansion has the same power spectrum (no correction from higher-order terms).

Finally, as we have seen before, we can relate the perturbations at a given time $\mathcal{I}(\tau, \mathbf{k})$ to the primordial fluctuations $\mathcal{R}(\mathbf{k})$, $\mathcal{S}(\mathbf{k})$ and $\mathcal{V}(\mathbf{k})$ thanks to the transfer functions. By injecting the full expansion (2.106) into (2.115) and by using Wick's theorem, one finds for ADI that:

$$\begin{aligned} P_{\mathcal{I}}(k_1) = \left(\mathcal{T}_{\mathcal{I}}^{(1)}(k_1)\right)^2 P_{\mathcal{R}}(k_1) &+ 2\mathcal{T}_{\mathcal{I}}^{(1)}(k_1) \int_{\mathbf{q_1 q_2}} \mathcal{T}_{\mathcal{I}}^{(2)}(q_1, q_2, k_1) B_{\mathcal{R}}(k_1, q_1, q_2) \\ &+ 2 \int_{\mathbf{q_1 q_2}} \left(\mathcal{T}_{\mathcal{I}}^{(2)}(q_1, q_2, k_1)\right)^2 P_{\mathcal{R}}(q_1) P_{\mathcal{R}}(q_2) \\ &+ \int_{\mathbf{q_1 q_1 q_3 q_4}} \mathcal{T}_{\mathcal{I}}^{(2)}(q_1, q_2, k_1) \mathcal{T}_{\mathcal{I}}^{(2)}(q_3, q_4, k_1) S_{\mathcal{R}}(q_1, q_2, q_3, q_4)\,, \end{aligned} \tag{2.121}$$

where it is always assumed implicitly that the power spectrum $P_{\mathcal{R}}$, the bispectrum $B_{\mathcal{R}}$ and the trispectrum $S_{\mathcal{R}}$ are evaluated at the primordial time τ_0. Remember that in the field expansion (2.106), we neglect all contributions higher than $\mathcal{R}^2$. Let us describe equation (2.121):

- The first term comes from the linear propagation of the primordial curvature perturbation. This term is of order $\mathcal{R}^2$ and is therefore dominant. If we consider only the linear evolution and vanishing PNG, it is the only term that does not vanish. Note that, as we shall see in section 3.1, $P_{\mathcal{R}} \sim 10^{-9}$.

- The second term of (2.121) does not vanish only for non-Gaussian initial conditions, *i.e.* $B_{\mathcal{R}} \neq 0$. The function $B_{\mathcal{R}}$ is the primordial curvature bispectrum, see the following section 2.5.4 for a detailed discussion about the bispectrum. It arises from the non-linear evolution of PNG, encapsulated in $\mathcal{T}^{(2)}$. As we will see, the local primordial bispectrum is $\propto P_{\mathcal{R}}^2$. A large amplitude that would compensate for this suppression is excluded by the Planck collaboration constraints, see section 2.5.4.

- To compute the last two terms, which are both of order $\mathcal{R}^4$, we have used equation (2.96). The third term arises from the 2-point correlation squared of equation (2.96). It also comes from the non-linear propagation but involves only the power spectrum. Hence, it is present even for vanishing PNG. This term becomes important only for large non-linearities, *i.e.* large $\mathcal{T}^{(2)}$. This is eventually the case for CDM [100]. This term becomes important in the third part of this thesis.

- The last term comes from the 4-point connected part of equation (2.96). We have defined the primordial trispectrum $S_{\mathcal{R}}(q_1, q_2, q_3, q_4)$, *i.e.* the connected part of the primordial 4-point correlation function in Fourier space:

  $$\langle \mathcal{I}(\mathbf{k}_1)\mathcal{I}(\mathbf{k}_2)\mathcal{I}(\mathbf{k}_3)\mathcal{I}(\mathbf{k}_4)\rangle = (2\pi)^3\delta(\mathbf{k}_1+\mathbf{k}_2+\mathbf{k}_3+\mathbf{k}_4)S_{\mathcal{I}}(k_1,k_2,k_3,k_4)\,. \tag{2.122}$$

  The trispectrum induced by inflation is a very powerful tool to study inflation see *e.g.* the Ph.D. thesis [106]. As explained in [100], the primordial trispectrum is generally proportional to $P_{\mathcal{R}}^3$. Thus, it can be neglected w.r.t. to all other terms, except for very large amplitude that would compensate this suppression (this is however excluded by the current observations in the common models [107]).

In practice, the power spectrum is dominated by the linear propagation of the primordial first-order curvature perturbation. As explained in [100], the CMB data fits the CMB power spectrum to high precision, see [108], which is a confirmation that both the PNG and the non-linearities due to the evolution are small for the photons. The question of whether it will be possible or not to detect the evolution due to the general relativistic non-linearities is the subject of the third part of this thesis.

Let us generalize the leading order of the power spectrum to the isocurvature modes. By using equation (2.100) we find

$$P_{\mathcal{I}}(\tau,k) = \sum_{IJ}\mathcal{T}^{(1)}_{I,\mathcal{I}}(\tau,\mathbf{k})\mathcal{T}^{(1)}_{J,\mathcal{I}}(\tau,\mathbf{k})P^{IJ}(k)\,, \tag{2.123}$$

where it is again always assumed implicitly that the power spectrum P_{IJ} is evaluated at the primordial time and where

$$(2\pi)^3\delta(\mathbf{k_1}+\mathbf{k_2})P^{IJ}(k_1) = \langle I(\mathbf{k_1})J(\mathbf{k_2})\rangle\ . \tag{2.124}$$

Note that at the linear level, if the primordial fluctuations are statistically Gaussian, the field will remain a Gaussian at any time with a changing standard deviation according to equations (2.123) and (2.119).

local	-2.5 ± 5.0
equilateral	-19 ± 48
orthogonal	-34 ± 24

Table 2.2: We give in this table the best estimated values of the adiabatic $f_{\rm NL}$ given the Planck results and by using the binned bispectrum estimator, see [107], as well as the associated standard deviation. The relation between the adiabatic $f_{\rm NL}$ and $\tilde{f}_{\rm NL}$ in the radiation domination era is $\tilde{f}_{\rm NL} = 6f_{\rm NL}/5$.

2.5.4 Bispectrum

The bispectrum is one of the most important objects to test inflation and study NG. There are at least two reasons for that. First, it is the next to leading order which means that it should be the largest correlator encoding deviations to Gaussianity. Second, it is an odd correlator which means that it vanishes in the Gaussian case. Hence, it is a "clean" test of NG in the sense that Gaussian perturbations do not source the bispectrum. Similarly to the power spectrum definition (2.114) and (2.115), the bispectrum $B(k_1, k_2, k_3)$ can be defined as:

$$\langle f(\mathbf{k}_1)f(\mathbf{k}_2)f(\mathbf{k}_3)\rangle = (2\pi)^3\delta(\mathbf{k}_1+\mathbf{k}_2+\mathbf{k}_3)B(k_1,k_2,k_3)\,, \tag{2.125}$$

where we again used the homogeneity and the isotropy. This definition can be generalized to higher order statistics. By replacing the Fourier modes $f(\mathbf{k})$ by their expression (2.50), we can show that

$$\langle f(\mathbf{k}_1)f(\mathbf{k}_2)f(\mathbf{k}_3)\rangle = \int d^3x d^3r d^3s\ \xi_3(r,s,t)e^{-i(\mathbf{k}_1+\mathbf{k}_2+\mathbf{k}_3)\mathbf{x}-i\mathbf{k}_2\mathbf{r}-i\mathbf{k}_3\mathbf{s}}\,, \tag{2.126}$$

where ξ_3 is the 3-point correlation function and where $\mathbf{t} = \mathbf{r} - \mathbf{s}$. The fact that ξ_3 is a function of the modulus of $\mathbf{r}$, $\mathbf{s}$ and $\mathbf{t}$ comes from the homogeneity and isotropy hypothesis. The integral over $\mathbf{x}$ gives the delta function which imposes that the modes should form a triangle. Hence, the bispectrum is the Fourier transform of the 3-point correlation function. For the same reason as for the power spectrum, the bispectrum is only a function of the modulus of the modes under the homogeneity and isotropy hypothesis. The scale invariance, similarly to (2.116), gives for the bispectrum:

$$B(\lambda k_1, \lambda k_2, \lambda k_3) = \lambda^{-6}B(k_1,k_2,k_3)\,. \tag{2.127}$$

It is usual to define the shape function $S(k_1, k_2, k_3)$:

$$B(k_1,k_2,k_3) = A\frac{S(k_1,k_2,k_3)}{(k_1k_2k_3)^2}\,, \tag{2.128}$$

where A is a normalization factor. In the case of scale invariance, by comparing equations (2.127) and (2.128), we can conclude that the shape function would be a function of the ratio between the scales k_1, k_2, k_3. Usually, we use the variables $x_1 = k_1/k_3$ and $x_2 = k_2/k_3$ so that the shape function only depends on x_1, x_2. We also usually normalize $S(x_1, x_2)$ in order to have $S(1, 1) = 1$. Moreover, the amplitude of the bispectrum is usually defined in an equilateral configuration, *i.e.* $k_1 = k_2 = k_3$, and w.r.t. the power spectrum:

$$\tilde{f}_{\rm NL}(k) = \frac{1}{3}\frac{B(k,k,k)}{P(k)^2}\,. \tag{2.129}$$

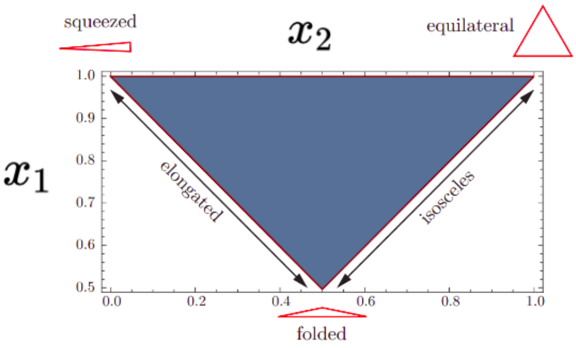

Figure 2.1: All triangle configurations are encompassed in this triangular two dimensional space as a function of x_1 and x_2 which are defined as the ratios of the first and second sides w.r.t. the third: $x_1 = k_1/k_3$ and $x_2 = k_2/k_3$. The variables x_1 and x_2 are ordered as $x_1 \leq x_2 \leq 1$ and must satisfy the triangle inequality $x_1 + x_2 \geq 1$. Figure from [89].

In the case of scale invariance, we therefore have

$$B(k_1, k_2, k_3) = \frac{1}{3}\tilde{f}_{\mathrm{NL}} A_s^2 \frac{S(x_2, x_3)}{(k_1 k_2 k_3)^2} \, . \tag{2.130}$$

In reality, the scale invariance is not verified exactly but we can still use the shape function. The shape is a powerful property that can differentiate the models of inflation.

For a Gaussian field, from Wick's theorem (2.120), the bispectrum vanishes. The leading order contribution to the auto-correlation bispectrum in the case of the Edgeworth expansion is proportional to $(\sigma_k)^4$, *i.e.* the spectrum squared $(\sigma_k)^2$ [109]. It is for this reason that the bispectrum amplitude is usually always compared to the power spectrum squared like in equation (2.129). In addition, in the most popular inflation models, the bispectrum can be expressed as a function of the power spectrum squared.

It turns out that the most common models of inflation predict a nearly-scale invariant bispectrum so that the way to distinguish between the models is to look at the shape function. Without loss of generality, we can assume $k_1 \leq k_2 \leq k_3$ which means $x_1 \leq x_2 \leq 1$. The two dimensional space generated by x_1, x_2 given these conditions is represented in figure 2.1. The different models will for example peak for a given triangular configuration, *i.e.* a given place in figure 2.1. The typical example is the so-called *squeezed* configuration which corresponds to the upper left region in the figure 2.1. The triangles in the squeezed limit have two large modes and one small which corresponds to a coupling between large and small modes. Of course, the universe may be non-Gaussian but with a very different shape from the ones we are looking for. In this situation, we could completely miss the non-Gaussian information of the universe. A way to quantify how an actual shape S_1 with bispectrum B_1 can be "seen" by looking at another shape S_2 with bispectrum B_2 is to define the "scalar product" [110, 111]:

$$B_1 \cdot B_2 = \sqrt{B_1^2 B_2^2} \cos(B_1, B_2) = \sum_{k_i} \frac{B_1(k_1, k_2, k_3) B_2(k_1, k_2, k_3)}{P(k_1)P(k_2)P(k_3)} \, , \tag{2.131}$$

where we mean $B_i^2 = (B_i \cdot B_i)$ and where we have also defined the cosine of the scalar product. The denominator is actually the variance of the bispectrum. If the scalar product is small, or equivalently $\cos(B_1, B_2) \sim 0$, it means that we would very badly detect a shape B_1 by looking at the shape B_2.

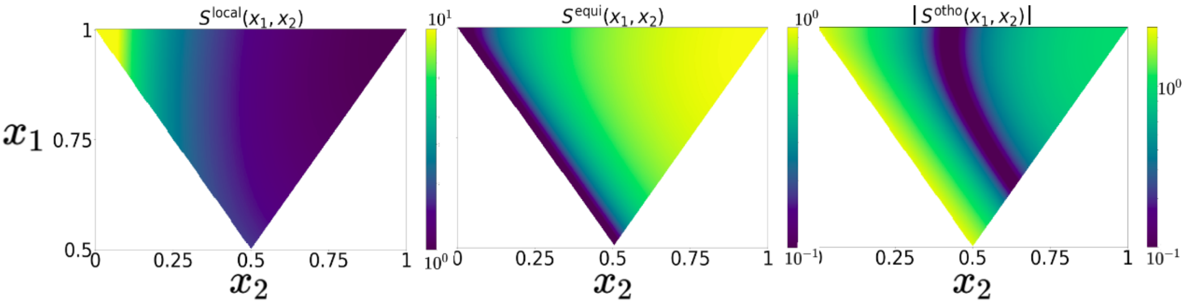

Figure 2.2: Three common bispectrum shapes tested by Planck. In the left, the local shape, equation (2.134) which peaks in the squeezed limit. In the middle, the equilateral shape, equation (2.136), peaking in the equilateral configuration. In the right, the absolute value of the orthogonal shape equation (2.138). It is positive in the equilateral corner, changes sign in the blue band and becomes negative on the elongated limit (the left side). All shapes are normalized such that $S(1,1) = 1$.

Let us review the three most famous shapes of primordial bispectra that have been constrained by [107]. The constraints are summarized in the table 2.2.

The local shape

The local shape is central in this thesis. We can derive it from the Komatsu and Spergel expansion of the Bardeen potential Φ, see equation (2.34):

$$\Phi(\mathbf{x}) = \Phi_G(\mathbf{x}) + f_{\mathrm{NL}}^{\mathrm{local}} \left(\Phi_G^2(\mathbf{x}) - \left\langle \Phi_G^2(\mathbf{x}) \right\rangle \right) , \tag{2.132}$$

where Φ_G is the purely Gaussian contribution.

Equation (2.132) was first introduced in [112]. The field Φ is given by a purely Gaussian contribution Φ_G and a non-Gaussian term, *i.e.* the one proportional to $f_{\mathrm{NL}}^{\mathrm{local}}$ in equation (2.132) often written Φ_{NG}, which is the square of Φ_G from which we subtract its expectation value in order to verify $\langle \Phi(\mathbf{x}) \rangle = 0$. The bispectrum of $\Phi(\mathbf{x})$ is then dominated by terms like $\langle \Phi_G \Phi_G \Phi_{NG} \rangle$. The local bispectrum can then be expressed at leading order as a function of the primordial curvature $\mathcal{R}$ power spectrum :

$$B_{\mathcal{R}}^{\mathrm{local}} = \tilde{f}_{\mathrm{NL}}^{\mathrm{local}} (P_{1,\mathcal{R}} P_{2,\mathcal{R}} + \mathrm{perm}) , \tag{2.133}$$

where for readability, the scale dependence (k_1, k_2, k_3) of the bispectrum is implicit and where we mean by $P_i^{\mathcal{R}}$ the primordial power spectrum of $\mathcal{R}$ as a function of k_i. Note that $\tilde{f}_{\mathrm{NL}}$ (with a tilde) is defined in terms of $\mathcal{R}$, or equivalently in terms of ζ as in [113]. The more usual f_{NL} used e.g. in [114, 115], are defined in terms of the gravitational potential Φ as in equation (2.132). Assuming scale invariance, we can factorize out a k^3 from the power spectrum. Hence, the local shape is given by

$$S_{\mathrm{local}} = \frac{1}{3} \left(\frac{k_3^2}{k_1 k_2} + \frac{k_1^2}{k_2 k_3} + \frac{k_2^2}{k_1 k_3} \right) . \tag{2.134}$$

The shape (2.134) has the very interesting property to peak in the squeezed limit, *e.g.* when $k_1 \ll k_2 \sim k_3$. We can see that on the left panel of figure 2.2. This shape is a prediction of multi-field inflation as we will see.

Equilateral shape

An equilateral shape can arise in single field inflation with non standard kinetic terms [116, 117]. A separable approximation of this bispectrum can be expressed as

$$B_{\mathcal{R}}^{\text{equi}} = \tilde{f}_{\text{NL}}^{\text{equi}} \left(3P_{1,\mathcal{R}} P_{2,\mathcal{R}}^{2/3} P_{3,\mathcal{R}}^{1/3} - \frac{3}{2} P_{1,\mathcal{R}} P_{2,\mathcal{R}} - (P_{1,\mathcal{R}} P_{2,\mathcal{R}} P_{3,\mathcal{R}})^{2/3} + \text{perm} \right) . \tag{2.135}$$

In the scale invariant limit, the shape can be written

$$S_{\text{equi}}(k_1, k_2, k_3) = \left(\frac{k_1}{k_2} + (5 \text{ perms}) \right) - \left(\frac{k_3^2}{k_1 k_2} + (2 \text{ perms}) \right) - 2 \, . \tag{2.136}$$

This shape has the particularity to peak when $k_1 \sim k_2 \sim k_3$ as we can see in the middle panel of figure 2.2.

Orthogonal

The orthogonal shape is constructed as being orthogonal to the equilateral shape: the scalar product $B_{\text{equi}} \cdot B_{\text{ortho}} = 0$ [110]. It reads

$$B_{\mathcal{R}}^{\text{equi}} = \tilde{f}_{\text{NL}}^{\text{ortho}} \left(9P_{1,\mathcal{R}} P_{2,\mathcal{R}}^{2/3} P_{3,\mathcal{R}}^{1/3} - \frac{9}{2} P_{1,\mathcal{R}} P_{2,\mathcal{R}} - 4(P_{1,\mathcal{R}} P_{2,\mathcal{R}} P_{3,\mathcal{R}})^{2/3} + \text{perm} \right) , \tag{2.137}$$

which gives in the scale invariant limit a shape function:

$$S_{\text{ortho}} = -3.84 \left(\frac{k_3^2}{k_1 k_2} + (2 \text{ perms}) \right) + 3.94 \left(\frac{k_1}{k_2} + (5 \text{ perms}) \right) - 11.10 \, . \tag{2.138}$$

In figure 2.2, we see that this shape peaks in two different limits: the equilateral for the positive values and in the elongated limit for the negative value. This change of sign ensure the cancellation of the scalar product $B_{\text{equi}} \cdot B_{\text{ortho}}$.

Link with inflation

Similarly to the power spectrum, let us compute the bispectrum of the perturbations $\mathcal{I}$ by assuming pure ADI and by injecting (2.106) into equation (2.125). We can find 3 different contributions [100]:

$$\begin{aligned} B_{\mathcal{I}}(k_1, k_2, k_3) = {} & \mathcal{T}_{\mathcal{I}}^{(1)}(k_1) \mathcal{T}_{\mathcal{I}}^{(1)}(k_2) \mathcal{T}_{f}^{(1)}(k_3) B_{\mathcal{R}}(k_1, k_2, k_3) \\ & + 2\mathcal{T}_{\mathcal{I}}^{(1)}(k_1) \mathcal{T}_{\mathcal{I}}^{(1)}(k_2) \mathcal{T}_{\mathcal{I}}^{(2)}(k_1, k_2, k_3) P_{\mathcal{R}}(k_1) P_{\mathcal{R}}(k_2) + 2 \text{ perm.} \\ & + \mathcal{T}_{\mathcal{I}}^{(1)}(k_1) \mathcal{T}_{\mathcal{I}}^{(1)}(k_2) \int_{\mathbf{q_1 q_2}} \mathcal{T}_{\mathcal{I}}^{(2)}(q_1, q_2, k_3) S_{\mathcal{R}}(k_1, k_2, q_1, q_2) + 2 \text{ perm.} . \end{aligned} \tag{2.139}$$

Note that for Gaussian initial condition ($B_{\mathcal{R}} = S_{\mathcal{R}} = 0$), the bispectrum vanishes for pure linear evolution ($\mathcal{T}^{(2)} = 0$). We see here appear the fact that, unlike the power spectrum, the bispectrum is a "clean" test of non-linearities in the universe.

Let us examine equation (2.139) line by line:

- On the first line we see appearing the primordial bispectrum of the curvature perturbation. This term comes from the product $\mathcal{I}_1 \mathcal{I}_2 \mathcal{I}_3$ where we recall that $\mathcal{I}_1 = \mathcal{I}(\tau, \mathbf{k_1})$. If we have vanishing PNG, it vanishes, else, it is linearly transported from the initial conditions. Thanks to this term, if the evolution of the universe is linear, we can have access to this primordial signal and in particular the PNG. For local PNG, it is of order $\tilde{f}_{\text{NL}} P_{\mathcal{R}}^2$.

- The second term is called the intrinsic bispectrum. Similarly to the third term of the power spectrum in equation (2.124), it comes from (2.96). The intrinsic bispectrum only involves the primordial curvature power spectrum and therefore arises from the second-order non-linearities of the dynamics encapsulated in $\mathcal{T}^{(2)}$. It does not vanish even for pure Gaussian IC. We directly see that it has the same dependence in the power spectrum as the so-called local shape introduced in equation (2.133). Therefore it can be confused with the primordial local shape even though this degree of similarity depends on the exact form of the second-order transfer function. Fortunately, it is not model-dependent in the sense that it depends only on general relativity and on the exact content of the universe and its interactions. Hence, the main question regarding this term is to determine its amplitude w.r.t. to the primordial amplitude $\tilde{f}_{\mathrm{NL}}$.

- In the third term, we see again a contribution of the primordial trispectrum $S_{\mathcal{R}}$ coming from the connected part of the decomposition (2.96). The function $S_{\mathcal{R}}$ is defined in equation (2.122). For the same reason as for the power spectrum (2.121), we can neglect it since it is suppressed by a factor $P_{\mathcal{R}}^3$.

The first two terms will be of major importance for this thesis. The first part of this thesis addresses the subject of improving the constraints on the primordial isocurvature modes introduced in section 2.4.5 by merging the information contained in their primordial power spectra and bispectra constraints. In the second part, we will be interested in quantifying the contamination of a local shape primordial bispectrum due to the intrinsic bispectrum in the large-scale structure.

Let us generalize the first term of equation (2.139) for isocurvature modes. The primordial bispectra are for a given mixture of IC:

$$(2\pi)^3\delta(\mathbf{k_1}+\mathbf{k_2}+\mathbf{k_3})B^{IJK}(k_1,k_2,k_3) = \langle I(\mathbf{k_1})J(\mathbf{k_2})K(\mathbf{k_3})\rangle \ . \tag{2.140}$$

By using equation (2.100) and (2.125) we find

$$B_f^{tot}(\tau,k_1,k_2,k_3) = \sum_{IJK}\mathcal{T}^{(1)}_{I,f}(\tau,k_1)\mathcal{T}^{(1)}_{J,f}(\tau,k_2)\mathcal{T}^{(1)}_{K,f}(\tau,k_3)B^{IJK}(k_1,k_2,k_3)\,. \tag{2.141}$$

Chapter 3

Inflation

3.1 Single-field inflation

As explained in the historical review, section 1.4, inflation is a causal mechanism that can explain the flatness, homogeneity, and isotropy of the universe. Moreover, it provides a quantum mechanism to generate small perturbations which are the seeds of the large-scale structure formation. During this period, the universe was dominated by a scalar field, called the inflaton, which has the property to accelerate the expansion of the universe. This property arises from a global non-zero potential energy of the field.

Today, only one fundamental scalar field has been discovered: the Higgs boson. The energy scale of inflation should be around $10^{14} - 10^{16}$ GeV which is 10 orders of magnitude larger than what we have access to with the most powerful particle accelerator on earth (the LHC). The extension of the standard model of particle at these energy scales, typically the so-called grand unified theory, can predict a large number of scalar fields by the mechanism of spontaneous symmetry breaking [88]. But the inflaton is not necessarily a fundamental particle but could be composite or could be just an effective parameter.

In this section, we will formally introduce inflation as a solution to the horizon problem and then explain the quantum mechanism that generates the perturbations.

3.1.1 Particle horizon

In the standard hot big bang model, where the early universe is dominated by radiation, the particle horizon is equal to the conformal and to the Hubble distance, see equation (2.55). At the period of the CMB emission, it corresponds to an angular size of a few degrees, as we said in the section 1.4. To solve the horizon problem, we could suppose that, actually, the particle horizon is much larger than we think, *i.e.* larger than the Hubble radius. To see how this is possible, let us re-write the particle horizon definition (3.1) as a function of $\mathcal{H}$:

$$x_{PH}(t_1) = \int_0^{a_1} d(\ln a)\frac{1}{\mathcal{H}}\,. \tag{3.1}$$

By looking at (3.1), a way to increase x_{PH} would be to make $\mathcal{H}$ very small, which means a large Hubble radius when $a \to 0$ such that the main contribution to the integral would come from very early times. Inflation can be defined as this very early period during which the Hubble radius was decreasing. Usually, we write this in terms of the time t as follows:

$$\frac{d}{dt}\left(\frac{1}{aH}\right) = -\frac{\ddot{a}}{(aH)^2} < 0\,. \tag{3.2}$$

Here we see that inflation is a period of accelerated expansion since, from equation (3.2), $\ddot{a} > 0$. Using the Friedmann equations we can rewrite (3.2) and define the slow-roll parameter ε

$$\varepsilon = -\frac{\mathcal{H}'}{\mathcal{H}^2} + 1 = -\frac{\dot{H}}{H^2} = -\frac{d\ln H}{d\ln a} < 1\,. \tag{3.3}$$

The condition $\varepsilon < 1$ can be used as the definition of inflation. Equation (3.3) also shows that during inflation, the Hubble parameter varies slowly. In the limit $\epsilon \to 0$ we recover the de Sitter limit. The common inflation model that is considered is a quasi de Sitter universe, *i.e.*

$$\varepsilon \ll 1\,. \tag{3.4}$$

A second condition is usually considered and is related to the duration of inflation. Indeed, if the condition (3.4) is verified, we have an inflation period, but it has to last long enough in order to homogenize the whole observable universe. This can be expressed in terms of the derivative of ε:

$$|\eta| = \left|\frac{\dot{\varepsilon}}{H\varepsilon}\right| \ll 1\,, \tag{3.5}$$

(note that there exist different definition of η, see *e.g.* [118]). The canonical inflation is then usually defined by $\varepsilon, |\eta| \ll 1$. To quantify the expansion of inflation, we often define the number of e-folds [89] as the logarithm of the scale factor at the end over the scale factor when inflation starts,*i.e.*

$$N = \ln\frac{a_{end}}{a_{start}} \geq 60\,. \tag{3.6}$$

To generate the flatness and the homogeneity/isotropy of our universe as we observe it, the number of e-fold should be a least 60. To give an idea, an expansion by 60 e-folds means that a region of one meter would become the whole observable universe, *i.e.* ~ 10 billion light-years.

3.1.2 Quasi de Sitter expansion

Canonical inflation is a phase of quasi-de Sitter expansion. As explained in section 1.2, the perfect de Sitter universe is an empty and cosmological constant dominated universe. From equation (2.40):

$$\dot{H} = 0, \qquad H^2 = \frac{\Lambda}{3}\,. \tag{3.7}$$

It follows directly that the condition (3.3) is verified since $\varepsilon = 0$. The evolution of the scale factor is obtained by the first equation of (2.40) by replacing H by its definition $\dot{a}/a$. By using (3.7) we find

$$a = e^{Ht}\,. \tag{3.8}$$

From equation (3.3) and (3.5) we find that in a de Sitter universe $\varepsilon = 0$ and $\eta = 0$. Since it has to end, inflation is a perturbed de Sitter universe where time translation symmetry is broken. An empty universe dominated by a cosmological constant can not be perturbed and would expand following (3.8) forever. Therefore, inflation cannot be due to a "real" cosmological constant so that we set it to 0. We suppose that the universe is filled with a field called the inflaton that has the property (2.44), *i.e.* to effectively imitate a cosmological constant with $\varepsilon, |\eta| \ll 1$. To find this property, let us write ε as a function of ω defined in equation (2.44), we find:

$$\varepsilon = \frac{3}{2}\left(1+\omega\right) . \tag{3.9}$$

In general, inflation must verify $\omega < -1/3$ from equation (3.3). In de Sitter cosmology, the cosmological constant would have $\omega = -1$ if we consider it as a fluid. For a canonical inflation we have $\varepsilon, |\eta| \ll 1$ and thus:

$$a \sim e^{Ht}, \qquad \dot{H} \sim 0, \qquad \omega \sim -1\,. \tag{3.10}$$

3.1.3 Inflaton

In the simplest scenario of inflation, the universe was dominated by a scalar particle, called the inflaton ϕ, minimally coupled to gravity. Its Lagrangian can be written [119]:

$$\mathcal{L}_\varphi = -\frac{1}{2} g^{\mu\nu} \varphi_{,\mu}\varphi_{,\nu} - V(\varphi)\,. \tag{3.11}$$

The function $V(\varphi)$ is a potential that we can keep general. The variation of the inflaton Lagrangian gives the evolution equation, also known as the Klein-Gordon equation:

$$\varphi'' + 3\mathcal{H}\varphi' - \Delta\varphi + a^2 V_{,\varphi} = 0\,. \tag{3.12}$$

The stress-energy tensor can be obtained with Noether's theorem

$$T_{\mu\nu} = \varphi_{,\mu}\varphi_{,\nu} + g_{\mu\nu}\mathcal{L}_\varphi\,. \tag{3.13}$$

We work with background quantities: $\varphi(t, \mathbf{x}) = \bar{\varphi}$, so that the gradient of that field vanishes. By analogy with a perfect fluid, we can write the homogeneous density and the pressure of the inflaton:

$$\bar{\rho}_\varphi = \frac{1}{2}\dot{\bar{\varphi}}^2 + V(\bar{\varphi}), \qquad \bar{p}_\varphi = \frac{1}{2}\dot{\bar{\varphi}}^2 - V(\bar{\varphi})\,. \tag{3.14}$$

We easily find ω_φ

$$\omega_\varphi = \frac{\dot{\bar{\varphi}}^2 - 2V(\bar{\varphi})}{\dot{\bar{\varphi}}^2 + 2V(\bar{\varphi})}\,. \tag{3.15}$$

For inflation to occur, ω_φ must satisfy the inequality (3.9) so that the kinetic energy of the field must be smaller than the potential.

$$\dot{\bar{\varphi}}^2 \ll V(\bar{\varphi})\,. \tag{3.16}$$

This is the reason why we usually speak about the *slow roll* condition to refer to equation (3.4) or (3.9). At leading order, the Klein-Gordon equation (3.12) reads:

$$\ddot{\bar{\varphi}} + 3H\dot{\bar{\varphi}} + V_{,\varphi} = 0\,, \tag{3.17}$$

which can also be obtained by substituting the density and the pressure (3.14) in the background conservation equation (2.41). Note also that the Friedmann equations read

$$3H^2 = \kappa\left(\frac{1}{2}\dot{\bar{\varphi}}^2 + V(\bar{\varphi})\right), \qquad \dot{H} = -\frac{\kappa}{2}\dot{\bar{\varphi}}^2 . \tag{3.18}$$

For the condition (3.16) to last long enough, the second derivative of φ should be small in comparison to the dragging term $3H\dot{\varphi}$ and the derivative of the potential $V_{,\varphi}$. From this condition we find that the second condition (3.5) can be translated in terms of φ as:

$$|\ddot{\bar{\varphi}}| \ll |3H\dot{\bar{\varphi}}|\,, V_{,\varphi}\,, \tag{3.19}$$

The slow-roll condition can also be expressed in terms of the potential derivative. Indeed, we can define

$$\varepsilon_V = \frac{1}{2\kappa}\left(\frac{V_{,\varphi}}{V}\right)^2, \qquad \eta_V = \frac{1}{\kappa}\frac{V_{,\varphi\varphi}}{V}\,. \tag{3.20}$$

If the slow-roll condition is verified, we can show that

$$\varepsilon_V \simeq \varepsilon, \qquad \eta \simeq 4\varepsilon - 2\eta_V\,. \tag{3.21}$$

3.1.4 Inflationary perturbations

To study the perturbations generation during inflation, it is convenient to work with the *Mukhanov-Sasaki* invariant variable defined in (2.36). Recall that in the spatially flat gauge ($\psi^{(1)} = 0$), we have $q^{(1)} = a\varphi^{(1)}$. Let us drop the (1) superscript again for this section since all results are first order. The evolution equation of the *Mukhanov-Sasaki* variable can be obtained by writing (2.60) in terms of q. It gives:

$$q_k{}'' + \left(k^2 - \frac{z''}{z}\right) q_k = 0\,, \tag{3.22}$$

where we have defined

$$z = a\sqrt{\kappa}\frac{\bar{\varphi}'}{\mathcal{H}} = a\sqrt{2\varepsilon}\,. \tag{3.23}$$

Note that we have already simplified the stochastic part so that q_k means $\mathcal{T}_q^{(1)}(k)$ while we note $q(\mathbf{k})$ (with a vector $\mathbf{k}$) the stochastic field. The Mukhanov-Sasaki equation is very convenient since it takes a very simple form in the two limits of interest, the sub- and super-horizon limits.

Let us now replace the Mukhanov-Sasaki variable by an operator and impose the canonical commutations relations between the operator $\hat{q}$ and its conjugate momentum $\hat{\pi}$:

$$\begin{aligned} [\hat{q}(\tau,\mathbf{x}), \hat{q}(\tau,\mathbf{x})] = [\hat{\pi}(\tau,\mathbf{x}), \hat{\pi}(\tau,\mathbf{x})] &= 0\,, \\ [\hat{q}(\tau,\mathbf{x}), \hat{\pi}(\tau,\mathbf{y})] &= i\delta(\mathbf{x}-\mathbf{y})\,. \end{aligned} \tag{3.24}$$

We use here the Heisenberg picture where the operators are time dependent. In Fourier space, a general solution of (3.22) can be written as

$$\hat{q}(\tau,\mathbf{x}) = \frac{1}{\sqrt{2}}\int \frac{d^3k}{(2\pi)^3}\left(q_k(\tau)\hat{a}_{\mathbf{k}}e^{i\mathbf{kx}} + q_k^*(\tau)\hat{a}_{\mathbf{k}}^\dagger e^{-i\mathbf{kx}}\right)\,, \tag{3.25}$$

where the operators $\hat{a}_{\mathbf{k}}^\dagger$ and $\hat{a}_{\mathbf{k}}$ are the creation and annihilation operators of a simple quantum harmonic oscillator satisfying the common commutation relations

$$\begin{aligned} [\hat{a}_{\mathbf{k}}, \hat{a}_{\mathbf{k}'}] = [\hat{a}_{\mathbf{k}}^\dagger, \hat{a}_{\mathbf{k}'}^\dagger] &= 0\,, \\ [\hat{a}_{\mathbf{k}}, \hat{a}_{\mathbf{k}'}^\dagger] &= (2\pi)^3\delta^{(3)}(\mathbf{k}-\mathbf{k}')\,. \end{aligned} \tag{3.26}$$

Sub-horizon

In the sub-horizon limit we have $\mathcal{H} \ll k$. The equation (3.22) takes the simple form of a harmonic oscillator with angular frequency k. The vacuum state and the solution in this limit can be written

$$\hat{a}_{\mathbf{k}} |0\rangle = 0, \qquad q_k = \frac{1}{\sqrt{2k}} e^{-ik\tau} \,. \tag{3.27}$$

The Mukhanov-Sasaki variable, and hence the primordial curvature perturbation, can then be seen as a quantum field and all of its mode functions $q_{\mathbf{k}}$ are harmonic oscillators in their ground states $|0\rangle$. The probability to measure a given state $q_{\mathbf{k}} = a_{\mathbf{k}} + ib_{\mathbf{k}}$ follows a Gaussian distribution:

$$\langle \hat{q}_{\mathbf{k}} |0\rangle \propto \exp\left(-(2\pi)^3 \frac{a_{\mathbf{k}}^2 + b_{\mathbf{k}}^2}{\sigma_k^2} \right) , \tag{3.28}$$

where σ_k is the variance of the quantum oscillator defined as the expectation value of the state $\hat{q}_{\mathbf{k}_2}$: $\langle 0| \hat{q}_{\mathbf{k}_1} \hat{q}_{\mathbf{k}_2} |0\rangle = \sigma_{k_1}^2 \delta(\mathbf{k_1} + \mathbf{k_2})$. It is then meaningful to identify the statistical expectation value of a Gaussian random field over a set of realizations and the quantum expectation:

$$\langle 0| \hat{q}(\tau, \mathbf{x}_1) \hat{q}(\tau, \mathbf{x}_2) |0\rangle = \langle q(\tau, \mathbf{x}_1) q(\tau, \mathbf{x}_2) \rangle \,. \tag{3.29}$$

And then, we can identify the power spectrum of q as σ_k. When we observe a given mode of the primordial curvature perturbation in the sky, we randomly draw a number given by the PDF (3.28) whose variance is $P_q(k)$.

The linear evolution of the perturbation leaves the fields in their ground states so that at any time, at the linear level, we will observe a Gaussian random field and the quantum expectation can be identified as the power spectrum of the field given equation (3.29).

Super-horizon

In the super-horizon limit $\mathcal{H} \gg k$, equation (3.22) reduces to

$$q'' - \frac{z''}{z} q = 0 \,. \tag{3.30}$$

If we neglect the decaying mode and use the sub-horizon limit to fix the constant, one finds

$$q_k = \frac{H(\tau_k)}{2\sqrt{k^3 \varepsilon(\tau_k)}} z \,, \tag{3.31}$$

where τ_k is the horizon crossing time of the mode k. To link the variable q with the curvature perturbation in the comoving gauge $\mathcal{R}$, we can identify the stress-energy tensor of a single scalar field (3.13) and the generic (2.30). We find that we can replace $v^{(1)} + B^{(1)}$ by $-\varphi^{(1)}/\bar{\varphi}'$ so that equation (2.35) can be written:

$$\mathcal{R} = \psi + \mathcal{H} \frac{\varphi}{\bar{\varphi}'} \,. \tag{3.32}$$

From (3.32), we also see that the Sasaki-Mukhanov variable (2.36) can be expressed in terms of $\mathcal{R}$ as

$$q = z\mathcal{R} \,. \tag{3.33}$$

Similarly to (3.29), the *power spectrum* $P_{\mathcal{R}}(k)$ is given by the variance of the quantum operator $\hat{\mathcal{R}}$:

$$\langle 0| \hat{\mathcal{R}}(\tau, k) \hat{\mathcal{R}}(\tau, k') |0\rangle = (2\pi)^3 \delta(k - k') P_{\mathcal{R}}(k) \,. \tag{3.34}$$

Hence, using equations (3.34), (3.33) and the solution (3.31), we find the power spectrum

$$P_{\mathcal{R}}(k) = \frac{\kappa H^2(\tau_k)}{4k^3\varepsilon(\tau_k)}\,. \tag{3.35}$$

The k dependence of the power spectrum is small. Hence, we usually expand (3.35) around a pivot scale k_0 so that the dimensionless power spectrum becomes

$$\Delta_{\mathcal{R}}(k) = A_s\left(\frac{k}{k_0}\right)^{n_s-1}\,, \tag{3.36}$$

where A_s is the amplitude of the power spectrum at the scale k_0 and n_s is the deviation from scale invariance. The fact that H and ε have a small dependence in k translates to the fact that n_s is close to 1. Remember that $\Delta(k)$ is defined in (2.117). By identifying (3.36) and (3.35) we find

$$A_s = \frac{\kappa}{8\pi^2}\frac{H^2(\tau_0)}{|\varepsilon(\tau_0)|}\,. \tag{3.37}$$

To find the scale dependence, we can write $n_s - 1$ as a logarithmic derivative of $\Delta_{\mathcal{R}}(k)$ [89]:

$$n_s - 1 = \frac{d\ln\Delta_{\mathcal{R}}}{d\ln k} = \frac{d\ln\Delta_{\mathcal{R}}}{d\ln a}\frac{d\ln a}{d\ln k} = \left(2\frac{d\ln H}{d\ln a} - \frac{d\ln\varepsilon}{d\ln a}\right)\frac{d\ln a}{d\ln k}\,, \tag{3.38}$$

where we have dropped the time dependence for readability. One can show that $d\ln H/d\ln a$ and $d\ln\varepsilon/d\ln a$ are exactly $-\varepsilon$ and η. On the other hand, we work at the horizon crossing, *i.e.* $k = aH$. Hence one can write:

$$\left(\frac{d\ln k}{d\ln a}\right)^{-1} = \left(1 + \frac{d\ln H}{d\ln a}\right)^{-1} = \frac{1}{1-\varepsilon}\,. \tag{3.39}$$

Finally, in the slow-roll approximation, we find

$$n_s - 1 = -2\varepsilon(\tau_0) - \eta(\tau_0)\,. \tag{3.40}$$

The two parameters A_s and n_s are well measured today by Planck whose last measurement gives $n_s = 0.9652 \pm 0.0042$ and $\ln 10^{10}A_s = 3.043 \pm 0.014$ [66]. These two measurements are a strong evidence of scalar perturbation but are not sufficient to solve for all three variables H, ε, η. One of the most promising measurement would be the tensor perturbation perturbation observation.

A very similar computation of the perturbation of h_{ij}, see equation (2.20), leads a tensor power spectrum [89]

$$\Delta_t(k) = A_t\left(\frac{k}{k_0}\right)^{n_t}\,, \tag{3.41}$$

where

$$A_t = \frac{2\kappa}{\pi^2}H^2(\tau_0), \qquad n_t = -2\varepsilon(\tau_0)\,. \tag{3.42}$$

In the expression of (3.37), we see a division by ε which in the slow-roll approximation is small. Thus, the scalar perturbations are boosted, and much easier to observe than tensor perturbations. However, the tensor power spectrum amplitude A_t is a simple function of H so that a measurement of this amplitude would give us a direct measurement of the energy scale of inflation. The usual parameter used by the community is the *tensor-to-scalar* ratio r:

$$r = \frac{A_t}{A_s} = 16\varepsilon(\tau_0)\,. \tag{3.43}$$

Comparing (3.43) and the expression of n_t in (3.42), we can deduce a very important consistency relation that is a consequence of single-field slow-roll inflation:

$$r = -8n_t\,. \tag{3.44}$$

Today, the constraints on the parameter r are $r < 0.06$ at 95% confidence level provided by the BICEP2 and Planck collaborations [120] which has combined Planck temperature, BAO and BICEP2 measurements.

3.1.5 Adiabatic initial condition

In a modern view of inflation [117], the inflaton field φ is regarded as a clock parameter and not a fundamental field dominating the universe. This means that the inflaton can be absorbed into a redefinition of the time. Conversely, we can introduce a perturbation with the time redefinition

$$t \to t + \pi^{(1)}(t, \mathbf{x})\,. \tag{3.45}$$

The parameter $\pi^{(1)}(t, \mathbf{x})$ is called Goldstone boson because it arises from a spontaneous symmetry breaking of a de Sitter universe. In a given gauge, any field can be expressed as its background value evaluated at the time $t + \pi^{(1)}(t, \mathbf{x})$:

$$f(t, \mathbf{x}) = \bar{f}(t + \pi^{(1)}(t, \mathbf{x})) = \bar{f}(t) + \bar{f}(t)'\pi^{(1)}(t, \mathbf{x})\,. \tag{3.46}$$

From equation (3.46), we can show that a time shift perturbation generates a specific type of perturbation called adiabatic fluctuations. Let us expand $\bar{\rho}_i(t + \pi(t, \mathbf{x}))$, where i means a given type of particle, to first order in $\pi^{(1)}$ and use the conservation equation (2.41). We find:

$$\rho_i(t, \mathbf{x}) - \bar{\rho}_i(t) = -3H\pi^{(1)}\left(\bar{\rho}_i(t) + \bar{p}_i(t)\right)\,. \tag{3.47}$$

We use the relation (2.44) and find:

$$\frac{1}{\omega_i + 1}\frac{\rho_i(t, \mathbf{x}) - \bar{\rho}_i(t)}{\bar{\rho}(t)} = \frac{\delta_i(t, \mathbf{x})}{\omega_i + 1} = -3H\pi^{(1)}(t, \mathbf{x})\,. \tag{3.48}$$

The right-hand side does not depend on the i index. This is an important prediction of a single-field inflation model: it generates adiabatic perturbation, *i.e.* a total perturbations with no variation of concentration of a species w.r.t. another. Since in the one field model we can link all the perturbations, by convention, we use the invariant comoving curvature perturbation $\mathcal{R}$ or ζ and to assimilate them to the adiabatic perturbations.

The Planck collaboration has constrained the non-adiabatic fraction α_{nad} to $\alpha_{nad} <$ 1.7% at 95% CL [121].

3.1.6 Non-Gaussianities

As explained in section 3.1.4, the Gaussian shape of the primordial fluctuation directly comes from the quantum ground state of a harmonic oscillator. At the linear level, the Gaussian PDF can be propagated as explained in the section 2.5.3 and (2.5.1). However, general relativity is a non-linear theory so that next-to-leading order corrections can generate non-Gaussianities by coupling different modes, see the section (2.5.1). A second source of non-linearities arises from the inflaton self-interactions. Two articles [122] and [123] have performed in very different ways the computation of the bispectrum in slow-roll single-field inflation with a standard kinetic term. See also [124]. They found

$$\tilde{f}_{\mathrm{NL}}^{SR} \simeq O(\varepsilon, \eta)\,. \tag{3.49}$$

And the shape of the bispectrum can be approximated by

$$S^{SR} \approx (2\varepsilon + \eta) S_{\mathrm{local}} + \frac{5}{3}\varepsilon S_{\mathrm{equi}}\,. \tag{3.50}$$

Although the local shape can be generated in the standard model of inflation and then generates a peak in the squeezed limit, this peak is suppressed by the slow roll parameter and more precisely by the deviation from scale invariance:

$$\tilde{f}_{\mathrm{NL}}^{\mathrm{local}} = \frac{1}{2}(n_s - 1)\,. \tag{3.51}$$

From Planck, we know that $n_s - 1 = -0.0335 \pm 0.0038$ [66]. This level of NG will probably be unobservable. Another very powerful theorem has been proved in [125]. Assuming only single-field inflation, they have shown that in the squeezed limit:

$$\lim_{k_3 \to 0} B_{\mathcal{R}}(k_1, k_2, k_3) = (n_s - 1) P_{\mathcal{R}}(k_1) P_{\mathcal{R}}(k_2)\,. \tag{3.52}$$

A measurement of a primordial bispectrum in the squeezed limit would therefore rule out *all* single-field inflation.

The current constraints on the three common shape amplitudes given by the 2018 Planck release are summarized in table 5.5. All amplitudes are compatible with 0. Recent measurements have also constrained the local shape amplitude using the LSS. From the power spectrum scale-dependent halo bias, they obtain $f_{\mathrm{NL}}^{\mathrm{local}} = -12 \pm 21$ (68% confidence) [126].

3.2 Multi-field Inflation

We have seen in the two last subsections 3.1.5 and 3.1.6 that single-field inflation predicts an adiabatic and Gaussian universe. The observations are compatible with these predictions. However, if we want to go beyond this phenomenological description and use a high-energy physics framework, the fact that only one scalar field would have been involved seems artificial, see for example [127]. Indeed, the aforementioned grand unified theory predicts a large number of scalar fields ($\sim$ 100 Higgs bosons). Moreover, supersymmetry also requires a large number of scalar fields while higher-dimensional particle theories like string theory provide again many effective scalar fields coming from the additional compact dimensions. If one scalar field is light, which means that the mass of the particle is smaller than the Hubble parameter, we expect this particle to generate super-Hubble fluctuations. Multi-field model of inflation have been developed over the 20 past years, see e.g. [124, 128–134] or the reviews [135, 136].

When additional active degrees of freedom enter into the game, isocurvature modes and large non-Gaussianities of the local type can be generated [88, 98, 118, 137–139]. As we have seen, if one of these two features would be detected, it would rule out all single-field inflation scenarios. On the other hand, multi-field inflation can also generate a Gaussian adiabatic universe (meaning here non-measurable isocurvature modes and non-Gaussianities) so that it cannot be ruled out by the absence of isocurvature or local PNG.

This section is mainly inspired by [71, 106, 140]. We first generalize the background to multi-field and give the leading order in slow-roll parameter perturbations. Then, we introduce the adiabatic/entropic decomposition and give the main results of two-field slow-roll inflation. Finally, we introduce the δN formalism and compute the bispectrum generated by inflation.

3.2.1 Leading-order multi-field inflation

The canonical multi-field inflation has been developed in [71, 138, 139, 141]. We now consider an ensemble of N scalar fields ordered in the vector φ^a where the index a ranges from 1 to N. We can interpret each scalar field as the coordinate φ^a of a real manifold with a metric G_{ab}. As for the usual metric $g_{\mu\nu}$, G_{ab} should be invariant under coordinate transformations $\varphi^a \to \tilde{\varphi}^a$. The Lagrangian (3.11) generalized to multiple fields can be written as

$$\mathcal{L}_\varphi = -\frac{1}{2} g^{\mu\nu} G_{ab} \varphi^a_{,\mu} \varphi^b_{,\nu} - V(\varphi^a)\,. \tag{3.53}$$

For simplicity, it is enough to consider here the simpler case $G_{ab} = \delta_{ab}$. We work in the slow-roll approximation that can be extended to the multi-field case. It is convenient here to use the slow-roll parameters defined in terms of the potential. Hence we have the same definition of $\varepsilon_V \simeq \varepsilon$ as usual, see (3.20) and (3.3). The second parameter becomes now

$$\eta_{ab} = \frac{1}{\kappa} \frac{V_{,ab}}{V}\,. \tag{3.54}$$

Following the same reasoning as for the single-field case, we find the density, the pressure and the Friedmann equations by simply substituting $\dot{\varphi}^2 \to \dot{\varphi}^a \dot{\varphi}_a$ in equations (3.14) and (3.18). Hence, the background equation of motion becomes

$$\bar{\varphi}''_a + 3\mathcal{H}\bar{\varphi}'_a + a^2 V_{,a} = 0\,, \tag{3.55}$$

where $V_{,a} = \partial V / \partial \bar{\varphi}_a$. If we now perturb the field $\varphi_a \to \varphi_a + \delta\varphi_a$, we can follow the same procedure as in the single-field case. In the multi-field case, the Mukhanov-Sasaki variable can be generalized to the N fields

$$q_a = a \left(\varphi_a^{(1)} + \frac{\bar{\varphi}'_a}{\mathcal{H}} \psi^{(1)} \right) = a Q_a\,. \tag{3.56}$$

Hence, we can show that at leading order in the slow-roll parameters, *i.e.* in a perfect de Sitter universe, the perturbation of all q_a are independent and of amplitude [140]

$$P_{q_a} = \left(\frac{\mathcal{H}(\tau_k)}{2\pi} \right)^2 . \tag{3.57}$$

Note that we usually define the effective mass squared of the field a by $m_a^2 = V_{,aa}$. To find (3.57), we have assumed that all scalar fields are light which means that $m_a^2 \ll H^2$. At higher order, the perturbations are correlated, see [71, 142] for more details.

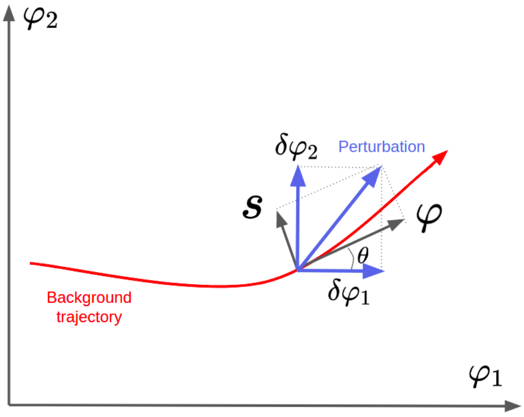

Figure 3.1: The background trajectory in the two-dimensional manifold (φ_1, φ_2) is represented in red. The perturbations $\delta\varphi_1, \delta\varphi_2$ are decomposed on a Frenet-like coordinate system (φ, s). The vector φ is tangential to the background trajectory while the vector s is perpendicular.

3.2.2 Adiabatic and Entropic decomposition

In multi-field inflation, the background dynamics can be described by using a single effective inflaton field that we call φ without any index to highlight the fact that, in the single-field limit, it can be identify as an inflaton. It can be shown that the effective inflaton φ verifies the Klein-Gordon equation (3.12) if [87]

$$\bar{\varphi}' = \hat{e}_\varphi \cdot \vec{\bar{\varphi}}', \qquad \bar{\varphi}'' = \hat{e}_\varphi \cdot \vec{\bar{\varphi}}'', \qquad V_{,\varphi} = \hat{e}_\varphi \cdot \vec{\nabla} V \,, \tag{3.58}$$

where we have defined the direction of the evolution of the field $\hat{e}_\varphi$:

$$\hat{e}_\varphi = \frac{\bar{\varphi}'_a}{\sqrt{(\bar{\varphi}'_a)^2}} \,. \tag{3.59}$$

Let us now consider the perturbations $\varphi_a^{(1)}$. We can decompose the total perturbation vector, see for instance the vector labeled "perturbation" in the figure 3.1, in one adiabatic component (tangential to the background trajectory) and $N-1$ entropic components:

$$\varphi^{(1)} = \hat{e}_\varphi \cdot \vec{\varphi}^{(1)}, \qquad s_a^{(1)} = \hat{e}_a^s \cdot \vec{\varphi}^{(1)} \,, \tag{3.60}$$

where the vectors $\hat{e}_a^s$ (with $a \in [1, N-1]$) are mutually orthogonal and orthogonal to $\hat{e}_\varphi$, *i.e.* $\hat{e}_\varphi \cdot \hat{e}_a^s = 0$. Note that it can be shown that the components b of the unit vectors $\hat{e}_a^s$ are proportional to the entropic perturbations $\mathcal{S}_{ab}$ [87].

3.2.3 Two-field slow-roll inflation

For simplicity, we will concentrate on the 2-field case. Given equation (3.54), we have in the two-field case three η parameters: $\eta_{\varphi\varphi}, \eta_{\varphi s}, \eta_{ss}$. Moreover, the basis vectors can be written

$$\hat{e}_\varphi = (\cos\theta, \sin\theta), \qquad \hat{e}_s = (-\sin\theta, \cos\theta) \,, \tag{3.61}$$

where in the two-field case, there is only one entropic component which is why $\hat{e}_s$ has no index here. The angle θ is defined in figure 3.1. Then, the different components can be written

$$\begin{aligned} \varphi^{(1)} &= \varphi_1^{(1)} \cos\theta + \varphi_2^{(1)} \sin\theta\,, \\ s^{(1)} &= -\varphi_1^{(1)} \sin\theta + \varphi_2^{(1)} \cos\theta\,. \end{aligned} \tag{3.62}$$

Effectively, we have performed a rotation in the field space. This can be seen by looking at figure 3.1. Instead of decomposing in the $\varphi_1^{(1)}, \varphi_2^{(1)}$ basis, we decompose in a Frenet-like basis defined by the vectors (3.61).

The entropic perturbations are gauge invariant, see section 2.4.4, but this is not the case of the adiabatic component $\varphi^{(1)}$. Remember that we gave the same name to the adiabatic component in the multi-field case and the scalar field in the single-field case, *i.e.* $\varphi^{(1)}$. Hence, in the single-field limit, we recover the same equations as in the single-field case. In particular, the Mukhanov-Sasaki variable (3.56) applied to the adiabatic direction takes the same form as (2.36) and it verifies also (3.33). On the other hand, it is convenient to define the variable S:

$$S^{(1)} = \frac{\mathcal{H}}{\bar{\varphi}'} Q_s^{(1)}, \quad \text{with} \qquad Q_s^{(1)} = \hat{e}_s \cdot \vec{Q}_{(1)} = s^{(1)}\,. \tag{3.63}$$

The general evolution equations of $\mathcal{R}$ and S can be derived from equations (2.60) and (2.81) where the stress-energy tensor components can be expressed as a function of the scalar field quantities. Let us concentrate our efforts on the super-Hubble limit and in the slow-roll approximation. Under these approximations, the evolution equation of the adiabatic and entropic components take a simple form [143]:

$$\mathcal{R}' = \alpha \mathcal{H} S, \qquad S' = \beta \mathcal{H} S\,, \tag{3.64}$$

where

$$\alpha = \frac{2\theta'}{\mathcal{H}} = -2\eta_{\varphi s}, \qquad \beta = -2\varepsilon + \eta_{\varphi\varphi} - \eta_{ss}\,. \tag{3.65}$$

The first equation of (3.64) is also valid beyond the slow-roll approximation. The form of the evolution equation given in (3.64) is generic [143] and the time-dependent coefficients α and β depend on the model we use. We find again by looking at (3.64) that the adiabatic mode is sourced by the entropic modes. However, we see here that the source of the adiabatic mode is also proportional to θ'. The time derivative of θ is the amplitude of the variation of the adiabatic component:

$$\hat{e}_\varphi' = \theta' \hat{e}_s\,. \tag{3.66}$$

This means that the entropic modes are a source for the adiabatic mode only if the trajectory is curved in field space ($\theta' \neq 0$). If, however, $\theta' = 0$, even if $s^{(1)} \neq 0$, the equations (3.64) are decoupled and the adiabatic evolution is the same as in the pure adiabatic case ($p_{nad} = 0$ in section 2.4.3).

In section 3.2.1, we have shown that the perturbations of the fields φ_1 and φ_2 are not correlated at the leading order in slow-roll and acquire both the same power spectrum amplitude (3.57). After the rotation, the same conclusion holds for the fields φ and s. In the case of single-field inflation, the power spectrum was fixed in the super-horizon region so that the power spectrum after horizon crossing is the same as the power spectrum deep in the radiation domination era. One of the main differences here is that the spectra evolve in the super-Hubble regime. To see that, we can solve the system (3.64) to relate the perturbations after horizon crossing (at τ_k) to the power spectrum at any later time τ meant to be the initial condition of the radiation domination era. It reads:

$$\begin{pmatrix} \mathcal{R} \\ S \end{pmatrix}_\tau = \begin{pmatrix} 1 & T_{\mathcal{R}S} \\ 0 & T_{SS} \end{pmatrix} \begin{pmatrix} \mathcal{R} \\ S \end{pmatrix}_{\tau_k} \tag{3.67}$$

where the transfer functions take the general form

$$T_{SS}(\tau_k,\tau) = \exp\left(\int_{\tau_k}^{\tau} \beta(\tau')\mathcal{H}(\tau')d\tau\right), \qquad T_{\mathcal{R}S}(\tau_k,\tau) = \int_{\tau_k}^{\tau} \alpha(\tau')T_{SS}(\tau_k,\tau)\mathcal{H}(\tau')d\tau\,. \tag{3.68}$$

Remember that the primordial power spectra of the different fields after horizon crossing are uncorrelated and equal, see equation (3.57). Hence, applying the transfer matrix to the initial spectra (3.57), we find that, deep in the radiation domination era, the perturbations of $\mathcal{R}$ and S are correlated in general [143]:

$$P = P_{\mathcal{R}} + P_S + P_{\mathcal{R}S} = (1+T_{\mathcal{R}S}^2)P_{\mathcal{R}}(\tau_k) + T_{SS}^2 P_{\mathcal{R}}(\tau_k) + T_{\mathcal{R}S}T_{SS}P_{\mathcal{R}}(\tau_k)\,. \tag{3.69}$$

We usually define the correlation angle Δ that we will constrain in this thesis:

$$\cos\Delta = \frac{P_{\mathcal{R}S}}{\sqrt{P_{\mathcal{R}}P_S}} = \frac{T_{\mathcal{R}S}}{\sqrt{1+T_{\mathcal{R}S}^2}}\,. \tag{3.70}$$

This correlation angle parameterizes how much of the adiabatic mode has been generated by the presence of a non-zero isocurvature mode.

The generic expressions of the tilts are given in [143]. They can be expressed as a function of the tilts of the initial power spectra and of the transfer functions which are also scale-dependent. Here, we restrict ourselves to two limit cases. If the curvature perturbation $\mathcal{R}$ has for sole origin the adiabatic fluctuation, we would have $T_{\mathcal{R}S} = 0$ and hence $\cos\Delta = 0$, and we recover the single-field result

$$n_{\mathcal{R}} - 1 = -6\varepsilon + 2\eta_{\varphi\varphi}\,. \tag{3.71}$$

Recall that $\eta_{\varphi\varphi}$ is defined w.r.t. the potential in (3.54) and is therefore equivalent to η_V defined in (3.21). Similarly for the entropic mode S, the tilt takes the form

$$n_S - 1 = -6\varepsilon + 2\eta_{SS}\,. \tag{3.72}$$

Let us now see what happens in the case where the curvature perturbation is produced by the entropic perturbation during inflation. We have now $T_{\mathcal{R}S} \gg 1$ and $\cos\Delta = 1$ which means that $\mathcal{R}$ and S would be fully correlated. In that case, we find the important result [87]:

$$n_S - 1 = n_{\mathcal{R}} - 1 = n_{\mathcal{R}S} - 1 = -2\varepsilon + 2\eta_{SS}\,. \tag{3.73}$$

In the analysis of Planck, this result is referred to as the "curvaton" scenario. This scenario has been proposed as a possible origin of the structure formation on super-Hubble scales [144, 145]. Indeed, the presence of entropic modes provides a natural mechanism to generate a curvature perturbation in the super-Hubble regime.

3.2.4 Non-Gaussianity and δN formalism

The second prediction of multi-field inflation is the possibility of large non-Gaussianity. To see this, we can use the so-called δN formalism. The current form of this method that is commonly used has been introduced in [93, 146].

The δN formalism is based on the "separate universe approach". Its states that two different super-Hubble patches can be seen as two universes evolving independently. Each super-Hubble patch is homogeneous and therefore the quantities (such as the density) obey a homogeneous FLRW evolution, see [87]. Hence, instead of using the perturbed Einstein equations, the local evolution can be described by a homogeneous evolution with perturbed initial conditions which is why we call this method the "separate universe approach", see for instance [147] and [87] for a very complete bibliography. Note that in the single-field case, the dynamics in all patches is identical, up to a time shift, as discussed in section 3.1.5. This provides an intuitive explanation of why the curvature perturbation is constant in the super-Hubble regime.

By using the separate universe principle, we can express the curvature perturbation $\zeta(t, x^i)$ as a function of different numbers of e-folds. Let us define $N(t_1, t_2, x^i)$ as the number of e-folds between an initial flat hypersurface ($\psi = 0$) at time t_1 and the uniform energy density hypersurface $\delta\rho = 0$ at time t_2. Then, the curvature perturbation takes the form [146]:

$$\zeta(t_2, x^i) = N(t_1, t_2, x^i) - \bar{N}(t_1, t_2)\,, \tag{3.74}$$

where $\bar{N}$ is the background value expressed in (3.6). Note that (3.74) is non-perturbative. In a separate universe approach, the dynamics is the perfectly known background, so the only unknown is the initial conditions. In multi-field inflation, this means the initial values of the fields φ^a. Hence, the spatial dependence of $N(t_1, t_2, x^i)$ can be encoded as $N(t_2, \varphi^a(t_1, x^i))$. The initial time-slicing is the flat hypersurface where the field can be expanded as $\varphi^a(t_1, x^i) = \bar{\varphi}^a(t_1) + \delta\varphi^a(t_1, x^i)$. Note that we have initially $\psi = 0$ so $\delta\varphi^a = Q^a$ given in (3.56). Finally we can expand equation (3.74) w.r.t. to the initial fluctuation Q^a. It gives the final important result

$$\zeta = N_a Q^a + \frac{1}{2} N_{ab} Q^a Q^b + \frac{1}{6} N_{abc} Q^a Q^b Q^c + ... \tag{3.75}$$

where

$$N_a = \left.\frac{\partial N}{\partial \varphi_1^a}\right|_{\bar{\varphi}_1^a}, \qquad N_{ab} = \left.\frac{\partial^2 N}{\partial \varphi_1^a \partial \varphi_1^b}\right|_{\bar{\varphi}_1^a}, \tag{3.76}$$

and where we mean $\varphi_1^a = \varphi^a(t_1)$. The derivation of (3.75) requires some conceptual effort. But from it, it is straightforward to relate the statistical properties of ζ to the primordial scalar fields φ^a. For example, the power spectrum takes the form [148]

$$P_\zeta(k) = N_a N_b \left\langle Q^a Q^b \right\rangle \tag{3.77}$$

and the bispectrum can be expressed as

$$\begin{aligned} B_\zeta(k_1, k_2, k_3) &= N_a N_b N_c \left\langle Q^a Q^b Q^c \right\rangle + N_a N_{bc} N_d \left(\left\langle Q^a Q^b \right\rangle \left\langle Q^c Q^d \right\rangle + \text{perms} \right) \\ &= N_a N_b N_c B_Q^{abc} + N_a N_{bc} N_d \left(P_Q^{ab} P_Q^{cd} + \text{perms} \right)\,. \end{aligned} \tag{3.78}$$

We see in (3.78) two possible sources of non-Gaussianities: if the fields have an intrinsic bispectrum B_Q^{abc} or if there exists a non-linear relation between ζ and the fluctuations of the fields at horizon crossing (non-vanishing N_{bc}). The first type of non-Gaussianity can come from the interactions between the fields before/during horizon crossing and has a quantum origin. We shall concentrate on the second type, which arises from non-linear evolution after horizon crossing, similar to the second term of (2.139). If we identify the amplitude of this second term with the one of the local shape (2.133), we find:

$$\tilde{f}_{\mathrm{NL}} = \frac{N_a N_b N^{ab}}{(N_c N^c)^2} \,. \tag{3.79}$$

Hence, we see by looking at (3.79), that multi-field inflation can generate large non-Gaussianities if the second derivatives N^{ab} are large, which means that the number of e-folds would depend strongly on the values of the fields at horizon crossing.

The δN procedure has been generalized to the isocurvature modes in [146, 149]. Hence, we can use a similar expansion (3.75) for the isocurvature mode S to compute the spectrum and the bispectrum for all components, ζ, and isocurvature modes. The coefficients can then be interpreted following [146, 149].

Part II

Joint analysis of the CMB power spectrum and bispectrum

Chapter 4

The cosmic microwave background

Inflation is driven, in the simplest models, by a single scalar field with a standard kinetic term as described in section 3.1. We have shown that these models predict scalar perturbations that are adiabatic with a power spectrum following equation (3.36), *i.e.* a power law with a small tilt. These perturbations are predicted to be nearly Gaussian with a NG amplitude suppressed by the slow-roll parameters, see equation (3.49). In section 3.2, we have seen that multi-field inflation can generate a higher level of NG. We have also shown that these models can generate one or more isocurvature modes in addition to the adiabatic mode. All these predictions, as well as the universe dynamics, can be probed by studying the CMB.

The Cosmic Microwave Background (CMB) radiation is a unique probe of the physics of the primordial universe. It has been emitted 380000 years after the Big Bang. The primordial fluctuations propagate through the cosmological history and leave an imprint in the CMB in the form of temperature and polarization fluctuations. This means that the inflation paradigm can be tested by measuring the statistics of the CMB anisotropies. In particular, the different initial conditions, adiabatic or isocurvature, will leave different imprints in the CMB power spectrum and bispectrum.

In this chapter, we will start by explaining the physical origin of the CMB and introduce the specific spherical formalism that is used to study its anisotropies. We will show that these anisotropies can be related to the primordial power spectra and bispectra thanks to the transfer functions. In the super-Hubble regime, the transfer function has a very simple form since there is no evolution in the adiabatic case. In the sub-Hubble regime, however, the initial perturbations will be convolved by the different interactions in the plasma. In the following, we will give some key features of the physics of the plasma to understand the basic differences between the different initial conditions. In section 2.4, we have introduced the isocurvature modes in a very general way. In general, for N species, we can have 1 adiabatic mode, $N-1$ density isocurvature modes, and $N-1$ velocity isocurvature modes. However, the physics of the plasma induces constraints on the possible isocurvature modes. In the last part of this section, we will review all possible isocurvature modes that will be constrained in the next section.

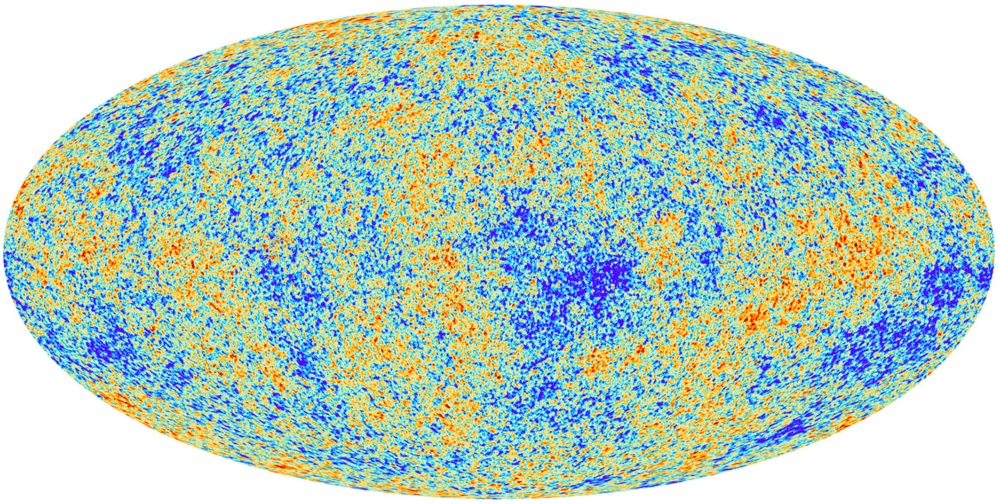

Figure 4.1: Temperature fluctuation map measured by Planck. The Galactic foregrounds have been removed. Taken from the ESA and Planck collaboration [150].

4.1 The cosmic microwave background

The discovery of the CMB, as explained in section 1.4, has provided strong confirmation of the standard model of cosmology. In this section, we introduce the basic physics of the primordial plasma and the physical origin of this relic radiation emitted 380000 years after the Big Bang.

4.1.1 Primordial plasma

At the initial condition, deep in the radiation domination era, the energy density is much higher than today. It results in strong coupling between the different species so that they can be considered as being in thermal equilibrium. All the particles together can be considered as a single plasma with a unique temperature and averaged kinetic energy. In the case of ADI, the composition of the plasma is the same everywhere. In the case of pure isocurvature IC, the plasma starts with no global density fluctuations (the potential vanishes) but there are fluctuations of compositions or velocities.

A given type of particle stays in thermal equilibrium as long as its reaction rate Γ_i with the plasma is larger than the expansion rate, *i.e.* the Hubble factor H:

$$H \lesssim \Gamma \,. \tag{4.1}$$

This condition is equivalent to saying that we have a decoupling when the mean free path becomes larger than the horizon. When the condition (4.1) is broken, we say that the given type of particle decouples. Radiation in thermal equilibrium follows a black body spectrum or equivalently a Planck distribution function whose density has been computed in equation (2.68). By looking at table 2.1, we see that the radiation density ρ scales like a^{-4} so that we can conclude that the temperature scales like a^{-1}. By combining the first Friedmann equation together with Stefan's law we also see that

$$H \sim \sqrt{\kappa} T^2 \propto a^{-2} \,. \tag{4.2}$$

From the measurement of the CMB temperature $T_0 = 2.72548 \pm 0.00057$ [57], one can compute the density of photons today thanks to equation (2.68). We find

$$\Omega_\gamma h^2 = 2.47 \times 10^{-5} \,. \tag{4.3}$$

This result confirms that today, the photons are subdominant.

4.1.2 Neutrino decoupling

Typically, the weak interaction rate between neutrinos and electrons Γ_w is proportional to T^5 [151]:

$$\Gamma_w \sim G_F T^5 \,, \tag{4.4}$$

with G_F the Fermi constant. By comparing (4.4) and the scaling of the Hubble rate given in equation (4.2), we find that the condition (4.1) breaks when the temperature reaches the decoupling temperature $T_{\nu d}$:

$$T_{\nu d} \sim \kappa^{1/6} G_F^{-2/3} \sim 1 \text{ MeV} \,. \tag{4.5}$$

These relic neutrinos form the so-called neutrino background. We do not have the sensitivity to observe this background today. Note that the temperature decreases with the expansion like a^{-1} as indicated by equation (4.2) so that the neutrinos will decouple from the plasma at a very early time $z \sim 10^{10}$. The neutrinos have a very small mass and can be considered as radiation at early time. Note that today, at least two neutrinos are not relativistic anymore. Indeed, we have access to the difference of the squared masses thanks to the oscillation neutrino experiments, see for instance [152]. See also [153] for constraints on the nature (Dirac or Majorana) and absolute masses of neutrinos. The differences of the squared masses indicate that even if one neutrino has a vanishing mass, the others would have a mass larger than their current kinetic energy ($\sim 10^{-4}$eV). However, since they decouple at a very early time when they were still extremely relativistic, and because there are no further interactions they are expected to still follow a relativistic Fermi-Dirac distribution at present (2.68) [97]. The neutrinos temperature then decreases like a^{-1} like for the photons. If we stop here, we should expect the relic neutrinos and photons to have the same temperature. However, another later effect called the *photon reheating* breaks this statement. The photon reheating should not be confused with the reheating which happened at the end of inflation. In the plasma, one of the reactions that couples photons to electrons is the electron/positron pair creation/annihilation:

$$\gamma + \gamma \rightleftharpoons e^+ + e^- \,. \tag{4.6}$$

The mechanism (4.6) from left to right means that two photons can create an electron/positron pair. This happens only if the photons have energy equal to or larger than the electron mass, *i.e.* 0.51 MeV. From right to left, the mechanism (4.6) is the annihilation of the pair that generates two photons with energy equal or larger than the mass of the electrons. As the photons are cooling down because of the expansion, we eventually reach the point where $T_\gamma < 0.51$ MeV. Then, the photons do not have enough energy to create the electron/positron pairs and therefore the reaction (4.6) from left to right becomes impossible. On the other hand, the electron/positron pairs will continue to create new photons until there are no more pairs. All this has the effect of reheating the photon thermal bath by increasing the number of photons (the photons are still coupled to electrons by Compton scattering). Neutrinos do not participate in this process since they were already decoupled ($T_{\nu d} > 0.51$ MeV). The temperature difference between the relic photons and neutrinos as well as the number density and the energy density of these species can be computed and reads

$$T_\nu = \left(\frac{4}{11}\right)^{1/3} T_\gamma, \qquad \bar{\rho}_\nu = \frac{7}{8} N_\nu \left(\frac{4}{11}\right)^{4/3} \bar{\rho}_\gamma \,. \tag{4.7}$$

The quantities T_i and ρ_i are the temperature and energy density of the species i and we have assumed that the neutrinos are Dirac neutrinos and not Majorana neutrinos. The number N_ν is the number of neutrinos species. For the detailed computation, we refer to [97, 119]. We just note here that the 7/8 factor comes from the computation of the neutrino density that has been performed in equation (2.68). The ratio between $\bar{\rho}_\nu$ and $\bar{\rho}_\gamma$ often appears in the computations, sometimes as f_ν which is the notation that we will use in the rest of this thesis.

From equation (4.7) and (4.3), one can compute the density parameter of neutrinos today and their expected temperature:

$$\Omega_\nu h^2 = 1.68 \times 10^{-5}, \qquad T_\nu = 1.85K \,. \tag{4.8}$$

4.1.3 Recombination

After the photon reheating, the reactions that maintain the coupling between the photons and the electrons are the Compton scattering (note that the electrons are also coupled by Coulomb interactions with the protons)

$$e^- + \gamma \rightleftharpoons e^- + \gamma \,, \tag{4.9}$$

and the photo-ionization

$$e^- + p^+ \rightleftharpoons^1 H + \gamma \,, \tag{4.10}$$

where ${}^1H$ is a hydrogen atom. The Compton scattering reaction rate takes the from [119]

$$\Gamma_C = \sigma_T n_e = \sigma_T n_b x_e \,, \tag{4.11}$$

where σ_T is the Thomson scattering rate, n_e and n_b are the number density of electron and baryon and x_e is the ionized electron fraction. From (4.11) we see that Γ_C scales like n_e, *i.e.* T^{-3} by dilution. If we set $x_e = 1$, which is a good approximation before the CMB emission, the equality $\Gamma_C \sim H$ can be computed and would give a decoupling redshift of ~ 40 [119]. In fact, it will end much earlier thanks to the second mechanism (4.10). Indeed, we see in (4.10) that for a photon to ionize a hydrogen atom, it has to be at least as energetic as the binding energy, *i.e.* 13.6 eV. As the universe is expanding and still cooling, it will reach the point where the photon temperature becomes smaller than the binding energy of ${}^1H$. In fact, the condition $T_\gamma < 13.6$ eV is not sufficient since there are many more protons than electrons (10^9 photons for one baryon). Moreover, the photon energy follows a black body spectrum. Thus, even if the photon mean temperature is below the binding energy of hydrogen, the small fraction of photons that will have an energy larger than 13.6 eV is enough to maintain the equilibrium (4.10). Therefore, the reaction from right to left cannot happen anymore and the reaction from left to right will remove the free electrons and protons. This process that forms the hydrogen atoms is called *recombination* and happens at an energy of ~ 0.35 eV.

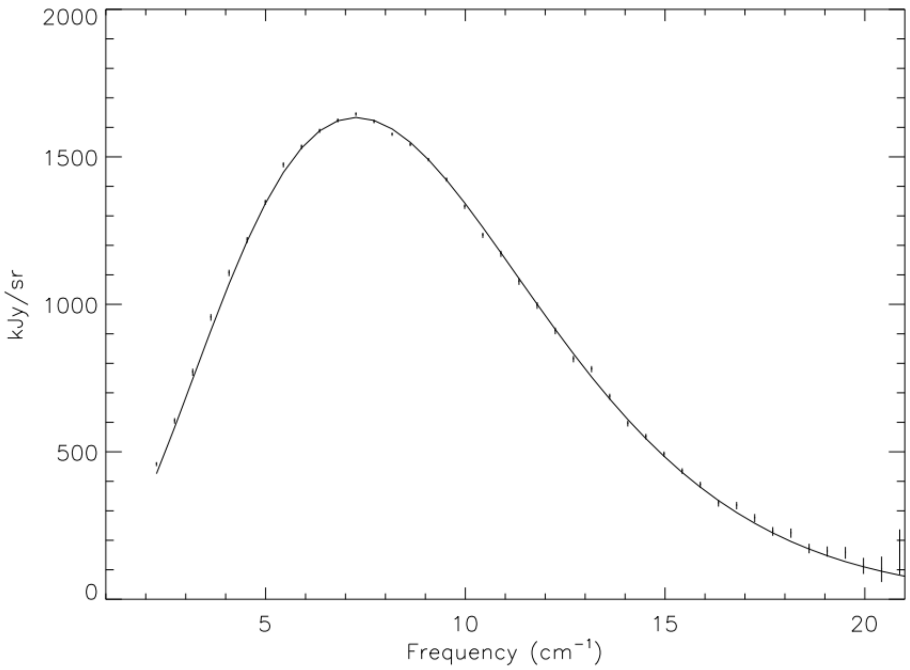

Figure 4.2: CMB frequency spectrum measurement by the satellite COBE [57]. The solid curve is the fit of the black body intensity (4.12) with temperature given in the second equation of (4.12).

After free electrons density drops, the ionized electron fraction falls to zero and the Compton scattering (4.9) naturally stops and the photons decouple from matter. This is the *decoupling*. The free photons can now travel through the entire observable universe carrying the information of the last scattering in the primordial plasma. If the decoupling process would be instantaneous, these photons would come from a two-dimensional sphere; this is the last scattering surface. In reality, the last scattering surface has a small thickness $\Delta z_\star \sim 100$. In 1996, the satellite COBE precisely measured the spectrum of the CMB [57]. The fit shows that the intensity of the CMB follows a black body spectrum

$$I(\nu) = 4\pi \frac{\nu^3}{e^{\nu/T_0} - 1}, \quad \text{where} \qquad T_0 = 2.72548 \pm 0.00057 \,. \tag{4.12}$$

The measurement and the fit of (4.12) is shown in figure 4.2. The Planck mission has provided a highly accurate measurement of the temperature (and polarization as we will see) fluctuations that we can see in figure 4.1. The distance to the last scattering surface is measured by Planck [66] as $z_\star = 1089.80 \pm 0.21$, it corresponds to an energy of about ~ 0.35 eV. The photons traveling through the universe are redshifted following $T_0 = T_\star/(1+z_\star)$, see equation (2.38). Knowing T_0 and $z_\star$ from measurements, we find that the emission temperature of the CMB is around 3000K.

4.2 CMB statistics

The last scattering surface is observed on a 2-dimensional sphere. The perturbations that we observe are a projection of an underlying 3-dimensional perturbed field integrated on a thin layer which can be linked with the inflation perturbation predictions, see sections 3.1, 3.2 and 2.5.1. In this section, we will first introduce the CMB power spectrum in a spherical harmonics framework. Then we will explain how we can link the 2 dimensional CMB fields and the 3-dimensional underlying distribution. Finally, we will define the CMB bispectrum and, by using the same projection, we will show how to link the CMB bispectrum with the primordial one.

4.2.1 CMB power spectrum

For the CMB there will be 3 types of fields: temperature, E-modes, and B-modes (we will give more details on this in the next section) usually noted as $\lambda \in [T, E, B]$. Note that T is the temperature contrast. Note also that the CMB fields depend on 3 different variables. The time of observation τ (in general today), the location of observation $\mathbf{x}$ (our location) and the direction of observation $\mathbf{\Omega}$. Hence, the temperature contrast reads [154]:

$$\frac{\delta T}{T_0}(\mathbf{\Omega}) = T(-\mathbf{\Omega}, \mathbf{x}, \tau)\,, \tag{4.13}$$

where there is a minus sign on the direction $\mathbf{\Omega}$ because the photon observed travels in the opposite direction of the observation. Strictly speaking, the transfer functions $\mathcal{T}^{(1)}$ depend on $\mathbf{\Omega}, \mathbf{k}, \tau$. Reminder that from isotropy, we can drop the direction dependence on the vector mode $\mathbf{k}$. Moreover, one can show that the transfer functions only depend on the direction through the angle between $\mathbf{\Omega}$ and $\mathbf{k}$ [119]. We therefore write $\mathcal{T}^{(1)}(\mu, k, \tau)$ where $\mu = \hat{\mathbf{k}} \cdot \mathbf{\Omega}$. To simplify the notation in the following, we will only keep apparent the $\mathbf{\Omega}$ dependence and write the other dependence only when it is relevant. The two-dimensional fields can be decomposed into spherical harmonics

$$\lambda(\mathbf{\Omega}) = \sum_{\ell=0}^{\infty} \sum_{m=-\ell}^{\ell} a^{\lambda}_{\ell m} Y_{\ell m}(\mathbf{\Omega})\,, \tag{4.14}$$

where ℓ is the multipole degree and m the order. They are respectively the Fourier transform equivalents of the modulus of the wave vector $\mathbf{k}$ and its direction. Therefore, isotropy is translated into an independence of the variable m as we shall see. The multipole ℓ is linked to an angular typical variation $\theta \sim \pi/\ell$. The spherical harmonics $Y_{\ell m}$ are the equivalent of the usual Fourier transform of $\exp(-i\mathbf{k}\mathbf{x})$. They are defined by

$$Y_{\ell m}(\theta, \phi) = \left(\frac{(2\ell+1)(\ell-m)!}{4\pi(\ell+m)!}\right)^{1/2} P_\ell^m(\cos(\theta)) e^{im\phi}\,, \tag{4.15}$$

where P_ℓ^m are the Legendre polynomials. The spherical harmonics form an orthonormal basis. This means that:

$$\int \mathrm{d}\mathbf{\Omega}\; Y^*_{\ell_1 m_1}(\mathbf{\Omega}) Y_{\ell_2 m_2}(\mathbf{\Omega}) = \delta^{\ell_1}_{\ell_2} \delta^{m_1}_{m_2}\,. \tag{4.16}$$

By looking at (4.15), one can show that $Y^*_{\ell_1 m_1} = (-1)^m Y_{\ell_1 - m_1}$. The spherical modes $a^\lambda_{\ell m}$ are the equivalent in the conventional Fourier decomposition of $f(\mathbf{k})$ defined in equation (2.50). Their expression can be found by inverting the equation (4.14). To do so, we use the orthogonality (4.16) and integrate over the direction. It reads

$$a^\lambda_{\ell m} = \int \mathrm{d}\mathbf{\Omega}\; \lambda(\mathbf{\Omega}) Y^*_{\ell m}(\mathbf{\Omega})\,. \tag{4.17}$$

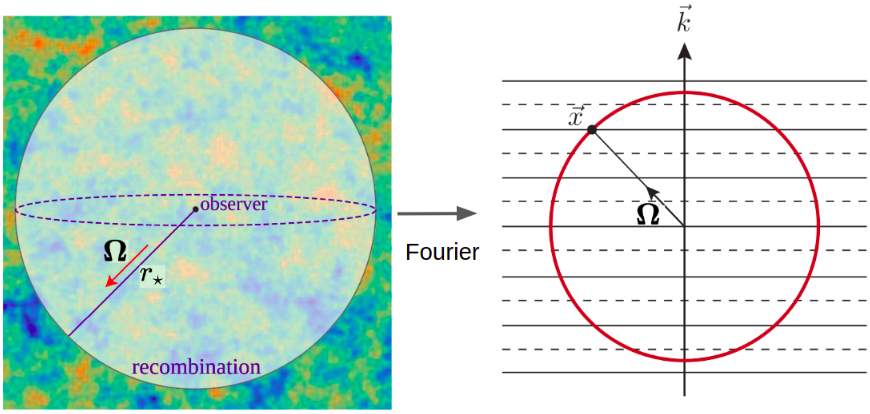

Figure 4.3: On the left, the 3-dimensional temperature fluctuation at the epoch of recombination is represented in the background. The observer in the center can only observe the last scattering surface sphere with radius $r_\star$. On the right, we represent with the dashed and solid lines the maxima and minima of a 3-dimensional Fourier mode of the underlying temperature fluctuations (represented on the left) propagating in the vertical direction. This has to be projected on the sphere of the same radius $r_\star$. Figure adapted from [155].

The (cross-)power spectrum on the sphere $C_\ell^{\lambda_1\lambda_2}$ of the fields λ_1 and λ_2 can then be defined by taking the covariance of the spherical Fourier modes

$$\left\langle a^{\lambda_1}_{\ell_1 m_1} a^{\lambda_2}_{\ell_2 m_2} \right\rangle = \delta^{\ell_2}_{\ell_1} \delta^{m_2}_{m_1} C^{\lambda_1\lambda_2}_{\ell_1} \,. \tag{4.18}$$

Since the universe is isotropic, the power spectrum does not depend on the mode m. We recall that the formal meaning of the expectation $\langle . \rangle$ is a mean over an infinite number of realizations, see section 2.5.1 for more details. Thanks to isotropicity, we can estimate the power spectrum $C_\ell^{\lambda_1\lambda_2}$ by averaging over m

$$C_\ell^{\mathrm{obs},\lambda_1\lambda_2} = \frac{1}{2\ell+1} \sum_{m=-\ell}^{\ell} a^{\lambda_1}_{\ell_1 m_1} a^{\lambda_2}_{\ell_2 m_2} \,. \tag{4.19}$$

The pre-factor in (4.19) comes from the number of m available for a given multipole. As explained in 2.5.1, this will give a cosmological variance inversely proportional to ℓ because the number of m available to compute the mean (4.19) is proportional to ℓ.

4.2.2 Projection

We have computed in section 3.1 the primordial fluctuation $\mathcal{R}(\mathbf{k})$ generated by inflation. These perturbations can be propagated at first order until the CMB thanks to the transfer functions defined in equation (2.100) and obtained by solving the fluid equations describing the photon fluid dynamics. The perturbations can then be translated into temperature and polarization perturbations. Let us consider the 3-dimensional fields λ evaluated at the time of CMB emission: $\lambda(\tau_\star, \mathbf{k})$ where the $\star$ indicates the CMB emission time. Let us see how we can project the 3-dimensional perturbation $\lambda(\mathbf{k})$ onto the sphere by following [155].

For simplicity, let us consider that recombination is instantaneous. Hence, the observed temperature field today at τ_0 in a given direction $\mathbf{\Omega}$ can be written as

$$T(\tau_0, \mathbf{\Omega}) = \int dr \; T(\tau_\star, \mathbf{x})\delta(r - r_\star) \,. \tag{4.20}$$

Without this approximation, the δ-function should be replaced by the *visibility function* usually called $g(\tau)$. This function peaks around recombination which allows us to perform this approximation. See [119] for further details. Note also that the radius $r_\star$ is the distance travelled by the photons since their emission at recombination, *i.e.* $r_\star = \tau_0$. Let us decompose $\lambda(\tau_0, \mathbf{x})$ on a Fourier basis, we find

$$T(\tau_0, \mathbf{\Omega}) = \int \frac{d^3k}{(2\pi)^3} T(\tau_\star, \mathbf{k}) e^{ir_\star \mathbf{k}\cdot\mathbf{\Omega}} \,. \tag{4.21}$$

The Fourier decomposition basis $\exp(ir_\star \mathbf{k}\cdot\mathbf{\Omega})$ can be projected onto a sphere using the identity:

$$e^{ir_\star \mathbf{k}\cdot\mathbf{\Omega}} = 4\pi \sum_{\ell m} i^\ell j_\ell(kr_\star) Y^*_{\ell m}(\mathbf{k}) Y_{\ell m}(\mathbf{\Omega}) \,, \tag{4.22}$$

where the functions j_ℓ are the spherical Bessel functions. By substituting the exponential in (4.21) by (4.22) and substituting the result into equation (4.17) we find

$$a^T_{\ell m} = 4\pi \int \frac{d^3k}{(2\pi)^3} T(\tau_\star, \mathbf{k}) i^\ell j_\ell(kr_\star) Y_{\ell m}(\mathbf{k}) \,. \tag{4.23}$$

Finally, by using the expression (4.23) in (4.18), one finds the relation between the 3-dimensional temperature contrast power spectrum $P_{TT}(\tau_\star, k)$ and the CMB spherical power spectrum C^{TT}_ℓ

$$C^{TT}_\ell = 4\pi \int \frac{k^2 dk}{2\pi^2} P_{TT}(\tau_\star, k) j^2_\ell(kr_\star) \,. \tag{4.24}$$

We usually define the angular power spectrum D_ℓ as

$$D^{TT}_\ell = \frac{\ell(\ell+1)}{2\pi} C^{TT}_\ell \,. \tag{4.25}$$

To understand why we prefer to plot the variable D_ℓ instead of C_ℓ, let us note that in the case of a nearly scale-invariant power spectrum, one can factorise out of the integral the dimensionless power spectrum Δ_I defined similarly as in equation (2.117) w.r.t. $P_{TT}(\tau_\star, k)$. Hence, equation (4.24) reads:

$$C^{TT}_\ell = 4\pi \Delta_{TT}(\tau_\star) \int d\ln k \; j^2_\ell(kr_\star) \,. \tag{4.26}$$

The main contribution to the integral will be at the peak of the spherical Bessel function so that we can evaluate the power spectrum at $k \sim \ell / r_\star$. The remaining integral is known. By using the definition (4.25), we can hence show that

$$D^{TT}_\ell \simeq \Delta^{TT}(\ell / r_\star) \,. \tag{4.27}$$

To link the CMB power spectrum with the initial conditions, we simply have to substitute equation (2.123) into (4.24).

To find the result (4.24), we have used the approximation (4.21). This is very convenient because it allows us to well separate the projection and the propagation effects. In general, the angular power spectrum can be expressed as a function of the underlying 3-dimensional power spectrum only by injecting equation (4.17) into (4.18) and decomposing the field λ in Fourier space, see [119]. The power spectrum $P^{\lambda_1\lambda_2}$ can be expressed as a function of the initial condition power spectrum thanks to the first-order transfer functions, see (2.123). The transfer functions can be decomposed with Legendre polynomials P_ℓ with the coefficients [119]:

$$\mathcal{T}^{(1)}_{\lambda_1,\ell}(k,\tau) = \frac{1}{(-i)^\ell}\int_{-1}^{1} \mathrm{d}\mu\ \mathcal{P}_\ell(\mu)\mathcal{T}^{(1)}_{\lambda_1}(\mu,k,\tau)\,, \tag{4.28}$$

where we only consider ADI. Hence, it can be shown that the angular power spectrum reduces to

$$C_\ell^{\lambda_1\lambda_2} = 4\pi\int \frac{k^2 dk}{2\pi^2}P_{\mathcal{R}}(k)\mathcal{T}^{(1)}_{\lambda_1,\ell}(\tau_\star,k)\mathcal{T}^{(1)}_{\lambda_2,\ell}(\tau_\star,k)\,. \tag{4.29}$$

By comparing with our first result (4.24), we find that assuming that the recombination is instantaneous implies that for temperature

$$\mathcal{T}^{(1)}_{T,\ell}(\tau_\star,k) = j_\ell(kr_\star)\mathcal{T}^{(1)}_{T}(\tau_\star,k)\,, \tag{4.30}$$

which can also be found directly from (4.28) and (4.21). In the case of polarization, the relation (4.30) receives an additional factor.

4.2.3 CMB bispectrum

To study the primordial non-Gaussianities, we need to define a spherical harmonics-based bispectrum of the temperature and polarization anisotropies. Indeed, we have seen in section 2.5.4 that the bispectrum of a field at a given time can be decomposed into 3 parts among which a linearly propagated primordial bispectrum. Similar to the power spectrum case studied in section **??**, the bispectrum of the CMB should be a projected picture of an underlying 3-dimensional density distribution bispectrum. The CMB provides a way to have access to the primordial non-Gaussian signal.

The CMB angular bispectrum can be defined as the correlation function of the spherical harmonics defined in equation (4.17) [156]

$$B^{\lambda_1\lambda_2\lambda_3,m_1m_2m_3}_{\ell_1\ell_2\ell_3} = \left\langle a^{\lambda_1}_{\ell_1m_1}a^{\lambda_2}_{\ell_2m_2}a^{\lambda_3}_{\ell_3m_3}\right\rangle\,. \tag{4.31}$$

This object is in practice impossible to compute. Regarding the Planck data, there are $\sim 10^9$ triplets of ℓ and for each of them, we have $2\ell+1$ possible values for each m. Fortunately, we can use the rotational invariance property to factorize the angular dependence such that

$$B^{\lambda_1\lambda_2\lambda_3,m_1m_2m_3}_{\ell_1\ell_2\ell_3} = \mathcal{G}^{m_1m_2m_3}_{\ell_1\ell_2\ell_3}b^{\lambda_1\lambda_2\lambda_3}_{\ell_1\ell_2\ell_3}\,, \tag{4.32}$$

where we have defined the Gaunt integral $\mathcal{G}$ which contains the raw m-dependence and where the remaining part is called *reduced angular bispectrum.* The Gaunt integral is defined as the angular integral of the product of 3 $Y_{\ell m}$. It reads:

$$\mathcal{G}^{m_1m_2m_3}_{\ell_1\ell_2\ell_3} = \int \mathrm{d}\mathbf{\Omega}Y^{m_1}_{\ell_1}(\mathbf{\Omega})Y^{m_2}_{\ell_2}(\mathbf{\Omega})Y^{m_3}_{\ell_3}(\mathbf{\Omega}) = h_{\ell_1\ell_2\ell_3}\begin{pmatrix}\ell_1 & \ell_2 & \ell_3\\ m_1 & m_2 & m_3\end{pmatrix}\,. \tag{4.33}$$

The quantity $h^2_{\ell_1\ell_2\ell_3}$ can be interpreted as the number of triangles which can be expressed as [157]

$$h^2_{\ell_1\ell_2\ell_3} = \frac{1}{4\pi}(2\ell_1+1)(2\ell_2+1)(2\ell_3+1)\begin{pmatrix}\ell_1 & \ell_2 & \ell_3\\ 0 & 0 & 0\end{pmatrix}^2 . \tag{4.34}$$

The parenthesis symbol stands for the Wigner-3j symbol. This symbol is a compact and equivalent way to express the Clebsch–Gordan coefficients. In particular, it ensures the parity, the triangular inequality: $|\ell_1 - \ell_2| \leq \ell_3 \leq \ell_1 + \ell_2$, the vanishing sum $\sum_i m_i = 0$ and the fact that $m \in [-\ell, \ell]$. The reduced bispectrum contains all the information of the bispectrum for an isotropic sky. However, it does not account for all the properties, for instance, the triangular inequality, of the total bispectrum defined in (4.31). Hence, it is useful to define the *angle-averaged bispectrum* $B^{\lambda_1\lambda_2\lambda_3}_{\ell_1\ell_2\ell_3}$ [112]:

$$B^{\lambda_1\lambda_2\lambda_3}_{\ell_1\ell_2\ell_3} = \sum_{m_1m_2m_3}\begin{pmatrix}\ell_1 & \ell_2 & \ell_3\\ 0 & 0 & 0\end{pmatrix} B^{\lambda_1\lambda_2\lambda_3,m_1m_2m_3}_{\ell_1\ell_2\ell_3} . \tag{4.35}$$

The angle-averaged bispectrum is the observable quantity and will be therefore of major importance. The link between the reduced and the angle-averaged bispectra is then [112]:

$$B^{\lambda_1\lambda_2\lambda_3}_{\ell_1\ell_2\ell_3} = h_{\ell_1\ell_2\ell_3} b^{\lambda_1\lambda_2\lambda_3}_{\ell_1\ell_2\ell_3} . \tag{4.36}$$

Like the power spectrum, the CMB bispectrum is a projection of a 3 dimensional field which itself is a result of a linear propagation of the primordial field, see (2.139) and (2.123) (we neglect here the non-linear dynamics and a possible primordial trispectrum). The use of equation (4.17) in equation (4.31) gives [112] (see also [106] for a detailed computation)

$$B^{\lambda_1\lambda_2\lambda_3}_{\ell_1\ell_2\ell_3} = h^2_{\ell_1\ell_2\ell_3}\left(\frac{2}{\pi}\right)^3 \int r^2 dr \left(\prod_{i=1}^{3} dk_i\, k_i^2 j_{\ell_i}(k_i r)\mathcal{T}^{(1)}_{\lambda_i,\ell_i}(k_i)\right) B_{\mathcal{R}}(k_1,k_2,k_3) , \tag{4.37}$$

where $B(k_1, k_2, k_3)$ is the primordial bispectrum in case of ADI, see the first term of equation (2.139). The equation (4.37) is general and can be seen as the equivalent of (4.29). To find the bispectrum under the instantaneous approximation, one can use (4.30).

4.3 CMB anisotropies

We have seen in the previous section 4.2 that the CMB power spectrum and bispectrum can be related to the primordial power spectrum and bispectrum thanks to the transfer functions. In the super-Hubble regime, the transfer functions have a very simple form since there is no evolution in the adiabatic case, see section 2.4. In the sub-Hubble regime, however, the initial perturbations will be convolved by the different interactions in the plasma. In this section, we will give some key features of the physics of the plasma to understand the basic differences between the different initial conditions. We only consider first-order perturbations. We also introduce the physical origin of the polarization of the CMB as well as the different later effects that add up this relic signal.

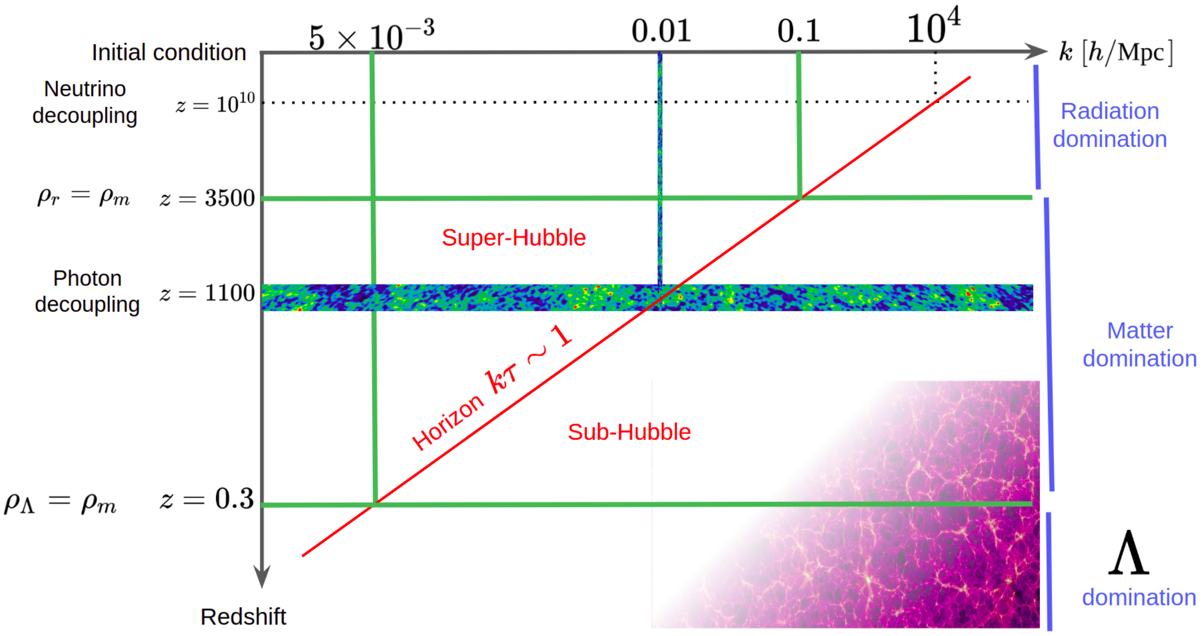

Figure 4.4: Diagram representing the history of the universe for different modes. The red line represents the horizon, *i.e.* $k\tau \sim 1$. The region above (below) this line can be treated as a super-horizon (sub-horizon). We represent 4 moments of interest: the neutrino decoupling, the radiation-matter equality, the photon decoupling and the $\Lambda-$matter equality. For each one, we give the redshift and the horizon scale. At the bottom right, we represent the structure formation.

4.3.1 Physics in the plasma

At the start, deep in the radiation domination era, we consider that all modes are super-horizon, see figure 4.4. Later, the modes progressively enter the horizon and start to evolve according to the interactions between the different species. At the photon decoupling time, photons have their last scattering which forms the last scattering surface at $z = 1090$. As we can see in figure 4.4, at the CMB emission time, all the modes on the left of the horizon (red line) have not evolved according to equation (2.65) (recall that the curvature perturbation does not evolve on super horizon scales if the initial conditions are adiabatic). On the other hand, the different modes that are on the right entered the horizon at different times. In the sub-Hubble regime, the primordial fluctuations propagate through the plasma like acoustic waves. To predict the temperature (and polarization) power spectrum on these scales, one needs to account for all the relevant interactions in the plasma. This is a highly non-trivial task and one needs a general relativistic kinetic theory of gases. In practice, one has to solve the Boltzmann equations. For non-relativistic matter like baryons and CDM, the Boltzmann equations reduce to the continuity and Euler equations (with source term for the baryons). For photons and neutrinos, however, we decompose the temperature distribution with respect to the direction into multipole moments according to (4.28). It leads to a coupled system of N equations if N is the number of multipoles considered. This is called the Boltzmann tower or hierarchy. For a complete description of this, see [119].

The dominant effect affecting the CMB anisotropies is the Compton scattering (4.9). The cross-section of this scattering is proportional to the inverse mass which explains why it is negligible for the protons. Right before the recombination, the mean free path λ_c is given by [155]:

$$\lambda_c = (\sigma_T n_e a)^{-1} \sim 2.5 \text{ Mpc}\,, \tag{4.38}$$

while the horizon at recombination is about 250 Mpc. The different contributions to the observed temperature are given by [119]

$$T(\mathbf{\Omega}) \simeq \frac{\delta_\gamma}{4} + \phi + \mathbf{\Omega}\cdot\mathbf{v} + \int_{\tau_\star}^{\tau_0} d\tau\,(\phi' + \psi')\;, \tag{4.39}$$

where we recall that $\mathbf{\Omega}$ is the normalized direction vector. Reminder that at first order, in the absence of anisotropic stress, which is the case for a coupled baryon-photon fluid, we have $\phi = \psi$. However, when we consider neutrino, we have to consider the anisotropic stress.

This analytical approximation has first been used in the works [158, 159]. We can also refer to the very intuitive demonstration in [154]. This equation can be understood in a very intuitive way. The temperature fluctuation at a given position is a superposition of 4 effects:

- δ_γ: The first source of temperature fluctuation is of course the density fluctuation of photons. This is simply a consequence of Stefan's law (2.68).
- ϕ: This is a gravitational shift term. A photon emitted from an over-dense region is hotter but must climb out of a deeper potential well which decreases its energy.
- $\mathbf{\Omega}\cdot\mathbf{v}$: This is a Doppler effect term. If the velocity on the last scattering surface of the fluid electron/photon projected into the line of sight direction is non-zero, we have a Doppler effect.
- $\int \mathrm{d}\tau\phi'$: This is the *integrated Sachs–Wolfe* (ISW) effect. The factor 2 comes from the fact the ISW effect depends on the variation or the sum of ϕ and ψ which are equal at first order if there is no anisotropic stress. Recall that by looking at equation (2.61) we have that during a specific domination era, the potential can be considered as constant on large scales. Therefore on super-Hubble scales, the ISW effect is only active during the two periods of transition, matter-radiation, and matter-Λ. As represented in the figure 4.4, the matter-radiation equality is before the CMB emission but it is still recent so that the potential decay is not complete. Intuitively, the blueshift and the redshift that are generated when the photon comes in and out respectively will not compensate if the potential varies.

The first two terms are dominant. Their combination $\delta_\gamma/4 + \psi$ is usually called the effective temperature of the SW effect. One expects that the intrinsic photon temperature and the gravitational redshift partially cancel. This is called the Sachs–Wolfe effect in honor of the original article [160].

A basic picture of the plasma physics can help to understand the behavior of the temperature power spectrum. Let us assume that the plasma is composed only of photons and baryons. The continuity and Euler equations, including the interactions terms, are given by [99]

$$\delta'_\gamma = -\frac{4}{3}\Delta v_g + 4\psi', \qquad v'_\gamma = -\frac{1}{4}\delta_\gamma - \phi - \frac{1}{6}\Delta\pi_\gamma + \lambda_c^{-1}(v_b - v_\gamma) \tag{4.40a}$$

$$\delta'_b = -\Delta v_b + 3\psi', \qquad v'_b = -\mathcal{H}v_b - \phi + (R\lambda_c)^{-1}(v_\gamma - v_b)\,, \tag{4.40b}$$

where we have defined $R = 3\bar{\rho}_b/4\bar{\rho}_\gamma$ and we recall that λ_c is the Compton mean free path (4.38).

Sachs-Wolfe plateau

At large scales, *i.e.* the modes outside the horizon at the recombination time, the potential is constant (except during the transition between radiation and matter domination) as we have seen in (2.61). Since deep in the radiation domination era we have $\bar{\rho} \simeq \bar{\rho}_\gamma$, the adiabatic initial condition (2.83) turns into

$$-2\psi^0 = \delta^0_\gamma = \frac{4}{3}\delta^0_b\,. \tag{4.41}$$

The photons and baryons velocities are set initially to 0 following (2.84) and do not grow significantly until the CMB [99]. Also, the Laplacians are negligible on super-horizon scales. Therefore the combination $\delta_\gamma - 4\psi$ and $\delta_b - 3\psi$ can be considered as constant. In addition, we can use the asymptotic relation between the radiation and matter domination eras for the potential (2.62) to link δ^{mat}_γ, δ^{mat}_b and ψ^{mat} to the initial conditions. One finds

$$\frac{1}{4}\delta^{mat}_\gamma = \frac{1}{3}\delta^{mat}_\gamma = -\frac{2}{3}\psi^{mat} = -\frac{3}{5}\psi^0\,. \tag{4.42}$$

Therefore, it follows from (4.42) that at large scales

$$\Theta_{SW} = \Theta + \psi = \frac{1}{3}\psi\,, \tag{4.43}$$

where we have used Stephan's law (2.68) to translate the photon density contrast into the intrinsic temperature contrast. Reminder that we work here at first order where $\phi = \psi$. A rigorous derivation of this has been performed in [161]. As expected, we see in (4.43) that the cancellation is partial. The remaining part is proportional to the potential. In the over-dense region ψ in negative (from the Poisson equation (2.48a)), therefore the observed cold spots, in blue in figure 4.1, correspond to photon over-dense regions.

In equation (4.27), we have shown that for nearly scale-invariant power spectra, the CMB power spectrum in the form D_ℓ is a direct measure of the amplitude of the three-dimensional power spectrum. In the case of the Sachs-Wolf plateau, by noting that in matter-domination we have from equation (2.63) $\psi = 3\zeta/5$. Recall that ζ is constant on super-Hubble scales so that the transfer function takes the trivial form: $\mathcal{T}^{(1)} = 1/5$. Hence, in the power spectrum, for $\ell \lesssim 100$, we observe the nearly scale-invariant curvature primordial power spectrum translated into effective temperature:

$$D_{\ell\lesssim 100} \simeq \frac{A_s}{25}\,. \tag{4.44}$$

If we use the baryon density isocurvature IC $S^0 \neq 0$, by solving (2.60) with $\psi^0 = 0$ we can show that in the matter domination era [98, 99]

$$\Theta_{SW} = 2\phi = -\frac{2}{5}S^0\,. \tag{4.45}$$

Using a similar reasoning as for the adiabatic IC, we find a Sachs-Wolf plateau in the super-horizon limit

$$D_{\ell\lesssim 100} \simeq \frac{72}{25}A_s\,. \tag{4.46}$$

As we will see, there cannot be baryon velocity isocurvature mode because of the tight coupling with the photon.

The Sachs-Wolf plateau can be seen on the left for small ℓ, *i.e.* large scales in figure 4.5.

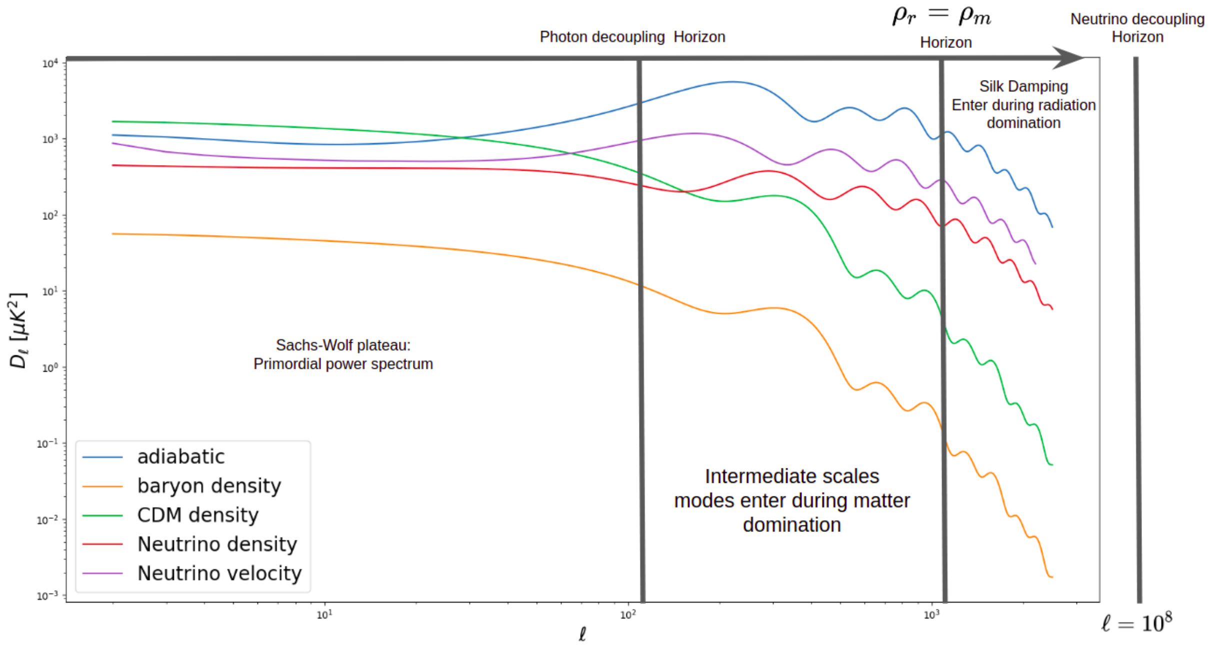

Figure 4.5: CMB temperature power spectra defined in (4.25) as a function of the multipole. They are computed for the 5 different initial condition possibilities: adiabatic, baryon, CDM and neutrino density isocurvature and neutrino velocity isocurvature.

Acoustic peaks

Let us now study the sub-horizon scales by following [99]. One can first consider the tight coupling regime $k\lambda_c \ll 1$. The expansion of (4.40) reads

$$v_b = v_\gamma, \qquad S'_{b\gamma} = 0\,. \tag{4.47}$$

In this regime, we can combine the continuity and the Euler equations (4.40) to find

$$\delta''_\gamma + \frac{R'}{1+R}\delta'_\gamma - c_s^2\Delta\delta_\gamma = 4\psi'' + 4\frac{R'}{1+R}\psi' - \frac{4}{3}\Delta\phi\,. \tag{4.48}$$

This equation describes a damped oscillator driven by the potential. The density contrast is subjected to two contrary forces: a driving gravitational force on the right-hand side and a restoring force due to radiative pressure $\propto \delta'_\gamma$. The result is an oscillation. These oscillations are damped by the second term of the left-hand side of (4.48) which increases with increasing contribution of baryons to the total energy of the fluid.

A general solution in Fourier space can be written for the transfer functions

$$(1+R)^{1/4}\mathcal{T}_{\delta_\gamma}(k) = \mathcal{D}(k)\left(A\cos kr_s + B\sin kr_s\right) + \int \mathrm{d}\tau' F(\tau')G(\tau,\tau')\,, \tag{4.49}$$

where $F(\tau')$ is the right hand side of equation (4.48), G the Green function, A and B integration constants and the function $\mathcal{D}$ is a damping term due to the second term of the left hand side of equation (4.48). The constant A and B can be determined from initial conditions. The distance r_s is the sound horizon at the recombination *i.e.* $r_s = (144.57 \pm 0.22)\mathrm{Mpc}$ [66]. The constant A is the photon density in the limit $kr_s \ll 1$ *i.e.* outside the sound Horizon.

Let us consider the scales that enter the horizon during the matter domination era but before recombination, $(0.01 \lesssim k \lesssim 0.1)$ $h\text{Mpc}^{-1}$, see figure 4.4. For these scales, the variable R can be considered as constant so that the damping term of equation (4.48) vanishes, *i.e.* $D(k) \sim 1$. Moreover, the potential is constant. Having still in mind that $\delta'_\gamma - 4\psi' = 0$, *i.e.* equation (4.42), we can show that $A = -\frac{2}{3}\psi^0$ and $B = 0$. The adiabatic IC, therefore, excites the cosine mode. Indeed, the potential and density fluctuation are primordially sit already in a "compressed" state. The oscillation after horizon crossing will therefore start at a maximum, *i.e.* a pure cosine mode.

On the contrary, the density isocurvature mode will excite the sine mode. By using (2.86), we can show that $\delta_\gamma = -4R\mathcal{S}^0/3$. The ratio R tends to zero deep in the radiation domination era which means that $A = 0$. The background solutions summarized in the table (2.1) tell us that $R = \tau$ which means that $\delta'_\gamma = -4\mathcal{S}^0/3$ initially. Hence, by deriving (4.49) where the source term vanishes initially and still with $\mathcal{D} = 1$, we show that $B = \sqrt{3}\mathcal{S}^0/k$. After horizon crossing, the oscillation will start by a phase of increasing density, *i.e.* a sine mode. We can observe this phase shift between the adiabatic and the isocurvature IC in figure 4.5 for the middle scales except for the velocity mode.

An approximation of the position of the peaks for the different IC can be obtained with the maximum of the cosine or sine $kr_s = n\pi$ or $(n - 1/2)\pi$. Recall that the angular scale θ associated with a given ℓ is given by π/ℓ. This angular scale can be expressed as a function of k by introducing the distance $r_\star$ of the last scattering surface. Finally

$$\ell = \frac{r_\star}{r_s} k r_s \,. \tag{4.50}$$

By using the value measured by Planck, one finds for the first peak $\ell \sim 220$ for adiabatic and $\ell \sim 330$ for density isocurvature modes [99].

For the velocity mode, by solving the system (4.40) for v, one can roughly speaking show that $v \sim \delta'$. Therefore a velocity isocurvature IC will again excite a cosine mode. This case will appear only for neutrinos (see next section).

Silk damping

When we consider the small scales, typically those that enter the horizon during the radiation domination era $k \gtrsim 0.1$ $h\text{Mpc}^{-1}$, the tight coupling approximation breaks. In this regime, it has been shown in [162] that an effect of photon diffusion becomes dominant. The photon trajectory on small scales can be described with a Brownian motion. The mean free path of the photon is λ_C which is given in (4.38). The distance traveled by a photon in a random walk with mean free path λ_C is $\lambda_C\sqrt{N}$, where N is the total number of steps. For scales smaller than this diffusion length, the primordial anisotropies are washed by the diffusion of the photons. It is shown in [162] that the photon density in this regime follows a solution of the type (4.49) with a suppression by $\mathcal{D} \sim \exp(-k^2/k_D^2)$ where k_D is the mode associated with the diffusion length. In Silk damping, the effect of the finite thickness of the last scattering surface becomes important because the mean free path of the photons becomes rapidly large (decoupling).

4.3.2 Polarization

The CMB is partially polarised ($\sim 10\%$). It arises from the local quadrupole at the decoupling. In this section, we will see how the movement of electrons on the last scattering surface due to the density anisotropies induces a polarization signal called E-mode. We

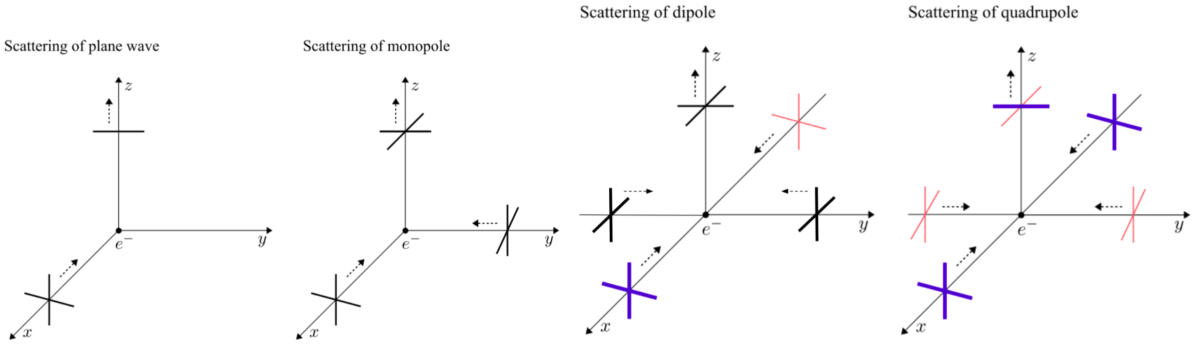

Figure 4.6: Illustration of the polarization of the resulting photon flux along the z-axis scattered off an electron at rest at the origin for different cases. From left to the right we consider the following incoming photon flux: one incoming photon flux on the x-axis, two photon fluxes with the same intensity coming from the x-axis and the y-axis (monopole), two opposite photon fluxes on the x-axis with different intensity represented by the different colors blue and red (dipole). Finally, the last configuration represents four different fluxes, two of them come from opposite directions on the x-axis with a given temperature and the two others come from opposite directions on the y-axis with another temperature, this is the quadrupole. Taken from [119].

will also mention that gravitational waves can produce another type of polarization: the B-modes.

Physical origin

In figure 4.6, we give a basic and intuitive picture of the different configurations that will, or will not, induce a polarised flux. The main point is that the scattering of a photon on an electron can only transmit the polarization of an incoming photon that is perpendicular to the line of sight. For instance, in the first panel of figure 4.6, we see that the z-axis polarization of the incoming photon on the x-axis cannot be transmitted. In a monopole and dipole configuration, represented in the second and third panel of figure 4.6, the outgoing photon cannot be polarized. Note that for the dipole, the y-axis polarization of the outgoing photon is a mean of the incoming photon on the x-axis. This is why a dipole gives the same result as a monopole. To observe a polarization, the only possible configuration is a quadrupole, represented on the fourth panel of figure 4.6. This time, the opposite direction does not cancel and the outgoing photon is polarized.

Therefore, the polarization field is generated by the local quadrupole distribution of the photon density. We have introduced in equation (4.28) the temperature anisotropies multipoles. We shall note that the result that we derived for the total temperature contrast Θ, for instance, the cosine mode exciting in the case of adiabatic IC, is still true for the monopole Θ_0. However, a smaller, but of the same order, contribution comes from the dipole Θ_1. This comes from the Doppler shift in equation (4.39). Because this term is due to the radial velocities, it can be shown that $\Theta_1 \propto \Theta_0'$ which means that Θ_1 oscillates like a sine for adiabatic IC.

Then, the leading contribution to the polarization is the quadrupole Θ_2. It can be shown that Θ_2 is proportional to Θ_1 [119] which means that it should oscillate also as a sine. Moreover, it is smaller by a factor $k\lambda_c$ since the quadrupole is suppressed by

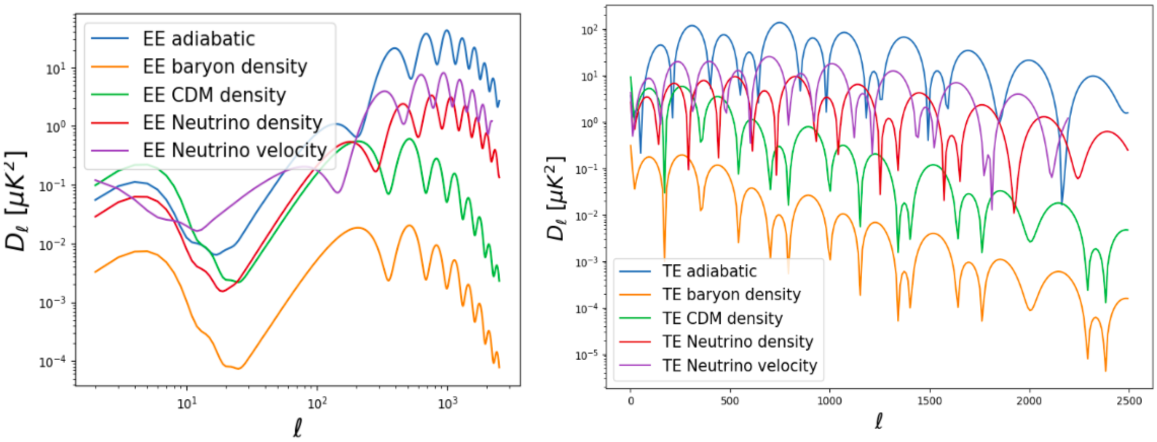

Figure 4.7: E-mode polarization power spectrum on the left for all considered initial conditions. On the right the cross-power spectrum of the temperature and the E-modes.

the Compton scattering. As we concluded from figure 4.6 that the polarization can be sourced by the quadrupole, we expect that the polarization spectrum should be out of phase with the temperature power spectrum. This can intuitively be understood since the polarization is maximal when the velocity of the electrons is large. As we have seen using equation (4.49), for adiabatic IC, the density of photons oscillates as a cosine; this is also true for the baryon/electron fluid. Therefore the velocity oscillates like a sine.

This can be intuitively understood by understanding the way a quadrupole can be generated. Let us picture an electron (E) that falls into a spherically symmetric potential well. Since electrons that are closer (further) to the potential well center fall faster (slower), the electron E sees on the $\vec{e}_r$ axis that all the electrons are moving away. By Doppler shift, the photon flux is lower. On the other hand, from the spherical symmetry of the potential, the electrons along the $\vec{e}_\theta$ axis seem to get closer. From the Doppler shift, we have this time a larger photon flux intensity. Hence, polarization arises from falling electrons. From this basic picture, we see that it should be positively correlated with the velocity of the electron. We also expect the polarization power spectrum to follow this behavior since the polarization should be large (small) for large (small) velocities. We also expect the polarization power spectrum to be smaller (by a factor $(k\lambda_c)^2$). For more details, see [119].

E- and B-modes

Generally, one can decompose a luminous signal in the Stokes basis (I, Q, U, V) where I is the intensity, Q measures the projection of the polarization on the horizontal axis ($Q > 0$) or on the vertical axis ($Q < 0$) (for instance on the x-axis and the y-axis respectively in the figure 4.6). The parameter U measures the projection of the polarization on the first diagonal axis (of equation $y = x$) ($U > 0$) or on the second diagonal axis (of equation $y = -x$) ($U < 0$). Finally, V measures the circular polarization and is rarely considered in cosmology since usual inflation models do not produce this type of perturbation and neither do Compton scattering. In [163] however, it is shown that a class of inflation model can produce this polarization but will be suppressed at the time of CMB emission by a factor $10^{10^{20}}$. However, a spin polarization quadrupole could be generated by the interaction of the hydrogen atoms with the anisotropic 21-cm radiation field, see *e.g.* [164].

The intensity is directly proportional to the temperature. A two dimensional polarization field on a sphere (Q, U) can be decomposed into spherical harmonics [165, 166]:

$$[Q \pm iU](\mathbf{\Omega}) = \sum_{\ell m} {}_{\pm 2}a_{\ell m}\ {}_{\pm 2}Y_{\ell m}(\mathbf{\Omega}) \,, \tag{4.51}$$

where the functions ${}_{\pm 2}Y_{\ell m}$ are the spin two harmonic functions. We can then define the E-modes and B-modes by

$$\begin{aligned} a^E_{\ell m} &= \frac{1}{2}\left({}_{+2}a_{\ell m} + {}_{-2}a_{\ell m} \right) \,, \\ a^B_{\ell m} &= i\frac{1}{2}\left({}_{+2}a_{\ell m} - {}_{-2}a_{\ell m} \right) \,. \end{aligned} \tag{4.52}$$

By analogy with electromagnetism, the E-mode is a pure scalar (parity invariance) and the B-mode is a pseudo-scalar (change sign under parity transformation). For these fundamental symmetry reasons, scalar perturbations can only generate E-modes in the polarization, see [167] for many details and representations of this symmetry. Hence, these E-modes are exactly the kind of polarization that will follow the features discussed in the previous subsection 4.3.2. This is illustrated by the figure 4.7, the EE polarization power spectra are out of phase w.r.t. to the TT power spectra shown in figure 4.5 and are much lower in amplitude by a factor ~ 100. Note that we do not observe a Sachs-Wolf plateau for large scales since polarization is not affected by redshifts. Furthermore, on the right, we see that the correlation between the E-modes and the temperature is non-zero and oscillates around zero. Indeed, we have plotted the absolute value of the cross-power spectra so that the bumps that we observe in figure 4.5 are due to the sign change.

The B-mode polarization on the other hand can be sourced by tensor and not by scalar perturbation. For this reason, it is a “clean” probe of tensor perturbations. Not that vector perturbation can also generate B-modes but, as explained in the section 3.1, they are not generated by inflation and would anyway decay rapidly. Conversely, the tensor perturbations generate E-mode and temperature fluctuations. The constraints on the tensor perturbations can therefore also come from the temperature and E-mode power spectra. As we have seen, the simplest model of inflation generates tensor perturbations, also called primordial gravitational waves, with a power spectrum given in (3.41). The measurement of the B-mode power spectrum amplitude is a direct measurement of the amplitude A_t. We could then infer the tensor-to-scalar ratio (3.43) which is directly proportional to the slow-roll parameter ε. The system H, ε, η, that entirely characterizes the single-field slow-roll model, can then be solved thanks to the observed A_s, n_s, r. Moreover, a measurement of the tensor primordial power spectrum slope n_t would be a strong test of the single-field slow-roll model because of the consistency relation (3.44).

For all these reasons, most of the current/future CMB experiments are hunting primordial B-modes, see for example the promising QUBIC experiment which just arrived in Argentina for its first light [168, 169]. In our analysis, we will also describe and provide forecasts for the future experiments LiteBIRD and CMB-S4, see section 5.4.

4.3.3 Secondary anisotropies

As described in the previous subsection, the CMB photons are emitted around $z \sim 1000$ and travel through the universe with the information of the temperature and the polarization. As we will describe here, several effects can disturb the CMB photon and contaminate the primary CMB emission. These effects can however bring additional information as we will see. In this section, we describe some of these secondary anisotropies.

Reionization

After the CMB emission, we enter the so-called dark ages. During this epoch, the universe is neutral, mostly composed of neutral hydrogen atoms. No structure nor stars are formed which is why we call this epoch the "dark" ages. This period could become crucial for the future of cosmology thanks to the 21cm hydrogen emission, see [170]. At a redshift of $z \sim 15$, the first stars, galaxies, and quasars start to form. Their light emission is more energetic than the binding energy of the hydrogen atom. Hence, the medium around these stars is re-ionized (remember that the universe was entirely ionized before the CMB emission). Recombination and ionization are in competition so that the universe is mostly neutral with bubbles of plasma around the light sources. Around a redshift $z_{re} = 7.82 \pm 0.71$ [66], the density of light sources in the universe finally becomes large enough to ionize the entire universe. The redshift z_{re} is a mid-point. The start and the end of reionization are believed to be $z = 15$ and $z = 6$. After the CMB, this is the second phase transition of the universe.

Today we live in a universe similar to the pre-CMB epoch in the sense that the universe is filled with a plasma and $x_e = 1$ in equation (4.11). This has been discovered thanks to the observation of the quasars spectra [171]. The temperature of the plasma which is reheated by the UV emission of the stars is $\sim 10^4$K. However, the baryon/electron density is smaller by a factor of 10^6. Therefore, the mean free path of the photons is $\lambda_C = 2.5 \times 10^6$Mpc, see equation (4.38) while the horizon today is 1.4×10^4Mpc (*i.e.* $\sim 100\times$ the horizon at $z = 1000$ because it grows like z). The universe is still transparent with a small absorption factor taken into account in the reionization depth parameter called τ. In the equation (4.21), this translates into the fact that the visibility function, that we approximated with a δ-function peaking at recombination, has a second small peak around at the late time.

The probability for a CMB photon to re-scatter at late time is $1 - e^{\tau_{re}}$. This has for effect to wash out the primordial anisotropies by decreasing the power A_s by a factor $e^{-2\tau}$. This effect can only affect the multipoles larger than the horizon multipole at the epoch of reionization, *i.e.* $\ell \lesssim 100$. Because of the cosmic variance, the error bars are large for the small multipoles and are not enough to well constrain A_s. From the large multipoles, there is a strong degeneracy between τ_{re} and A_s. This degeneracy can be broken by looking at the polarization power spectra. Contrary to the temperature power spectrum, the reionization epoch generates additional anisotropies by the same mechanism of converting the local temperature quadrupole into a polarized signal via Compton scattering. However, in the sub-horizon regime, the quadrupole is suppressed by the free-streaming of the photon between recombination and reionization. This means that the reionization generates an additional power in the C_ℓ^{EE} (and C_ℓ^{TE}) for the small multipoles, this is visible at $\ell \lesssim 10$. The amplitude of this additional power is $\propto \tau_{re}^2$ so that combining C_ℓ^{TT}, C_ℓ^{EE} and C_ℓ^{TE} breaks the degeneracy of A_s and τ_{re}.

Integrated Sachs–Wolfe effect

The ISW effect has already been mentioned in section 4.3. It is due to the evolution of the potential generating an asymmetric shift of the photon that is not compensated. We can distinguish two different periods where this effect is important. First, the early ISW effect, corresponding to the radiation/matter transition, affects mostly, in an adiabatic universe, the modes that entered the sound horizon between matter/radiation equality and the recombination, *i.e.* intermediate scales. For isocurvature, the potential grows

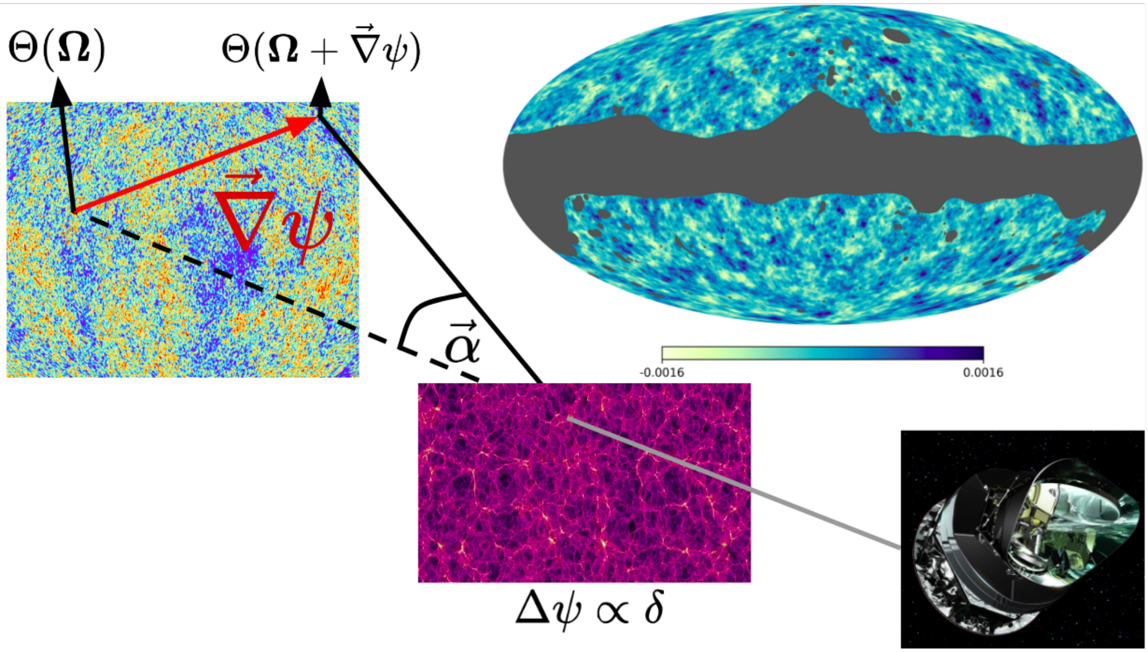

Figure 4.8: Representation of the weak lensing effect of the CMB photons traveling through the LSS. On the bottom, the satellite Planck receives the CMB photons from the direction that is extended n dashed black to represent the line of sight. The photon is deviated from the line of sight by an angle α which is proportional to the projected gradient of the gravitational potential. This gradient is generated by the density fluctuation in the LSS. Finally, Planck observes the temperature fluctuation $\Theta(\mathbf{\Omega}+\vec{\nabla}\psi)$ at the position $\mathbf{\Omega}$. On the top right, the reconstructed lensing map by Planck [173].

for the modes larger than the sound horizon so that the ISW contribution affects larger multipoles.

The second contribution is called the late ISW effect. It arises when the potential decays during Λ domination, *i.e.* for redshifts lower than $z \sim 1$. In figure 4.4, we see that these modes correspond to large scales so that the late ISW effect affects mostly the Sachs-Wolfe plateau. It turns out that this is one of the direct impacts of the cosmological constant in the CMB. It can be studied by correlating the large-scale CMB with LSS [172].

Lensing

The photons of the cosmic microwave background that we observe have crossed the large-scale structure (LSS) that started to form around $z \sim 10$ until today. The LSS induces a gravitational potential gradient which has the property to deflect photons, as represented in figure 4.8. The final effect is a remapping of the temperature (and polarization) so that (see [174, 175] and the review [176]):

$$X(\mathbf{\Omega}) = X^{lens}(\mathbf{\Omega}+\vec{\nabla}\psi(\mathbf{\Omega})) \simeq X^{len}(\mathbf{\Omega}) + \nabla_i\psi(\mathbf{\Omega})\nabla^i X(\mathbf{\Omega})\,, \tag{4.53}$$

where $\psi(\mathbf{\Omega})$ is the line-of-sight projection of the gravitational potential. Similarly to the convolution integral equation (2.106), the second term appearing in equation (4.53) produces in harmonic space a coupling between the modes and non-Gaussianities. If we compute the power spectrum of the lensed observable, one finds that the lensing contributes to the off-diagonal elements in the covariance:

$$\left\langle a^{X,lens}_{\ell_1 m_1} a^{Y,lens}_{\ell_2 m_2} \right\rangle = (-1)^m \delta^{\ell_2}_{\ell_1} \delta^{m_1}_{-m_2} C^{XY,lens}_{\ell_1} + \sum_{LM} (-1)^M \begin{pmatrix} \ell_1 & \ell_2 & L \\ m_1 & m_2 & -M \end{pmatrix} \mathcal{W}^{XY}_{\ell_1 L \ell_2} a^{\psi}_{LM} \, , \tag{4.54}$$

where the functions $\mathcal{W}^{XY}_{\ell_1 L \ell_2}$ depend on the power spectra and are given in [175]. For the temperature for example, two of the terms in $\mathcal{W}^{XY}_{\ell_1 L \ell_2}$ are $C^{TT}_{\ell_1} + C^{TT}_{\ell_2}$. By using the equation (4.54), one can construct an estimator for the potential

$$\tilde{a}^{\psi}_{LM} = \frac{(-1)^M}{2M^{XY}_L} \sum_{\ell_1, \ell_2, m_1, m_2} \begin{pmatrix} \ell_1 & \ell_2 & L \\ m_1 & m_2 & -M \end{pmatrix} \mathcal{W}^{XY}_{\ell_1 L \ell_2} a^{X}_{\ell_1 m_1} a^{Y}_{\ell_2 m_2} \, , \tag{4.55}$$

where M^{XY}_L is chosen such that the estimator is unbiased. To reconstruct the projected potential field, as we can see in (4.55), we need to correlate the observables. This can be understood by noting that the lensing has as effect of mixing the different observables. In particular it is well known that the leakage of the E-modes into the B-modes actually dominates the B-modes power spectrum as small angular scales. This means that the correlation between the E- (or T) and B-power spectrum is high while it should be zero in the standard model of cosmology. This correlations is a direct signal of the lensing. Interestingly, as a consequence of (4.55), the power spectrum of the lensing potential turns out to be a connected part of the 4-point correlation function of the CMB, *i.e.* the trispectrum.

Sunyaev-Zeldovitch effects

At low redshift, the temperature after reionization is 10^4 K while in the clusters it can be 10^7 K. The low-energy CMB photons that scatter off high-energy electrons will on average gain energy by inverse Compton scattering. This effect is called the thermal Sunyaev Zeldovitch effect (SZ) [177, 178]. The main effect on the CMB is a spectral distortion in the black-body frequency spectrum. These spectral distortions are a measure of the integrated pressure along the line-of-sight [119]. This allows us to map the integrated pressure.

Moreover, the SZ effect is also a probe of the galaxy clusters since they are much hotter and denser thereby generating strong local spectral distortions. In addition, a kinetic effect can arise if the cluster has a peculiar motion w.r.t. to the last scattering surface's electrons rest frame, this is called the kinetic SZ effect. Based on this effect, the Planck satellite has provided a catalog of galaxy clusters [179].

Foregrounds

Finally, we will quickly review the different foreground sources that emit at the same frequency range as the CMB. They can be split into galactic and extragalactic sources.

One of the main contaminants, especially for the B-mode polarization, is our galaxy. First, the dust which composes $\sim 10\%$ of the Milky Way has a thermal radiation > 250 GHz. Moreover, this dust is composed of carbonate and silicate grains. The magnetic field of our galaxy partially aligns these grains. Hence, the dust emission is also polarised. Moreover, these grains can be in rotation which produces an electric dipole radiation called AME (for anomalous microwave emission). Then, there is the synchrotron emission which is also polarized and is generated by charged particles accelerated in the galactic magnetic field. Other physical processes contaminating the CMB are the bremsstrahlung and CO emission. See for example [180] for a more detailed description of these effects. All these effects have a specific emission law that can be fitted thanks to the measurements at different frequencies and then subtracted.

These galactic effects also take place in other galaxies. For instance we observe a cosmic infrared background (CIB) peaking at $z \sim 2$, see *e.g.* [181]. This radiation comes from the dust heated by young stars and is redshifted to the infrared. The synchrotron and bremsstrahlung emissions of the other galaxies are also redshifted and are observed as radio sources.

Primordial bispectrum contamination

The bispectrum of the observed CMB is a superposition of many effects, from the PNG to the late NG. Here we briefly review these effects.

- The first source of NG is a primordial non-Gaussianity due to multi-field inflation for instance. We have reviewed three popular shapes in section 2.5.4 and we gave more details on their origin in the case of multi-field inflation in section 3.2. In section 2.5.4, we explained that, at leading order, PNG are linearly propagated through the history of the universe.

- The *intrinsic* NG, as explained in section 2.5.4, arises from the non-linear dynamics. To compute them, we need to expand the Einstein equations beyond the linear order. At second order, we need to solve for the second-order transfer functions. This particular type of contamination can generate a local shape of NG. Many authors worked on the estimation of the effective $f_{\rm NL}$ [100, 101, 182–184]. It has been shown, in particular in [100], that this effect is of order $f_{\rm NL} \sim 1$, *i.e.* subdominant compared to the current error bars, see table 5.5. This could, however, become very important when estimating NG in the LSS since we expect constraints of $\Delta f_{\rm NL} \sim 1$. This is the subject of the third part of this thesis.

- A crucial contamination of the local PNG comes from the coupling between the lensing and the ISW effect. These two effects have the same physical origin: the lensing comes from the potential gradient and the ISW effect comes from the temporal evolution of this potential. The cross-bispectrum peaks in the squeezed limit because the lensing affects mostly the small scales while the ISW affects the large scales. It was predicted in [185] and detected by the Planck satellite. The constraint is: $f_{\rm NL} = 0.81 \pm 0.27$ [107].

- Similarly, there is a correlation between the lensing and the thermal SZ effect [185]. The frequency dependence of the SZ effect allows us to well separate it from the CMB and therefore it is not a large contamination.

- Many other effects have been studied and taken into account in the Planck analysis. For instance, the CIB increases the bispectrum power at high ℓ and is also correlated with the lensing [186]. In addition, there are the unclustered radio galaxies which have a similar and even stronger effect on the bispectrum. Moreover, the bispectra of the galactic foregrounds (dust, bremsstrahlung, synchrotron, and AME) have been studied in [187]. They found that all the shapes peak in the squeezed limit. However, no residual is found in the cleaned CMB map (after component separation). This is however not the case for the unclustered radio galaxies but it is not correlated with PNG.

4.4 General primordial cosmic perturbations

Now that we have understood the behavior of the power spectrum we note that we have shown in figure 4.5 only five different possibilities: adiabatic, baryon/CDM/neutrino density isocurvature and only one velocity isocurvature mode. Indeed, it has been shown in [137] that for a universe composed of baryons, neutrinos, CDM, and photons (b, ν, c and γ respectively), there is only a combination of these 5 possibilities. For a very complete bibliography on mechanisms that can generate isocurvature modes, see [188].

For our universe, there is one adiabatic mode often denoted by the total curvature perturbation ζ defined in equation (2.72). Imposing adiabatic initial conditions is equivalent to $\zeta^0 \neq 0$. From equations (2.37), (2.82) and (2.83), one finds:

$$\zeta^0 = -\frac{3}{2}\psi^0 \,. \tag{4.56}$$

Then, we know from adiabaticity that all density contrasts are proportional (2.83). In addition, note that at an early times, $\bar{\rho} = \bar{\rho}_\gamma + \bar{\rho}_\nu$ since we are in the radiation domination era. With simple algebra, one can show that from $\delta_\nu = \delta_\gamma$ follows $\delta_r = \delta_\nu = \delta_\gamma$ where δ_r is the density contrast of radiation. By making use of the 00 Einstein equation (2.48a), we find

$$-2\psi^0 = \frac{4}{3}\delta_c^0 = \frac{4}{3}\delta_b^0 = \delta_\nu^0 = \delta_\gamma^0 \,. \tag{4.57}$$

We have also shown that all velocities vanish at first order.

On the other hand, as discussed in subsection 2.4.5, we can have in general $N-1$ density isocurvature IC ($\zeta^0 = 0$) and $N-1$ velocity isocurvature IC (where N is the number of fields). First, we consider the density case. This corresponds to breaking one of the equalities (4.57) and by convention, we always take the photon density as reference. It means:

$$S_i^d = \frac{1}{1+\omega_i}\delta_{i\neq\gamma}^0 - \frac{3}{4}\delta_\gamma^0 \,. \tag{4.58}$$

It turns out that the baryon and CDM IC modes are indistinguishable in the CMB apart from a rescaling factor Ω_c/Ω_b. We see this in the figure 4.5, the CMB power spectrum with pure CDM isocurvature IC and pure baryons isocurvature IC have the same shape and would be identical for $\Omega_b = \Omega_c$. To understand this, let us consider the non-relativistic density modes CDM and baryons. The IC is set deep in the radiation era and by definition of isocurvature modes, the total density contrast vanishes initially. Hence for CDM and baryons we have $\delta_\gamma^0 = 0$ from which follows $S_i^d = \delta_i^0$ with $i \in [c, b]$. Now we can solve for the density, the velocity, and the potentials for all fields by using the continuity equation (4.40) (and similar continuity and Euler equations for neutrinos and CDM, see [137]) by expanding the fields as a power-law series (remember that we are in the tight coupling approximation and the super-Hubble regime for the IC)

$$\xi = \sum_i \frac{(k\tau)^i}{n!}\xi^i \,. \tag{4.59}$$

From the continuity equation, by noting that $v_\gamma^0 = 0$ and by making use of the 00 Einstein equation, one finds that the super-horizon solution reads

$$\delta_\gamma = \left(-\frac{8}{3}\tau + 4\tau^2\right)\Omega_i S_i^d\,, \tag{4.60}$$

where we have defined $\Omega_i = f_b\Omega_b + f_c\Omega_c$ with f_i the fraction $\bar{\rho}_i/(\bar{\rho}_b + \bar{\rho}_c)$. Equation (4.60) shows that the photon density is only sensitive to the total amount of cold matter Ω_i. Hence, the CMB power spectra are insensible to the composition parameters f_b and f_c. Moreover, it has been argued in [189] that indeed, the evolution of all perturbed quantities of the other fluids only depend on δ_b and δ_c through the metric perturbation, *i.e.* 00 Einstein equation. Therefore, even after horizon crossing the evolution of δ_γ cannot differentiate between S_b^d and S_c^d. For more details, see [190] which also discusses how these modes could be distinguished with the 21cm surveys. In the rest of this thesis, we will not consider the baryons isocurvature mode.

Let us now consider the baryons velocity initial condition. Those perturbations may exist initially but the tight coupling of the baryons with the photons will make $S_b^v \to 0$ very rapidly given the considered time scales, see equation (4.47). It is then useful to always consider $v_b = v_\gamma = v_{\gamma b}$. Next, the CDM velocity mode is always zero. We can see that by switching to the synchronous gauge. The synchronous gauge is defined by free-falling observers, so it is always possible to use the CDM particles to define the coordinates since these particles interact only through gravity. Thus, in this gauge $v_c = 0$, see [191]. Furthermore, we can show that imposing $\delta_i = 0$ in this gauge fixes the baryon/photon velocity to zero. It follows that in all gauges $S_c^v = 0$, as it is gauge-invariant. In the end, the only velocity isocurvature mode that we have to consider is the neutrino one. From our definition of $\mathcal{V}_{ij}$ (2.80) and the constraint that the total initial velocity should vanish, see (2.88), we find that for neutrinos

$$\mathcal{V}_{\nu\gamma} = v_\nu^0(1 + f_\nu)\,, \tag{4.61}$$

where we recall that f_ν is the ratio of the background neutrino energy density over the photon energy density which is given in equation (4.7). It is therefore common to define

$$S_\nu^v = \frac{1}{1+f_\nu}(v_\nu^0 - v_\gamma^0) = \frac{1}{1+f_\nu}\mathcal{V}_{\nu\gamma}\,. \tag{4.62}$$

By using (4.61) and (4.62), we find that S_i^v exactly matches v_ν^0. To conclude, we will consider the adiabatic mode and 3 isocurvature modes: the CDM density mode, the neutrino density mode, and the neutrino velocity mode. In practice, we will always consider only a single isocurvature mode in addition to the adiabatic mode (which can be correlated), because otherwise the number of free parameters, in particular for the bispectrum, would be too high to get meaningful constraints.

After this general introduction to CMB physics, we now move on to one core of this thesis: the joint analysis of the CMB power spectrum and bispectrum. The underlying main goal of that work is to constrain the isocurvature modes and the PNG.

Chapter 5

Joint analysis

In the last chapter 4, we have seen that the CMB temperature and polarization fluctuations result from fluctuations of the metric generated during inflation, which has been described in section 3.1. This means that the inflation paradigm can be tested by measuring the statistics of these CMB anisotropies. We have stressed that in the simplest models of inflation the perturbations are predicted to be adiabatic and nearly Gaussian with a power spectrum given by a power law with a small tilt. These predictions for the scalar fluctuations are compatible with the Planck mission measurements [107, 121].

Then in section 3.2, we have shown that in multi-field inflation, a higher level of non-Gaussianity can be generated. They might be detectable with future CMB experiments as well as with future large-scale structure surveys, see e.g. [192]. Moreover, multi-field models can generate one or more isocurvature modes in addition to the adiabatic mode. Even if the CMB is mostly adiabatic, isocurvature components can still be present at the level of 25% at 2σ given the Planck measurements [121].

Given that a detection of isocurvature modes would rule out single-field inflation as the sole source of the cosmological fluctuations, it is important to improve our constraints on these modes as much as possible. The Planck constraints mentioned above come from an analysis of the CMB power spectrum alone. However, isocurvature modes can also have an impact on the CMB bispectrum [113, 124, 149, 193–200] (the Fourier or spherical harmonic transform of the three-point correlation function). This was independently tested in the Planck bispectrum analysis [107], where no primordial non-Gaussianity was detected.

Joint analyses have been discussed in [201–203] in the context of resonance models of inflation. This method has then been used to improve the constraints of these models in [121]. A similar joint analysis will be performed in the context of large-scale structure surveys to constrain primordial non-Gaussianities, see for example [204]. The main point is that specific models can have specific impacts on the power spectrum and the bispectrum. In these models, the parameters of the power spectrum and the bispectrum can be related to more fundamental parameters. Hence, it could be possible, by merging the information of the bispectrum and power spectrum, to improve the constraints on these fundamental

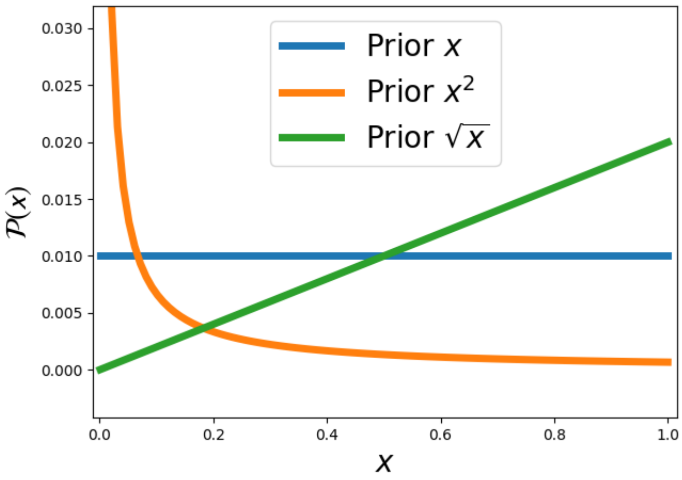

Figure 5.1: Three equivalent priors for three different parameterizations. A flat prior between 0 and 1 on the parameter x, *i.e.* the blue curve, is equivalent to the orange prior on the parameter x^2 and to the green prior on the parameter $\sqrt{x}$.

parameters by, for example, breaking degeneracies. In this section, we describe the first main work of this thesis, published in [205], a joint analysis of the power spectrum and the bispectrum to improve the constraints on isocurvature modes in the context of a generic class of two-field inflation model.

This chapter is organized as follows. In section 5.1, we introduce the Bayesian and MCMC statistical methods that we will use in the following. In sections 5.2 and 5.3, we first introduce the power spectrum and bispectrum observables independently. Then, in section 5.3.4, we establish the link between them by introducing a general class of two-field inflation models. In section 5.4, we discuss the power spectrum and bispectrum likelihoods for Planck and LiteBIRD and CMB-S4, and how we combine them into a joint likelihood. In section 5.5, we first show and discuss the results of our joint analysis of the Planck data, both for the general model and for the case where we fix additional parameters. We then give a general theoretical explanation of these results, that also provide guidance for the forecasts for future experiments. Finally, we investigate in which Planck-allowed regions of the parameter space the joint analysis will improve the constraints on isocurvature modes (compared to an analysis of the power spectrum alone) for LiteBIRD+CMB-S4. We perform joint analyses for certain choices of fiducial parameters, also looking at the consequences for the other cosmological parameters. We summarize and conclude in section 5.6. This chapter follows closely our publication [205].

5.1 Statistical analysis

To perform the analyses, we use the Markov chain Monte-Carlo (MCMC) statistical method, [206, 207], with different power spectrum likelihoods; the Planck likelihood and LiteBIRD and CMB-S4 forecasts. These likelihoods will be defined in the following sections. For this section, we consider a generic likelihood $\mathcal{L}$.

5.1.1 Bayesian analysis

Let us consider a theoretical power spectrum C_ℓ^{th}, which is a function of the cosmological parameters $\boldsymbol{\theta}$, and an observed power spectrum C_ℓ^{obs}. We consider for simplicity here only one power spectrum, for instance, the temperature power spectrum. In the case of forecasts, the observed power spectrum is a fiducial power spectrum. We can relate the posterior distribution to the likelihood with the Bayes formula:

$$\mathcal{P}(C_\ell^{th}(\boldsymbol{\theta})|C_\ell^{obs}) = \frac{\mathcal{P}(C_\ell^{obs}|C_\ell^{th}(\boldsymbol{\theta})) \times \mathcal{P}(\boldsymbol{\theta})}{\mathcal{P}(C_\ell^{obs})} \,. \tag{5.1}$$

The probability of the model given the data, *i.e.* the left-hand side of (5.1), is usually called the *posterior*. This is the function that we want to maximize and we use an MCMC method. The probability of the observations given the model, $\mathcal{P}(C_\ell^{obs}|C_\ell^{th}(\boldsymbol{\theta})$, is the likelihood $\mathcal{L}(\boldsymbol{\theta})$. This likelihood is usually considered as a function of the cosmological parameters while the data/fiducial power spectrum is fixed. The probability of the data $\mathcal{P}(C_\ell^{obs})$ is difficult to estimate in general. However, it is a constant w.r.t. the parameters $\boldsymbol{\theta}$ and is, therefore, a normalization factor. Finally, the probability of the cosmological parameters $\mathcal{P}(\boldsymbol{\theta})$ is called the *prior*. This prior does not contain data; it transcribes our *a priori* knowledge of the cosmological parameters. We consider sometimes flat priors on $\boldsymbol{\theta}$ between a maximum and a minimum value. This means that *a priori*, all values between the maximum and minimum values are equally probable. It is important to note that a flat prior does not mean that we have no “a priori” and that we are perfectly ignorant regarding the considered parameter. Indeed, considering all values equally probable is already injecting knowledge in the analysis and, more importantly, when we impose a flat prior on parameters, we do so on a specific parameterization. The prior is not invariant by changing the parameterization; for instance, if we consider the parameterization $\boldsymbol{\theta}$ and an alternative parametrization of the cosmological parameters $\boldsymbol{\varphi}(\boldsymbol{\theta})$, then the prior on the parameters $\boldsymbol{\varphi}$ can be expressed as:

$$\mathcal{P}(\boldsymbol{\varphi}) = \mathcal{P}(\boldsymbol{\theta}) \left| \frac{\partial \boldsymbol{\theta}}{\partial \boldsymbol{\varphi}} \right| \,. \tag{5.2}$$

In figure 5.1, we represent three equivalent priors on three different parameterizations. The blue curve is a simple flat prior between 0 and 1. By using (5.2), one finds that this is equivalent to imposing a prior $\propto 1/x$, the orange curve, on the parameter x^2 and $\propto x$ on the parameter $\sqrt{x}$, in green. Hence, the choice of prior is arbitrary and never “blind” so that comparing to a different analysis that uses different priors can be difficult. For instance, this will be the case when comparing the Planck bispectrum analysis result and ours.

However, depending on the situation, some parametrization may give more easily physically interpretable results than others, especially in the case where we do not have a significant detection. This problem will arise in the parameterization of the primordial power spectrum as we will discuss later. Finally, note that the likelihood is invariant by changing the parametrization.

5.1.2 Markov Chain Monte-Carlo

Once we have defined our likelihoods and our priors, we need an efficient method to maximize and sample the posterior function $\mathcal{P}(C_\ell^{th}(\boldsymbol{\theta})|C_\ell^{obs})$. In general, the posterior is

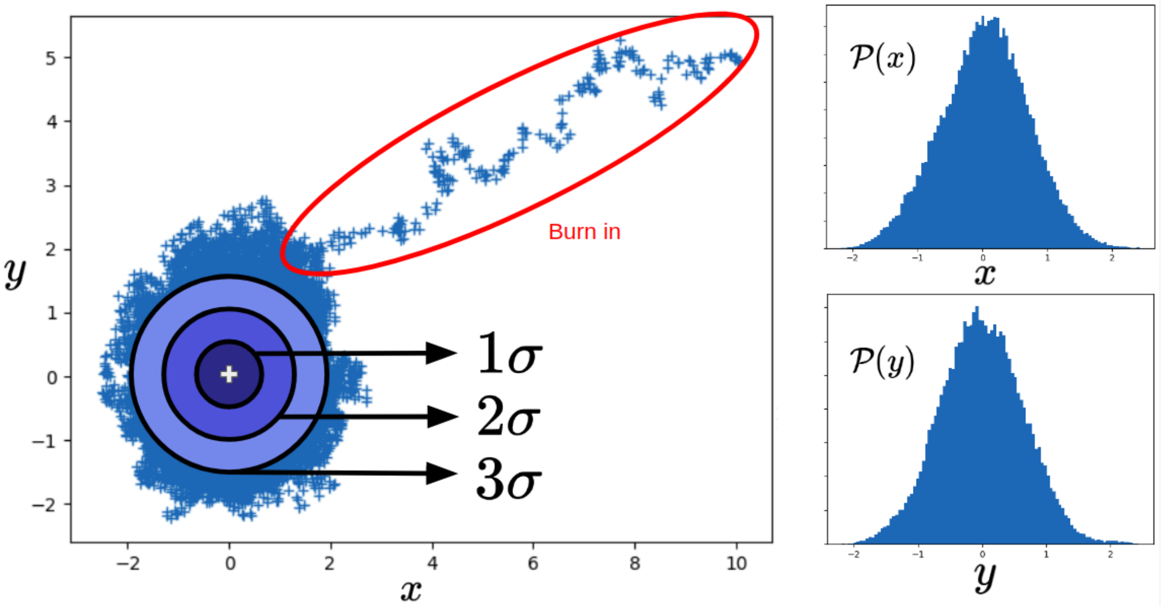

Figure 5.2: Chain obtained with an MCMC with a two-dimensional Gaussian as likelihood. The points surrounded in red are considered as the first phase of “burn-in” and are usually not considered. The white dot represents the maximum of the likelihood, *i.e.* also the point of maximum density. It is surrounded by 3 contours: the smallest representing the 1σ, the middle the 2σ, and the largest the 3σ contour. In the right panels, the marginalized PDF of the x and y parameters after having removed the burn-in.

a multi-dimensional function and cannot be maximized or sampled analytically. One of the most efficient methods to sample this kind of function is the so-called Markov Chain Monte-Carlo. More precisely, we will use a Metropolis-Hastings algorithm. It can be explained as follows:

- First of all, we define a starting point for the cosmological parameters $\boldsymbol{\theta_0}$ and we evaluate the posterior at this point $\mathcal{P}(\boldsymbol{\theta_0})$.
- We define an arbitrary probability density function $p(\boldsymbol{\theta})$ and we randomly pick, given $p(\boldsymbol{\theta})$, one new point in the parameter space $\boldsymbol{\theta_1}$. The posterior is evaluated: $\mathcal{P}(\boldsymbol{\theta_1})$ and we compute the ratio $\alpha = \mathcal{P}(\boldsymbol{\theta_1})/\mathcal{P}(\boldsymbol{\theta_0})$.
- We randomly pick another number u with a uniform PDF between 0 and 1.
- If $u \leq \alpha$: we “accept” the point $\boldsymbol{\theta_1}$ and we restart from the first step with the substitution $\mathcal{P}(\boldsymbol{\theta_0}) \to \mathcal{P}(\boldsymbol{\theta_1})$.
- If $u > \alpha$: we “reject” the point $\boldsymbol{\theta_1}$ and we restart from the first step by staying at the same point $\mathcal{P}(\boldsymbol{\theta_0})$.

This algorithm generates the list of accepted points, the so-called *chains*. One can show that, in theory, the density of these points, or their histogram, is proportional to the underlying posterior. It is important to note that in theory, after the burn-in phase that we will introduce below, the result of this algorithm is independent of the PDF $p(\boldsymbol{\theta})$ and on the starting point. However, the efficiency of the algorithm is strongly dependent on

$p(\boldsymbol{\theta})$ and on the initial point. One way to improve significantly the efficiency is to update $p(\boldsymbol{\theta})$ during the chain.

There are two different possibilities in this algorithm. If $\mathcal{P}(\boldsymbol{\theta_0}) < \mathcal{P}(\boldsymbol{\theta_1})$, the ratio α is larger than 1 and hence the point is always accepted. If we reject all the other points, the algorithm would never accept a point with a smaller probability. Such an algorithm would be efficient to find the point that maximizes the posterior.

If $\mathcal{P}(\boldsymbol{\theta_0}) > \mathcal{P}(\boldsymbol{\theta_1})$, there is still the possibility to accept the point. Let us picture the case were $\mathcal{P}(\boldsymbol{\theta_1})$ is smaller but close to $\mathcal{P}(\boldsymbol{\theta_0})$ which means that α is smaller but close to 1. In this case, it is very likely for the random number u to fall between 0 and α since $\alpha \sim 1$ and then it is very likely to accept the point. On the contrary, if $\mathcal{P}(\boldsymbol{\theta_0}) \gg \mathcal{P}(\boldsymbol{\theta_1})$, then $\alpha \sim 0$ and it is very unlikely for the random number to fall between 0 and $\alpha \sim 0$ and hence to accept the new point. Hence, we see intuitively that, in this case, the probability to accept a new point is exactly α. Hence, if we run the algorithm long enough, the density of points that will be accepted at a given place is proportional to the underlying posterior so that the posterior can be sampled.

In figure 5.2, we show a MCMC chain. We have used a two-dimensional Gaussian of the parameters x and y as likelihood. We made the common choice to use a Gaussian PDF centered on the current point for $p(x, y)$ and the starting point is $x_0 = 10$ and $y_0 = 5$. In the left panel, we observe two distinct regimes. The chain starts by a phase of so-called *burn in*, surround in red in figure 5.2. This is a phase during which the algorithm is not stabilized because it is still far away from the maximum. After, the burn-in, we say that the chain has *converged* and we start a new phase of sampling the function as described above. We see here that the burn-in should be ignored since it is not representative of the underlying posterior, unlike the second phase of sampling. In the right panels of figure 5.2, we show the marginalized PDF of each parameter, *i.e.* the histograms, after having ignored 1/3 of the chain to remove the burn-in phase. As we can see, it reproduces the Gaussian underlying posterior.

Once we have the chains, we can find the maximum value and the $n\sigma$ contours. For example, in the case of figure 5.2, the 1σ contour is the contour centered on the maximum that encompasses 68% of the points. In our case, the posterior has the same standard deviation along x and y, and the two parameters are uncorrelated. Thus, these contours are circles. If the standard deviations would be different, let us say σ_x and σ_y with $\sigma_y > \sigma_x$, the contours would be ellipses with semi-major and semi-minor corresponding to σ_y and σ_x respectively. A correlation between the parameters x and y would be translated into a rotated ellipse. The Gaussian approximation of the posterior is valid for all parameters in the ΛCDM model. However, in general, the behaviors of the posterior can be very complicated so that these contours can have complicated behavior and can even surround different regions.

Implementation

We modified the code `Cobaya`, [208], which includes the advanced MCMC sampler *CosmoMC* and allows to sample arbitrary priors and posteriors. We generate all the power spectra by calling `CAMB` [209, 210] twice in order to make linear combinations, because `CAMB` can only calculate the power spectra for total positive or negative correlation, *i.e.* $\cos\Delta = \pm 1$. If we call the totally correlated power spectrum $C_\ell^{\lambda_1\lambda_2,+}$ and the totally anti-correlated power spectrum $C_\ell^{\lambda_1\lambda_2,-}$, we can compute the power spectrum for the case of an arbitrary

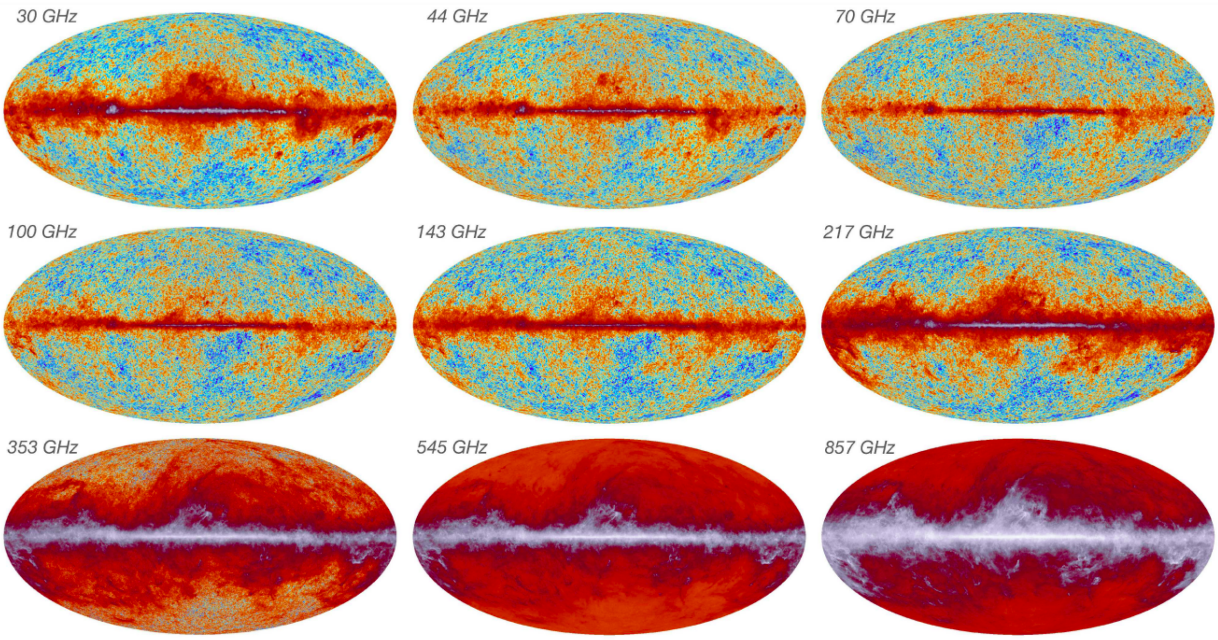

Figure 5.3: The nine Planck temperature maps, one for each frequency channel. The CMB is well observed on the frequencies 30 − 217Ghz. Taken from [150].

correlation as follows:

$$C_\ell^{\lambda_1\lambda_2} = \frac{1}{2}\left(C_\ell^{\lambda_1\lambda_2,+} + C_\ell^{\lambda_1\lambda_2,-} + \cos\Delta\left(C_\ell^{\lambda_1\lambda_2,+} - C_\ell^{\lambda_1\lambda_2,-}\right)\right). \tag{5.3}$$

Then `Cobaya`calls the relevant power spectrum likelihood. The chains obtained are analyzed using GetDist [211]. This is an advanced tool that allows us to plot the different marginalized PDF and two-dimensional contours in a very simple way.

5.2 Planck power spectrum constraints

5.2.1 Parametrization

The usual parametrization for a purely adiabatic primordial power spectrum has been given in (3.36). It uses one amplitude A_s defined at a given pivot scale k_0, usually $0.05\ \mathrm{Mpc}^{-1}$. As already mentioned in section 3.1, Planck has provided a strong detection of the adiabatic mode: $n_s = 0.9652 \pm 0.0042$ and $\ln 10^{10} A_s = 3.043 \pm 0.014$ [66].

Given the strong evidence of adiabatic mode domination and to keep a low number of parameters to estimate, we consider only a single isocurvature mode in addition to the adiabatic one. For isocurvature modes, the primordial power spectra are modeled as power laws with the amplitudes fixed at two pivot scales k_1 and k_2 [121, 212]:

$$P^{IJ}(k) = \exp\left(\frac{\ln(k) - \ln(k_2)}{\ln(k_1) - \ln(k_2)} \ln\left(P_{IJ}^{(1)}\right) + \frac{\ln(k) - \ln(k_1)}{\ln(k_2) - \ln(k_1)} \ln\left(P_{IJ}^{(2)}\right)\right), \tag{5.4}$$

where I and $J \in [\zeta, S]$ where ζ is defined in (2.37) and S in (4.58) for the density isocurvature modes and in (4.62) for the velocity isocurvature modes. The quantities $P_{IJ}^{(1)}$ and $P_{IJ}^{(2)}$ are the amplitudes at the two pivot scales. They are chosen to cover most of the observable range of Planck: $k_1 = 0.002$ Mpc^{-1} and $k_2 = 0.1$ Mpc^{-1}. As explained in 5.1, the choice of the parametrization is related to the question of priors. Indeed, a change of parametrization, *i.e.* a change of the parameters on which we apply a flat prior, changes the posterior distribution. Applying a flat prior to the usual amplitudes and spectral indices is not equivalent to applying a flat prior to $P^{(1)}_{IJ}$ and $P^{(2)}_{IJ}$. The usual approach with amplitudes and spectral indices as free parameters produces a strongly prior-dependent posterior for the isocurvature modes, especially if the isocurvature spectral index is free, given the absence of a significant detection. The resulting contours are then difficult to interpret as explained in [213]. Unless specified differently, we will always apply flat priors to $P^{(1)}_{\zeta\zeta}$, $P^{(2)}_{\zeta\zeta}$, $P^{(1)}_{\zeta S}$ and $P^{(1)}_{SS}$. The link between A^{IJ}, n_s^{IJ} and $P^{(1)}_{IJ}, P^{(2)}_{IJ}$ is straightforward:

$$
\begin{aligned}
A_s^{IJ} =& \exp\left(\frac{(\ln P^{(1)}_{IJ} - \ln P^{(2)}_{IJ})\ln k_0 + \ln P^{(1)}_{IJ}\ln k_1 - \ln P^{(2)}_{IJ}\ln k_2}{\ln k_1 - \ln k_2}\right), \\
n_s^{IJ} =& \frac{\ln P^{(1)}_{IJ} - \ln P^{(2)}_{IJ}}{\ln k_1 - \ln k_2} + 1\,.
\end{aligned} \tag{5.5}
$$

The cross-correlation amplitude is constrained by the Schwarz inequality [98], which means that

$$
\left(P^{\zeta S}(k)\right)^2 \leq P^{SS}(k) P^{\zeta\zeta}(k)\,. \tag{5.6}
$$

In order for the condition (5.6) to be true for all k, the slope of the cross-power spectrum should be fixed, and then one of the two amplitudes $[P^{(1)}_{\zeta S}, P^{(2)}_{\zeta SJ}]$ is a derived parameter. It gives

$$
n_s^{\zeta S} = \frac{1}{2}(n_s^{\zeta\zeta} + n_s^{SS}), \qquad P^{(2)}_{\zeta S} = P^{(1)}_{\zeta S}\left(\frac{P^{(2)}_{\zeta\zeta}P^{(2)}_{SS}}{P^{(1)}_{\zeta\zeta}P^{(1)}_{SS}}\right)^{1/2}\,. \tag{5.7}
$$

In practice we choose the prior of $\mathcal{P}^{(1)}_{\zeta S}$ to be such that the second equation of (5.7) can be satisfied. It is convenient to define two parameters also used in [121, 212]:

$$
\beta^{(i)}_{\text{iso}} = \frac{P^{(i)}_{SS}}{P^{(i)}_{\zeta\zeta} + P^{(i)}_{SS}}, \qquad \cos\Delta = \frac{P^{(i)}_{\zeta S}}{\sqrt{P^{(i)}_{\zeta\zeta}P^{(i)}_{SS}}}\,. \tag{5.8}
$$

The first parameter measures the relative amplitude of the isocurvature mode w.r.t. the adiabatic mode. Note that it is scale-dependent, *i.e.* it depends on the choice of the pivot scale (i). The second parameter measures the correlation between the adiabatic mode and the considered isocurvature mode. Thanks to (5.7), it is scale-independent which explains why the choice of the pivot scale, denoted by (i), does not matter (otherwise we would have to write $\cos\Delta^{(i)}$).

Since the bispectrum parametrization with a free isocurvature spectral index would have too many parameters to be constrained in the near future, we are interested in the cases where $n_s^{SS} = n_s^{\zeta\zeta} = n_s^{\zeta S} = n_s$, which is for example motivated by the curvaton scenario. This restriction imposes:

$$
P^{(2)}_{SS} = \frac{P^{(2)}_{\zeta\zeta}}{P^{(1)}_{\zeta\zeta}}P^{(1)}_{SS}, \qquad P^{(2)}_{\zeta S} = \frac{P^{(2)}_{\zeta\zeta}}{P^{(1)}_{\zeta\zeta}}P^{(1)}_{\zeta S}\,. \tag{5.9}
$$

In this case, β_{iso} defined in equation (5.8) becomes scale independent so that we do not note the index (i) anymore.

Once we have the primordial power spectra in (5.4), we can relate them to the CMB power spectrum, as explained in detail in section 4.2, thanks to the transfer functions. We gave some elements about how to compute them in section 4.3.

Using equations (4.29) and (2.123), the theoretical total angular power spectrum of the CMB is given by:

$$C_\ell^{th,\lambda_1\lambda_2} = A_s^{\zeta\zeta}\left(\bar{C}_\ell^{\lambda_1\lambda_2,\zeta\zeta} + \alpha\,\bar{C}_\ell^{\lambda_1\lambda_2,SS} + 2\cos\Delta\sqrt{\alpha}\,\bar{C}_\ell^{\lambda_1\lambda_2,\zeta S}\right)\,, \tag{5.10}$$

where $\bar{C}_\ell$ are the normalized power spectra with $A_s^{IJ} = 1$. For simplicity we have used here the usual parameters A_s^{IJ} which are the amplitudes of the primordial power spectra at $k_0 = 0.05$ Mpc^{-1}. We have also introduced $\alpha \equiv \beta_{\rm iso}/(1-\beta_{\rm iso})$. We will always use α in the theoretical part because expressions are more compact. But in the analyses, we will use $\beta_{\rm iso}$ so that we can compare our results with the Planck collaboration analysis. Remember that in the section 3.2, we have shown that α and $\cos\Delta$ are directly related to inflation by the functions $T_{\mathcal{R}S}$ and T_{SS} defined in equations (3.68), see also (3.70). Hence constraining these parameters is equivalent to constraining the multi-field inflation transfer functions.

5.2.2 Power spectrum

The Planck satellite was launched in 2009 and worked until 2013. It has provided a cosmic variance limited measurement of the temperature power spectrum from $\ell = 2$ to $\ell \simeq 2000$ and the best measurement of the full-sky E-mode polarization so far. It was composed of two instruments: the low-frequency instrument (LFI) and the high-frequency instrument (HFI) observing the sky on 9 different frequency bands. They can be seen in figure 5.3.

The measurement of the power spectrum is split into low-ℓ ($\ell < 30$) and high-ℓ multipoles ($\ell > 30$). As we will see, only the high-ℓ power spectra are used in the likelihood analysis. Their measurement are based on a pseudo-power spectrum estimator given the equation (4.24), see for example [214]. Basically, instead of the pure CMB signal $a_{\ell m}$, they use the sky signal which includes the Milky-Way mask, point sources mask, beam and noise. Note that the CMB is dominant for frequencies around 100 GHz. This can be seen by looking at the maps in figure 5.3; for the three large frequencies, for example, the foregrounds emission are dominant. The other contributions are reviewed in section 4.3.3. The intrinsic CMB signal can be corrected from the contamination by fitting the different frequency dependencies for each source. This is the component separation. Very accurate modeling of the instrumental and astrophysics have been performed to measure the power spectra that are shown in figure 5.4 [108]. In the case of lensing power spectrum that we can see in the last panel of figure 5.4, the combination of all the estimators briefly described in section 4.3.3 has been used [173].

5.2.3 Likelihood

The Planck 2018 likelihood is described in [108]. This likelihood combines two parts covering two different multipoles ℓ ranges. The low-ℓ part contains multipoles lower than 30, and a pixel-based likelihood is used to account for the non-stationarity of the signal and noise. This likelihood assumes Gaussian statistics for the maps, which means that its expression can be written as:

$$\mathcal{L}(C_\ell) = \mathcal{P}(\mathbf{m} \mid C_\ell) = \frac{1}{2\pi|M|^{1/2}}\exp\left(-\frac{1}{2}\mathbf{m}^{\mathbf{T}}M^{-1}\mathbf{m}\right)\,, \tag{5.11}$$

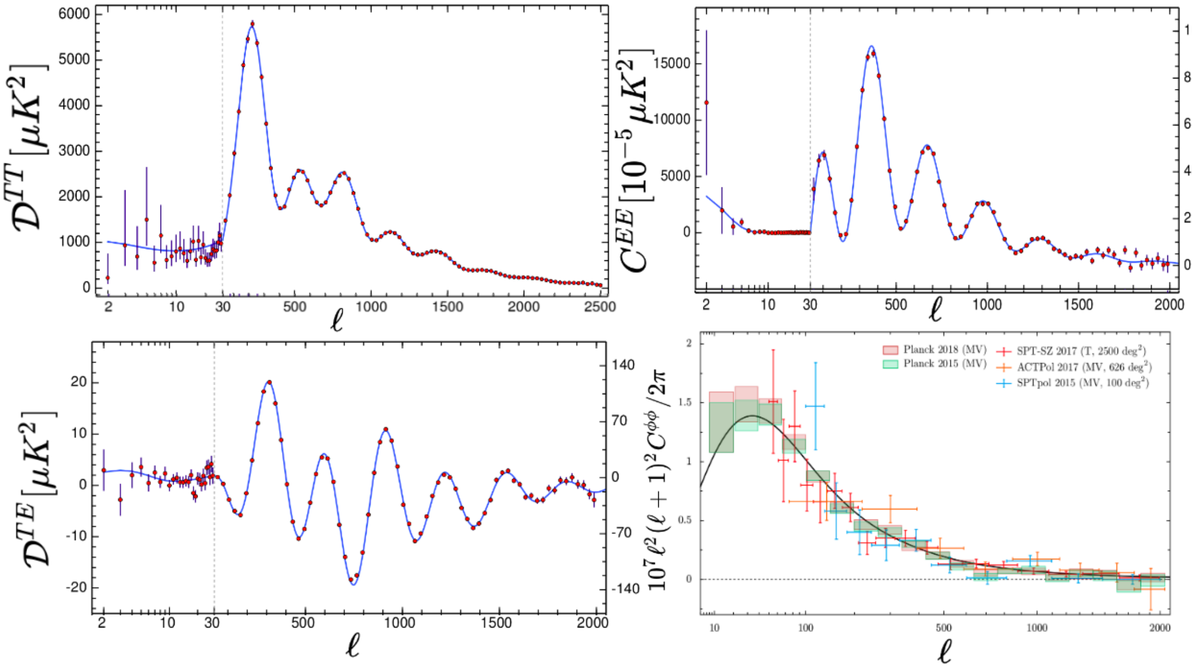

Figure 5.4: Planck power spectra of the CMB based on the 9 maps shown in figure (5.3). On the first three plots, the red points are the power spectra measurement by Planck. The blue curve is the best fit cosmological standard model ΛCDM. In reading order, the plots are respectively the temperature (T) power spectrum, the E-mode polarization (E) power spectrum and the cross-power spectrum TE [108]. The last plot is the lensing power spectrum. In red and green are shown the measured power spectra by Planck following the 2015 and 2018 releases. It also contains the lensing power spectrum measurement of other ground experiments: SPT and Actpol, see [173] for more details.

where $\mathbf{m}$ represents the data vector after the component separation and masking while M is the covariance matrix (of dimension: number of pixels squared × number of maps squared) which contains the CMB and the noise covariance matrices. The CMB covariance matrix depends on the theoretical power spectrum C_ℓ^{th}.

At high ℓ the accurate calculation of the pixel covariance matrix is impossible. The likelihood for $\ell \geq 30$ can be approximated assuming Gaussian statistics of the power spectra since each of the power spectrum amplitudes is estimated with a large number of modes.

$$-\ln \mathcal{L}(\tilde{\mathbf{C}}^{\mathbf{obs}} \mid \tilde{\mathbf{C}}^{\mathbf{th}}(\theta)) = \frac{1}{2}\left[\tilde{\mathbf{C}}^{\mathbf{obs}} - \tilde{\mathbf{C}}^{\mathbf{th}}(\theta)\right]^T \Sigma^{-1}\left[\tilde{\mathbf{C}}^{\mathbf{obs}} - \tilde{\mathbf{C}}^{\mathbf{th}}(\theta)\right] + const\,, \tag{5.12}$$

where $\tilde{\mathbf{C}}^{\mathbf{th}}(\theta)$ is the theoretical power spectrum matrix, with elements (TT,EE,TE) for different frequencies. The theoretical power spectra depend on the cosmological parameters θ that we have to specify. We denote with a tilde the fact that the power spectra include also the foregrounds, the noise and the beam. The matrix Σ is the covariance matrix, we refer to [215] for its expression and derivation. The total number of estimated parameters, taking into account all nuisance parameters, is 27.

We will also use the lensing term as in the Planck 2018 likelihood, see [173]. The Planck collaboration used the quadratic estimator developed by [174] to reconstruct the lensing field from the statistical anisotropies of the temperature and polarization fields.

		CDM density	ν density	ν velocity
n_s^{SS} free	β_{iso}	$[0.01, 0.26]$	$[0.03, 0.17]$	$[0.01, 0.08]$
$\cos\Delta$ free	$\cos\Delta$	$[-0.12, 0.15]$	$[-0.13, 0.08]$	$[-0.20, 0.00]$
$n_s^{SS} = n_s^{\zeta\zeta}$	β_{iso}	0.039	0.089	0.058
$\cos\Delta$ free	$\cos\Delta$	$[-0.41, 0.31]$	$[-0.18, 0.19]$	$[-0.25, 0.06]$
$n_s^{SS} = n_s^{\zeta\zeta}$	β_{iso}	0.001		
$\cos\Delta = 1$	$\cos\Delta$	1	1	1
$n_s^{SS} = n_s^{\zeta\zeta}$	β_{iso}	0.001		
$\cos\Delta = -1$	$\cos\Delta$	-1	-1	-1

Table 5.1: We give in this table for each isocurvature mode the 95% CL or upper bounds of β_{iso} and $\cos\Delta$ for different models given the Planck results [121]. On the first line, the general model constraints with all parameter free. Remember that in this case, the amplitude β_{iso} given in (5.8) is scale dependent. Hence we only report the amplitude at the pivot scale 0.05Mpc^{-1}. In the second line, we report the constraints for the most general model of interest in this thesis, *i.e.* $n_s^{SS} = n_s^{\zeta\zeta}$ and $\cos\Delta$ free. In this case, the constraints are only given for CDM density, we provide the two others [121]. Finally, on the two last lines, we report the constraints for the curvaton scenario, where the correlation is $\cos\Delta = \pm 1$. For this last case, the constraints for the neutrino isocurvature modes are not given.

Then, they estimated the lensing power spectrum from the connected part of the CMB trispectrum, see section (2.5.1) and section 4.3.3. The lensing likelihood is assumed to be Gaussian with respect to the power spectrum.

In the table 5.1, we give the constraints given by the Planck 2018 likelihood on the isocurvature parameters (5.8) for different models [121]. The theoretical power spectrum used is given in 5.10. The constraints for the model where $n_s^{SS} = n_s^{\zeta\zeta}$ and where $\cos\Delta$ is free are not provided by [121] in the case of the neutrino modes. By performing the same analysis and using the same likelihood, we have estimated these constraints. More details will be given in section 5.1.

In the case of the most general model where both n_s^{SS} and $\cos\Delta$ are free, we see that an isocurvature component of order 10% for the neutrino velocity mode and 25% for the CDM isocurvature mode are still compatible with the data at 2σ. For this general model, a vanishing isocurvature component is even excluded at more than 95% CL for all isocurvature modes. For the curvaton model that is of particular interest for us, the constraints are larger allowing an isocurvature component $\sim$ 4% to 8%. The model with 100% (anti)correlation has the largest constraints with only 0.1% allowed a 95% CL.

5.3 Planck bispectrum constraints

5.3.1 Parametrization

The usual parametrization of the bispectrum is a normalized theoretical template $\hat{B}^{\text{t}}$ times an amplitude $\tilde{f}_{\text{NL}}^{t}$:

$$B^{\text{t}} = \tilde{f}_{\text{NL}}^{\text{t}} \hat{B}^{\text{t}} , \tag{5.13}$$

where the subscript t means "local", "equilateral" of "orthogonal". The definition of $\tilde{f}_{\text{NL}}^{t}$ is given in (2.129). Examples of these templates are the "local", "equilateral" and "orthogonal" defined in (2.133), (2.135) and (2.137). By injecting equation (5.13) into equation (4.37), we see that the factor $\tilde{f}_{\rm NL}^{\rm t}$ can be factored. The normalized CMB template is therefore given by

$$\hat{B}^{\lambda_1\lambda_2\lambda_3,t}_{\ell_1\ell_2\ell_3} = h^2_{\ell_1\ell_2\ell_3}\left(\frac{2}{\pi}\right)^3 \int r^2 dr \left(\prod_{i=1}^{3} dk_i\, k_i^2 j_{\ell_i}(k_i r)\mathcal{T}^{(1)}_{\lambda_i,\ell_i}(k_i)\right) \hat{B}^t(k_1,k_2,k_3)\,. \tag{5.14}$$

We recall here that the indices λ_i stand for the temperature and polarization.

Following [113], if we include isocurvature perturbations, we can assume a generalized local shape for the primordial bispectrum. This choice is theoretically justified by the fact that, as explained in section (3.2), multi-field inflation models generate isocurvature modes and non-Gaussianities of the local shape. Here, we consider one isocurvature mode in addition to the adiabatic mode (otherwise there would be too many free parameters and no meaningful constraints could be obtained). To understand the construction of the generalized local shape, note that equation (2.140) is invariant under exchange of the momenta k_i only if $I = J = K$, where we recall that $(I,J,K) \in [\zeta, S]$. For this reason, in the adiabatic case, one has only one $\tilde{f}_{\rm NL}^{\rm local}$ that can be factorized, see equation (2.133). In general, the expression (2.140) is invariant by the simultaneous exchange of two modes, *e.g.* (I and J), and the corresponding momenta (k_1 and k_2). Therefore, the primordial bispectra, for each tuple of IJK, can be expressed as the sum [113]:

$$B^{IJK}(k_1,k_2,k_3) = \tilde{f}_{\rm NL}^{I,JK} P_{\zeta,2}P_{\zeta,3} + \tilde{f}_{\rm NL}^{J,KI} P_{\zeta,1}P_{\zeta,3} + \tilde{f}_{\rm NL}^{K,IJ} P_{\zeta,1}P_{\zeta,2}\,, \tag{5.15}$$

where we recall that we have assumed that all spectral indices are equal and that the notation $P_{\zeta,i}$ means $P_\zeta(k_i)$. The symmetry of (2.140) should also be satisfied in (5.15) which imposes that

$$\tilde{f}_{\rm NL}^{I,JK} = \tilde{f}_{\rm NL}^{I,KJ}\,. \tag{5.16}$$

To mark this symmetry, we use a comma to note that the order of the two last indices does not matter. Finally, note that we have dropped the specifications "local" since for isocurvature modes, we will always use a local shape.

Equivalently to (5.13), we want to define a local isocurvature template $\hat{B}^{IJK}$. If we substitute equation (5.15) into equation (2.141), the sum can be distributed over each of the three terms of (5.15). The indices IJK are dummy variables so that they can be renamed in order to have the same $\tilde{f}_{\rm NL}^{I,JK}$ as a factor of each term of the sum. Finally, equation (2.141) can be rewritten as

$$B^{tot}_{\lambda_1\lambda_2\lambda_3}(\tau,k_1,k_2,k_3) = \sum_{IJK} \tilde{f}_{\rm NL}^{I,JK} \hat{B}^{IJK}_{\lambda_1\lambda_2\lambda_3}(\tau,k_1,k_2,k_3)\,, \tag{5.17}$$

where

$$\hat{B}^{IJK}_{\lambda_1\lambda_2\lambda_3} = \left(\mathcal{T}^{(1),IJK}_{\lambda_1\lambda_2\lambda_3}P_{23} + \mathcal{T}^{(1),JIK}_{\lambda_1\lambda_2\lambda_3}P_{13} + \mathcal{T}^{(1),KJI}_{\lambda_1\lambda_2\lambda_3}P_{12}\right)\,, \tag{5.18}$$

and where for compactness, we have defined

$$P_{23} = P_{\zeta,2}P_{\zeta,3}, \quad \mathcal{T}^{(1),IJK}_{\lambda_1\lambda_2\lambda_3} = \mathcal{T}^{(1)}_{I,\lambda_1}(\tau,k_1)\mathcal{T}^{(1)}_{J,\lambda_2}(\tau,k_2)\mathcal{T}^{(1)}_{K,\lambda_3}(\tau,k_3)\,. \tag{5.19}$$

We see in equation (5.17) how the $\tilde{f}_{\rm NL}$ factorize and how they can be interpreted as the amplitudes of each normalized bispectrum. To finish, by using (4.28), we can substitute equation (5.17) into (4.37) which gives the CMB bispectrum template $\hat{B}^{\lambda_1\lambda_2\lambda_3,IJK}_{\ell_1\ell_2\ell_3}$. It can be written in a compact form [113]:

$$\hat{B}^{\lambda_1\lambda_2\lambda_3,IJK}_{\ell_1\ell_2\ell_3} = 3h^2_{\ell_1\ell_2\ell_3}\left(\frac{2}{\pi}\right)^3 \int r^2 dr \mathcal{A}^I_{(\ell_1}(r)\mathcal{B}^J_{\ell_2}(r)\mathcal{B}^K_{\ell_3)}(r)\,, \tag{5.20}$$

where we use the notation $(\ell_1\ell_2\ell_3) = (\ell_1\ell_2\ell_3 + 5\text{perms})/3!$ and where

$$\mathcal{A}^I_\ell(r) = \int dk k^2 j_\ell(kr)\mathcal{T}^{(1)}_{\lambda,\ell}(k), \qquad \mathcal{B}^I_\ell(r) = \int dk k^2 j_\ell(kr)\mathcal{T}^{(1)}_{\lambda,\ell}(k)P_\zeta(k)\,. \tag{5.21}$$

Similarly to (5.17), the template $\hat{B}^{\lambda_1\lambda_2\lambda_3,IJK}_{\ell_1\ell_2\ell_3}$ can be considered as the normalized CMB bispectrum so that the total bispectrum reads:

$$B^{\lambda_1\lambda_2\lambda_3,tot}_{\ell_1\ell_2\ell_3} = \sum_{IJK} \tilde{f}^{I,JK}_{\text{NL}}\, \hat{B}^{\lambda_1\lambda_2\lambda_3,IJK}_{\ell_1\ell_2\ell_3}\,. \tag{5.22}$$

There are six different $\tilde{f}_{\text{NL}}$ (and not eight) because of the symmetry of the local shape, *i.e.* equation (5.16). The total angular bispectrum is a function of these six $\tilde{f}_{\text{NL}}$ parameters, of the $A^{\zeta\zeta}_s$ and n_s through the primordial power spectra and of the cosmological parameters through the transfer functions: the current baryon and CDM densities Ω_b, Ω_c, the sound horizon at recombination θ_{MC} and the re-ionization optical depth τ_{reio}. In the rest of this thesis we will denote the cosmological parameters $(\Omega_b, \Omega_c, \theta_{MC}, A^{\zeta\zeta}_s, n_s, \tau_{reio})$ as $\boldsymbol{\theta}$. The other power spectrum amplitudes A^{SS}_s and $A^{S\zeta}_s$ do not appear in the definition of $\hat{B}^{IJK}$ and therefore only play a role in the power spectrum parameterization (5.10).

5.3.2 Binned bispectrum estimator

It is impossible to calculate the full bispectrum for each multipole combination ℓ_1, ℓ_2, and ℓ_3 because of the high cost of the operation. Thus we use the binned bispectrum estimator [157, 216] in which we average the bispectrum over ranges of ℓ. This operation is feasible because the theoretical bispectra we are looking for have features typically on the scale of the acoustic peaks. The information we lose, $\sim 1\%$ with a very limited number of bins ~ 50, is very small and provides a huge gain in calculation time and memory. We change the indices ℓ to i to express this binning, *i.e.* $B_{i_1i_2i_3}$ is the averaged value of the bispectrum over the intervals labeled i_1, i_2, i_3 of ℓ_1, ℓ_2, ℓ_3 values. We use a matched filter to estimate the amplitude of specific theoretical shapes in the observed bispectrum, see (5.22).

First, let us define the filtered map $M^\lambda_i(\boldsymbol{\Omega})$ of the field λ:

$$M^\lambda_i(\boldsymbol{\Omega}) = \sum_{\ell\in\Delta_i}\sum_{m=-\ell}^{\ell} a^\lambda_{\ell m} Y_{\ell m}(\boldsymbol{\Omega})\,, \tag{5.23}$$

where Δ_i is a given bin in multipole space and $a^\lambda_{\ell m}$ is the pure CMB signal. One can compute the observed binned angle-averaged bispectrum (4.35) with the following integral:

$$B^{\lambda_1\lambda_2\lambda_3,\text{obs}}_{i_1i_2i_3} = \frac{1}{\Xi_{i_1i_2i_3}} \int \mathrm{d}\boldsymbol{\Omega}\; M^{\lambda_1}_{i_1}(\boldsymbol{\Omega})M^{\lambda_2}_{i_2}(\boldsymbol{\Omega})M^{\lambda_3}_{i_3}(\boldsymbol{\Omega})\,, \tag{5.24}$$

where $\Xi_{i_1i_2i_3}$ is the number of valid ℓ-triplets in the bin-triplet $(i_1i_2i_3)$. Note that, if all bins contain only one ℓ, equation (5.24) matches exactly the angle averaged bispectrum defined in (4.35).

The estimator (5.24) is nearly optimal only for rotationally invariant maps. However, for real observations, rotational invariance is broken because of the mask and the non-uniform noise. We can restore the optimality of the estimator by subtracting a “linear term” (linear in $a_{\ell m}$) from the observed bispectrum [217, 218]:

$$B^{\lambda_1\lambda_2\lambda_3,\mathrm{obs}}_{i_1i_2i_3} \to B^{\lambda_1\lambda_2\lambda_3,\mathrm{obs}}_{i_1i_2i_3} - B^{\lambda_1\lambda_2\lambda_3,\mathrm{lin}}_{i_1i_2i_3} \,. \tag{5.25}$$

Moreover, in addition to the mask, one needs to account for the instrumental beam and noise. Taking these into account, the real observed bispectrum becomes $\tilde{B}$ (with a tilde) by the instrument is:

$$\tilde{B}^{\lambda_1\lambda_2\lambda_3,\mathrm{X}}_{i_1i_2i_3} = b^{\lambda_1}_{i_1} b^{\lambda_1}_{i_2} b^{\lambda_3}_{i_3} B^{\lambda_1\lambda_2\lambda_3,\mathrm{X}}_{i_1i_2i_3} + n^{\lambda_1\lambda_2\lambda_3}_{i_1i_2i_3} \,, \tag{5.26}$$

where n is the bispectrum noise with variance $\propto C_{\ell_1}C_{\ell_2}C_{\ell_3}$, the subscribe X stands here for “obs”. This equation (5.26) will also be used for $X = th$, *i.e.* the theoretical bispectra template of equations (5.13) and (5.22). The beam function b_ℓ is typically a Gaussian function characterized by the full width at half maximum FWHM θ_{FWHM}:

$$b_\ell = w_\ell \exp\left(-\frac{\ell(\ell+1)}{16\ln 2}\theta^2_{FWHM}\right) , \tag{5.27}$$

where w_ℓ is a window function which takes into account the pixelization of the map.

The covariance of the bispectrum can be shown to be diagonal [157]. It results:

$$V^{\lambda_{1:6}}_{\ell_1\ell_2\ell_3} = \left\langle \tilde{B}^{\lambda_1\lambda_2\lambda_3}_{\ell_1\ell_2\ell_3} \tilde{B}^{\lambda_4\lambda_5\lambda_6}_{\ell_1\ell_2\ell_3} \right\rangle - \left\langle \tilde{B}^{\lambda_1\lambda_2\lambda_3}_{\ell_1\ell_2\ell_3} \right\rangle \left\langle \tilde{B}^{\lambda_4\lambda_5\lambda_6}_{\ell_1\ell_2\ell_3} \right\rangle \,, \tag{5.28}$$

where we mean by $\lambda_{1:6}$ the compact form of $\lambda_1\lambda_2\lambda_3\lambda_4\lambda_5\lambda_6$. In the weak non-Gaussianity approximation, one can neglect $\langle B^{\lambda_1\lambda_2\lambda_3}_{\ell_1\ell_2\ell_3} \rangle$. By using equation (4.35), (4.31), the Wick theorem and by binning the variance, one can show that the variance takes the form [157]

$$V^{\lambda_{1:6}}_{i_1i_2i_3} = \frac{g_{i_1i_2i_3}}{\Xi^2_{i_1i_2i_3}} \sum_{\ell_1\in\Delta_1} \sum_{\ell_2\in\Delta_2} \sum_{\ell_3\in\Delta_3} h^2_{\ell_1\ell_2\ell_3} \tilde{C}^{\lambda_1\lambda_2}_{\ell_1} \tilde{C}^{\lambda_3\lambda_4}_{\ell_2} \tilde{C}^{\lambda_5\lambda_6}_{\ell_3} \,, \tag{5.29}$$

where $g_{i_1i_2i_3} \in [6, 2, 1]$ depending on whether 3, 2, or no i’s are equal, respectively. Similarly to equation (5.26), we have used the $\tilde{C}^{\lambda_3\lambda_4}_{\ell_2}$ power spectra defined as:

$$\tilde{C}^{\lambda_1\lambda_2}_i = \left(b^{\lambda_1\lambda_2}_i\right)^2 C^{\lambda_1\lambda_2}_i + n^{\lambda_1\lambda_2}_i \,, \tag{5.30}$$

where $C^{\lambda_1\lambda_2}$ are the best estimated power spectra, *i.e.* the blue curves in figure 5.4.

5.3.3 Bispectrum likelihood

It is useful to generalize the inner product that we used in equation (2.131):

$$B \cdot B' = \sum_{i_1\le i_2\le i_3} \sum_{\lambda_{1:6}} B^{\lambda_1\lambda_2\lambda_3}_{i_1i_2i_3} \left(V^{-1}\right)^{\lambda_{1:6}}_{i_1i_2i_3} B'^{\lambda_4\lambda_5\lambda_6}_{i_1i_2i_3} \,. \tag{5.31}$$

At first order, the bispectrum can be considered as following a Gaussian distribution so that we can write the χ^2 as [112, 113] :

$$\chi^2 = \left(\tilde{B}^{obs} - \tilde{B}^{th}\right) \cdot \left(\tilde{B}^{obs} - \tilde{B}^{th}\right) \tag{5.32}$$

		$\zeta,\zeta\zeta$	$\zeta,\zeta S$	ζ,SS	$S,\zeta\zeta$	$S,\zeta S$	S,SS
CDM	$\tilde{\mathbf{f}}^{\mathbf{0}}_{\mathrm{NL}}$	-4.8	5.6	413	-345	-228	256
	$\Delta\tilde{\mathbf{f}}_{\mathrm{NL}}$	12	8	207	181	221	162
ν density	$\tilde{\mathbf{f}}^{\mathbf{0}}_{\mathrm{NL}}$	64	-64	547	-158	-420	800
	$\Delta\tilde{\mathbf{f}}_{\mathrm{NL}}$	34	43	224	176	289	389
ν velocity	$\tilde{\mathbf{f}}^{\mathbf{0}}_{\mathrm{NL}}$	-2.4	-100	280	133	-28	-15
	$\Delta\tilde{\mathbf{f}}_{\mathrm{NL}}$	29	34	118	93	91	113

Table 5.2: We give in this table for each isocurvature mode the best estimated value $\tilde{f}^{0}_{\mathrm{NL}}$ stored in the vector $\tilde{\mathbf{f}}^{0}_{\mathrm{NL}}$ given the Planck results [107] as well as the associated standard deviation $\Delta\tilde{f}_{\mathrm{NL}}$ stored in $\Delta\tilde{\mathbf{f}}_{\mathrm{NL}}$.

where B^{obs} is the observed bispectrum defined in (5.24), B^{th} is one theoretical template, for instance (5.13) for the adiabatic local, equilateral and orthogonal shapes and equation (5.22) for the local shape generalized to isocurvature modes. The tildes stand for the fact that the bispectra include the noise and the instrumental beam following equation (5.26). The estimator of the $\tilde{f}_{\mathrm{NL}}$ can then be obtained by minimizing (5.32). Hence, we can construct the following estimator for the $\tilde{f}^{(i)}_{NL}$ bispectra amplitude parameters:

$$\tilde{f}^{(i),0}_{\mathrm{NL}} = \sum_{(j)} (\mathbf{F}^{-1})_{ij} \left(\hat{\tilde{B}}^{(j)} \cdot \tilde{B}^{\mathrm{obs}} \right) . \tag{5.33}$$

where (i) and (j) label the theoretical shape, *i.e.* "local", "equilateral", "orthogonal" or any of the six combinations $(\zeta,\zeta\zeta)$, $(\zeta,\zeta S)$, (ζ,SS), $(S,\zeta\zeta)$, $(S,\zeta S)$ or (S,SS) and where we have defined the Fisher matrix $\mathbf{F}$ with components [113, 157]:

$$F_{ij} = \hat{\tilde{B}}^{(i)} \cdot \hat{\tilde{B}}^{(j)} , \tag{5.34}$$

In principle, the theoretical bispectrum is a function of all the cosmological parameters and of the six different isocurvature $\tilde{\mathbf{f}}_{\mathrm{NL}}$. However, as shown in [219], the statistical estimation of the cosmological parameters $\boldsymbol{\theta}$ would have a significant impact on the $\tilde{\mathbf{f}}_{\mathrm{NL}}$ error bars only if the detected $\tilde{\mathbf{f}}_{\mathrm{NL}}$ would have large signal-to-noise, equivalent to the signal-to-noise of the cosmological parameters. This is why we fix $\boldsymbol{\theta}$ to the best-estimated values determined from the power spectra alone in the Planck 2018 analysis [66], $\boldsymbol{\theta}^0$, so that the theoretical bispectrum is now only a function of the $\tilde{\mathbf{f}}_{\mathrm{NL}}$, even if we allow $\boldsymbol{\theta}$ to vary for the power spectrum in our joint analysis.

The constraints of the three primordial shapes described in section 2.5.4 summarized in table 2.2 have been produced by using the binned bispectrum estimator. As we can see from these constraints, no evidence of PNG is observed. In the table 5.2, we give the constraints on the isocurvature bispectrum amplitudes $\tilde{\mathbf{f}}_{\mathrm{NL}}$ [107]. These constraints are independent of the constraints of the power spectrum parameters given in table 5.1. The joint analysis aims to merge these two pieces of information to improve the constraints on fundamental parameters. For this, we need to establish a link between the power spectrum and the bispectrum parameters with the help of a generic model of two-field inflation.

5.3.4 Two-field model: link between parameters

To perform a joint analysis, we assume a model with two scalar fields acting during inflation: ϕ and σ. This model is crucial for our analysis because it provides the link between what is measured in the bispectrum, see table 5.2 and in the power spectrum, see table 5.1. Without such a theoretical link there would be no point in a joint analysis. We want the model to be as general as possible, so that our analysis applies to as broad a class of models as possible, while at the same time we must restrict the number of additional free parameters to just a few to get any meaningful constraints. In the most general non-Gaussian two-field model, up to second order in cosmological perturbation theory, we would have 10 parameters to constrain. This would be too much to obtain meaningful results given the current experimental constraints. To reduce the number of parameters, we make the following two assumptions (similar to the model in the final section of [113]): we suppose that the isocurvature mode is dominated by the contribution of one field, which we assume to be ϕ, and that this same field ϕ also dominates the second-order terms for both the adiabatic and the isocurvature mode. The field σ then only contributes to the linear adiabatic mode. These two assumptions remove 5 parameters and allow for a good compromise between generality and the number of free parameters. We can then write, up to second order:

$$\zeta = \zeta_\sigma \delta\sigma + \zeta_\phi \delta\phi + \frac{1}{2}\zeta_{\phi\phi}\delta\phi^2, \qquad S = S_\phi \delta\phi + \frac{1}{2} S_{\phi\phi}\delta\phi^2\,, \tag{5.35}$$

where the coefficients of the expansion can be physically interpreted in the δN formalism, see section 3.2.4 and [149]. As explained in the section 3.2, the field perturbations $\delta\phi$ and $\delta\sigma$ can be considered independent and quasi-Gaussian with the same power spectrum, whose amplitude is given in (3.57). We can then calculate $\langle I(\mathbf{k}_1)J(\mathbf{k}_2)\rangle$ where $I, J \in [\zeta, S]$. Using (5.10) and (2.124), we can establish the link between the parameters of the model and the analysis parametrization of (5.8):

$$A_s^{\zeta\zeta} = \zeta_\phi^2 + \zeta_\sigma^2, \qquad \alpha = \frac{\beta_{\rm iso}}{1-\beta_{\rm iso}} = \frac{S_\phi^2}{\zeta_\phi^2 + \zeta_\sigma^2}, \qquad \cos\Delta = \frac{\zeta_\phi}{\sqrt{\zeta_\phi^2 + \zeta_\sigma^2}}\,. \tag{5.36}$$

Then, by using the generalization of (3.79) which consists on adding the isocurvature and adiabatic indices IJK, we can express the $\tilde{f}_{\rm NL}$ as follows:

$$\begin{aligned} \tilde{f}_{\rm NL}^{\zeta,\zeta\zeta} &= \kappa_\zeta \cos^2\Delta & \tilde{f}_{\rm NL}^{S,\zeta\zeta} &= \kappa_S \cos^2\Delta \\ \tilde{f}_{\rm NL}^{\zeta,\zeta S} &= \kappa_\zeta \cos\Delta\sqrt{\alpha} & \tilde{f}_{\rm NL}^{S,\zeta S} &= \kappa_S \cos\Delta\sqrt{\alpha} \\ \tilde{f}_{\rm NL}^{\zeta,SS} &= \kappa_\zeta\,\alpha & \tilde{f}_{\rm NL}^{S,SS} &= \kappa_S\,\alpha\,, \end{aligned} \tag{5.37}$$

where we have defined the two κ_I as the coefficients of the second-order terms normalized by the adiabatic power spectrum:

$$\kappa_\zeta = \frac{\zeta_{\phi\phi}}{\zeta_\sigma^2 + \zeta_\phi^2}, \qquad \kappa_S = \frac{S_{\phi\phi}}{\zeta_\sigma^2 + \zeta_\phi^2}\,. \tag{5.38}$$

This parametrization differs from [113]. Our parametrization has the advantage that it remains valid in the limit of uncorrelated modes, $\cos\Delta \to 0$.[1] Looking at these equations

---

[1] In [113], authors use μ_I instead of κ_I where $\mu_I = \kappa_I/\cos^2\Delta$ and hence we find that μ_I is infinite when $\cos\Delta = 0$. Furthermore, we inverted the symbols used for the fields so that in the single-field limit, the single field is ϕ instead of σ. Finally, they use a parameter Ξ which is related to $\cos\Delta$ by $\cos\Delta = \epsilon_{\zeta S}\sqrt{\Xi}$ with $\epsilon_{\zeta S} = \pm 1$ denoting the relative sign of ζ and S.

(5.37), we see that the $\tilde{f}_{NL}^{I,\zeta S}$ are proportional to the amplitude of the cross-power spectrum $C_\ell^{\zeta S}$ and that the $\tilde{f}_{NL}^{I,SS}$ are proportional to the amplitude of the pure isocurvature power spectrum C_ℓ^{SS}. In this model, the single-field limit corresponds to $\delta\sigma \to 0$. Of course, in this limit we must have a zero isocurvature component, *i.e.* $S_\phi = S_{\phi\phi} = 0$. All of this translates into $\cos\Delta = 1$ and $\alpha = \kappa_S = 0$. In equations (5.37), it means that the only non-zero quantity is $\tilde{f}_{\mathrm{NL}}^{\zeta,\zeta\zeta}$ in that case.

The power spectrum (5.10) depends on the 6 ΛCDM parameters. Two of these parameters are related to the inflationary adiabatic mode, A_s and n_s, which are in this paper derived parameters from $\mathcal{P}_{\zeta\zeta}^{(1)}$ and $\mathcal{P}_{\zeta\zeta}^{(2)}$. We also have two additional parameters related to the isocurvature mode, the relative amplitude α and the correlation parameter $\cos\Delta$ derived from $\mathcal{P}_{SS}^{(1)}$, $\mathcal{P}_{\zeta S}^{(1)}$ (and $\mathcal{P}_{\zeta\zeta}^{(1)}$). In the following we will call $\tilde{\mathbf{f}}_{\mathrm{NL}}$ the vector of the 6 $\tilde{f}_{\mathrm{NL}}$. Using this model, the bispectrum, which is a function of 12 parameters (the 6 parameters $\boldsymbol{\theta}$ and the 6 parameters $\tilde{\mathbf{f}}_{\mathrm{NL}}$), can be reduced to a function of 10 parameters (the 6 parameters $\boldsymbol{\theta}$ plus $\kappa_\zeta, \kappa_S, \alpha, \cos\Delta$). Only three of the $\tilde{f}_{\mathrm{NL}}$ are independent since we can easily find these three relations:

$$\tilde{f}_{\mathrm{NL}}^{I,\zeta\zeta}\,\tilde{f}_{\mathrm{NL}}^{I,SS} = \left(\tilde{f}_{\mathrm{NL}}^{I,S\zeta}\right)^2, \qquad \tilde{f}_{\mathrm{NL}}^{\zeta,\zeta\zeta}\,\tilde{f}_{\mathrm{NL}}^{S,SS} = \tilde{f}_{\mathrm{NL}}^{S,\zeta\zeta}\,\tilde{f}_{\mathrm{NL}}^{\zeta,SS}, \tag{5.39}$$

where the first equation contains two relations for $I \in [\zeta, S]$. At the end, we have three independent $\tilde{f}_{\mathrm{NL}}$ which are expressed in terms of the four parameters $\{\kappa_\zeta, \kappa_S, \alpha, \cos\Delta\}$. Hence, the system is under-determined. The first equation in (5.39) also offers a simple refutable prediction of the model: $\tilde{f}_{\mathrm{NL}}^{I,\zeta\zeta}$ and $\tilde{f}_{\mathrm{NL}}^{I,SS}$ must share the same sign, *i.e.* the sign of κ_I. The second equation does not add more information on the signs. Looking at equations (5.37), we also have constraints on the sign of the correlation: if $\kappa_I > 0$ ($\kappa_I < 0$) then $\tilde{f}_{\mathrm{NL}}^{I,\zeta S}$ must have the same (opposite) sign as the correlation $\cos\Delta$.

5.4 Joint analysis methodology

In this section, we describe the combination of the power spectrum likelihood with a "bispectrum likelihood" to perform the joint analysis, as well as its implementation.

5.4.1 Joint likelihood

Rigorously, the power spectrum and bispectrum estimators are not statistically independent since they are calculated from the combination of the same modes in the observed maps. However, the calculation of the two estimators involves the linear combination of a large number of pairs and triplets of $a_{\ell m}$ modes (they are averaged over all multipole moments m and in large bins of multipoles ℓ) leading to nearly Gaussian statistics of the estimated power spectra and bispectra in the limit of weak non-Gaussianity of the CMB. Consequently, the cross-correlation of the two- and three-point functions, which involves averaging a large number of products of five Gaussian $a_{\ell m}$, vanishes, so that the estimators are uncorrelated. The independence of the two estimators can also be assumed since higher-order statistics are negligible because of the nearly Gaussian statistics of the power spectra and bispectra. We can then multiply the two distributions to obtain the total likelihood. The independence of the two-point and the three-point statistics has also been stressed in [201–203]. The power spectrum likelihood $\mathcal{L}$ is a function of all cosmological parameters stored in $\boldsymbol{\theta}$ and of $(\alpha, \cos\Delta)$. The bispectrum likelihood P is a function of

LiteBIRD			
Channel [GHz]	Noise [μK^2]		Beam FWHM [arcmin]
	Temperature	Polarization	
119	3.58e-06	1.43e-05	23.7
140	2.29e-06	9.17e-06	20.7
100	5.45e-06	2.18e-05	37.0
119	3.58e-06	1.43e-05	31.6
140	2.29e-06	9.17e-06	27.6
166	4.60e-06	1.84e-05	24.2
195	3.12e-06	1.24e-05	21.7
235	5.75e-06	2.30e-05	19.6

Table 5.3: We summarize in this table the characteristics of the full-sky LiteBIRD experiment. The values are taken from [220]. In the left column are indicated the frequency channels where the CMB emission is dominant. In the second column are indicated the amplitude of the noise power spectrum for temperature and polarization, and in the third column the beam size of the instrument.

$\tilde{\mathbf{f}}_{\rm NL}$. Thanks to (5.37), we translate the $\tilde{f}_{\rm NL}$ into $\boldsymbol{\xi} = (\alpha, \cos\Delta, \kappa_\zeta, \kappa_S)$ such that

$$\mathcal{L}^{tot}(\boldsymbol{\theta}, \boldsymbol{\xi}) = \mathcal{L}(\boldsymbol{\theta}, \alpha, \cos\Delta) \times P(\boldsymbol{\xi})\,. \tag{5.40}$$

Both likelihoods will be further specified in the next sections.

5.4.2 Power spectrum likelihood

For the joint analysis, we will use the Planck likelihood described in section 5.2.2. In addition, we will also consider the future experiments LiteBIRD and CMB-S4.

LiteBIRD

After the analysis of the Planck data, we will study the forecasts for future experiments. The LiteBIRD space mission is the fourth generation of CMB measurement. It is a JAXA led mission with contribution from the USA and Europe [221–224]. CNES is conducting a phase A study, leading the European consortium in charge of the MHFT (Medium and High-Frequency Telescope) while Japan leads the LFT (Low-Frequency Telescope). It will map the full sky polarization in 15 frequencies with unprecedented precision thanks to 4508 detectors which will reduce the noise by a factor of 10 with respect to Planck. Its main scientific objective is to test the paradigm of inflation by measuring the primordial B-modes.

The first step is to compute the expectation of the observed power spectrum. Of course, we do not have the observations now so that we will assume a fiducial set of parameters $\boldsymbol{\theta}$ whose theoretical power spectra $C_\ell^{\lambda_1\lambda_2,\rm fid}$ are assumed to be the observed ones. For the forecasts, we only consider the diagonal and the cross-correlations $TE = ET$, so that

$$\mathbf{C}_\ell^X = \begin{pmatrix} C_\ell^{X,TT} & C_\ell^{X,TE} & 0 \\ C_\ell^{X,ET} & C_\ell^{X,EE} & 0 \\ 0 & 0 & C_\ell^{X,\Phi\Phi} \end{pmatrix} \tag{5.41}$$

where the non-zero off-diagonal terms are the cross-correlations $TE = ET$ and where we neglect the correlation spectra ΦT and ΦE. The index X means either fiducial or theoretical, the last being calculated for any parameter set (not only fiducial) and defined in equation (5.10). In [225], it was shown that considering unlensed spectra does not change significantly the result for the CORE experiment. CORE was another experiment which has not been selected by ESA. For more details about CORE, see [226]. Given these results we only consider lensed power spectra.

To add the noise and the beam, we define the matrices $\tilde{\mathbf{C}}_\ell^{\mathbf{X}}$ with a tilde similarly to (5.30) as:

$$\tilde{C}_\ell^{X,\lambda_1\lambda_2} = C_\ell^{X,\lambda_1\lambda_2} + \left(b_\ell^{\lambda_1\lambda_2}\right)^{-2} n_\ell^{\lambda_1\lambda_2}\,, \tag{5.42}$$

where $n_\ell^{\lambda_1\lambda_2}$ is the $\lambda_1\lambda_2$-component of the noise matrix, which is diagonal because we assume that there are no correlation between the temperature and the polarization noise, and $b_\ell^{\lambda_1\lambda_2}$ is the beam transfer function defined in equation (5.27). We use the noise specifications for LiteBIRD from [220] given in table 5.3. We assume that the channels are combined by weighting with the inverse noise variance, neglecting the effect of component separation. We assume that each channel has white noise, $n_\ell^{\lambda_1\lambda_2,f}$, and a Gaussian beam, $b_\ell^{\lambda_1\lambda_2,f}$. We combine them to obtain the second effective term of equation (5.42) as follows:

$$\left(b_\ell^{\lambda_1\lambda_2}\right)^{-2} n_\ell^{\lambda_1\lambda_2} = \left(\sum_f \frac{\left(b_\ell^{\lambda_1\lambda_2,f}\right)^2}{n_\ell^{\lambda_1\lambda_2,f}}\right)^{-1}\,. \tag{5.43}$$

The beam-convolved noise of the lensing power spectrum has a different origin because we measure it indirectly using temperature and polarization as discussed in section 4.3.3. In [175], approximations of the lensing noise at large scales are given for the temperature and the polarization estimators. Given these approximations, the most powerful lensing estimator for LiteBIRD is the one obtained from E and B power spectrum correlations. For simplicity and because it is the most powerful estimator, we only consider the EB estimator. The approximation on large scales of the noise given in [175] is:

$$\left(b_L^{\Phi\Phi}\right)^{-2} n_L^{\Phi\Phi} = \left(\frac{L^4}{2}\sum_\ell \frac{2\ell+1}{4\pi}\frac{\left(C_\ell^{\mathrm{fid},EE}\right)^2}{\tilde{C}_\ell^{\mathrm{fid},EE}\tilde{C}_\ell^{\mathrm{fid},BB}}\right)^{-1}\,, \tag{5.44}$$

In [175], it is shown that for CORE this approximation is valid for low ℓ. We place a cutoff for LiteBIRD at $\ell = 165$. This value is obtained by multiplying $\ell = 550$, which is the value determined in [175] for CORE, by the ratio of the beam FWHM for the two experiments.

The fiducial power spectra are created after choosing the cosmological parameters $\boldsymbol{\theta}$ as well as for the isocurvature parameters, by using (5.42), as will be discussed later. We can then fit our theoretical power spectrum defined in (5.10) to the fiducial one, which replaces the observed one for the forecasts. To do so, we assume that the $a_{\ell m}$ are, for a given ℓ, Gaussian and statistically isotropic, [227], which is true for a full-sky CMB observation and is anyway an accurate approximation in the case of weak non-Gaussianities. If we define the vector $\tilde{\mathbf{a}}_{\ell m} = (\tilde{a}_{\ell m}^T, \tilde{a}_{\ell m}^E, \tilde{a}_{\ell m}^\Phi)^T$ where the tilde, as usual, means that we include the noise and beam of the experiment. We can then write:

$$\mathcal{L}(\boldsymbol{\theta}, \alpha, \cos\Delta) = \prod_\ell \frac{1}{2\pi|\tilde{\mathbf{C}}_\ell^{\mathrm{th}}|}\exp\left(-\frac{1}{2}\sum_{m=-\ell}^{\ell}\tilde{\mathbf{a}}_{\ell m}^\dagger\left(\tilde{\mathbf{C}}_\ell^{\mathrm{th}}\right)^{-1}\tilde{\mathbf{a}}_{\ell m}\right)\,. \tag{5.45}$$

CMB-S4			
Channel [GHz]	Noise [μK^2]		Beam FWHM [arcmin]
	Temperature	Polarization	
SAT			
145	2.13e-06	8.53e-06	25.5
155	4.13e-06	1.65e-05	22.7
220	1.32e-05	5.27e-05	13.0
270	3.87e-05	1.55e-04	13.0
LAT (Chile)			
145	1.22e-06	4.86e-06	1.4
155	1.16e-05	4.62e-05	1.0
220	7.20e-05	2.88e-04	0.9
LAT (South Pole)			
145	2.43e-06	4.86e-06	1.4
155	2.89e-05	4.62e-05	1.0
220	1.80e-04	2.88e-04	0.9

Table 5.4: We summarize in this table the characteristics of the CMB-S4 configuration with 4 instruments, where the 2 LAT in Chile are considered as one instrument with twice the number of detectors. The effective survey time is 10% of 5 years. These characteristics are taken from [228].

The sum over m with the $a_{\ell m}$s can be expressed as a function of the power spectrum estimator following equation (4.19). Moreover, we can take into account a partial coverage of the sky due to the Milky-Way mask by substituting $(\tilde{\mathbf{C}}^{\rm th}_\ell)^{-1} \rightarrow f_{\rm sky}(\tilde{\mathbf{C}}^{\rm th}_\ell)^{-1}$ where $f_{\rm sky}$ is the fraction of the sky observed. Intuitively, observing a fraction of the sky means that we have less measurement points which increases the error bars by a factor $\sqrt{f_{\rm sky}}$. Hence, by using (4.19) and by normalizing the distribution such that $\ln\mathcal{L} = 0$ when $\tilde{\mathbf{C}}^{\rm th}_\ell = \tilde{\mathbf{C}}^{\rm fid}_\ell$, one finds [225, 227]:

$$-2\ln\mathcal{L}(\boldsymbol{\theta},\alpha,\cos\Delta) = \sum_\ell f_{\rm sky}(2\ell+1)\left[\frac{\tilde{D}_\ell}{|\tilde{\mathbf{C}}^{\mathbf{th}}_\ell|} - \ln\left(\frac{|\tilde{\mathbf{C}}^{\mathbf{th}}_\ell|}{|\tilde{\mathbf{C}}^{\mathbf{fid}}_\ell|}\right) - n\right], \tag{5.46}$$

where the power spectra matrices are defined in equation (5.41) and the tildes again mean that we include the beam and noise following equation (5.42). The quantity n is the number of observables, *i.e.* T, E and Φ. The quantity $\tilde{D}_\ell$ is defined as follows:

$$\begin{aligned}\tilde{D}_\ell = \tilde{C}^{{\rm th},TT}_\ell\tilde{C}^{{\rm th},EE}_\ell\tilde{C}^{{\rm fid},\Phi\Phi}_\ell + \tilde{C}^{{\rm th},TT}_\ell\tilde{C}^{{\rm fid},EE}_\ell\tilde{C}^{{\rm th},\Phi\Phi}_\ell + \tilde{C}^{{\rm fid},TT}_\ell\tilde{C}^{{\rm th},EE}_\ell\tilde{C}^{{\rm th},\Phi\Phi}_\ell \\ -\tilde{C}^{{\rm th},TE}_\ell\left(2\tilde{C}^{{\rm fid},TE}_\ell\tilde{C}^{{\rm th},\Phi\Phi}_\ell + \tilde{C}^{{\rm th},TE}_\ell\tilde{C}^{{\rm fid},\Phi\Phi}_\ell\right).\end{aligned} \tag{5.47}$$

In this expression, complications such as masks and anisotropic noise are neglected.

CMB-S4

For completeness' sake, we extend our analysis to the future ground-based experiment CMB-S4 described in [228, 229]. This survey will in particular improve the observations at high-ℓ. The current CMB-S4 proposal consists of 4 instruments:

- 3 Large-Aperture Telescopes (LAT) which can access high multipoles thanks to a very small beam, but are limited by atmospheric noise at low-ℓ. The range of multipoles is assumed to be $[1000, 5000]$.
- 1 Small-Aperture Telescope (SAT) which has low noise at low-ℓ but a large beam. The range of multipoles is assumed to be $[30, 1000]$.

These telescopes will be shared between the South Pole and Chile. At the South Pole, one SAT and one LAT will be installed to observe one single patch of 3% of the sky, since a small and deep patch is needed to detect a small value of r at the recombination peak. The LAT is useful to have access to high multipoles for de-lensing. In Chile, 2 LAT will be installed to have access to almost 70% of the sky (60% after the galactic cut) and very high multipoles to achieve high accuracy on the effective number of neutrino species N_{eff}. The high-multipole measurement will allow the reconstruction of the lensing up to at least $\ell \sim 1000$. Therefore, as for LiteBIRD, we will suppose a flat lensing noise (5.44) on large scales up to $\ell = 1000$ and neglect the information at larger multipoles. We use the configuration given in table 5.4 for our analysis.

In addition to the usual white noise, we have to consider the atmospheric noise, which limits the measurements at low-ℓ. Following [230], we model the noise as the usual white noise plus a contribution coming from the atmosphere:

$$n_\ell^{\lambda_1\lambda_2} = n_{\text{white}}^{\lambda_1\lambda_2} + N_{\text{red}}^{\lambda_1\lambda_2}\left(\frac{\ell}{\ell_{\text{knee}}^{\lambda_1\lambda_2}}\right)^{\alpha_{\text{knee}}^{\lambda_1\lambda_2}}, \tag{5.48}$$

where the subscript red means that we expect red noise from the atmosphere, *i.e.* with α_{knee} negative. Recall that $n_\ell^{\lambda_1\lambda_2}$ is diagonal. As in [228] and given [230], we take $\ell_{\text{knee}} = 55$ and $\alpha_{\text{knee}} = -2.5$ for both polarization and temperature in the case of the SAT. Actually, the temperature measurements of the SAT do not bring additional constraints for our purposes, since Planck temperature measurements in the SAT ℓ-range are already almost cosmic variance limited. Regarding the LAT, for temperature we take $\ell_{\text{knee}} = 1000$ and $\alpha_{\text{knee}} = -3.5$ and for polarization we take $\ell_{\text{knee}} = 700$ and $\alpha_{\text{knee}} = -1.4$ following [230]. In general we assume $N_{\text{red}}^{\lambda_1\lambda_2} = n_{\text{white}}^{\lambda_1\lambda_2}$, where $n_{\text{white}}^{\lambda_1\lambda_2}$ is the amplitude of the white noise given in table 5.4, except for LAT temperature where we take $[9.51, 108, 196] \times 10^{-5}\mu\text{K}^2$, respectively, for the three LAT channels.

Since we do not have access to the full sky from the ground, the power spectrum measurements are correlated between different ℓ. We then bin the power spectra, given that the typical correlation length is $\Delta\ell \sim 1/f_{sky}$. This was neglected for LiteBIRD because the correlation length would be much smaller than 2 ($\sim 1/0.7$). For each bin, we assume the values of the power spectra to be the mean values inside the bin. Thus, the likelihood given in (5.46) becomes:

$$-2\ln\mathcal{L}(\boldsymbol{\theta}, \alpha, \cos\Delta) = \sum_i \sum_{\ell\in i} f_{sky}(2\ell+1)\left[\frac{D_i}{|\tilde{\mathbf{C}}_i^{\mathbf{th}}|} - \ln\left(\frac{|\tilde{\mathbf{C}}_i^{\mathbf{th}}|}{|\tilde{\mathbf{C}}_i^{\mathbf{fid}}|}\right) - n\right], \tag{5.49}$$

where i stands for the bin number and the quantities with subscript i have been averaged over the bin i.

5.4.3 Bispectrum likelihood

The PDF of the $\tilde{f}_{\text{NL}}$ is estimated as being well described by a Gaussian. We can then reduce the bispectrum data to only 6 observables, the $\tilde{f}_{\text{NL}}^{I,JK}$, by constructing an effective

		$\zeta,\zeta\zeta$	$\zeta,\zeta S$	ζ,SS	$S,\zeta\zeta$	$S,\zeta S$	S,SS
LiteBIRD	CDM	9	8	72	75	70	57
	ν density	20	25	107	87	113	155
	ν velocity	19	10	36	50	33	18
CMB-S4	CDM	12	20	211	173	201	283
	ν density	29	51	214	141	245	473
	ν velocity	42	38	108	118	113	100

Table 5.5: We give in this table for each isocurvature mode the value of the $\tilde{f}_{\mathrm{NL}}$ error forecasts for LiteBIRD and CMB-S4.

likelihood directly of the $\tilde{f}_{\mathrm{NL}}$, instead of using the bispectrum distribution. This has the huge advantage of saving a lot of computation time with negligible impact on the performance. We use (5.33) with the transformation (5.25) to obtain the best estimated values $\tilde{\mathbf{f}}^{\mathbf{0}}_{\mathrm{NL}}$ and use (5.34) to estimate the Fisher matrix. Estimations of $\tilde{\mathbf{f}}^{\mathbf{0}}_{\mathrm{NL}}$ and F_{ij} are model-independent, in particular they do not use the relations (5.37). The $\tilde{f}_{\mathrm{NL}}$ estimator (5.33) depends linearly on the observed bispectrum. The observed bispectrum is obtained from the product of three $a_{\ell m}$ and is not Gaussian. However, the bispectrum value in each bin is the result of the average over many multipoles ℓ and m, such that the Gaussianity can be ensured by the central limit theorem. Therefore, we express the bispectrum likelihood as an effective six-dimensional Gaussian function of the $\tilde{f}_{\mathrm{NL}}$:

$$-2\ln P(\boldsymbol{\xi}) = \left(\tilde{\mathbf{f}}_{\mathrm{NL}}(\boldsymbol{\xi}) - \tilde{\mathbf{f}}^{\mathbf{0}}_{\mathrm{NL}}\right)^T \mathbf{F} \left(\tilde{\mathbf{f}}_{\mathrm{NL}}(\boldsymbol{\xi}) - \tilde{\mathbf{f}}^{\mathbf{0}}_{\mathrm{NL}}\right), \tag{5.50}$$

where $\tilde{\mathbf{f}}_{\mathrm{NL}}(\boldsymbol{\xi})$ is defined in equation (5.37). The values $\mathbf{f}^{\mathbf{0}}_{\mathrm{NL}}$ without tilde can be found in [107]. We recall that the $\mathbf{f}^{\mathbf{0}}_{\mathrm{NL}}$ are defined with respect to the gravitational potential ψ, while the $\tilde{\mathbf{f}}^{\mathbf{0}}_{\mathrm{NL}}$ are defined with respect to the curvature perturbation ζ.[2] The resulting values for $\tilde{\mathbf{f}}^{\mathbf{0}}_{\mathrm{NL}}$ and its error bars are given in 5.2 while the error bars for the future experiments are given in table 5.5.

5.5 Results

This section contains the results of our analyses. In section 5.5.1, we perform a joint analysis of the Planck power spectrum and bispectrum assuming two different cases: fixing $\cos\Delta$ or fixing κ, as we will see that when all parameters are left free, the joint analysis does not improve constraints. In section 5.5.2, we discuss and summarize the usefulness of the joint analysis for many possible configurations using theoretical arguments. Finally, in section 5.5.3, we compute forecasts for future experiments. We first investigate the possibility to detect isocurvature modes and their non-Gaussian features in these experiments. We then show the result of the joint analysis in the favorable cases.

In this section, we will always show results for β_{iso} instead of α. Recall that $\beta_{\mathrm{iso}} = \alpha/(1+\alpha)$. It is convenient for the analysis to use β_{iso} because it is bounded between 0

---

[2] The exact conversion factors are for $(\zeta,\zeta\zeta)$, $(\zeta,\zeta S)$, (ζ,SS), $(S,\zeta\zeta)$, $(S,\zeta S)$, (S,SS): -6/5, -2/5, -2/15, -18/5, -6/5, -2/5, respectively.

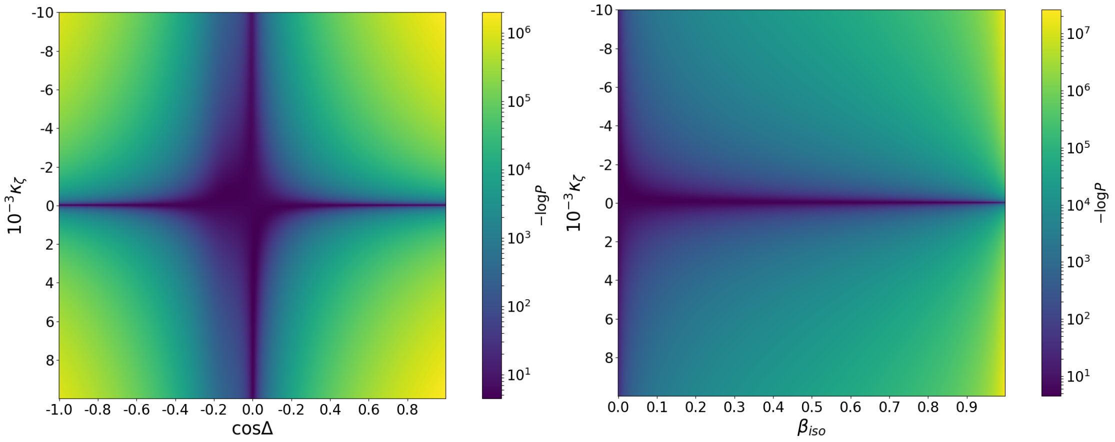

Figure 5.5: CDM isocurvature bispectrum PDF, $-\ln P$ defined in (5.50), as a function of $\cos\Delta$ and κ_ζ with $\beta_{\rm iso} = 0.016$ and $\kappa_S = 0$ in the panel on the left, and of $\beta_{\rm iso}$ and κ_ζ with $\cos\Delta = -0.1$ and $\kappa_S = 0$ in the panel on the right.

and 1. Moreover, all the results of Planck are given in terms of $\beta_{\rm iso}$. However, for the small values of $\beta_{\rm iso}$ allowed by the power spectrum, we can say that $\alpha \approx \beta_{\rm iso}$. Recall that we apply a flat prior on $P^{(1)}_{IJ}$ and $P^{(2)}_{\zeta\zeta}$ defined in (5.4).

5.5.1 Planck joint analysis

The joint analysis, given our model, does not improve constraints in general in the case of Planck, *i.e.* without detection of isocurvature modes in the power spectrum and detection of primordial non-Gaussianity in the bispectrum. We can directly see this from figure 5.5. There is a strong degeneracy between the parameters κ_I in the bispectrum and the power spectrum parameters $\beta_{\rm iso}$ and $\cos\Delta$. For total (anti-)correlation, *i.e.* $\cos\Delta = \pm 1$, we have well-constrained κ_I which in that case are directly linked to $\tilde{f}^{I,\zeta\zeta}_{\rm NL}$. However, for $\cos\Delta$ close to and compatible with 0, as the power spectrum constraints that we gave in tables 5.1 tell us, the parameters κ_I can take arbitrarily large values as we see in the left panel of figure 5.5 for κ_ζ. In principle, the 1σ and 2σ contours should go to infinity, but for very large κ_I, the width in the $\cos\Delta$ dimension becomes very small so that it becomes difficult to sample. The right panel of figure 5.5 is similar, but this time as a function of $\beta_{\rm iso}$ instead of $\cos\Delta$. Again, for $\beta_{\rm iso}$ close to and compatible with 0, as given by the power spectrum constraints, κ_ζ can take arbitrarily large values, so the space to sample in this direction is infinite.

The previous paragraph concerned the bispectrum analysis alone. If we add the power spectrum constraints, only the measurements of $\cos\Delta$ and $\beta_{\rm iso}$ will be improved since the power spectrum does not depend on the κ_I. The constraints are compatible with 0 for both the isocurvature amplitude and the correlation to a high probability, thus the remaining space to sample is again infinite. One could integrate numerically over the κ_I and obtain constraints on $\beta_{\rm iso}$ and $\cos\Delta$. However, these constraints would be meaningless because they depend completely on the chosen parametrization and are independent of the Fisher matrix. In other words, the κ_I absorb all the constraints from the bispectrum and since the power spectrum does not depend on κ_I, the constraints on the other parameters are not improved.

For the joint analysis with the bispectrum to have any effect for Planck, we have to fix some of the parameters. Some models can predict $\cos\Delta = \pm 1$, and we assume it

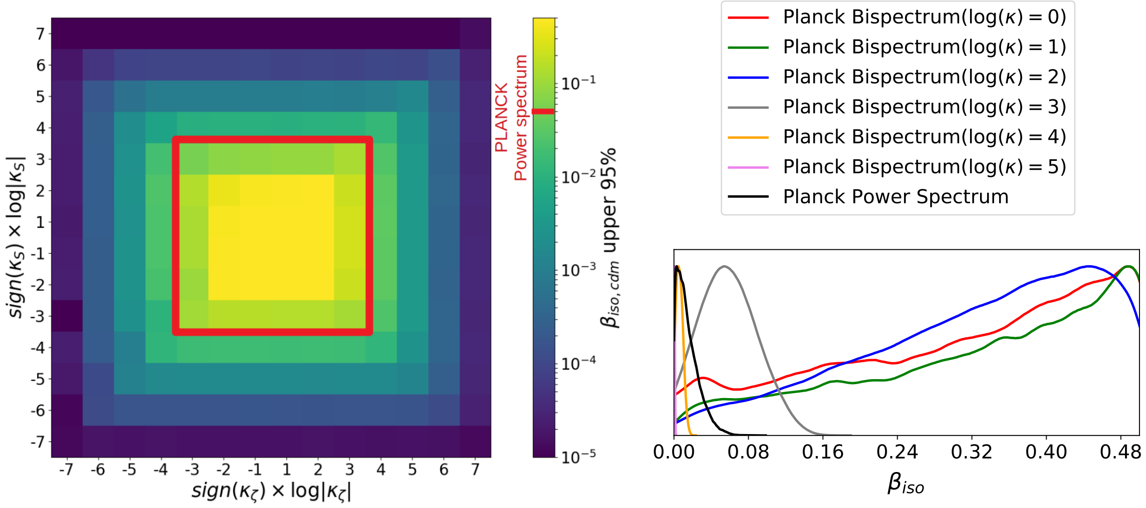

Figure 5.6: In the left panel, we show the 2σ upper bound of the parameter $\beta_{iso,cdm}$, marginalizing over $\cos\Delta$, as a function of the two parameters κ_ζ, κ_S. The upper bound is calculated with a MCMC using only the bispectrum likelihood of equation (5.50) and fixing the couple κ_ζ, κ_S. The red square is the 95% upper bound given by the Planck power spectrum. In the right panel, except for the black curve, we show the probability distribution for the specific case where $\kappa_\zeta = \kappa_S$. So the curves of the right panel correspond to the positive diagonal in the left panel. We also plot the PDF obtained with the power spectrum alone (black curve).

might be possible to have models that predict other non-zero values as well. Fixing the correlation is equivalent to choosing as bispectrum likelihood a slice of constant $\cos\Delta$ in the left panel of figure 5.5. Other theoretical models might have specific predictions for the κ_I parameters.

General correlation, fixed κ_I

Constraints on β_{iso}: We assume here a model where the parameters κ_I are predicted by theory. In the model studied in [113, 149, 197], where the curvaton decays into CDM and radiation, the parameters κ_I can be expressed as a function of two parameters f_c and r. The former represents the fraction of CDM created by the decay and the latter quantifies the transfer between the pre-decay and post-decay perturbations. It is not hard to imagine that in some specific particle theory those quantities could be computed and hence the values of the κ_I would be fixed by theory. In equation (5.37), we see that $\cos^2\Delta$, β_{iso} and combinations of the two depend on $\tilde{f}_{\mathrm{NL}}/\kappa_I$ directly. Two parameters are fixed: for $I = \zeta$ and for $I = S$. In figure 5.6, we show the constraints from the bispectrum by representing the 2σ upper value of $\beta_{iso,cdm}$ obtained with a MCMC chain marginalized over $\cos\Delta$ using only (5.50) as a function of the chosen values of κ. The flat priors of $P^{(1)}_{SS}$ and $P^{(1)}_{\zeta\zeta}$ have the same upper limit, so that we can have the same amplitude in the adiabatic and in the CDM isocurvature mode. It corresponds to $\alpha = 1$ and $\beta_{\mathrm{iso}} = 0.5$. We should have no constraint on α coming from the bispectrum for small κ, so that we find the same posterior distribution as our prior which is flat for $P^{(1)}_{SS}$ and hence α. The change of variable $\alpha \to \beta_{\mathrm{iso}}$ contracts intervals of α and hence makes higher β_{iso} values more likely. This happens for $\log\kappa = 0, 1, 2$. When $\log\kappa \geq 3$, the bispectrum provides additional constraints on the isocurvature amplitude. The larger κ is, the more

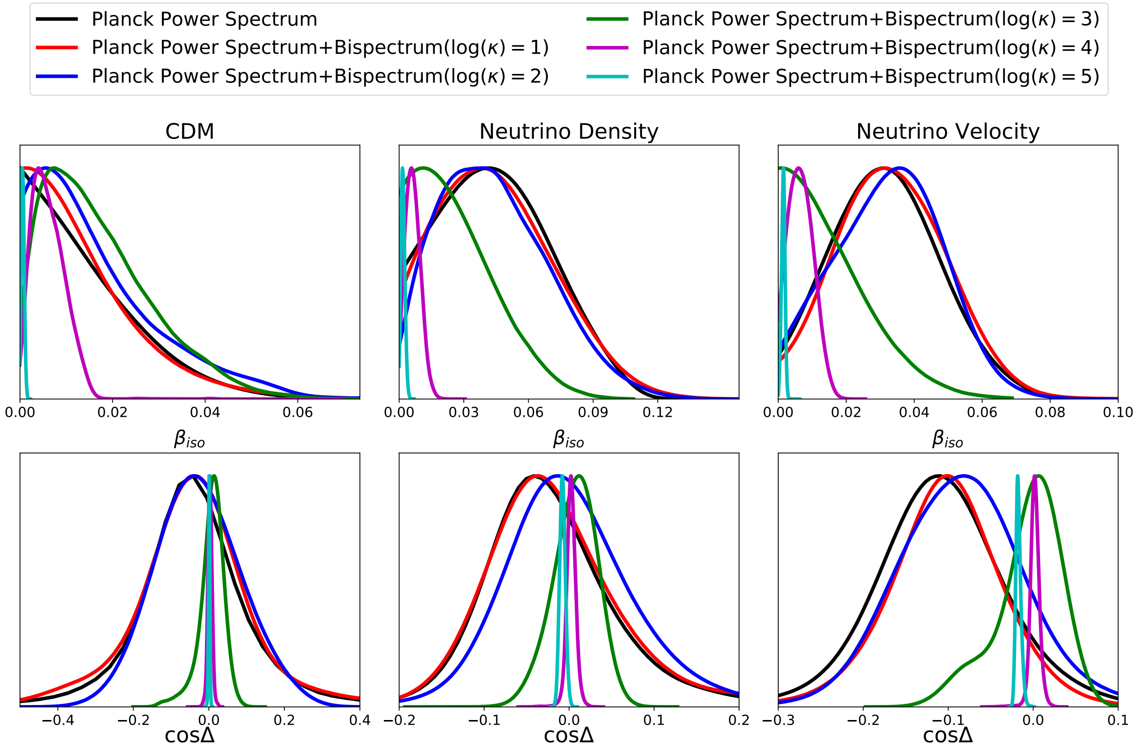

Figure 5.7: Marginalized constraints of β_{iso} and $\cos\Delta$ for the joint analysis with fixed κ. Respectively, the first, second, and third columns correspond to CDM, neutrino density, and neutrino velocity. The black curve shows the constraint obtained using the power spectrum alone.

the bispectrum constrains β_{iso}. It provides better constraints than the power spectrum for $\log\kappa \geq 4$.

Hence we predict that the joint analysis will be able to improve the constraints for the models that are outside the red square in figure 5.6. To make the analysis simpler and because only the largest κ is relevant, we can set $\kappa_\zeta = \kappa_S = \kappa$ and only study the joint analysis for the diagonal of that figure.

In figure 5.7 we see that for large enough κ, values of $\cos\Delta$ and β_{iso} compatible with data are close to zero for all isocurvature modes. This result is consistent with what we observed in figure 5.6 (right panel). The joint analysis starts to be efficient when the bispectrum constraints become comparable to the power spectrum constraints, represented by the black curve in figure 5.6. In figure 5.7, for $\log\kappa = 1, 2$ the constraints on the isocurvature parameters obtained with the joint analysis are comparable with the power spectrum constraints. We observe that the size of the β_{iso} contour increases slowly to allow higher β_{iso} for the CDM isocurvature mode. Finally for $\log\kappa = 3, 4, 5$ contours are contracted near 0. The intermediate behavior where the contour increases slowly for $\log\kappa = 1, 2$ can be understood by looking at the (β_{iso}, $\cos\Delta$) space for the CDM isocurvature mode in the left panel of figure 5.8. The power spectrum allows values of $\cos\Delta$ from 0.3 to -0.4 at 2σ level. When κ increases and the bispectrum constraints start to have an impact, regions where $|\cos\Delta| > 0.3$ start to be excluded, see also the $\cos\Delta$ panel of figure 5.7. Then, the posterior distribution can include higher values of β_{iso} due to the renormalization of the distribution. We have reproduced the same effect by imposing a prior with bounds 0.2 and -0.2 for the correlation.

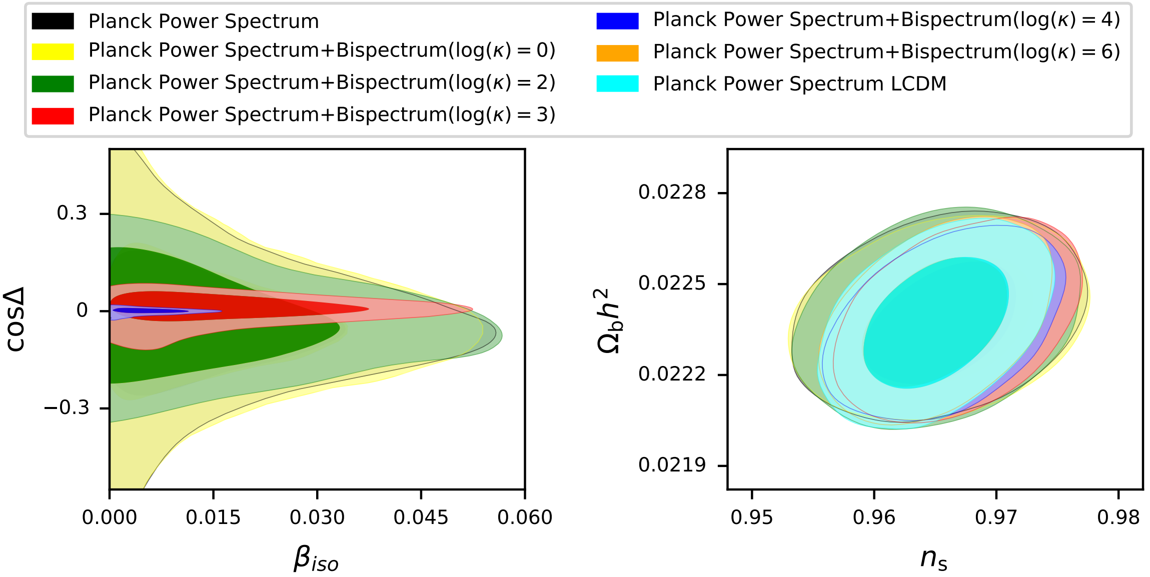

Figure 5.8: Left: constraints of the joint analysis and of the power spectrum alone in the $(\cos\Delta,\ \beta_{\rm iso})$ space for CDM isocurvature modes. Right: the result of this analysis in $(\Omega_b,\ n_s)$ space, *i.e.* constraints from the power spectrum alone compared with the joint analysis at different fixed values of κ. We also show the constraints given by the power spectrum in the case of the standard ΛCDM model, *i.e.* without isocurvature modes. For low values of κ, the joint analysis $(\Omega_b,\ n_s)$ contour and the power spectrum contour assuming a model with one isocurvature mode are similar. For large κ, the joint analysis $(\Omega_b,\ n_s)$ contour is similar to the contour given by ΛCDM without isocurvature mode. This behavior of the constraints with respect to the joint analysis is similar for all other cosmological parameters.

Regarding the cosmological parameters, we can see in the right plot of figure 5.8 that for $\log\kappa = 0$, the contours of the joint analysis in the $(\Omega_b,\ n_s)$ space are similar to contours obtained from the power spectrum alone including isocurvature modes. This means that the bispectrum does not constrain the isocurvature modes for κ too small. However, when $\log\kappa \geq 5, 6$, the contours of Ω_b and n_s are equivalent to the contours given by the power spectrum alone assuming no isocurvature modes. In general, the contours of the cosmological parameters are not degraded by the estimation of the isocurvature mode parameters if κ_I is large. The other parameters of ΛCDM have the same behavior. We understand this result because when κ tends to infinity, the constraints on the $\tilde{f}_{\rm NL}$ from the bispectrum provide very tight constraints on $\beta_{\rm iso}$ and $\cos\Delta$ given (5.37). In other words, setting $\log\kappa \geq 6$ gives the same constraints on the parameters as a purely adiabatic model. While figure 5.8 is for CDM isocurvature, results are similar for the other isocurvature modes.

Constraints on $\tilde{f}_{\rm NL}$: Fixing κ can improve the power spectrum constraints on $\beta_{\rm iso}$ and $\cos\Delta$ if $\kappa > 10^3$. However, a fixed κ in combination with the constraints on $\beta_{\rm iso}$ and $\cos\Delta$ also allows us to derive constraints on the $\tilde{f}_{\rm NL}$ parameters, thanks to (5.37). In the range where the bispectrum does not improve $\beta_{\rm iso}$ and $\cos\Delta$, *i.e.* when $\kappa < 10^3$, we might even say that the $\tilde{f}_{\rm NL}$ error bars are strongly improved since the 2σ ranges are $\tilde{f}_{\rm NL}^{I,\zeta\zeta} < 0.18$, $-0.03 < \tilde{f}_{\rm NL}^{I,\zeta S} < 0.02$ and $\tilde{f}_{\rm NL}^{I,SS} < 0.04$ for the case where $\kappa = 1$. In the range where the bispectrum improves the constraints we obtain the following 2σ ranges: $\tilde{f}_{\mathrm{NL}}^{I,\zeta\zeta} < 2 \times 10^{-4}$, $-6 \times 10^{-4} < \tilde{f}_{\mathrm{NL}}^{I,\zeta S} < 9 \times 10^{-4}$ and $\tilde{f}_{\mathrm{NL}}^{I,SS} < 0.01$ for the case where $\log(\kappa) = 4$. Indeed, the equations (5.37) give the $\tilde{f}_{\mathrm{NL}}$ as products of κ with β_{iso} (or α) and $\cos\Delta$, which are constrained to very small values by the power spectrum. However, we must be careful with this interpretation, since the $\tilde{f}_{\mathrm{NL}}$ error bars obtained in the usual Planck analysis are model-independent, while we have assumed here a model which implies relations between the $\tilde{f}_{\mathrm{NL}}$. Furthermore, we have assumed a flat prior on $\boldsymbol{\xi}$ (defined above (5.40)), while we would obtain the same results as the Planck analysis if we used a flat prior on the $\tilde{f}_{\mathrm{NL}}$ (and did not have those relations between the $\tilde{f}_{\mathrm{NL}}$). Hence our constraints are not directly comparable with the published Planck results regarding the $\tilde{f}_{\mathrm{NL}}$.

Fixed correlation, general κ_I

Constraints on β_{iso}: In this section, we assume a model where the correlation between the isocurvature mode and the adiabatic one is predicted. On the other hand, the κ_I are now free parameters. Fixing $\cos\Delta$ can be seen as a re-scaling of $\tilde{f}_{\mathrm{NL}}$, but contrary to the previous case of fixed κ, each $\tilde{f}_{\mathrm{NL}}^{I,JK}$ is not re-scaled by the same factor, see (5.37). We can also deduce from the formulas (5.37) that κ_I and $\cos\Delta$ will have opposite effects on the β_{iso} distribution: given the first equation involving $\tilde{f}_{\mathrm{NL}}^{I,\zeta\zeta}$, we see that fixing κ to a high value is equivalent to fixing $\cos\Delta$ to a small value. We first show the result for $\cos\Delta = -1$, since this total anti-correlation can be theoretically motivated by a curvaton scenario as described for the first time in [144, 145]. Then we take $\cos\Delta = -0.4$, which is the 2σ bound from the power spectrum for the CDM isocurvature mode [121], and finally two smaller values on a log-scale: $\cos\Delta = -0.1, -0.01$. As in the case of fixed κ, negative and positive values give very similar results. We choose here a negative correlation since that is more likely for every isocurvature mode given the Planck constraints.

In figure 5.9, we see that for $\cos\Delta = -1, -0.4$ there is no improvement of the constraints compared to the power spectrum constraint alone, as expected since it is equivalent to small values of κ_I. In the range of correlations $\cos\Delta = -0.1, -0.01$, the bispectrum induces a contraction effect of more than 1σ for CDM and neutrino density. In the case of neutrino velocity, the bispectrum has pushed β_{iso} to larger values. This mode has the advantage to have two signal-to-noise values larger than 2 in the model-independent bispectrum analysis: 2.9σ for $\tilde{f}_{\mathrm{NL}}^{\zeta,\zeta S}$ and 2.3σ for $\tilde{f}_{\mathrm{NL}}^{\zeta,SS}$, see table 5.2. The ratio of the two can then directly constrain β_{iso} (through α). For $\cos\Delta = -0.1$, we obtain from the bispectrum alone a central value of 0.07 for β_{iso} for this mode, which is larger than the constraint of the power spectrum. The detection of this mode in this configuration is improved to 4.0σ thanks to the bispectrum. For $\cos\Delta = -0.01$, the ratio gives a central value for β_{iso} of about 8×10^{-4} (*i.e.* from the bispectrum alone), which leads to a central value of 6×10^{-4} for the joint analysis. Again, for the neutrino velocity mode, the “detection” of the two $\tilde{f}_{\mathrm{NL}}$ improves the detection of β_{iso} to 3.5σ for this configuration (which cannot be seen in figure 5.9 because of the scale).

At this point, we could claim that in the case of a model predicting a correlation of order -0.1 or -0.01, the joint analysis can detect β_{iso} for the neutrino velocity isocurvature mode in the Planck data. This result should be taken with care for the following reasons. First, our signal-to-noise values for the $\tilde{f}_{\mathrm{NL}}$ are slightly different from the ones given in [107] because we use the Fisher error bars given in table 5.5 while [107] computes the error bars from simulations. The Fisher error bars are smaller in the case of the neutrino velocity mode compared with the true error bars given in [107] for $\tilde{f}_{\mathrm{NL}}^{\zeta,\zeta S}$ and $\tilde{f}_{\mathrm{NL}}^{\zeta,SS}$, which increases

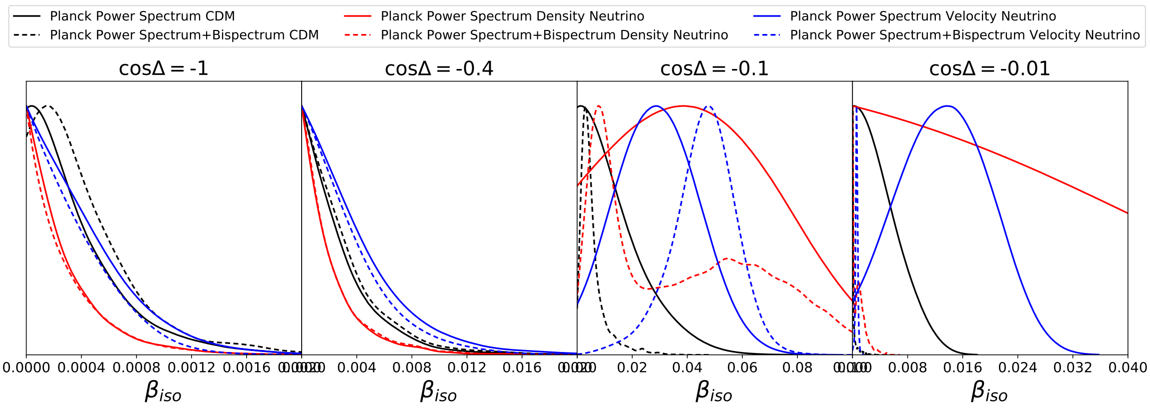

Figure 5.9: Constraints obtained on $\beta_{\rm iso}$ when fixing $\cos\Delta$. We show for every isocurvature mode (CDM in black, neutrino density in red, and neutrino velocity in blue) the result of the power spectrum analysis alone (solid curve) and of the joint analysis with the bispectrum (dotted curve).

their signal-to-noise (recall also that we use in this thesis $\tilde{f}_{\rm NL}$ defined in terms of ζ, S instead of $f_{\rm NL}$ defined in terms of the gravitational potential), see section 2.5.4. Second, as discussed in [107], having one signal-to-noise larger than 2.5 cannot be considered a detection given the large number of parameters measured and the lack of consistency between the temperature-only and the temperature+polarization results. Hence these might very well be simple statistical fluctuations, and basing any conclusions on them is risky. However, [107] does not discuss the probability of having two signal-to-noise values larger than 2 in the same mode.

In figure 5.9, we observe for neutrino density a second bump for a correlation of -0.1 and, although it cannot be seen because of the scale, there is actually also a similar second bump for $\cos\Delta = -0.01$. This is due to the strong correlation between κ_I and $\beta_{\rm iso}$. For all modes, when $\cos\Delta$ goes to 0, the isocurvature amplitude space also goes to 0. For a very small correlation, κ_I could take any large value up to infinity and, as we saw in the case of fixed κ, the results in the ΛCDM parameter space then tend to what one would get with purely adiabatic initial conditions. This explains the first peak. When κ_I becomes smaller, the power spectrum dominates the constraints, which gives us the second bump.

Constraints on $\tilde{f}_{\rm NL}$: As in section 5.5.1, we can obtain constraints on $\tilde{f}_{\rm NL}$ as derived parameters. But exactly as before, we believe that those constraints are trivial given the relations (5.37) and they are prior dependent. Furthermore, in this particular case where we fix the correlation between the adiabatic and the isocurvature mode, the infinite degeneracy between κ and $\beta_{\rm iso}$ makes the marginalized constraints on $\tilde{f}_{\rm NL}^{I,\zeta\zeta}$ even weaker when we add the constraints of the power spectrum to the bispectrum. For all these reasons, we believe that these constraints are not meaningful.

5.5.2 Theoretical assessment

In this section, we give theoretical arguments to justify the choices we made in section 5.5.1 and to prepare the investigation of what will be possible with future experiments as described in the next section. More generally, we will study for all different possible

	$\cos\Delta$	$\tilde{f}_{\mathrm{NL}}$	α or β_{iso}	κ fixed	Joint analysis improves constraints
1	not detected	×	×	×	×
2	""	×	✓	×	×
3	""	×	×	✓	if κ_I large enough
4	""	✓	×	×	×
5	""	✓	✓	×	constraints/detections of $\cos\Delta$ and κ_I
6	detected	×	✓	×	if $\cos\Delta$ small enough
7	""	✓	✓	×	constraints on $\cos\Delta$ and κ_I
8	fixed $\neq 0$	×	×	×	if $\cos\Delta$ small enough
9	""	✓	–	×	constraint/detection of α
10	fixed $= 0$	–	–	×	×
11	""	×	×	✓	if $\kappa \uparrow$, $\alpha \downarrow$
12	""	✓	×	✓	detection of α

Table 5.6: Summary of the usefulness of performing a joint analysis of the power spectrum and the bispectrum (compared to an analysis of the power spectrum alone) for all possible configurations of detection/non-detection and fixed/free parameters as explained in the main text. The table is divided into two parts: from line 1 to 7, the correlation $\cos\Delta$ is free and from line 8 to 12, it is fixed. In the right column we give a brief conclusion for each case; for more details, see the corresponding description in the main text. (A – symbol means that the conclusion is independent of that choice.)

cases of detection/non-detection and fixed/free parameters what we expect regarding the impact of a joint analysis of the power spectrum and the bispectrum.

As we pointed out before, the six relations (5.37) for the $\tilde{f}_{\mathrm{NL}}$ parameters are not independent. Only 3 of them are independent and these are expressed in terms of 4 parameters. Unfortunately, the parameters κ_I are degenerate with both $\cos\Delta$ and α. This means in general that if we do not detect isocurvature modes, no constraints can be established on the κ_I. A detection, however, can break the degeneracy. Thus, our results depend on the detection of α, $\cos\Delta$ and $\tilde{f}_{\mathrm{NL}}$. Alternatively, we might have models where some of the parameters have a predicted value. For example, some models predict the adiabatic and isocurvature modes to be fully (anti-)correlated. One could also imagine models in which the κ_I parameters are predicted.

In table 5.6 we give the conclusions for different cases of detection of α, $\cos\Delta$ and $\tilde{f}_{\mathrm{NL}}$ and of fixing the parameters $\cos\Delta$ and κ_I. What we mean by "detection" in this section is that the value 0 is excluded by at least 4σ. The symbol "×" means the condition ($\tilde{f}_{\mathrm{NL}}$ and α being detected, κ being fixed to a specific value) is not satisfied, while "✓" means it is. As for $\cos\Delta$ we have to consider both detection and fixing, we are more explicit in that column. In the table we have put only the most important conclusions for each case; for more information, see the corresponding discussion in the rest of this section.

We will now discuss table 5.6 line by line. To refer to a specific equation of (5.37), we will just give for example the combination $(I, \zeta\zeta)$ to refer to the two equations involving $\tilde{f}_{\mathrm{NL}}^{\zeta,\zeta\zeta}$ and $\tilde{f}_{\mathrm{NL}}^{S,\zeta\zeta}$. We start with the cases where $\cos\Delta$ is a free parameter:

1. Here, $\cos\Delta$ is not detected in the power spectrum and there is neither detection of $\tilde{f}_{\mathrm{NL}}$ in the bispectrum nor detection of isocurvature modes in the power spectrum. We have $\cos\Delta$ and β_{iso} compatible with zero and then κ_I can take any arbitrarily large value. Since κ_I is strongly degenerate with $\cos\Delta$ and β_{iso}, a joint analysis

would give artificial constraints that are only due to parametrization effects as we can see in figure 5.5. Furthermore, the κ_I are also compatible with zero with high probability. This means that if we only consider the bispectrum, α can also take any arbitrarily large value, so the constraints only come from the power spectrum.

2. If we have a detection of α from the power spectrum with a future experiment, the PDF of κ is now constrained, since from the equation (I, SS) in (5.37) we have $\kappa_I = \tilde{f}_{\rm NL}^{I,SS}/\alpha$. But κ remains compatible with zero because we have no detection of $\tilde{f}_{\rm NL}$, so we see from the equations $(I, \zeta S)$ and $(I, \zeta\zeta)$ that no additional constraint can be imposed on α or even on $\cos\Delta$.

3. Next we study the effect of fixing the κ_I without any detection. Just by looking at equation (I, SS) we see immediately that the more κ is fixed to a large value, the more the PDF of α will be contracted to 0 such that the product with κ fits with the PDF of $\tilde{f}_{\rm NL}^{I,SS}$. Actually, the same conclusion can be drawn from a combination of equations $(I, \zeta S)$ and $(I, \zeta\zeta)$. The product $\kappa_I \cos^2\Delta$ in equation $(I, \zeta\zeta)$ is constrained by the PDF of $\tilde{f}_{\rm NL}^{I,\zeta\zeta}$, so if we fix κ_I to a large enough value, the square of $\cos\Delta$ can be very small while the product $\kappa_I \cos\Delta$ can still be very big in equation $(I, \zeta S)$, pushing α towards zero.

4. Let us now study the consequences of a detection of $\tilde{f}_{\rm NL}$. Of course it is possible to have all intermediate cases where just one or some $\tilde{f}_{\rm NL}$ are detected, but let us assume the ideal case where all the $\tilde{f}_{\rm NL}$ are detected. The system (5.37) has more parameters $(\alpha, \cos\Delta, \kappa_\zeta, \kappa_S)$ than independent $\tilde{f}_{\rm NL}$. Therefore, we cannot break the degeneracy between the parameters. Moreover, if α and $\cos\Delta$ are still compatible with 0, the κ_I PDF is not bounded which would give results that are difficult to interpret even if ratios of $\tilde{f}_{\rm NL}$ with the same first index I are defined and do not depend on κ_I. For example we have that $\tilde{f}_{\rm NL}^{I,\zeta\zeta}/\tilde{f}_{\rm NL}^{I,SS} = \cos^2\Delta/\alpha$.

5. Let us assume here that we detect α in the power spectrum. This avoids the problem of unbounded κ_I. We then just need to detect one $\tilde{f}_{\rm NL}^{I,SS}$ to determine the corresponding κ_I, which will then also be detected. Thanks to the relations $(I, \zeta\zeta)$ and $(I, \zeta S)$, we could in that case improve the constraints on $\cos\Delta$ and possibly even improve the detection of α, depending on the accuracy of the $\tilde{f}_{\rm NL}$ measurements. If we also detect $\tilde{f}_{\rm NL}^{I,\zeta S}$ or $\tilde{f}_{\rm NL}^{I,\zeta\zeta}$, the detection of the correlation $\cos\Delta$ could also be performed with the joint analysis. If $\tilde{f}_{\rm NL}^{I,SS}$ is not detected, we can still have constraints from the bispectrum by detecting either the couple $\tilde{f}_{\rm NL}^{\zeta,\zeta\zeta}, \tilde{f}_{\rm NL}^{\zeta,\zeta S}$ or $\tilde{f}_{\rm NL}^{S,\zeta\zeta}, \tilde{f}_{\rm NL}^{S,\zeta S}$. This way we can determine and detect both κ_I and $\cos\Delta$. The other relation imposed by our model might then allow improvements of constraints on α and $\cos\Delta$. As we can determine the κ_I from the data in this case, there is no need to study the case where they are fixed as well.

6. We can now study the case where the isocurvature modes are detected in the power spectrum as well as their correlation with the adiabatic mode ($\cos\Delta$=0 excluded). Here again, we will have a bounded PDF for κ_I. In general, the first equations $(I, \zeta\zeta)$ lead to the smallest error bars. If the detected value of $\cos\Delta$ is small enough, the same effect that contracts the PDF of α to 0 in point 3 will here contract the PDF of α around its smallest allowed value. We can also observe an impact on the PDF of the $\tilde{f}_{\rm NL}$ itself: e.g. if $\cos\Delta$ is detected as being close to 1, then κ_ζ will be constrained by equation $(\zeta, \zeta\zeta)$ to $\kappa_\zeta \sim 1$. The detected value of α should be around 0.01 (from

current Planck constraints). Then, $(\zeta, \zeta S)$ gives $\tilde{f}_{\mathrm{NL}}^{\zeta,\zeta S} \sim \sqrt{\alpha} = 0.1$. In general, the error bars of $\tilde{f}_{\mathrm{NL}}$ from the bispectrum are much larger than 1, so this appears to be a significant improvement. But as we already said in section 5.5.1, we cannot directly compare our results to those obtained in the Planck analysis, since, unlike Planck, we assume the model (5.37) as well as a flat prior on $\boldsymbol{\xi}$.

7. If we add to the previous case a detection of $\tilde{f}_{\mathrm{NL}}$, or equivalently add the detection of $\cos\Delta$ to the case of point 5, any single $\tilde{f}_{\mathrm{NL}}$ suffices to detect the corresponding κ_I, while in point 5 it had to be $\tilde{f}_{\mathrm{NL}}^{I,SS}$ or both the others. As in point 6, effects of contraction due to small detected $\cos\Delta$ can also occur. Again, once we have constraints on κ_I, the other relations allow improving constraints on β_{iso} and $\cos\Delta$.

Next, we will study models that predict a specific non-zero value of $\cos\Delta$. This is motivated by the curvaton scenario [144, 145] that predicts a value equal to ±1. For more generality, we will also assume that there exist models predicting other values for the correlation. In these cases, we reduce the number of free parameters to three.

8. Here, we assume that the correlation is fixed to a certain non-zero value and that nothing is detected or fixed for the rest. The same mechanism already described in points 3 and 6 still holds: if we fix $\cos\Delta$ to a small enough value, κ_I can be very large and still satisfy $(I, \zeta\zeta)$, while at the same time providing strong constraints on α through $(I, \zeta S)$ or (I, SS). Furthermore, like in the cases described in points 6 and 7 where the correlation parameter is detected, we can improve the constraints on $\tilde{f}_{\mathrm{NL}}$, although the same caveats apply.

9. If we have at least a detection of $\tilde{f}_{\mathrm{NL}}^{I,\zeta\zeta}$, and independently of if we detect α in the power spectrum, the bispectrum allows to further constrain α. Because in that case we can determine κ_I from the $(I, \zeta\zeta)$ equation, and use the other two equations to constrain α. As in the previous case, that constraint will be better than with the power spectrum alone if $\cos\Delta$ is small. Furthermore, if we also detect another $\tilde{f}_{\mathrm{NL}}$, it can lead to a detection of α.

Other models, for example involving axion-like particles during inflation, predict uncorrelated adiabatic and isocurvature modes. For a review of the axion in cosmology, see [231]. Having $\cos\Delta = 0$ reduces the six equations (5.37) to only two equations:

$$\tilde{f}_{\mathrm{NL}}^{\zeta,SS} = \kappa_\zeta \alpha, \qquad \tilde{f}_{\mathrm{NL}}^{S,SS} = \kappa_S \alpha\,. \tag{5.51}$$

10. Here, the two parameters κ_I absorb all the constraints coming from the $\tilde{f}_{\mathrm{NL}}$. Using our model, the joint analysis cannot improve the constraints in the case of uncorrelated adiabatic and isocurvature modes if the κ_I are free. This conclusion is independent of if we have a detection of α and $\tilde{f}_{\mathrm{NL}}$ or not.

11. The only possibility to improve the constraints is to fix κ_I. Then we simply have that $\alpha = \tilde{f}_{\mathrm{NL}}^{I,SS}/\kappa_I$. So the more we fix κ_I to a large value, the more the PDF of α contracts to zero. In the case of a non-detection of the $\tilde{f}_{\mathrm{NL}}$, we have for $\kappa \to \infty$: $\alpha \to 0$.

12. Finally, if in addition to the previous point we have a detection of $\tilde{f}_{\mathrm{NL}}^{I,SS}$, then we have a detection of α.

Given all these theoretical results, we can now decide which cases will be the most interesting to study for each experiment. For Planck, we do not have any detection of isocurvature modes nor of $\tilde{f}_{\mathrm{NL}}$, neither in the power spectrum nor in the bispectrum. Hence, we already know that the joint analysis cannot help unless we fix κ_I or $\cos\Delta$ as in points 3 and 8. This explains the choices we made in the previous section. For future experiments like LiteBIRD and CMB-S4, we first have to determine if a detection is possible, and at what level, in the power spectrum, and the bispectrum, given the specifications of the instruments and the constraints from Planck.

5.5.3 Future experiments

In this section, we will determine for which region of parameter space the joint analysis will improve the constraints in the context of future experiments. We will then present the joint analysis results assuming a set of fiducial parameters in this region.

Separate analyses of the power spectrum and the bispectrum

We start by looking at the power spectrum alone. To study forecasts for future experiments, we have to assume a true cosmology $(\boldsymbol{\theta}^0, \beta_{\mathrm{iso}}^0, \cos\Delta^0)$ compatible with the Planck data. Then using equation (5.42), we determine the fiducial power spectra $\tilde{\mathbf{C}}_\ell^{obs} = \tilde{\mathbf{C}}_\ell(\boldsymbol{\theta}^0, \beta_{\mathrm{iso}}^0, \cos\Delta^0)$. We will naturally set all the cosmological parameters $\boldsymbol{\theta}^0$ to their best estimated value given the Planck power spectrum with one non-vanishing isocurvature mode. We set the fiducial value of $P_{SS}^{(1)}$ (from which β_{iso} is derived) to its 1σ upper value which is $P_{SS}^{(1)|0} = 4.4 \times 10^{-11}$ for the CDM isocurvature mode, $P_{SS}^{(1)|0} = 1.7 \times 10^{-10}$ for neutrino density and $P_{SS}^{(1)|0} = 1.1 \times 10^{-10}$ for neutrino velocity. In the case of no detection, the 1σ (or any other) upper limit is computed using one tail. More explicitly, the one tail 1σ upper value means the largest value after excluding 32% of the largest values.

We choose $\cos\Delta^0 = -0.1$, which is compatible with the Planck data for all three modes. To be in a more favourable case, we will push the fiducial value of β_{iso} to the upper limits of what is allowed by Planck, expressing this deviation from the Planck central value in terms of the number of σ determined from the marginalized distribution of the parameter from Planck. However, to properly judge the (un)likeliness of the β_{iso} fiducial values that we choose, we should also take into account the chosen value of $\cos\Delta^0$, since, as we see for example in figure 5.8 for the CDM isocurvature mode, these parameters are correlated. For example, a value of β_{iso} at the 1.5σ upper limit together with a small non-zero value of $\cos\Delta$ is actually likely at a level of 1σ.

In figure 5.10, we show the marginalized constraints on β_{iso} in the first row and on $\cos\Delta$ in the second, for Planck, LiteBIRD and LiteBIRD+CMB-S4. LiteBIRD alone significantly improves all constraints compared to Planck, while adding CMB-S4 further improves the correlation parameter error bars by more than 20%. The CDM isocurvature mode has a low chance of being detected by a future experiment; we obtain at most a 2σ detection for LiteBIRD+CMB-S4 for the favourable configuration where the fiducial value of the isocurvature mode is at the 1σ upper limit of what is allowed by Planck. The dashed curves in the CDM plots of figure 5.10 correspond to an even more favourable configuration: the chosen fiducial parameters are $P_{SS}^{(1)} = 6.9 \times 10^{-11}$, which is the 1.5σ upper value of Planck, and $\cos\Delta = -0.25$ that will be used in the joint analysis (this will be justified later). This configuration has a detection probability by LiteBIRD+CMB-S4 of at least 3σ for β_{iso} and more than 5σ for the correlation. On the other hand, results are

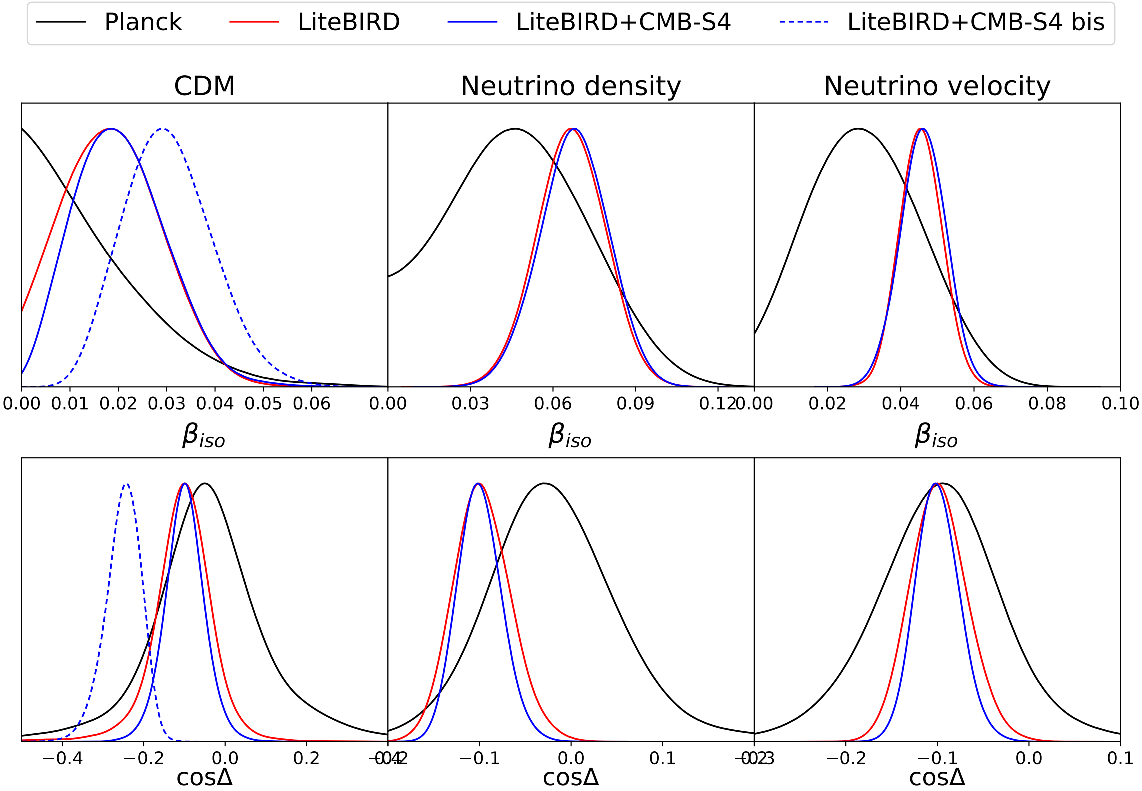

Figure 5.10: Marginalized PDF of β_{iso} (first row) and $\cos\Delta$ (second row) for Planck, LiteBIRD, and LiteBIRD+CMB-S4, for the three isocurvature modes CDM, neutrino density and neutrino velocity. These results are obtained from an analysis of the power spectrum alone. For the solid red and blue curves, we have chosen a fiducial value of β_{iso} at the 1σ upper limit of Planck and $\cos\Delta = -0.1$. The dashed blue curves show a more favourable case of fiducial values (for CDM only) of β_{iso} at the 1.5σ upper limit of Planck and $\cos\Delta^0 = -0.25$ that will be used (and justified) for the joint analysis.

more promising for the neutrino density and velocity isocurvature modes, which would be detected at respectively 5σ and 7σ with the standard configuration described above.

Next, we consider the bispectrum alone. Unlike for the power spectrum, we will use here the sum of the Fisher matrices of all experiments: Planck+LiteBIRD+CMB-S4. Including the Planck likelihood for the power spectrum would bias our analysis because we chose for the isocurvature parameters fiducial values different from those maximizing the Planck likelihood. Furthermore, adding the Planck power spectrum likelihood to the one for LiteBIRD and CMB-S4 does not improve the constraints on β_{iso} and $\cos\Delta$ significantly. However, for the bispectrum the situation is different. Adding the Planck Fisher matrix of the $\tilde{f}_{\text{NL}}$ to the LiteBIRD and CMB-S4 Fisher matrices improves some $\tilde{f}_{\text{NL}}$ constraints depending on the modes. Figures 1 and 2 of [107] show that the constraints on the different modes are not equally improved by temperature and polarization measurements. For example, the neutrino density mode is mostly constrained (71%) by temperature measurements alone. Hence Planck, which has a nearly optimal measurement of the temperature anisotropies, cannot be neglected. On the other hand, the polarization has a larger impact on the neutrino velocity mode, since temperature-only contributes here at a level of only 17%. For these reasons, there is a benefit in considering jointly Planck, LiteBIRD, and CMB-S4 for the bispectrum.

For this study, we need to fix each fiducial value $\tilde{f}_{\rm NL}^0$ such that they are compatible with the Planck results. Assuming our model, we determine each $\tilde{f}_{\rm NL}^0$ by using equations (5.37). To do so, let us define the vector $\boldsymbol{\kappa}$ and the matrix $\mathcal{M}$:

$$\boldsymbol{\kappa} = \begin{pmatrix} \kappa_\zeta \\ \kappa_S \end{pmatrix}, \qquad \mathcal{M} = \begin{pmatrix} \cos^2\Delta & \cos\Delta\sqrt{\alpha} & \alpha & 0 & 0 & 0 \\ 0 & 0 & 0 & \cos^2\Delta & \cos\Delta\sqrt{\alpha} & \alpha \end{pmatrix}. \tag{5.52}$$

In order to choose the fiducial values κ_I^0 given $\beta_{\rm iso}^0$ and $\cos\Delta^0$, we want to determine the best estimated value of Planck given the PDF of equation (5.50). Using equation (5.52), we substitute $\tilde{\mathbf{f}}_{\rm NL}$ by κ in (5.50):

$$-2\ln P = \left(\mathcal{M}^T\boldsymbol{\kappa} - \tilde{\mathbf{f}}_{\rm NL}^{\mathbf{0}}\right)^T \mathbf{F} \left(\mathcal{M}^T\boldsymbol{\kappa} - \tilde{\mathbf{f}}_{\rm NL}^{\mathbf{0}}\right). \tag{5.53}$$

The best estimated value, $\hat{\boldsymbol{\kappa}}$, is the vector which maximizes the PDF (5.53). We find the following best estimated value and the covariance matrix of the parameters:

$$\hat{\boldsymbol{\kappa}} = \boldsymbol{\Sigma}\mathcal{M}\mathbf{F}\tilde{\mathbf{f}}_{\rm NL}^{\mathbf{0}}, \qquad \boldsymbol{\Sigma} = \left(\mathcal{M}\mathbf{F}\mathcal{M}^T\right)^{-1}. \tag{5.54}$$

For a fixed couple $\beta_{\rm iso}^0$ (and hence α^0) and $\cos\Delta^0$, we now have to choose the κ_I^0 such that they give $\tilde{f}_{\rm NL}$ compatible with Planck measurements. Moreover, we define the signal-to-noise N of $\tilde{f}_{\rm NL}$ as:

$$N^{I,JK}(\kappa_I^0, \cos\Delta^0, \beta_{\rm iso}^0) = \frac{\left|\tilde{f}_{\rm NL}^{I,JK|0}(\kappa_I^0, \cos\Delta^0, \beta_{\rm iso}^0)\right|}{\sqrt{F_{I,JK}^{-1}}}, \tag{5.55}$$

where $\sqrt{F_{I,JK}^{-1}}$ means the marginalized errors on each $\tilde{f}_{\rm NL}^{I,JK}$ given a future experiment, which correspond to the square root of the diagonal entries of the inverse of the Fisher matrix. For LiteBIRD and CMB-S4, the values are given in table 5.5.

In the case where the isocurvature mode amplitude is detected in the power spectrum, the joint analysis of the power spectrum and the bispectrum will bring further constraints if we detect either the $\tilde{f}_{\rm NL}^{I,SS}$ or the couple $(\tilde{f}_{\rm NL}^{I,\zeta\zeta}, \tilde{f}_{\rm NL}^{I,\zeta S})$ for a fixed I, which gives us 4 possibilities in total (see point 5 of section 5.5.2). If, in addition, we also detect the correlation, only one $\tilde{f}_{\rm NL}$ needs to be detected in order to improve the constraints (see point 7 of section 5.5.2). In figure 5.11, we give the $(\beta_{\rm iso}, \cos\Delta)$ constraints from Planck in red. In order to determine for which region of parameter space the constraints would be improved by the joint analysis, we calculate for each couple $(\beta_{\rm iso}, \cos\Delta)$, the best estimation $\hat{\boldsymbol{\kappa}}$ and the error Σ using equation (5.54). Then, using equation (5.55), we calculate the signal-to-noise $N^{I,JK}(\hat{\kappa}_I \pm \sqrt{\Sigma_I}, \beta_{\rm iso}, \cos\Delta)$. The green bands correspond to the region of the parameter space where at least one $N^{I,SS}$ is larger than 4. Similarly, the orange bands correspond to ($N^{I,\zeta\zeta} > 4$ and $N^{I,\zeta S} > 4$) and $N^{I,SS} < 4$ and the black bands correspond to ($N^{I,\zeta\zeta} > 4$ or $N^{I,\zeta S} > 4$) and $N^{I,SS} < 4$. The signal-to-noise coefficients have been calculated using the Planck+LiteBIRD+CMB-S4 Fisher matrix.

Given point 5 of section 5.5.2, if we detect the amplitude of the isocurvature mode but not the correlation using the power spectrum alone, the joint analysis would improve constraints for the ensemble of the fiducial values represented in green and orange. Given point 7 of section 5.5.2, if we detect both the amplitude and the correlation with the power spectrum alone, the joint analysis would improve the constraints for the ensemble of fiducial parameters represented in green, orange, and black. The first (second) row

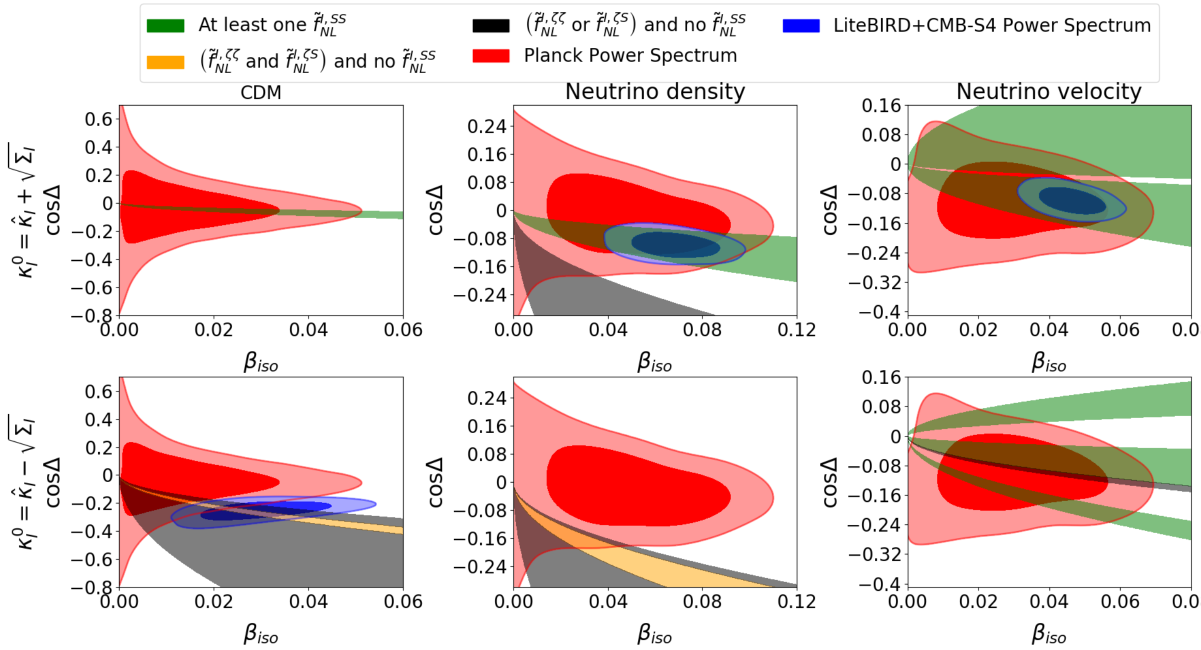

Figure 5.11: Constraints from the power spectrum alone for Planck, in red, and for LiteBIRD+CMB-S4, in blue (see the main text to understand the position of these blue contours). The green bands show the regions of the $(\beta_{\rm iso}, \cos\Delta)$ space where one of the $\tilde{f}_{\rm NL}^{I,SS}$ will be detected by these future experiments given the indicated chosen value of κ_I. The region in orange indicates the set of fiducial parameters where none of the $\tilde{f}_{\rm NL}^{I,SS}$ are detected but where we detect the couple $(\tilde{f}_{\rm NL}^{I,\zeta\zeta}, \tilde{f}_{\rm NL}^{I,\zeta S})$. Similarly, the region in black indicates the set of fiducial parameters where none of the $\tilde{f}_{\rm NL}^{I,SS}$ are detected but where we detect one (and one only) of the parameters $(\tilde{f}_{\rm NL}^{I,\zeta\zeta}, \tilde{f}_{\rm NL}^{I,\zeta S})$. If we detect the isocurvature amplitude in the green or the orange region and if we do not detect the correlation parameter, then we are in the situation of point 5 of section 5.5.2 and the joint analysis will improve the constraints. If we detect the isocurvature amplitude in the green, orange or black regions and we also detect the correlation parameter, then we are in the situation of point 7 and the joint analysis will also improve the constraints. The κ_I^0 are chosen at the $\pm 1\sigma$ value (first and second row, respectively). All the bands are calculated using the Planck+LiteBIRD+CMB-S4 constraints.

corresponds to a fiducial value of κ such that the $\tilde{f}_{\rm NL}$ are at the 1σ upper (lower) value from their maximum probability for the Planck data. The blue contours correspond to the solid blue curves in figure 5.10 for neutrino density and neutrino velocity and to the dashed blue curve for CDM.

Let us choose for each mode a couple $(\beta_{\rm iso}^0, \cos\Delta^0)$ in one of the bands that will give at least a detection of the amplitude in the power spectrum. For CDM, the 1σ upper value of κ_I^0 leaves us a very thin green band close to $\cos\Delta = 0$. We could choose our fiducial parameters in this band, but to detect the amplitude in the power spectrum, we need a 2σ Planck compatible value of $\beta_{\rm iso}$. Instead we choose the 1σ lower value of κ_I^0, but this still requires fiducial values at the edge of the 2σ Planck contour in order to have a detection of $\beta_{\rm iso}$, $\cos\Delta$ and satisfy point 7. Our choice is arbitrary since none of the two possibilities is statistically more likely. The configuration we choose gives the marginalized PDF of the dashed blue curves in the CDM plots of figure 5.10.

For neutrino density and velocity, the total parameter space, in which the fiducial

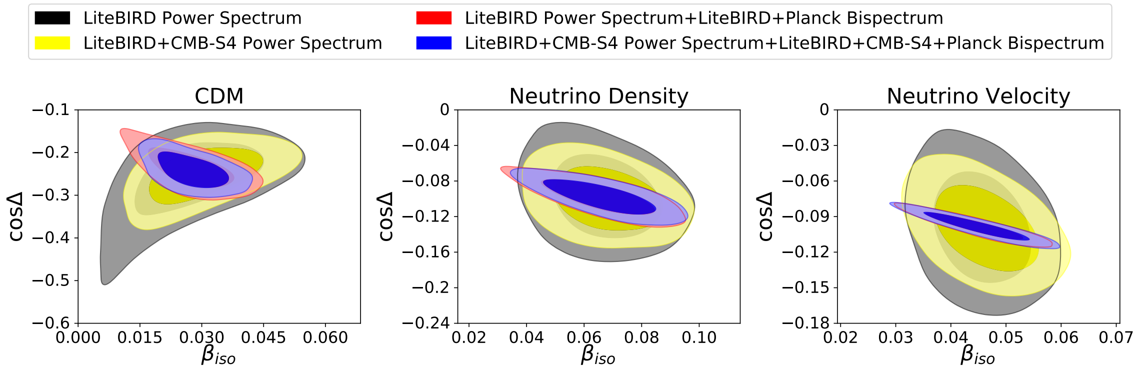

Figure 5.12: Constraints in the $(\beta_{\text{iso}}, \cos\Delta)$ space for the case of CDM (left), neutrino density (center), and neutrino velocity isocurvature (right). The different colors show constraints from the power spectrum alone and from the joint analysis of the power spectrum and the bispectrum, of LiteBIRD with and without CMB-S4, as indicated in the legend.

values can be chosen in order to have better constraints with the joint analysis, is larger than for the CDM case. In particular for the neutrino velocity mode more than half of the 1σ Planck contour is covered by the green band, as can be seen in the top right of figure 5.11. Instead of having to consider a more favorable case as for CDM, for the neutrino modes, we can safely keep the fiducial values used for the solid blue curves in the neutrino plots of figure 5.10 and take the 1σ upper value for κ_I. The power spectrum analysis for LiteBIRD+CMB-S4 given all these final fiducial values gives us the blue contours in figure 5.11. We have chosen not to put any blue contours in the subplots with the values of κ that we do not use for our subsequent analysis.

Joint analysis

In section 5.5.3, we have determined the fiducial values of the isocurvature parameters for which the joint analysis will provide a clear improvement compared to an analysis with the power spectrum alone. We choose the fiducial values for the isocurvature mode power spectrum amplitude $P_{SS}^{(1)|0} = 6.9 \times 10^{-11}$ for CDM, $P_{SS}^{(1)|0} = 1.7 \times 10^{-10}$ for neutrino density and $P_{SS}^{(1)|0} = 1.1 \times 10^{-10}$ for neutrino velocity, which are compatible with the Planck results while being significantly detectable by LiteBIRD, thus avoiding the parameters κ_I to be unbounded which would lead to results that are difficult to interpret. Furthermore, we have shown that the fiducial value of the correlation $\cos\Delta$ has a strong impact on the $\tilde{f}_{\text{NL}}$ detection. To see the effect of the bispectrum constraints, we have chosen the correlation and the κ_I such that they verify point 7 for CDM and point 5 for neutrino density and velocity. Fiducial parameters are for CDM $P_{\zeta S}^{(1)|0} = -1.0 \times 10^{-10}$, for neutrino density $P_{\zeta S}^{(1)|0} = -6.3 \times 10^{-11}$ and for neutrino velocity $P_{\zeta S}^{(1)|0} = -5.1 \times 10^{-11}$.

The results for the β_{iso} and $\cos\Delta$ constraints are shown in figure 5.12 for each isocurvature mode, both for the analysis of the power spectrum alone and the joint analysis, and both excluding and including the contribution of CMB-S4. We show results in the $(\beta_{\text{iso}}, \cos\Delta)$ space, because we expect the bispectrum to bring further constraints in this parameter space. As we have seen in figure 5.10, the addition of CMB-S4 to LiteBIRD does not significantly improve the marginalized β_{iso} constraints in a power-spectrum-only analysis, while there is some improvement for $\cos\Delta$. As always, the marginalized distri-

		$\Omega_b h^2$	$\Omega_c h^2$	τ	$100\theta_{MC}$	$\log 10^{10} A_s$
CDM	PS	5.1e-05	0.00044	0.0023	0.00013	0.0058
	PS+B	5.1e-05	0.00044	0.0022	0.00013	0.0053
	improvement	No	No	No	No	9%
ND	PS	4.5e-05	0.00038	0.0023	0.00015	0.0063
	PS+B	4.6e-05	0.00037	0.0023	0.00012	0.0051
	improvement	No	No	No	20%	19%
NV	PS	4.5e-05	0.00039	0.0025	0.00015	0.0082
	PS+B	4.7e-05	0.00038	0.0025	0.00011	0.0057
	improvement	No	No	No	30%	31%

		n_s	β_{iso}	$\cos\Delta$	κ_ζ	κ_S
CDM	PS	0.0021	0.009	0.045		
	PS+B	0.0022	0.006	0.028	133	1767
	improvement	No	35%	38%		
ND	PS	0.0017	0.012	0.024		
	PS+B	0.0015	0.013	0.013	428	3567
	improvement	10%	No	45%		
NV	PS	0.0016	0.006	0.024		
	PS+B	0.0016	0.006	0.008	897	549
	improvement	No	No	67%		

Table 5.7: Marginalized 1σ uncertainties of the six cosmological parameters and the four parameters of our model obtained for each isocurvature mode (ND/NV being neutrino density and neutrino velocity, respectively) from the LiteBIRD+CMB-S4 power spectrum (PS) likelihood and from the LiteBIRD+CMB-S4+Planck bispectrum likelihood for the joint analysis (PS+B). The third line of each isocurvature mode shows the percentage of improvement of the error bars for the joint analysis compared to the analysis of the power spectrum alone. If the absolute value of the improvement is smaller than 5%, we consider it as being not significant and then write simply “No”.

butions just contain partial information; here in figure 5.12 we can see the improvement of the 2D contours (yellow versus gray). We also see a small improvement in the joint analysis results when adding CMB-S4 (blue versus red). The most important contribution of CMB-S4, in our analysis, is to increase the detection of some $\tilde{f}_{\mathrm{NL}}$ and thus to increase the size of the bands in parameter space where the joint analysis is useful, see figure 5.11. The quantitative results of the rest of this section, for example, the error bars summarized in table 5.7, are for LiteBIRD+CMB-S4.

The CDM isocurvature mode constraints are improved significantly by the joint analysis of the power spectra and bispectra. We detect in this case $\tilde{f}_{\mathrm{NL}}^{S,\zeta\zeta}$ (5.7σ) and $\tilde{f}_{\mathrm{NL}}^{S,\zeta S}$ (4.0σ). Thanks to the relation $(S,\zeta\zeta)$ of (5.37), we detect κ_S and obtain: -6243^{+3564}_{-5830} (99% confidence level), while the fiducial value is -5788. The relation (S,SS) then improves the uncertainty of β_{iso} to 0.006. Thus, in table 5.7 we see that adding the bispectrum improves the detection of β_{iso} by 35%. Moreover, very small values of $\cos\Delta$ are suppressed, which improves the error bars of the correlation by 38%.

For the neutrino density isocurvature mode, we detect $\tilde{f}_{\mathrm{NL}}^{S,SS}$ at a level of 7σ. This allows a detection of κ_S with a measured value of 13362^{+11539}_{-7056} (99% CL) for a fiducial value of 12611. The constraints on $\tilde{f}_{\mathrm{NL}}^{S,\zeta\zeta}$ and $\tilde{f}_{\mathrm{NL}}^{S,\zeta S}$ improve the error bars of the correlation $\cos\Delta$

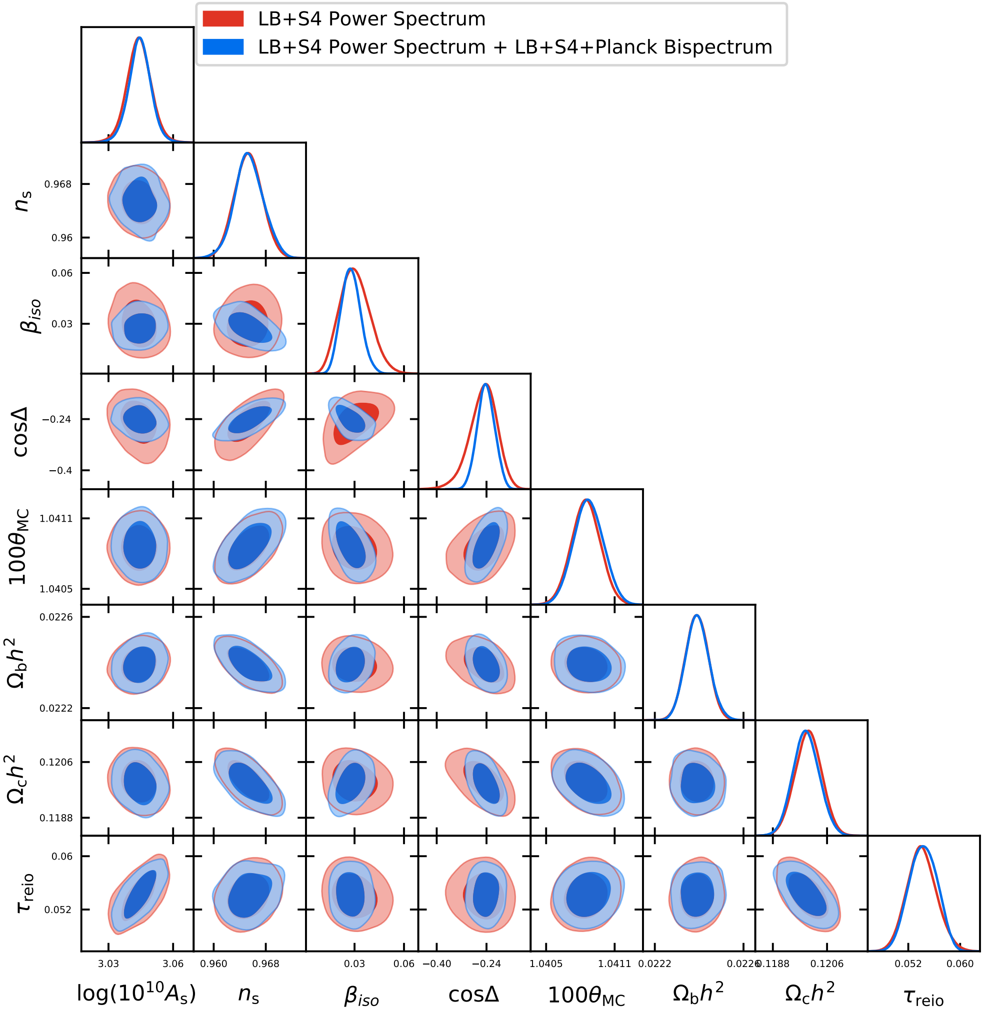

Figure 5.13: Two dimensional 68% and 95% contours assuming ΛCDM plus a CDM isocurvature mode for LiteBIRD+CMB-S4 (+Planck for the bispectrum). The red contours show the results from the power spectrum alone and the blue contours the results from the joint analysis.

by 45%. However, there is no improvement of $\beta_{\rm iso}$.

For the neutrino velocity isocurvature mode, both $\tilde{f}_{\rm NL}^{\zeta,\zeta S}$ and $\tilde{f}_{\rm NL}^{\zeta,SS}$ are detected, at a level of 11σ and 7σ, respectively. Thanks to relation (ζ, SS), κ_ζ is detected and we find 4836^{+3073}_{-1741} (99% CL) for a fiducial value of 4653. Actually we also detect $\tilde{f}_{\rm NL}^{S,SS}$ at the level of 4σ, but this has only a weak influence on the error bars of $\beta_{\rm iso}$ and $\cos\Delta$, although it gives a detection of κ_S with a measured value of 2455^{+1849}_{-1133} (99% CL) for a chosen fiducial value of 2346. Relation $(\zeta, \zeta S)$ provides a detection of the correlation $\cos\Delta$ at the level of 12σ. The error bars of the correlation parameter are also constrained significantly thanks to the $(\zeta, \zeta\zeta)$ relation. The final uncertainty on the correlation parameter will shrink by 67% in this configuration thanks to the joint analysis. As in the case of neutrino density, the parameter $\beta_{\rm iso}$ is not affected since all $\tilde{f}_{\rm NL}$ constraints are absorbed by κ_I and $\cos\Delta$.

Figures 5.13, 5.14 and 5.15 show the 2D contours for all pairs of the parameters of the model (excluding the κ parameters), and provide an estimation of the correlation between the parameters. For all isocurvature modes we observe an anti-correlation between $\beta_{\rm iso}$ and $\cos\Delta$ (except for the case of CDM power spectrum only because of the lack of a detection

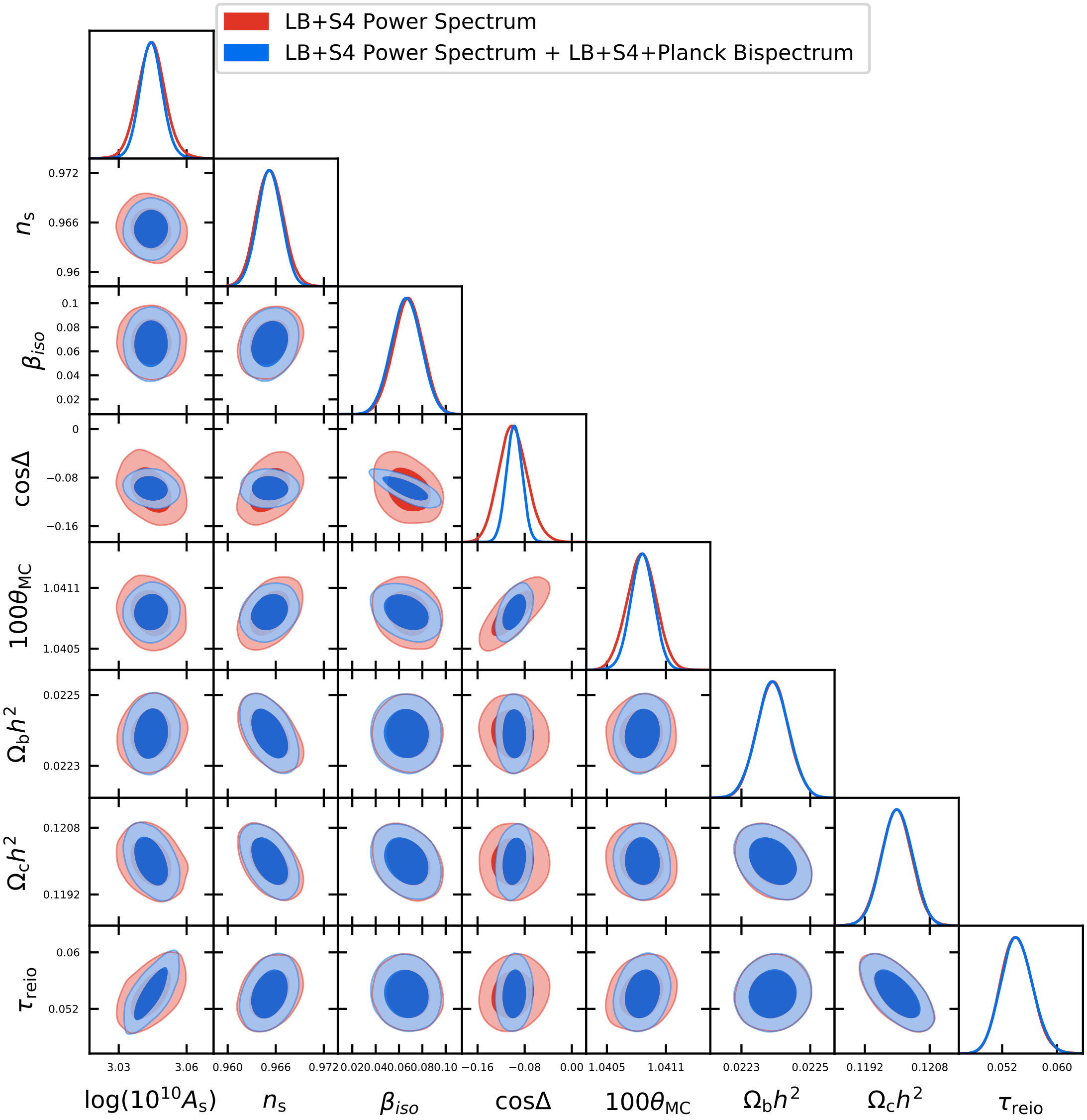

Figure 5.14: Same as figure 5.13 but for the neutrino density isocurvature mode.

of $\beta_{\rm iso}$). It can be understood as follows: both $\beta_{\rm iso}$ and the correlation parameter lead to an increase of the power spectrum, so one parameter can be compensated by the other and lead to a similar amplitude of the power spectrum.

The improvement of the constraints on the correlation parameter $\cos\Delta$ coming from the bispectrum also induces improvements on the constraints of the cosmological parameters that are correlated with $\cos\Delta$, as can be seen in table 5.7. The cosmological parameters that are correlated most with $\cos\Delta$ for all isocurvature modes are A_s, n_s, and θ_{MC}. We observe for the neutrino modes in figures 5.14 and 5.15 an anti-correlation between $\cos\Delta$ and A_s, which is always suppressed by the joint analysis. The marginalized error of A_s is improved by 19% and 31% for neutrino density and neutrino velocity, respectively. We see in those figures a reduction of the A_s uncertainty independently of $\cos\Delta$. This means that the bispectrum constrains A_s directly. The effect of the bispectrum is very weak in the case of the CDM isocurvature mode in figure 5.13, only 9% of improvement, probably because this mode is only detected at 2σ.

The constraints on n_s mostly come from the relative amplitude of the power spectrum

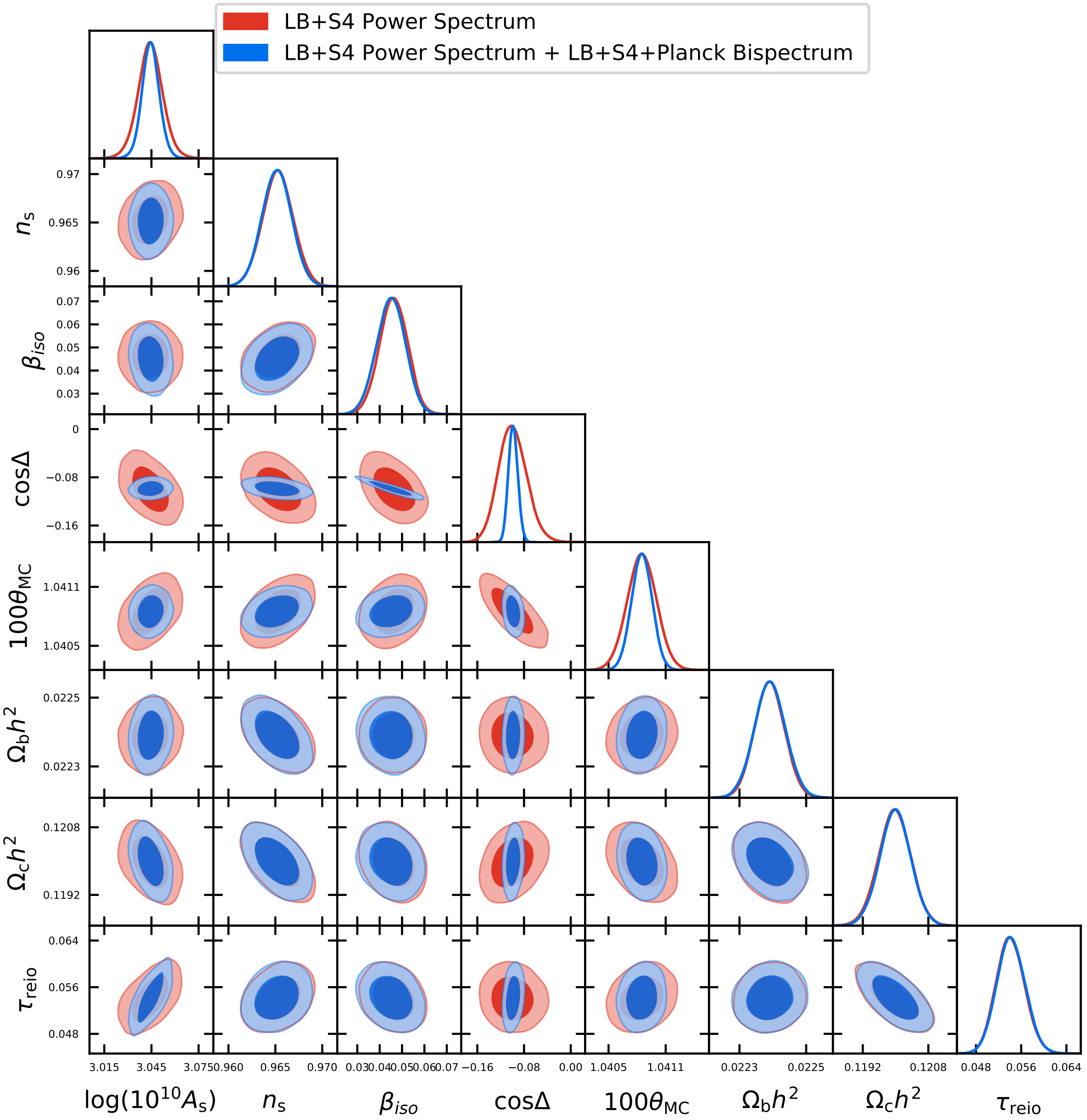

Figure 5.15: Same as figure 5.13 but for the neutrino velocity isocurvature mode.

between small ℓ and large ℓ. The CDM isocurvature mode contributes most at low ℓ. As in figure 2 of [113], increasing $\cos\Delta$ will increase the low-ℓ part of the total power spectrum, which corresponds to a small n_s. It can then be compensated by a larger n_s which means that the parameters are correlated. For neutrino density, the relative amplitude between low-ℓ and the second peak is almost unity, while for the adiabatic mode, the second peak is roughly two times higher. Thus, increasing $\cos\Delta$ will decrease the ratio between the low-ℓ and the second peak amplitudes, which corresponds to a smaller n_s. This leads to a correlation between $\cos\Delta$ and n_s as with the CDM isocurvature mode. On the contrary, the neutrino velocity isocurvature mode has a larger contribution to the second peak compared to the low-ℓ part (see once more figure 2 of [113]). Hence we find here an anti-correlation between $\cos\Delta$ and n_s. The joint analysis breaks this correlation only for neutrino density and then improves the marginalized error bar of n_s by 10% in that case. No significant improvement is observed for the other modes.

The constraints on θ_{MC} come from the positions of the peaks in the power spectrum. As we can see in figure 2 of [113], all isocurvature-adiabatic cross power spectra are phase-

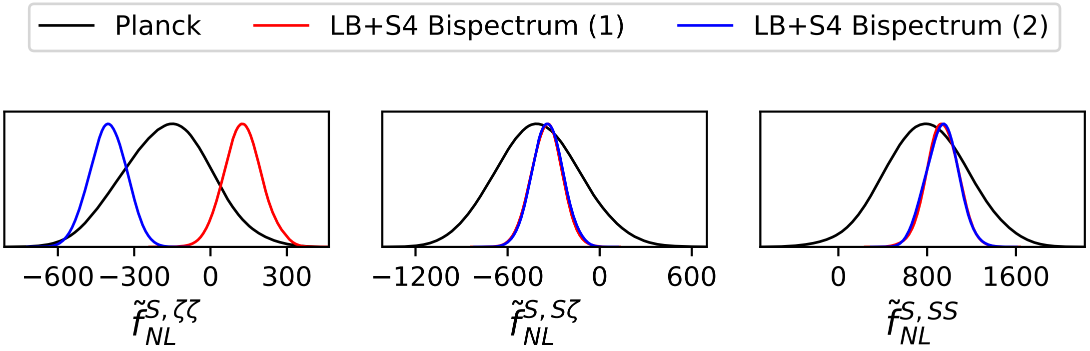

Figure 5.16: Marginalized constraints for $\tilde{f}_{\rm NL}^{S,IJ}$ for the case of neutrino density isocurvature. In black the model-independent (bispectrum-only) Planck results. In red, the bispectrum-only LiteBIRD+CMB-S4 constraints, assuming fiducial values computed with (5.37) using the same $(\beta_{\rm iso}^0, \cos\Delta^0, \kappa_I^0)$ as in section 5.5.3. The blue curves are similar to the red ones but with a different fiducial value for $\tilde{f}_{\rm NL}^{S,\zeta\zeta}$.

shifted compared to the pure adiabatic mode. Thus increasing $\cos\Delta$ will automatically shift the position of the peaks and hence directly affect the estimation of θ_{MC}. As can be seen in figures 5.13 and 5.14, for the CDM and neutrino density isocurvature modes, there is a positive correlation between the $\cos\Delta$ and θ_{MC} parameters, because increasing $\cos\Delta$ shifts the position of the peaks to higher ℓ since the density isocurvature modes have their first peaks on the right of the adiabatic first peak. On the contrary, the neutrino velocity isocurvature mode, which is roughly the derivative of the neutrino density mode and hence is in counter phase with the latter, has its peak on the left of the adiabatic one. This gives an anti-correlation between the $\cos\Delta$ and θ_{MC} parameters. The joint analysis, by improving the $\cos\Delta$ constraint, is then able to improve the θ_{MC} error bar by 20% and 30% for the neutrino density and velocity isocurvature modes, respectively. There is only a small improvement for the CDM isocurvature mode since the correlation between $\cos\Delta$ and θ_{MC} is weak.

Excluding the model with future experiments

Up to this point, we have investigated the improvements a joint analysis of the power spectrum and the bispectrum can provide regarding the constraints (or detection) of the isocurvature parameters. To make a joint analysis possible, we assumed the quite general class of inflation models described in section 5.3.4. However, it is also interesting to see if it would be possible to rule out this class of inflation models with LiteBIRD and CMB-S4. This turns out to be the case, if the values detected by LiteBIRD/CMB-S4, while being compatible with Planck, do not satisfy the relations discussed in section 5.3.4.

Among those relations, equation (5.39) implies that $\tilde{f}_{\rm NL}^{I,\zeta\zeta}$ and $\tilde{f}_{\rm NL}^{I,SS}$ must share the same sign, and this can be tested using just a bispectrum-only analysis. In figure 5.16, we show Planck's model-independent (bispectrum-only) estimation of the $\tilde{f}_{\rm NL}^{S,IJ}$ for the case of neutrino density in black. The red and blue curves are two LiteBIRD+CMB-S4 bispectrum constraints that differ in their choice of fiducial value for $\tilde{f}_{\rm NL}^{S,\zeta\zeta}$: the red curve corresponds to the choices made in section 5.5.3, while for the case in blue we have changed the fiducial value of $\tilde{f}_{\rm NL}^{S,\zeta\zeta}$ in order to get a detection at a negative value. As in this blue case $\tilde{f}_{\rm NL}^{I,\zeta\zeta}$ and $\tilde{f}_{\rm NL}^{I,SS}$ have different signs at a high level of confidence, such a detection would rule out the class of models (5.35).

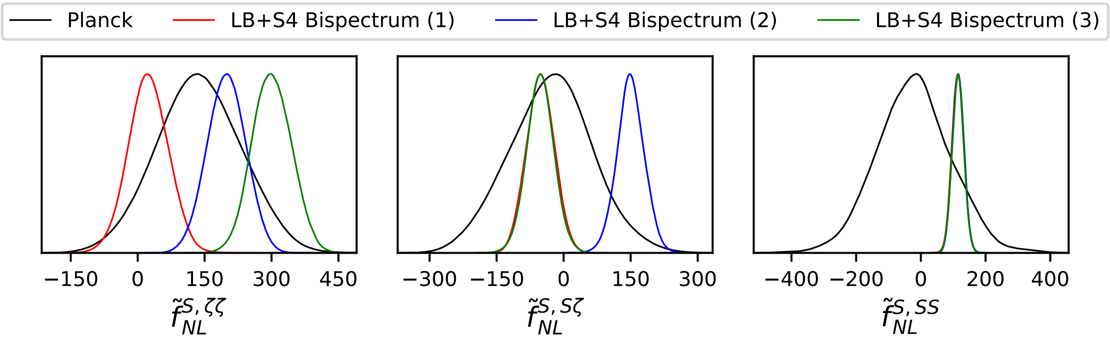

Figure 5.17: Marginalized constraints for $\tilde{f}_{\rm NL}^{S,IJ}$ for the case of neutrino velocity isocurvature. Black and red curves are the same as in figure 5.16 but for neutrino velocity. The blue and green curves are similar to the red ones but with different fiducial values for $\tilde{f}_{\rm NL}^{S,\zeta\zeta}$ (blue and green) and $\tilde{f}_{\rm NL}^{S,\zeta S}$ (blue only).

The test above required only an analysis of the bispectrum. Next, we investigate if adding information from the power spectrum can rule out the model in cases where the bispectrum alone would not suffice. In figure 5.17, which is similar to figure 5.16 but for neutrino velocity, we show again the Planck model-independent bispectrum-only constraints in black and, this time, three cases of LiteBIRD+CMB-S4 constraints with different Planck-compatible fiducial values, in red, blue, and green. The red curves show the same choice of fiducial parameters as in section 5.5.3, and hence they are by construction compatible with the model. The blue curves show a set of fiducial values that would invalidate the model thanks to combining information from the power spectrum and the bispectrum. Indeed, we have here a detection of all $\tilde{f}_{\rm NL}^{S,IJ}$ at a positive value. However, if we also detect a negative correlation $\cos\Delta$ in the power spectrum like in section 5.5.3, the model would be ruled out, since another prediction of the model is that if $\tilde{f}_{\rm NL}^{I,\zeta\zeta}$ and $\tilde{f}_{\rm NL}^{I,SS}$ are both positive, then $\tilde{f}_{\rm NL}^{I,\zeta S}$ must have the same sign as the correlation $\cos\Delta$.

The third case in figure 5.17, in green, corresponds also to a set of fiducial values that would rule out the model thanks to combining information from the power spectrum and the bispectrum. In this case, $\tilde{f}_{\rm NL}^{S,SS}$ is detected at more than 6σ: 114 ± 18. If we assume that we detect the relative amplitude $\beta_{\rm iso}$ (and hence α) and the correlation $\cos\Delta$ of the neutrino velocity isocurvature mode thanks to the power spectrum at the same values as in section 5.5.3, then equation (S, SS) of (5.37) would give us $\kappa_S = 2425 \pm 526$. That, in its turn, would lead to the following prediction from equation $(S, \zeta\zeta)$: $\tilde{f}_{\rm NL}^{S,\zeta\zeta} = 23 \pm 13$. However, as we see in figure 5.17, this is excluded at more than 5σ with the bispectrum analysis.

These three examples show that LiteBIRD+CMB-S4 will potentially be able to exclude the class of models (5.35) that we have assumed for the joint analysis, depending on what values for the different parameters will finally be observed. In the first example, the bispectrum-only analysis is enough to exclude the model. In the other two examples, we need to add information from the power spectrum. Thus, combining information from the power spectrum and the bispectrum can allow us to check if the model is consistent with the data.

5.6 Conclusion

The presence of isocurvature modes (in addition to the dominant adiabatic mode) in the CMB would be a direct proof that the cosmological perturbations are produced by at least two primordial degrees of freedom, which in the context of the inflationary paradigm would mean multi-field inflation. Hence this would rule out single-field inflation, which for the moment is still consistent with all observations. Given the matter content of the universe, we have three possible isocurvature modes: CDM density, neutrino density, and neutrino velocity (a fourth possibility, a baryon density isocurvature mode, is observationally indistinguishable from the CDM mode in the CMB, and hence will not be considered separately here). The Planck power spectrum analysis did not find any sign of these isocurvature modes and put tight constraints on their amplitudes [121]. Similarly, the Planck bispectrum analysis did not detect any isocurvature non-Gaussianity (nor any other type of primordial non-Gaussianity in fact) [107].

In this second part of the thesis, based on our paper [205], we have performed a joint analysis of the power spectrum and the bispectrum in order to improve the isocurvature constraints using the Planck data, and we have made forecasts for the future satellite LiteBIRD and the future ground-based CMB-S4 experiments. To do so, we need to assume a model that allows us to express both the power spectrum observables and the bispectrum observables in terms of a set of common model parameters. In our choice of model, we had to make a compromise between, on the one hand, keeping the model as general as possible so that our analysis applies to as broad a class of inflation models as possible, and, on the other hand, keeping the number of additional free parameters limited, otherwise we do not get any meaningful constraints. This compromise led us in the first place to consider only two-field inflation models, with a single isocurvature mode (which can be any of the three mentioned above) in addition to the adiabatic mode. Secondly, we assumed that one of the fields dominates both the linear isocurvature mode and the second-order (non-Gaussian) parts of the adiabatic and the isocurvature mode, the other field only contributing to the linear adiabatic mode (see (5.35)). For the rest, however, this model is completely general. It is the same model as considered in the last section of [113] and has five free parameters, one of which is fixed by the adiabatic amplitude of the power spectrum. Hence our model has four extra parameters compared to the standard ΛCDM cosmology, which can be viewed as the isocurvature amplitude of the power spectrum β_{iso}, the linear correlation between the adiabatic and the isocurvature mode $\cos\Delta$, and the adiabatic and isocurvature bispectrum amplitudes κ_ζ and κ_S. The power spectrum only depends on the first two. As was explained in [113], in such a configuration there are six different $\tilde{f}_{\text{NL}}^{I,JK}$ parameters (with $I, J, K = \zeta, S$ and symmetric under interchange of J and K, where ζ indicates the adiabatic mode and S the isocurvature mode) that can be extracted from the bispectrum, although the relations imposed by the model mean that only three of them are independent.

First, we applied our methodology to the Planck data. We built a joint power spectrum and $\tilde{f}_{\text{NL}}$ likelihood, which is simply the product of the two likelihoods as we argue that they can be considered to be statistically independent. We used the Planck 2018 likelihood for the power spectrum. In addition to the cosmological parameters, we have estimated all the nuisance parameters including those of the foregrounds. As a full bispectrum likelihood cannot be calculated, we consider a much simpler $\tilde{f}_{\text{NL}}$ likelihood based on the Fisher matrix. This is nonetheless a nearly optimal procedure, because it is directly related to the fact that the $\tilde{f}_{\text{NL}}$ estimator (5.33) is nearly optimal. We have shown that in the general case where all four additional parameters are left free, the joint analysis is not useful for Planck: it does not give better constraints than the power spectrum alone. We also gave a theoretical argument for why this must be so with no detection of isocurvature modes in the power spectrum and no detection of non-Gaussianity (any constraints coming from the bispectrum can be absorbed by the κ in this case).

However, if we consider a more restricted class of models where either $\cos\Delta$ or the κ's are fixed to a specific non-zero value (certain curvaton models predict for example $\cos\Delta = \pm 1$), then the joint analysis can improve the constraints even in the case of Planck. In particular, we showed that for $|\kappa| > 10^3$ fixed, the joint analysis will give better constraints on β_{iso} and $\cos\Delta$ than the power spectrum alone. The larger κ is, the smaller the allowed interval of those parameters around zero is, and hence the closer to a pure ΛCDM cosmology we are. Similarly, for a fixed value of $|\cos\Delta| \leq 0.1$ (but distinct from zero) the joint analysis improves the constraints on β_{iso} (and pushes the most likely value of κ upwards). Remarkably, for such values of $\cos\Delta$ in the case of the neutrino velocity isocurvature mode, the joint analysis even seems to indicate a detection of β_{iso} at the level of 3–4σ. However, because of different reasons including the differences between the Fisher error bars and the simulation-based error bars for exactly those $\tilde{f}_{\text{NL}}$ components on which this conclusion is based, we consider this to be a statistical fluke.

Going beyond Planck, to future experiments like LiteBIRD and CMB-S4, we use a simplified model of the observations without foreground residuals and a simplified power spectrum likelihood. We should keep in mind that foregrounds could have an impact on parameter estimation by correlating modes in the power spectrum/bispectrum estimation. Although, in the case of Planck, comparisons between forecasts [113] and real results have shown that the effect of foreground residuals is small for adiabatic and isocurvature $\tilde{f}_{\text{NL}}$ estimation. Forecasts for isocurvature parameter estimation from the power spectrum, like in [232–234], are also in good agreement with the real Planck results. However, the impact of foreground residuals in the case of LiteBIRD and CMB-S4, and for the joint analysis, must still be studied carefully in the future, as well as other effects like anisotropic noise, although the scanning strategy of LiteBIRD with a large precession angle will lead to a more uniform coverage than for Planck. For completeness' sake, let us recall here all the other assumptions we made (not only for LiteBIRD and CMB-S4 but also for Planck): all spectral indices are equal, only one isocurvature mode is considered at a time in addition to the adiabatic mode and the correlation of the two, the cosmological parameters are fixed in the bispectrum analysis to find the $\tilde{f}^{0}_{\text{NL}}$, we assumed a two-field model where only one field contributes to the isocurvature mode and the non-Gaussianity, as well as statistical independence of the two- and three-point statistics.

Our theoretical assessment showed that in the general case (leaving all four parameters free) the joint analysis can improve the constraints if two conditions are satisfied. Firstly, the isocurvature mode amplitude β_{iso} must be detected in the power spectrum, otherwise, the parameter space to sample is infinite and strongly degenerate, which gives results that are difficult to interpret. Secondly, one of the two κ_I must be detected. This means that one must detect either one of the two $\tilde{f}^{I,SS}_{\text{NL}}$ (for $I = \zeta$ or S), or both $\tilde{f}^{I,\zeta\zeta}_{\text{NL}}$ and $\tilde{f}^{I,\zeta S}_{\text{NL}}$ with the same first index I. If in addition, we have a detection of the correlation $\cos\Delta$ in the power spectrum, then even detecting any single $\tilde{f}^{I,JK}_{\text{NL}}$ suffices. We constructed a combined power spectrum and $\tilde{f}_{\text{NL}}$ likelihood for LiteBIRD and CMB-S4 and investigated in what region of the $(\beta_{\text{iso}}, \cos\Delta)$ parameter space compatible with the Planck results these conditions are satisfied, given also fiducial values for the κ parameters compatible with Planck within 1σ. In all our results we found that LiteBIRD is the main driver of the improvements compared to Planck, with CMB-S4 providing only a marginal further improvement.

For the CDM isocurvature mode we found that, given the current Planck constraints, the probability of a detection by LiteBIRD+CMB-S4 is unfortunately rather low. We had to choose an unlikely couple of β_{iso} and $\cos\Delta$ fiducial values, which are compatible only at 2σ with Planck. In that case, however, the joint analysis improves the constraints on both β_{iso} and $\cos\Delta$ very significantly.

For the neutrino isocurvature modes, the situation is more hopeful. We can easily find fiducial values for β_{iso} and $\cos\Delta$ within the Planck 1σ contours where the above conditions are satisfied. For the neutrino velocity mode about half of the region within the Planck 1σ contour even satisfies these conditions. Our chosen fiducial values mean that β_{iso} would be detected by LiteBIRD+CMB-S4 in the power spectrum with 5σ and 7σ for neutrino density and velocity, respectively. The joint analysis will then provide very significant improvements on the error bars of $\cos\Delta$ compared to the power spectrum alone. To give an example for the neutrino velocity isocurvature mode, for our chosen fiducial values the error bar of $\cos\Delta$ improves by 67%, leading to a highly significant detection at 12σ.

We have shown that in particular $\cos\Delta$ is correlated with the standard cosmological parameters A_s, n_s, and θ_{MC}. Hence, the improvement of its error bars with the joint analysis as discussed above can induce a non-negligible improvement in these parameters. For the configuration, we studied we find for example improvements of the error bars of A_s and θ_{MC} of about 20% and about 30% for neutrino density and neutrino velocity, respectively, compared to an analysis of the power spectrum alone of the ΛCDM + one isocurvature mode cosmology.

While the main focus of this second part of the thesis was to investigate improvements of the isocurvature constraints using a joint analysis of the power spectrum and the bispectrum, we also discussed three simple examples of possible future measurements by LiteBIRD+CMB-S4 that would rule out the general class of two-field inflation models that we assumed for the joint analysis. The model predicts certain relations between the $\tilde{f}_{\text{NL}}$ parameters themselves (in particular regarding their signs), as well as between the $\tilde{f}_{\text{NL}}$ and the power spectrum parameters β_{iso} and $\cos\Delta$. As we showed, the LiteBIRD+CMB-S4 measurements can be incompatible at a high confidence level with those relations, while staying within the Planck-allowed region.

Of course, no isocurvature modes may be detected by LiteBIRD+CMB-S4 (and that is even very likely for the CDM isocurvature mode), in which case the joint analysis will be useless for the general four-parameter model. One should also not forget the various assumptions we made in our analyses. Still, it is interesting to see that for the neutrino isocurvature modes, and in particular, for the neutrino velocity mode, there are significant regions of the parameter space compatible with Planck where a detection by LiteBIRD+CMB-S4 is possible, and where the joint analysis can provide a very significant improvement compared to an analysis of the power spectrum alone. In addition, we saw for Planck that in the case of a more restricted model with fewer free parameters, the joint analysis could be useful for improving the constraints even without detection. While we will leave forecasts for LiteBIRD+CMB-S4 for those more restricted models to future work, it seems reasonable to expect similar results in that case.

Part III

Relativistic effects in the large-scale structure

Chapter 6

Relativistic effects

After the CMB, the matter perturbations continue to evolve without coupling with radiation. Around redshift $z \sim 10$ (depending on the scale), the perturbations evolving since the end of inflation finally collapse on scales smaller than the horizon to form the so-called large-scale structure (LSS). It is composed of galaxy clusters and filaments. This structure is today well observed, for instance by the SDSS collaboration, as we can see in figure 6.1. Since the seeds for the large-scale distribution are the same as the CMB, one should be able to extract additional information about the early universe. Unlike the two-dimensional last scattering surface, the LSS is a three-dimensional object. Hence, it contains more modes, which means that the statistics could in principle be more powerful than the CMB. The third dimension, *i.e.* the radial redshift dimension, also contains information on the history of the universe because the observations are performed on the light-cone. In particular, the radial distance range of the cosmic web covers the whole Λ domination epoch of the universe ($z < 2$) so that it is a unique probe for the study of dark energy.

Given the increasingly large and precise galaxy surveys in planned experiments such as Euclid, the Vera Rubin Observatory or SPHEREx [204, 235, 236], the possibility of probing the largest scales of our universe with the large-scale structure is becoming reality. For scales with $k \leq 1$ Mpc^{-1}, the resolution of the future observational data of the matter distribution of our late universe will be at the percent level [237]. One consequence of the prospective percent accuracy of the future observational data is that it opens the possibility to add more constraints on the primordial scenarios [238]. The extraction of primordial physics from the future data requires however the greatest care, as galaxy clustering is a non-linear process.

As explained in section 3.1.6, the so-called squeezed limit of the bispectrum is a powerful tool to constrain PNG. In particular, the detection of a squeezed limit signal with an amplitude $f_{\rm NL} \gtrsim 0.1$ would definitely rule out all single-field inflation models. The next mission Euclid is expected to constrain $f_{\rm NL}$ with a standard deviation $\sigma_{f_{\rm NL}} \sim 1$ [239] while surveys like SPHEREx and SKA could reach $\sigma_{f_{\rm NL}} \sim 0.1$ [192, 204, 240]. However, the modelization of the squeezed limit in the LSS is very challenging. Indeed, the squeezed limit is a coupling between the large and the small scales where the physics are very different. On large scales, $k < 0.1$ hMpc^{-1}, relativistic effects are expected to become important since we approach the horizon. On the small scales, $k > 0.1$ hMpc^{-1}, analytical computations become impossible and one needs numerical simulations. See

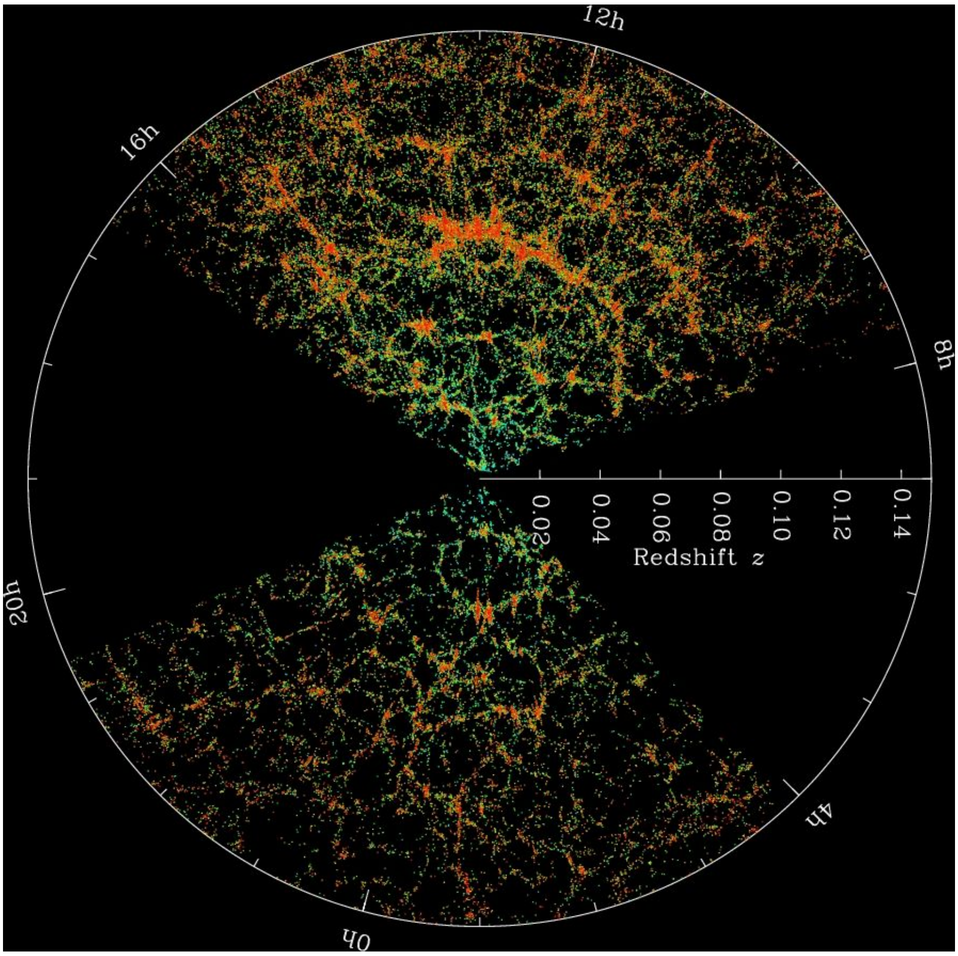

Figure 6.1: Two-dimensional slice of the large-scale structure of the universe as observed by the Sloan Digital Sky Survey (SDSS). The survey observes up to a redshift $z = 0.14$. We can see the filament structure and the galaxy clusters, typically at the intersection of the filaments. We can also see a typical behavior of the redshift space distortions: the galaxy clusters seem to point in our direction. Taken from the SDSS collaboration.

figure 6.2 for a review of the scales of interest. Send til annen e-post The relativistic effects can be split into two different categories. Firstly, relativistic effects arise in the cosmological dynamics of the perturbations. The leading order of these corrections is proportional to $\mathcal{H}^2/k^2$. Hence, deep in the sub-horizon limit, they can be neglected and the Newtonian dynamics is sufficient. A review of the Newtonian perturbation theory can be found in [94]. When we approach the horizon these corrections cannot be neglected anymore. Many studies have been performed over the last 30 years to account for these effects up to second order [241–249]. The recent work [250] extended the computed up to the fourth order. One of the main conclusions of these works, highlighted in [250], is that the dynamical relativistic effects are degenerate with PNG in the momentum and in the redshift space. Their precise modelization is therefore crucial in order to achieve the aforementioned limit on the local PNG amplitude in the forthcoming LSS surveys. Numerical codes accounting for non-linear effects up to second order were first developed to compute the CMB intrinsic bispectrum [100, 251]. The purpose of this chapter is to give a brief overview of the analytical results regarding the specific contamination of the squeezed limit of the PNG. The numeric code `SONG` [100] will then be briefly described and used in the next chapter 7.

The second type of relativistic effect arises because the cosmological perturbations in the LSS are not observed on a constant-time hypersurface but on our past light-cone. The photons travel along perturbed geodesics. Hence, they are subjected to redshift, lensing and redshift space distortions for instance [252, 253]. These effects have been taken into account at first order, see *e.g.* [254, 255], and then extended to second order, see for instance [256–258]. See also [248] for a very complete bibliography. In this thesis, we will concentrate our efforts on the first type of relativistic effects, *i.e.* dynamical relativistic effects, since we will only consider constant-time hypersurfaces. The second type will have to be considered in future works.

As explained above, in order to study the squeezed limit, one also needs to account for the small-scale physics. Deep in the non-linear regime, analytical computations become impossible. For this reason, N-body simulations have been developed. Numerical methods [259], pioneered by the cosmological codes `RAMSES` [260] and `Gadget` [261] are in principle able to resolve such scales within a box of the size of the universe [262]. However, running simulation is computationally expensive and they suffer from numerical artifacts that need to be well identified and understood. To correctly account for all relativistic effects, we need a fully relativistic N-body simulation. We will use the first simulation code derived consistently from general relativity: `gevolution` [263].

The main purpose of this third part is to take one step further in the dialog between numerical and analytical methods: we propose a generator of relativistic second-order initial conditions for N-body simulations (NIC for N-body initial condition to be differentiated from the primordial initial condition (PIC)).

In this chapter 6, we will introduce the main theoretical results concerning the contamination of the PNG squeezed limit. In section 6.1, we will first write down the second-order Einstein equations in an Einstein-de Sitter universe. Then in section 6.2, we will introduce the standard perturbation theory of LSS, also known as the Eulerian perturbation theory. We will present the basic Newtonian results and their extension to include relativistic effects which appear when we extend the Newtonian gravity to general relativity. Then, we will show how the relativistic corrections, together with the early radiation effects, can contaminate a PNG signal. Finally, we will introduce the second-order Boltzmann solver that we will use as a starting point for our work: the Second-Order Non-Gaussianities Boltzmann solver `SONG`.

In the next chapter 7, we present the main work of this third part of the thesis: the second-order RELativistic Initial Condition generator `RELIC`. In section 7.1, we start by reviewing similar works on non-Gaussian initial conditions in different contexts and using different approximations. Then, we explain our main working hypothesis: the long/short splitting. Finally, we describe the implementation of the code, from the first- to the second-order fields. In section 7.2, we briefly describe the N-body code `gevolution` and we compute all the quantities needed for the initial condition, *i.e.* the displacement field and the velocity. In section 7.3, we give some preliminary results: a performance test of `RELIC`, the power spectrum and bispectrum of the CDM density fields at the initial time. Finally, in section 7.4, we conclude.

6.1 Einstein equation up to second order

For this part, we need the expressions of the first and second-order transfer functions. We will suppose an adiabatic (ADI) Einstein-de Sitter universe (EdS) because we want

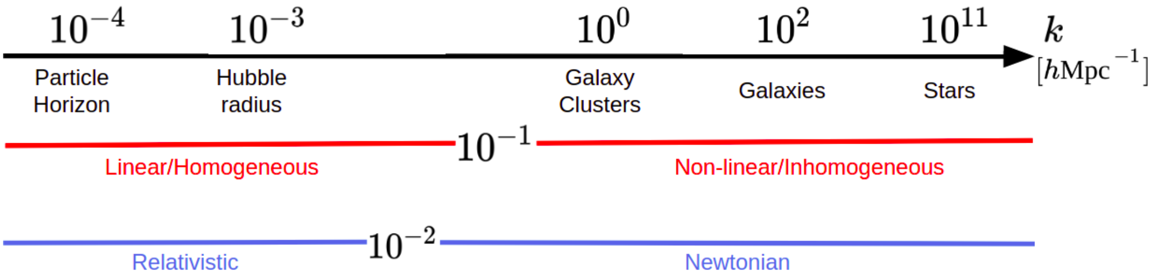

Figure 6.2: Representation of the different scales of the different objects, from the stars to the particle horizon today. In red, we represent the separation between the linear and the non-linear regime which also corresponds to the homogeneity transition. In blue, we show the relativistic/Newtonian regime.

to set the NIC deep in the matter domination era. Recall from section 1.4 that an EdS universe is a flat and cosmological constant free universe dominated by non-relativistic matter. Let us start by writing down the explicit Einstein equation at first and second order. Note that, as a consequence of an ADI, there is only one scalar degree of freedom. We will then express all transfer functions as a function of the density contrast transfer function.

6.1.1 First order

Let us first recall that in the absence of anisotropic stress, we have found in equation (2.58) $\chi^{(1)} = \psi^{(1)} - \phi^{(1)} = 0$. Then, note that for matter we have $\omega = 0$ and it is also well known that $c_s^2 = \omega$ if ω is constant which is the case in EdS. Therefore, equation (2.60) simplifies to

$$\psi''_{(1)} + 3\mathcal{H}\psi'_{(1)} = 0\,, \tag{6.1}$$

which has two solutions: one constant and one decaying mode $\propto \tau^{-5}$ (recall that $\mathcal{H} = 2/\tau$ in EdS). Therefore, we can neglect the decaying mode to find $\psi'_{(1)} = 0$. The expansion of the 00 equation (2.48a) gives the relativistic Poisson equation:

$$\frac{3\mathcal{H}^2}{2}\delta^{(1)} = -3\mathcal{H}^2\psi^{(1)} + \Delta\psi^{(1)}\,, \tag{6.2}$$

which is the generalization of the Poisson equation to first order in the Poisson gauge. Finally the equation (2.48b) reads:

$$\frac{3\mathcal{H}^2}{2}v^{(1)}_{,i} = -\mathcal{H}\psi^{(1)}_{,i}\,. \tag{6.3}$$

Recall that we are considering for now only scalar perturbation. Going to Fourier space, we can write all the first-order transfer functions (2.100) as a function of the density transfer function

$$\mathcal{T}^{(1)}_\phi = \mathcal{T}^{(1)}_\psi = -\frac{1}{2}\frac{3\mathcal{H}^2}{3\mathcal{H}^2 + k^2}\mathcal{T}^{(1)}_\delta\,, \qquad \mathcal{T}^{(1)}_v = -\frac{2}{3\mathcal{H}}\mathcal{T}^{(1)}_\psi = \frac{\mathcal{H}}{3\mathcal{H}^2 + k^2}\mathcal{T}^{(1)}_\delta\,. \tag{6.4}$$

Reminder from section 2.100 that the transfer function should have an additional subscript I referred to the initial condition. In this part, we only consider ADI so that the subscript $\mathcal{R}$ is implicit in the following.

6.1.2 Second order

Now we expand the Einstein equation at second order in an EdS universe. As explained in section 2.4, the second-order expansion gives the same terms as the first order just by changing (1) → (2) and with an additional quadratic source term. Then, by performing a Fourier transform, we can express all second-order transfer functions as a function of one single degree of freedom, again $\mathcal{T}_\delta^{(2)}$.

Expression for $\mathcal{T}_\chi^{(2)}$: Let us start with the traceless part of the Einstein equation (2.48c). This equation tells us that the second order χ is directly equal to the second order source term. It reads

$$\Delta^2\chi^{(2)} = 5\left(\psi^{(1)}_{,i}\psi^{(1)}_{,j}\right)^{,ij} - \frac{5}{3}\Delta(\psi^{(1)}_{,i})^2\,, \tag{6.5}$$

where we have used (6.3). Note that the time derivative of $\chi^{(2)}$, given (6.5), vanishes. Indeed, we know from equation (6.1) that $\psi^{(1)}$ is constant in EdS. Therefore $\chi^{(2)}$ is also a constant which means that $\psi'_{(2)} = \phi'_{(2)}$. The second order transfer function of χ therefore reads:

$$\mathcal{T}_\chi^{(2)} = \frac{5}{k^4}\left(\frac{2}{3}(k_1^2+k_2^2)\vec{k_1}\cdot\vec{k_2}+\frac{1}{3}(\vec{k_1}\cdot\vec{k_2})^2 + k_1^2k_2^2\right)\mathcal{T}_\psi^{(1)}(k_1)\mathcal{T}_\psi^{(1)}(k_2)\,. \tag{6.6}$$

Expression for $\mathcal{T}_\psi^{(2)}$: We take to second order the 00 Einstein equation (2.48a) to find

$$\left(3\mathcal{H}^2-\Delta\right)\psi^{(2)} = 3\mathcal{H}^2\left(-\frac{1}{2}\delta^{(2)} - \frac{1}{2}(v_i^{(1)})^2 + \chi^{(2)} - \frac{\psi'_{(2)}}{\mathcal{H}} + \psi^2_{(1)}\right) - \frac{1}{2}\left(\psi^{(1)}_{,i}\right)^2 + 2\psi^{(1)}\Delta\psi^{(1)}\,. \tag{6.7}$$

In principle, at second order, there will also occur quadratic terms that contain ϕ', but in matter domination we would always defer those to higher order because $\phi'_{(1)} = 0$ for the growing mode. Thus, we can write (6.7) in Fourier space:

$$\begin{aligned}\mathcal{T}_\psi^{(2)} = \frac{3\mathcal{H}^2}{2(3\mathcal{H}^2+k^2)}\Bigg[&-\mathcal{T}_\delta^{(2)} + 2\mathcal{T}_\chi^{(2)} - 2\frac{\mathcal{T}_{\psi'}^{(2)}}{\mathcal{H}} + \vec{k_1}\cdot\vec{k_2}\mathcal{T}_v^{(1)}(k_1)\mathcal{T}_v^{(1)}(k_2)\\ &+\left(2+\frac{\vec{k_1}\cdot\vec{k_2}}{3\mathcal{H}^2} - \frac{2(k_1^2+k_2^2)}{3\mathcal{H}^2}\right)\mathcal{T}_\psi^{(1)}(k_1)\mathcal{T}_\psi^{(1)}(k_2)\Bigg]\,.\end{aligned} \tag{6.8}$$

Expression for $\mathcal{T}_{\psi'}^{(2)}$: Now, using the trace equation equation (2.48d), we find at second order

$$\psi''_{(2)} + 3\mathcal{H}\psi'_{(2)} = Q_{TR}^{(2)} = \frac{1}{2}\mathcal{H}^2v^2_{(1)} - \frac{1}{6}\left(\psi^{(1)}_{,i}\right)^2 - \frac{1}{3}\Delta\chi_{(2)}\,. \tag{6.9}$$

As expected and unlike the first-order equation (2.60), we now have a constant source term. The full solution reads

$$\psi_{(2)} = \frac{2}{7\mathcal{H}^2}Q_{TR}^{(2)} + C^+ + C^-a^{-5/2}\,. \tag{6.10}$$

Note that the first term on the rhs scales like a. Hence, we can neglect the decaying mode proportional to $a^{-5/2}$ and express the time derivative of the potential as:

$$\psi'^{(2)} = \frac{2}{7\mathcal{H}} Q^{(2)}_{TR} \,, \tag{6.11}$$

where we have used the explicit expression of $\mathcal{H}$ in a matter-dominated universe $\mathcal{H} = 2/\tau$, see table 2.1. It gives in Fourier space:

$$\mathcal{T}^{(2)}_{\psi'} = \frac{-3\vec{k_1}\cdot\vec{k_2}\mathcal{H}^2\mathcal{T}^{(1)}_v(k_1)\mathcal{T}^{(1)}_v(k_2) - 2k^2\mathcal{T}^{(2)}_\chi + \vec{k_1}\cdot\vec{k_2}\mathcal{T}^{(1)}_\psi(k_2)\mathcal{T}^{(1)}_\psi(k_1)}{21\mathcal{H}} \,. \tag{6.12}$$

At first order, we have expressed all transfer functions in equation (6.4) as a function of the density contrast transfer function. Then, we have expanded the Einstein equation at second order (except the $0i$ component that we keep for the discussion of the velocity). The final results are given in equations (6.6), (6.8) and (6.12). In all these equations, there is again one single degree of freedom. Let us see now how we can close the system by computing δ_{cdm} with analytical approximations able to predict the shape of the CDM power spectrum.

6.2 Eulerian dynamics

To set NIC, we can restrict ourselves to an EdS universe. The typical NIC are set at $z \sim 100$. However, to understand the full shape of the CDM power spectrum, we will also mention the modes that enter the horizon during radiation and Λ domination.

The non-relativistic matter has a vanishing pressure and anisotropic stress so that the stress-energy tensor defined in equation (2.30) greatly simplifies. The continuity and the Euler equation can be written non-perturbatively

$$\delta' u^0 + \left([1+\delta]u^i\right)_{,i} + (1+\delta)\left[(\mathcal{H} + \phi' - 3\psi')u^0 + (\phi_{,i} - 3\psi_{,i})u^i + (u^0)'\right] = 0\,, \tag{6.13a}$$

$$u^0\left((u^i)' + u^0 e^{2\phi+2\psi}\phi^{,i} + 2u^i(\mathcal{H} - \psi')\right) + u^j u^i_{,j} - 2u^i u^j \psi_{,j} + u^2\psi^{,i} = 0\,. \tag{6.13b}$$

To solve these equations (6.13) in the quasi-linear regime, we can work in a more general framework than the perturbation theory used in section 2.2. Indeed, on small scales, the density can become much larger than the FLRW background by many orders of magnitudes so that the variable δ cannot be expanded following equation (2.15). However, even if the density can become large, the metric potential remains in general small. Even when looking at a very small structure like the solar system [263], the potential remains small while the density can vary by 25 orders of magnitude (center of the sun). An FLRW perturbed expansion of the metric potential would only break for example near a black hole horizon, *i.e.* scales that are far beyond the considered scales. Therefore, many LSS theoretical studies and N-body simulations work under the *weak field* approximation [250, 263–265]. This means that we can expand the Einstein tensor w.r.t. to all the potentials ϕ, ψ, S_i but keep the stress-energy tensor non-perturbative. The 4-velocity u^i under the weak-field approximation can be written as

$$u^\mu = \frac{1}{a}\left(1 + \delta u^0, v^i + \delta u^i\right)\,. \tag{6.14}$$

As we will see, deep inside the horizon, *i.e.* $\mathcal{H}^2/k^2 \to 0$, we will recover the standard Newtonian perturbation theory [94, 266–268]. Note that the square is important since the first relativistic corrections are of order $\mathcal{H}^2/k^2$, see for instance the Poisson equation (6.2). This means that inside the horizon, we can write the density and velocity fields as Newtonian contributions of order $\leq (\mathcal{H}/k)^1$ and relativistic corrections of order $\geq (\mathcal{H}/k)^2$. Moreover, in standard perturbation theory, it is common to describe the scalar degree of freedom of the velocity in terms of its divergence instead of v. We preferably use v because it matches the derivative of the displacement field that we will define later. The variable θ is defined as the divergence of the 3-velocity, *i.e.*

$$\theta = v^i_{,i} = \Delta v\,. \tag{6.15}$$

Note that the velocity has a transverse contribution of order $(\mathcal{H}/k)^3$, see for instance [250], hence we only consider here its scalar part. Under the weak-field approximation, the equations (6.13) can be written at order (n):

$$\delta'_{(n)} + \theta_{(n)} = Q^{(n)}_\delta\,, \tag{6.16a}$$

$$\theta'_{(n)} + \mathcal{H}\theta_{(n)} + \Delta\phi_{(n)} = Q^{(n)}_\theta\,. \tag{6.16b}$$

Similarly to the source term in the Einstein equation (2.48), $Q^{(n)}_\delta$ and $Q^{(n)}_\theta$ contain the non-linear mode coupling. At the linear level we have $Q^{(1)}_\delta = Q^{(1)}_\theta = 0$. To close the system, we can use the 00 Einstein equation (2.48a). Thus, by differentiating the first equation of (6.16), we can combine the two equations into a single second-order equation for δ_I:

$$\begin{aligned}\delta''_{(n)} + \mathcal{H}\delta'_{(n)} - \frac{3}{2}\mathcal{H}^2\delta^{(n)} &= S^{(n)}_p + Q^{(n)}_{TT} + (Q^{(n)}_\delta)' + \mathcal{H}Q^{(n)}_\delta - Q^{(n)}_\theta \\ &= S^{(n)}_p + Q^{(n)}\,,\end{aligned} \tag{6.17}$$

where $S^{(n)}_p = 3\mathcal{H}(\psi'_{(n)} + \mathcal{H}\phi^{(n)})$ which comes from the general Poisson equation (2.48a). Let us stress again that the evolution equation (6.17) is valid at any order for the density contrast δ. The general solution in EdS of (6.17) can be written

$$\delta^{(n)}_I = D_+(\tau)\delta^{(n)}_+(\mathbf{k}) + D_-(\tau)\delta^{(n)}_- + \int_{\tau_0}^{\tau} d\tau' G(\tau,\tau') \int_{\mathbf{k}_1\mathbf{k}_2} Q^{(n)}\,, \tag{6.18}$$

where $G(\tau,\tau')$ is the Green function of equation (6.17). This solution is composed of 3 terms: the first two terms, that come from the homogeneous equation, are the growing and decaying modes determined by the initial conditions. The last term is the particular solutions. We will now expand δ up to second order and solve equation (6.17) in the Newtonian limit first and in GR next.

Another and equivalent way of solving equations (6.16) is to write the density and the velocity as power series of τ or equivalently of $a(\tau)$. As we will see, the linear solution in EdS scales like a (if we neglect the decaying mode). Therefore, at any order, a field can be expanded w.r.t. the linear solution. Hence, at second order, the density field can be written

$$\delta^{(2)}(\mathbf{k}) = a^2 \int_{\mathbf{k}_1\mathbf{k}_2} F_2(\tau, k_1, k_2, k)\delta^{(1)}(\tau_0, \mathbf{k}_1)\delta^{(1)}(\tau_0, \mathbf{k}_2) \tag{6.19}$$

Note that, unlike in equation (2.110), the fields $\delta^{(1)}$ are evaluated today (τ_0) and not at the primordial time. We recover the second-order result of section 2.5 equation (2.110) where by identification (with $\mathcal{R}^{(2)} = 0$):

$$\mathcal{T}^{(2)}_\delta(\tau, k_1, k_2, k) = F_2(k_1, k_2, k)\mathcal{T}^{(1)}_\delta(\tau, k_1)\mathcal{T}^{(1)}_\delta(\tau, k_2) \tag{6.20}$$

If we do not consider the primordial bispectrum and trispectrum, equation (2.139) takes a simpler form:

$$B_\delta(k_1,k_2,k_3) = 2\left(F_2(k_1,k_2,k_3)P_\delta(k_1)P_\delta(k_2) + 2\text{ perm.}\right) . \tag{6.21}$$

It is also common to define a similar convolution kernel for the velocity, usually called G_n, its expression can be found in *e.g.* [94]. Equation (6.19) is the Fourier transform of (6.18). As we will see, in the analytical case we will consider, the kernel F_2 can be written in the following form, which follows the notation of [245, 269]:

$$F_2(k_1,k_2,k) = \frac{\beta-\alpha+\frac{\beta}{2}\mathbf{k_1}\cdot\mathbf{k_2}\left(\frac{k_1}{k_2}+\frac{k_2}{k_1}\right)+\alpha\left(\mathbf{k_1}\cdot\mathbf{k_2}\right)^2+\gamma\left(\frac{k_1}{k_2}-\frac{k_2}{k_1}\right)^2}{\omega} , \tag{6.22}$$

where the coefficients $\alpha,\beta,\gamma,\omega$ will take different values depending on the approximation used, *e.g.* Newtonian or GR.

6.2.1 Newtonian limit

Let us start by looking at the standard Newtonian limit result. In this limit, we set $\mathcal{H}^2 \ll k^2$ which means that we can neglect the δu^0 and δu^i terms in equation (6.14). For δu^0, we can see this by expanding equation (2.28). The next to leading order in proportional to ϕ and v^2. By looking at equation (6.4), we see that $\mathcal{T}_\phi^{(1)} \propto \mathcal{H}^2/k^2$ and $\mathcal{T}_v^{(1)} \propto \mathcal{H}/k$ which confirms that $\delta u^0 = 0$ in the Newtonian limit $\mathcal{H}/k \to 0$. Similarly, if we expand (2.27), we find that $\delta u^i = 0$ in this limit.

At the linear level we usually define the *linear growth factor* $D^{(1)}(\tau)$:

$$\delta_N^{(1)}(\tau,\mathbf{k}) = D^{(1)}(\tau)\mathcal{T}_\delta^{(1)}(\tau_0,k)\mathcal{R}^{(1)}(\mathbf{k}) . \tag{6.23}$$

At first order, there are no mode couplings so that the right hand side of equation (6.17) vanishes. Moreover, the Poisson equation is the classical Newtonian one, which means that $S_p = 0$. One can substitute δ using equation (6.23) to find a similar equation for the linear growth function. We find [94]:

$$D''_{(1)} + \mathcal{H}D'_{(1)} = \frac{3}{2}\mathcal{H}D_{(1)} . \tag{6.24}$$

Equation (6.23) is sometime called the Meszaros equation [270]. In 2002, Weinberg obtained the same equation in a GR framework by decomposing the density into a slow δ_{slow} and a fast δ_{fast} component [271]. The slow modes vary over the Hubble time scale (a/a') while the fast modes vary over the acoustic oscillation time scale which is linked with the acoustic sound horizon, see section 4.3.1. The main point of this decomposition is that non-relativistic matter (if not coupled with photons) satisfies $|\delta_{\text{slow}}| \gg |\delta_{\text{fast}}|$ while it is the contrary for radiation. Hence, we can show that at first order in full GR, this assumption gives the exact same equation (6.23), see also [272]. Note that, to find an equation valid also during radiation and Λ domination, we should add a term $\bar{\rho}_m/\bar{\rho}_{tot}$ on the right hand side. Therefore, in radiation domination, we have $\bar{\rho}_m/\bar{\rho}_{tot} \to 0$ and we know from the table 2.1 that $\mathcal{H} = 2/\tau$ and $a \propto \tau$, hence the solution in the radiation domination era is

$$D_+ = \ln a, \qquad D_- = \text{const} . \tag{6.25}$$

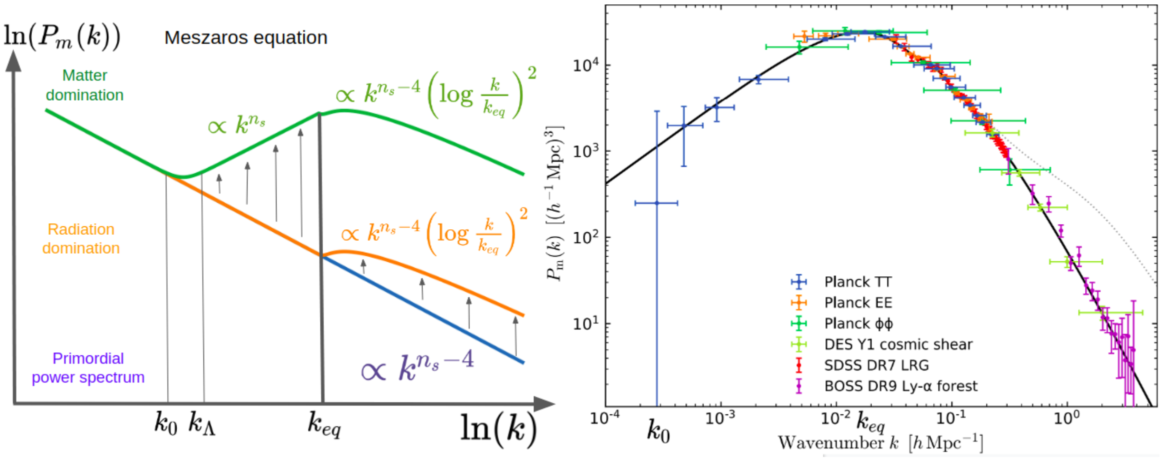

Figure 6.3: On the left, we represent the two different regimes of the Meszaros equation at $z = 0$. This plot is inspired by [154]. The blue curve is the primordial power spectrum. For small scales, $k > k_{eq}$, the modes enter the horizon during the radiation domination era where the CDM density grows like $\log(k)$. The orange curve represents the power spectrum that we could measure at the period of equality. Then, for the intermediate scales $k_\Lambda < k < k_{eq}$, the modes enter the horizon during matter domination. There, the CDM density grows like k^2 and the power spectrum is hence boosted by a factor $(k/k_\Lambda)^4$ w.r.t. the primordial power spectrum k^{-3}. The modes that enter the horizon during radiation domination ($k > k_{eq}$) are also affected by the matter domination. But the growth factor is constant so that the k dependence does not change. The amplitude is boosted by a factor $(k_{eq}/k_\Lambda)^4$. The radiation plus the matter domination effects are taken into account in the green curve. The modes larger than k_0 by definition cannot be observed. On the right, the Planck 2018 measurement of the matter power spectrum linearly propagated to $z = 0$ provided by the temperature (TT), the polarization (EE) and the lensing $\Phi\Phi$ superposed with the different available LSS measurements: SDSS, DES and BOSS [84]. Note that k_0, *i.e.* the particle horizon mode, is very close to the last scattering surface distance but is still smaller.

The growth of the structure is logarithmic during radiation domination. We represent the effect on the matter power spectrum of the radiation domination era in figure 6.3. The primordial power spectrum is the simple power-law k^{n_s-1} represented in blue. The radiation affects all the modes larger than k_{eq} whose amplitudes grow like D_+^2.

Now we come back to the EdS universe dominated by non-relativistic matter: $\bar{\rho}_m/\bar{\rho}_{tot} \to 1$ and where we recover exactly equation (6.24). This equation has two analytical solutions, by identifying with equation (6.18) we find

$$D_+ = a, \qquad D_- = a^{-3/2}\,, \tag{6.26}$$

where again from table 2.1, we know that in EdS $a \propto \tau^2$. The linear density therefore grows like the scale factor and is only sourced by the IC. By imposing ADI (2.82), one can show with the Newtonian Poisson equation that [245].

$$\delta^{(1)}_{N,+} = -\frac{k^2}{6}\psi^{(1)}\,. \tag{6.27}$$

Recall that ψ is constant in both sub- and super-horizon in matter domination. Therefore, for the modes that enter the horizon during matter domination, ψ in equation (6.27) can be linked with ζ^0 thanks to equation (2.63). The modes that enter the horizon during radiation domination are affected during the entire period of matter domination. The matter power spectrum is therefore boosted by a constant $(k_{eq}/k_\Lambda)^4$. The shape for $k > k_{eq}$ is not affected. The modes $k_\Lambda < k < k_{eq}$ progressively enter the horizon so that the power spectrum is boosted by $(k/k_\Lambda)^4$. Between the matter regime $k_\Lambda < k < k_{eq}$ and the radiation regime $k > k_{eq}$ the slope changes sign. Thanks to this, we observe a maximum power corresponding to $\sim k_{eq}$. The modes larger than k_0 by definition are not observable and are expected to follow the primordial power spectrum power law.

Baryons

The Meszaros equation gives a nice physical intuition for the global shape of the matter power spectrum. Since CDM is the dominant non-relativistic matter, the global shape of the matter power spectrum is fixed by the Meszaros equation. However, additional effects coming from baryons and neutrinos generate smaller features that also need to be taken into account for precise measurements. We have already discussed in section 4.3.1 the physics in the primordial plasma before recombination. We have explained that the primordial perturbations propagate in the photon/baryon fluid-like acoustic waves. The competition between radiation pressure and gravity generates the so-called baryon acoustic peaks that are well observed in the CMB, see figure 5.3. Note that equation (4.49) is also valid for baryons because baryons and photons are strongly coupled. Given the adiabatic initial condition, we have $\delta_b = \frac{2}{3}\delta_\gamma$.

The baryon/photon decoupling is not exactly symmetric. They are so many more photons than baryons that, even after the photon decoupling, the baryons remain coupled to the photons. This is the so-called *baryon drag* period. When finally the baryons decouple from photons, at τ_{drag}, they are only coupled through gravity with CDM so that δ_{CDM} and δ_b equalize. The final matter power spectrum is a weighted sum of the CDM power spectrum, that we know and the baryon power spectrum that follows the oscillatory features. Since CDM is dominant the final power spectrum is a perturbed Meszaros power spectrum with small oscillatory features around $k \sim 10^{-1}\ h\mathrm{Mpc}^{-1}$.

6.2.2 Newtonian limit at Second order

Let us now expand the density contrast to second order. The source term of (6.17) is

$$Q_N^{(2)} = \alpha\left(\mathbf{k}_1, \mathbf{k}_2\right)\left[\left(\delta_N(k_1)\theta_N(k_1)\right)' + \mathcal{H}\delta_N(k_1)\theta_N(k_1)\right] - \beta\left(\mathbf{k}_1, \mathbf{k}_2\right)\delta_N(k_1)\theta_N(k_1)\,, \quad (6.28)$$

where the functions $\alpha\left(\mathbf{k}_1, \mathbf{k}_2\right)$ and $\beta\left(\mathbf{k}_1, \mathbf{k}_2\right)$ are the kernels of the source integrals of the continuity and the Euler equations respectively, see equation (6.16), and should not be confused with the coefficients α, β, γ and ω of equation (6.22). Their expressions are

$$\begin{aligned} \alpha\left(\mathbf{k}_1, \mathbf{k}_2\right) &= 1 + \frac{\mathbf{k_1}\cdot\mathbf{k_2}}{2k_1k_2}\left(\frac{k_1}{k_2} + \frac{k_2}{k_1}\right)\,, \\ \beta\left(\mathbf{k}_1, \mathbf{k}_2\right) &= \frac{\mathbf{k_1}\cdot\mathbf{k_2}}{k_1k_2}\left(2 + \frac{k_1}{k_2} + \frac{k_2}{k_1}\right)\,. \end{aligned} \quad (6.29)$$

Note that these expressions are symmetrized unlike in [94].

In Newtonian gravity, the Poisson equation with a vanishing source term and with $S_p = 0$ is valid at any order and is the only equation relating the density and the potential.

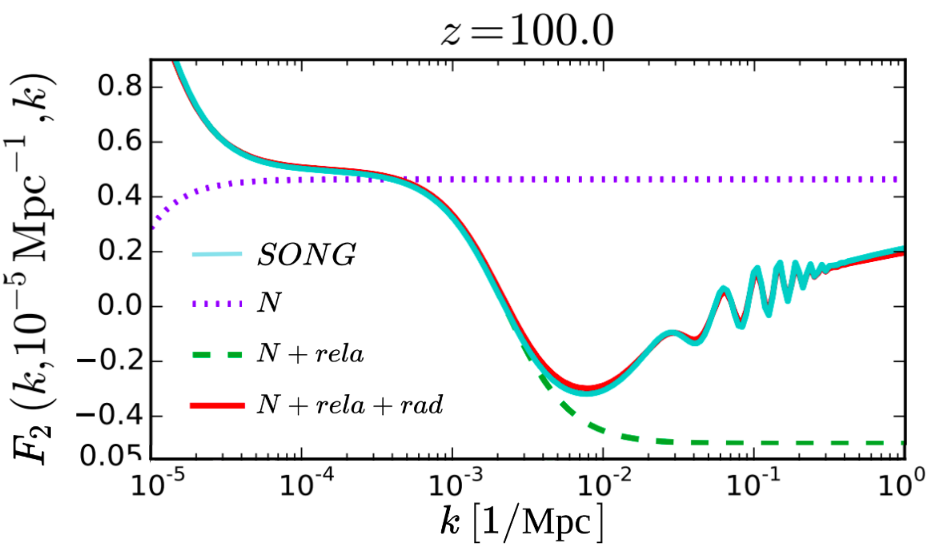

Figure 6.4: Second order kernel F_2 as a function of $k = k_2$. The first argument and the third are equal ($k = k_2$ in equation (6.20)) and vary while the second one is fixed to the minimum value of the x-axis in the plot. When $k \sim 10^{-5}$ Mpc^{-1}, the configuration is equilateral at large scales. When $k \sim 1$ Mpc^{-1}, the configuration is squeezed. The plots show four different analytical kernels computed with equation (6.22): the Newtonian (N) where the coefficients are given in (6.30), the relativistic ($N+rela$) kernel with (6.36) and equations (6.36) with (6.43) for the $N+rela+rad$ kernel. In fact, the kernel corresponding to *rela* is more general but is equivalent to the EdS (6.36) at redshift 100, see [269] for more details. Finally, SONG is the numerical result computed by `SONG`. Figure from [269].

Hence, it is straightforward to show that in the Newtonian case and for Gaussian IC, *i.e.* $\zeta^0_{(2)} = 0$, we have a vanishing initial $\delta^{(2)}$ in the case of vanishing PNG. Note that at second order also, the time derivative of the curvature perturbation on uniform-density hypersurfaces vanishes [105]. Hence, in the Newtonian limit, the source term is the only source of non-linearities [243]. By inserting (6.28) in the solution (6.18) where the IC vanishes, we can find that the Newtonian convolution kernel F_2 defined in (6.19) takes the form (6.22) with [241, 245, 269]

$$\alpha_N = \frac{7}{2}, \qquad \beta_N = 1, \qquad \gamma_N = 0, \qquad \omega_N = 1\,. \tag{6.30}$$

All coefficients are constant in time which means that the Newtonian non-linearities grow like $\delta^{(2)}_N \propto a^2$ while the growing mode scales like a. For this reason, at late times non-linearities dominate while they decay at early times. It is therefore a good approximation to set the initial condition only at first order. In figure 6.4, we show in dotted purple the evaluation of the Newtonian kernel for a configuration that is equilateral in the left and squeezed in the right. Compared with the numerical code `SONG` which solves the full second-order Einstein-Boltzmann equation, we see that, if we are optimistic, it can only be considered as a good approximation on a small range $k \in [10^{-3}, 10^{-4}]$.

The Newtonian bispectrum computed with (6.22) and (6.30) is shown in figure 6.5 for two different k_3. The peak locations depend on the scales considered. We see in figure 6.5 that the lower k_3 is, the more the Newtonian bispectrum peaks for an equilateral configuration. For small scales, however, the bispectrum peaks for an intermediate

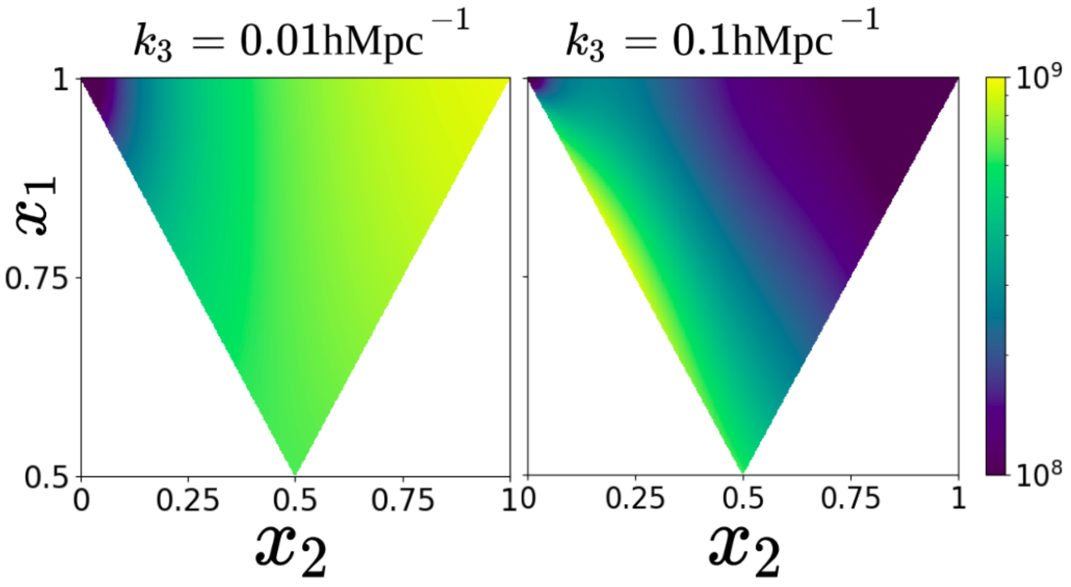

Figure 6.5: Triangular plot at $z = 0$ of the absolute value of the Newtonian bispectrum with $k_3 = 0.01\ h\text{Mpc}^{-1}$ on the left and $k_3 = 0.1\ h\text{Mpc}^{-1}$ on the right. See figure 2.1 for more details on triangular plots. We used the kernel (6.22) with the coefficients (6.30).

enfolded/squeezed configuration. Note however that for both plots, it decreases in the squeezed limit.

6.2.3 Relativistic corrections

The same first-order reasoning as in the Newtonian case leads to the same homogeneous solution (6.27) for δ without source terms. However, GR adds a correction to the Poisson equation; from equation (6.2) we see that $S_p^{(1)} = -3\mathcal{H}^2\psi^{(1)}$. The potential being constant at all scales during the matter domination era, the full solution is the growing mode which reads

$$\delta^{(1)} = -\left(\tau^2 k^2 + 12\right)\frac{\psi^{(1)}}{6}\,. \tag{6.31}$$

In the relativistic second-order case, none of the terms of the Poisson equation, nor the quadratic source terms, vanish. This case is considered in [243–247] in matter and radiation domination and in ΛCDM in [249], see also [241, 242, 273] for early computations and [248] for a recent comprehensive study summarizing the main results.

As in all previous cases, we have one growing mode which takes the same expression as the homogeneous first-order case, *i.e.* $D_+ = 12 + k^2\tau^2$. In the Newtonian case at first order, we have argued that Gaussian initial conditions for ζ implied a vanishing $\delta_{N,+}^{(2)}$. This is no longer the case now [243, 274]. It can be shown that in EdS at large scales [245]

$$\zeta^{(2)} = -\psi^{(2)} - \frac{2}{3}\phi^{(2)}\,. \tag{6.32}$$

We can link $\psi^{(2)}$ and $\phi^{(2)}$ by using equation (6.5). Assuming Gaussian adiabatic IC $\zeta^{(2)} = 0$ we therefore find

$$\psi_0^{(2)} = \frac{2}{5}\chi_0^{(2)}\,. \tag{6.33}$$

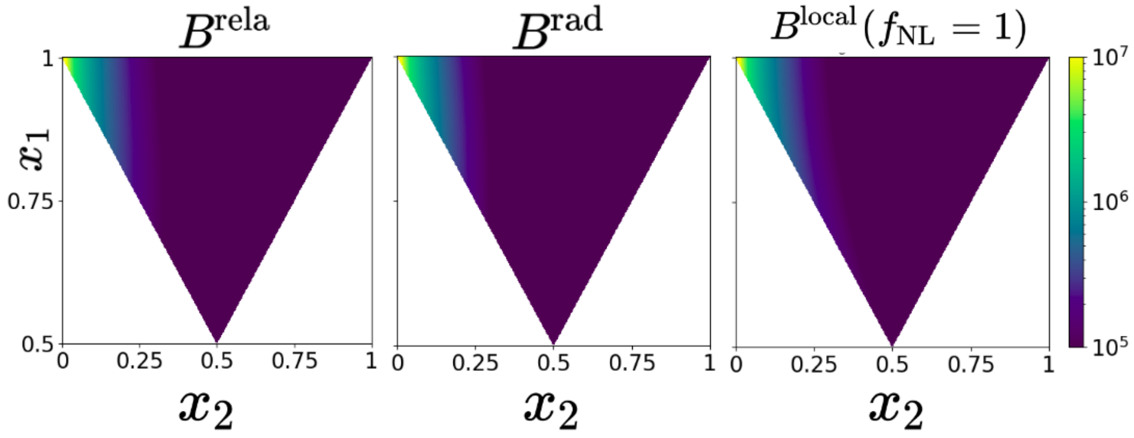

Figure 6.6: Triangular plot at $z = 0$ of the absolute value of the bispectrum with $k_1 = 0.1\ h\mathrm{Mpc}^{-1}$. See figure 2.1 for more details on triangular plots. The bispectra are computed using equation (6.21). Except for $B^{\rm local}$, we used the kernel (6.22) with (6.30) where we have subtracted the constant Newtonian term from the relativistic bispectrum correction $B^{\rm rela}$. For the radiation bispectrum correction $B^{\rm rad}$, we used $\alpha = \beta = 0$ and equation (6.43) where we kept only the term $\propto \partial \log T/\partial \log k$. The bispectrum $B^{\rm local}$ is computed with the kernel given in equation (6.37) with $\tilde{f}_{\rm NL} = 5/6$ which corresponds to $f_{\rm NL} = 1$.

Then, by using the early time limit of equation (6.7), we can find the IC imposed on large scales in the matter domination era. The second-order initial condition therefore reads

$$\delta_0^{(2)} = \frac{6}{5}\chi_0^{(2)} + 2\left(\psi^0_{(1)}\right)^2 , \tag{6.34}$$

where we know from equation (6.5) that $\chi^{(2)}$ is a simple function of $\psi_{(1)}$. This condition fixes $\delta^{(2)}_{R,+}$ and the full solution therefore reads

$$\delta^{(2)} = -\left(\frac{\tau^2 k^2}{12} + 1\right)\delta_0^{(2)} . \tag{6.35}$$

Note that this second-order initial condition, as in the linear case, grows like a. Additionally, the second-order case admits also a particular solution that also includes additional relativistic corrections, see [245] for the full expression of this particular solution. We can Fourier transform the full solution and compute the new relativistic kernel F_2^R. It takes the exact form of equation (6.22) with

$$\begin{aligned}
\alpha_R &= \frac{2}{7} + \frac{59}{14}\frac{\mathcal{H}^2}{k^2} + \frac{45}{2}\frac{\mathcal{H}^4}{k^4} ,\\
\beta_R &= 1 - \frac{1}{2}\frac{\mathcal{H}^2}{k^2} + 54\frac{\mathcal{H}^4}{k^4} ,\\
\gamma_R &= -\frac{3}{2}\frac{\mathcal{H}^2}{k^2} + \frac{9}{2}\frac{\mathcal{H}^4}{k^4}\\
\omega_R &= \left(1 + \frac{3\mathcal{H}^2}{k_1^2}\right)\left(1 + \frac{3\mathcal{H}^2}{k_2^2}\right) .
\end{aligned} \tag{6.36}$$

The computation for ΛCDM was performed in [249] and the full expression of the corresponding $\alpha_{VR}, \beta_{VR}, \gamma_{VR}$ (the subscript VR stands form Villa and Rampf, the author of

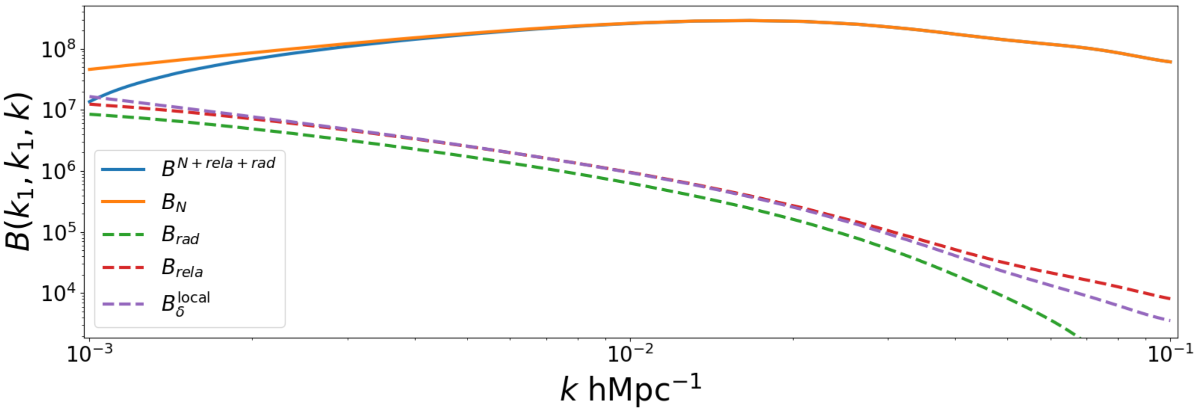

Figure 6.7: Absolute value of the bispectrum at $z = 0$ with $k_1 = 0.1$ hMpc^{-1} as a function of k. If the bispectra are negative, we plot them in dashed curves. The lower the k is, the more the triangle configuration is squeezed. The value $k = 0.1$ hMpc^{-1} corresponds to an equilateral configuration. The name convention are the same as in figure 6.6 and 6.4.

[249]) can be found in [269] while ω_R remains the same. The kernel F_2 with the coefficient $\alpha_{VR}, \beta_{VR}, \gamma_{VR}$ is plotted in figure 6.4 and is equivalent to the EdS kernel (6.36) since we are at $z = 100$. By comparing (6.36) and (6.30), we see a new bunch of terms proportional to $\mathcal{H}^2/k^2$ and $\mathcal{H}^4/k^4$. These are the relativistic corrections. Indeed, we recover the Newtonian result in the limit $\mathcal{H}^2/k^2 \to 0$, *i.e.* for the small scales with $\mathcal{H}^2 \ll k^2$. The relativistic corrections are therefore important near the horizon as expected. This is confirmed in figure 6.4; when we go to large scales, *i.e.* at small values of k, we reach a large scale equilateral configuration which deviates a lot from the Newtonian solution and follows the numerical solution of `SONG` with a relative error of $\sim 1\%$ [269].

To recover the time dependence, given equation (6.19), we must multiply F_2 by a^2. This means multiplying all coefficients of equation (6.36) by a^2. Recall that in EdS, the scale factor scales like τ^2 and $\mathcal{H}$ like τ^{-1}. Therefore, we find that the last terms of α_R, β_R and γ_R ($\propto \mathcal{H}^4/k^4$) are constant in time and directly come from the IC of the growing mode, *i.e.* the constant term in equation (6.35). On the other hand, the terms proportional to $\mathcal{H}^2/k^2$, which come from a combination of the growing mode and the source term, scale like a, *i.e.* exactly like the first-order terms.

To conclude, to build initial conditions for Newtonian N-body simulations, we can stay at the linear level because the second-order density grows like a^2, which means that if we go far enough into the past, they can be neglected. If, however, we consider GR, we have first seen that the second-order initial conditions do not vanish and stay constant while the relativistic non-linearities generated by the source and the growing mode grow exactly like the linear perturbations. Thus, they cannot be neglected in the IC. It has been shown in [250], that higher-order corrections ($\delta^{(3)}$ and $\delta^{(4)}$) receive additional power of a and can therefore be neglected in the initial conditions. Let us now explain what are the possible consequences of neglecting this effect by looking at the squeezed limit.

6.2.4 Squeezed limit

In figure 6.6, we show in the left panel the GR correction bispectrum, calculated by equation (6.36) where we subtract the Newtonian constant terms: $\alpha_{rela} = \alpha_R - \alpha_N$ and

$\beta_{rela} = \beta_R - \beta_N$ and $\gamma_{rela} = \gamma_R - \gamma_N$. We see that, unlike the Newtonian kernel, it peaks in the squeezed limit. This is also a known feature of the local PNG as explained in section 2.5.4. A one dimensional slice is also shown in figure 6.7. Let us derive the kernel F_2 arising from a primordial local bispectrum. This can be done by starting to write down the density bispectrum by using the definition (2.125). We can transform ψ to δ thanks to the first-order Poisson equation (6.2) and ψ to $\mathcal{R}$ thanks to equation (2.63). Then we use the local bispectrum equation (2.133). The result can be compared with (6.21), it gives

$$F_2^{\rm local}(k_1, k_2, k) = -\frac{5\mathcal{H}}{2}\tilde{f}_{\rm NL}\frac{k^2}{k_1^2 k_2^2}\,. \tag{6.37}$$

The bispectrum associated with the kernel (6.37) is shown in the right panel of figure 6.6 and a one dimensional slice is shown in figure 6.7. As expected, a local PNG generates a squeezed coupling for the matter density.

We can derive analytically an effective GR $f_{\rm NL}$ translating the fact that the relativistic corrections peak in this squeezed limit. To do so, we assume local PNG and then use the equation (2.132). The initial ζ can therefore expanded

$$\zeta = \zeta^{(1)} + \zeta^{(2)} = \zeta^{(1)} + \frac{3}{5}f_{\rm NL}\zeta^2_{(1)}\,, \tag{6.38}$$

where the factor 3/5 comes from the translation of Φ to ζ during matter domination, see equation (2.63). In Fourier space, the constant term can be absorbed in the zero mode and ignored. Then, if $f_{\rm NL} \neq 0$, equation (6.33) should be rewritten

$$\psi_0^{(2)} = \frac{2}{5}\chi_0^{(2)} - f_{\rm NL}\left(\psi_0^{(1)}\right)^2\,. \tag{6.39}$$

Finally, by using the early time limit of equation (6.7),

$$\delta_0^{(2)} = 2(1+f_{\rm NL})\left(\psi_0^{(1)}\right)^2 + \frac{6}{5}\chi_0^{(2)}\,. \tag{6.40}$$

Now we can take the squeezed limit of equation (6.40), *i.e.* $k_1 \to 0$ which means that $k \to k_2$. It is straightforward to show that in this limit $\chi^{(2)} \to 0$ and thus

$$\delta_0^{(2)} \overset{k_1\to 0}{=} 2(1+f_{\rm NL})\left(\psi_0^{(1)}\right)^2\,. \tag{6.41}$$

The second-order growing mode grows exactly like the linear solution, it can therefore not be neglected like the Newtonian second-order perturbations. Moreover, from (6.41), we see that if we ignore the second-order term in the IC, which means $\delta_0^{(2)} = 0$, in a relativistic framework, it is equivalent to suppose PNG that exactly cancels the GR effects:

$$f_{\rm NL} = -1\,, \tag{6.42}$$

so that the effective $f_{\rm NL}$ arising only from GR is therefore the opposite of (6.42): $f_{\rm NL}^R = 1$. This is confirmed by looking at the figure 6.7. It represents a one-dimensional slice of the bispectrum. More precisely, we have fixed the first and the second argument to $k_1 = 0.1\ h\mathrm{Mpc}^{-1}$ and we plot it as a function of the third argument. Therefore, for $k = 0.001\ h\mathrm{Mpc}^{-1}$, it is a squeezed configuration, and for $k = 0.1\ h\mathrm{Mpc}^{-1}$, it is equilateral. Similarly to figure 6.6, we have only plotted the relativistic corrections, *i.e.* (6.36) where we have subtracted equation (6.30). We recover that the relativistic corrections follow

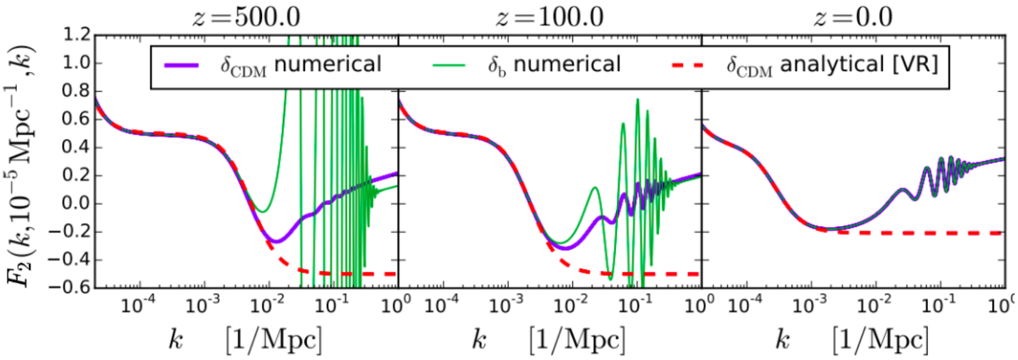

Figure 6.8: Squeezed configuration for three different redshifts for the CDM analytical approximation of the kernel computed in ΛCDM [249] and which is equivalent to the kernel (6.36) in the EdS limit, compared to the numerical kernel for both baryons and CDM. Figure from [269].

the local bispectrum with the same amplitude as we go to a squeezed configuration which is coherent with $f_{\rm NL}^R = 1$. However, this statement is gauge dependent. The historical computation is performed in the comoving-synchronous gauge [243, 246, 273, 274] and gave $f_{\rm NL}^R = -5/3$. However, even though no computation of the observable gauge-invariant $f_{\rm NL}^R$ has been performed, the concordance of the orders of magnitude of the different gauges makes us believe that $f_{\rm NL}^R \sim 1$.

Note also that we have now a completely new term for γ_R in equation (6.36) that vanishes in the Newtonian limit. We can rapidly show that in the squeezed limit when $k_2 \ll k_1 \sim k$, the kernel is dominated by γ_R, see equation (6.22). The function γ_R is composed of $(\mathcal{H}/k)^2$ and $(\mathcal{H}/k)^4$ terms. We could expect an additional GR contribution coming from the particular solution (source). However, it has been shown in [274] that in the synchronous-comoving gauge, this contribution vanishes in the squeezed limit. This can therefore be considered as a gauge effect coming from a different time/space slicing.

6.2.5 Radiation effects

Up to now, except for the linear power spectrum that we have computed in section 6.2.1, we have only considered the modes that enter the horizon during the matter domination era. It was possible to set IC without considering the radiation domination era since they were outside the horizon at that time and therefore "frozen". That is for $k < k_{eq}$. For this reason, we expect the approximation (6.36) to fail for $k > k_{eq}$ and this is exactly what we can observe in figure 6.4. While the numerical result computed with `SONG` produces wiggles because of the baryon oscillations, the relativistic EdS approximation does not see at all any radiation. Indeed, once we consider the squeezed limit, *i.e.* $k_1 \ll k \sim k_2$, GR effects that appear at large-scale and the small-scale radiation effect are mixed. Hence, we also expect the radiation to have an impact on the squeezed limit.

The effect of radiation on the CDM bispectrum has been discussed *e.g.* in [100, 245, 269]. One "standard" way to account for the radiation would be, similarly to the linear level, to inject all the radiation effects in the IC of the matter domination after having solved the non-linear equations in the radiation domination era. This means that the computation in EdS still holds and that the IC of the growing mode should be corrected to include radiation for the modes $k > k_{eq}$.

Exactly like in the matter power spectrum, the baryons and the photons are coupled via Compton scattering and the plasma oscillates. The CDM is coupled with baryons via gravity so that the baryon oscillations leave an imprint in the CDM bispectrum. This is shown in figure 6.8. At an early redshift $z = 500$ (left plot), the CDM particles, which are only weakly coupled to the other fluid by gravity, only show weak oscillations while the amplitude of the oscillations for the baryons is huge. As time increases, CDM and baryons attract each other until $\delta_{CDM} = \delta_b$. The oscillations of the baryons decrease and on the other hand, the ones of CDM increase until equilibrium. At redshift 0, in the right panel of figure 6.8, the kernels of baryons and CDM are equal.

A numerical approach to solve the second-order equations for all scales has been used in [245]. They found that the radiation could generate a contamination of order $f_{\rm NL} \sim 4$ around k_{eq}. An analytical approximation has been found in [269]. They used a separate universe approach, see section 3.2.4 for a short description of it. They found a new term arising in the squeezed limit, *i.e.* γ:

$$\gamma_+ = -\frac{3}{2}\frac{\mathcal{H}^2}{k^2} + \frac{9}{2}\frac{\mathcal{H}^4}{k^4} + \frac{5}{6}\left(\frac{\mathcal{H}^2}{k^2} + 3\frac{\mathcal{H}^4}{k^4}\right)\frac{\partial \log \mathcal{T}_\psi^{(1)}}{\partial \log k}\,. \tag{6.43}$$

This analytical approximation gives a 99% accuracy in the squeezed limit as we can see in figure 6.4, and the new term does not affect the other variables α and β which means that the other triangle configurations are not affected. Similarly to the relativistic corrections, the radiation correction bispectrum can be computed with $\alpha = 0$, $\beta = 0$ and $\gamma = \gamma_+ - \gamma_R$. In figures 6.6 and 6.7, we find that it is degenerate with the local PNG.

6.3 Boltzmann solver: `SONG`

In this section, we give some elements to understand what the code `SONG` computes. For a very detailed description, see [100]. We have written the first and second-order Einstein equation in section 6.1. As we have noticed, they are not a closed system of equations. There is one degree of freedom which we choose to be the density δ. To close the system, we have used in this thesis the continuity and the Euler equations introduced in section 2.4 and valid for each kind of particle. We have used them in section 4.3 to derive the fundamental evolution equation of the photon density in different regimes. It was enough to understand the shape of the CMB temperature anisotropies. Similarly, in section 6.2, we applied these equations to predict the CDM power spectrum and to find, up to second order, an analytical expression of the second-order kernel F_2. We have discussed the Newtonian limit and we have introduced the relativistic and early radiation effects to find an accurate second-order kernel. In general, for non-relativistic matter such as baryons and CDM, the continuity and Euler equations are sufficient. For relativistic species, however, we need in general a much more elaborate description. One of the main reasons for that is that radiation can have higher multipoles that can be excited if they free-stream, see *e.g.* section 4.3.1. The multipole decomposition of the temperature is given in equation (4.28). A second reason is that the Compton interaction between photons and baryons is not a *long-range force* like gravity. A long-range force arises from the mean field generated collectively by point particles. The Compton interaction arises from the collisions between two particles. This is called a *short-range force.* These collisions are associated with an occurrence probability, *i.e.* a cross-section.

A better description is the *kinetic theory of gases in general relativity* [275]. The fundamental equation of this theory is the so-called *Boltzmann* equation. Its general form is quite simple even though this form is unusable as it stands. The fundamental object in this description is the *phase space density function* $f(\tau, \mathbf{x}, \mathbf{p})$ that we used *e.g.* in section 2.4 to compute the density of fermions and bosons as a function of their temperature. The full Boltzmann equation reads

$$\frac{\mathrm{d}f}{\mathrm{d}\lambda} = C[f] \tag{6.44}$$

where λ parametrizes the geodesics (in our framework, gravity is the only long-range force) and in practice, the time. The right-hand side C is a functional of the phase space density function f. It accounts for the averaged collision rate of the particle momenta. In our case, the collisions are due to the Compton scattering. What equation (6.44) means is that, for an observer following geodesics, the phase space density is conserved if there is no collision. In that case, the equation is called the Liouville equation $\mathrm{d}f/\mathrm{d}\lambda = 0$. If however, $C \neq 0$, it induces a variation in f. For CDM, which is the species of interest here, the collision term vanishes because CDM is "cold". However, CDM is coupled through gravity with baryons that are coupled with photons. This interaction needs to be taken into account for CDM.

At first order, the well known codes `CAMB` [209, 210], that we used in the second part of this thesis, and `CLASS` [276], have been developed. At second order, one of the most efficient solver is the `SONG` code [100, 277, 278].

The second-order Boltzmann code `SONG` was developed in 2015 by G. Pettinari. It is a C OpenMP parallelized code, based on the structure of the first-order Boltzmann solver `CLASS`. The main point of using `SONG` for LSS is to compute the CDM second-order transfer function $\mathcal{T}^{(2)}$. Once this is done, we can use the second-order Einstein equation to compute the metric potentials, see section 6.1. Note that we also have to use the first-order transfer function $\mathcal{T}^{(1)}$ provided by `CLASS`.

Even though the use of the Boltzmann equation is not strictly obligatory for CDM, to use a unified treatment of all species, `SONG` uses also the Boltzmann equation for CDM. To do so, it uses the beta-moments formalism, also called momentum-integrated multipoles. It consists of expanding the distribution function f in term of particle velocity powers, *e.g.* the nth beta-moment is the momentum integral of the density function f times $(p/E)^{n-1}$ with p and E the momentum and the energy of the particles. By using this formalism, we can write down unified differential equations valid for all types of particles.

6.3.1 Gauge

`SONG` works in the same Poisson gauge as we done in this thesis but does not use the same definition of the potentials. The line element of `SONG` is

$$ds^2 = a^2(\tau)\left(-(1+2\psi_s)d\tau^2 + (1-2\phi_s)\delta_{ij}dx^i dx^j\right) . \tag{6.45}$$

By comparing with our line element given in equation (2.20), we can identify up to second order

$$\begin{aligned} \psi_s^{(1)} &= \phi^{(1)}, & \psi_s^{(2)} &= \phi_{(2)} + \phi_{(1)}^2 , \\ \phi_s^{(1)} &= \psi^{(1)}, & \phi_s^{(2)} &= \psi_{(2)} - \psi_{(1)}^2 . \end{aligned} \tag{6.46}$$

Other definitions of the metric variables in the Poisson gauge can be found in the literature. In [100], one can find a nice review of the different definitions and the link between all the variables.

6.3.2 Second-order initial conditions

Since `SONG` solves the second-order Einstein-Boltzmann system, it has to set PIC up to second order. Exactly like in section 2.4.5, PIC are set deep in the radiation domination era ($a \sim 10^{-6}$) in the super-Hubble regime. As we already said, we restrict ourselves to ADI. Similarly to the first-order case, we set $\mathcal{S}_{ij} = 0$, see (2.83), and expand now to second order. We find

$$\frac{\delta_i^{(2)}}{1+\omega_i} - \frac{\omega_i}{2(1+\omega_i)^2}\left(\delta_i^{(1)}\right)^2 = \frac{\delta_j^{(2)}}{1+\omega_j} - \frac{\omega_i}{2(1+\omega_j)^2}\left(\delta_j^{(1)}\right)^2 . \tag{6.47}$$

Recall from section 2.4.3 that on super-horizon scales, the growing mode is constant in the radiation domination era. Hence, we can use equation (6.7). Neglecting the spatial derivatives, one finds

$$\delta_0^{(2)} = 2\left((\psi_0^{(1)})^2 - \phi_0^{(2)}\right) . \tag{6.48}$$

Initially we neglect the non-relativistic matter which means that

$$\delta_0^{(2)} = \Omega_\gamma \delta_\gamma^{(2)} + \Omega_\nu \delta_\nu^{(2)} = \delta_\gamma^{(2)}(\Omega_\gamma + \Omega_\nu) , \tag{6.49}$$

where we have used the ADI (6.47) which reads for neutrinos and photons $\delta_\gamma^{(2)} = \delta_\nu^{(2)}$. A similar calculation can be done for the velocity and we find that all velocities are equal also at second order. The time-space Einstein equation can also be used since we are on super-horizon scales. It gives us an expression for the adiabatic velocity as a function of the second order metric potential ϕ, see [100, 101].

As discussed in section 6.2, we set Gaussian ADI by imposing $\zeta^{(2)} = 0$ which does not imply that the initial condition of the other variables vanishes at second order. The relation between ζ and ψ in radiation domination is given by [101]:

$$\zeta^{(2)} = -\psi^{(2)} - \frac{1}{2}\phi^{(2)} . \tag{6.50}$$

Chapter 7

Second order relativistic initial conditions

In the previous chapter, we have described how the relativistic effects and the early radiation can generate a signal that can be confused with a PNG signal. We have shown that the leading order non-linearities grow like the linear growing mode, *i.e.* like $a(\tau)$, so that they cannot be neglected in the initial conditions. Moreover, the relativistic PIC cannot be zero in a GR framework at second order. This means that if we do not account for the relativistic PIC, since they cannot be generated by the source term, we would lose this information. We have also noted that it was shown in [250] that higher-order corrections are negligible in the initial condition because of their scaling $\geq a^2$. Finally, we have presented the second-order Boltzmann solver `SONG`. Accounting for all the effects of interest, it can compute the second-order kernel deep in the matter domination era where we want to build the NIC.

All these analytical predictions are valid only when perturbation theory still works, *i.e.* in the linear regime, see figure 6.2. Typically, for the modes $k \gtrsim 0.1h\text{Mpc}^{-1}$, perturbation theory breaks down because the non-linearities become too large. To study the squeezed limit, which mixes large and small scales, it is crucial to account for these small-scale non-linearities and for the large scales where relativistic effects are important. The perfect tool for this purpose is the fully relativistic N-body code `gevolution`, which can take into account both limits (large-scale relativistic effects and small-scale non-linearities). Currently, the initial conditions used for the `gevolution` simulations are purely Gaussian and therefore only take into account the linear dynamics.

The next step to build a fully relativistic pipeline is to generate second-order relativistic initial conditions at high enough redshift, typically deep in the matter domination era at $z = 100$. At these high redshifts, perturbation theory still holds and we can use the second-order kernel produced by `SONG` to build NIC up to second order. Then we can give this to `gevolution` and run the simulation. This should be a consistent pipeline that takes into account all dynamics relativistic effects, influencing the large scales, and the early radiation and large non-linearities influencing the small scales. It should allow us to perform complete numerical experiments to give a final answer on the exact PNG contamination of the relativistic and radiation effects in the LSS.

7.1 The second-order initial conditions code `RELIC`

The main goal of the RELativistic Initial Conditions generator `RELIC` is to compute the second-order initial condition for NIC such as $\delta^{(2)}$ and $v_i^{(2)}$. The computation of such quantities involves the convolution integral of equation (2.106). Thanks to the δ-function, any second-order field $\mathcal{I}^{(2)}$ can be rewritten:

$$\mathcal{I}^{(2)}(\tau,\mathbf{k}) = \int \frac{d^3k_1}{(2\pi)^3}\mathcal{T}_{\mathcal{I}}^{(2)}(\tau,k_1,|\mathbf{k}-\mathbf{k_1}|,k)\mathcal{R}^{(1)}(\mathbf{k}_1)\mathcal{R}^{(1)}(\mathbf{k}-\mathbf{k}_1)\,. \tag{7.1}$$

The computation of (7.1) can be more costly than the N-body simulation itself. Indeed, for each mode $\mathbf{k}$, one has to sum over the raw space. For a cubic grid of size N, it means N^3 operations to calculate the value of $\mathcal{R}$ at one point and therefore N^6 operations for the entire grid. To imagine what this complexity represents, note that a modern laptop can perform an operation in $\sim 10^{-8}$s. Accurate measurement in an N-body simulation would require at least $N = 1000$ modes. Let us suppose that the total number of operations is N^6, it means at least 10^{18} operations in total. There are $\sim \pi 10^7$ seconds in a year, we can therefore conclude that on a single processor, the full computation would take $\pi 10^3$ years. This problem was pointed out in previous works, we review now some of the solutions proposed.

7.1.1 Previous works

A numerical implementation of the integral (7.1) was worked out in [279]. Their goal was to build the NIC up to second order given a generic bispectrum $B_\phi(k,k_1,k_2)$. For this, they assumed the ansatz

$$\mathcal{T}_{\phi}^{(2)}(k_1,k_2,k) = \frac{B_\phi(k_1,k_2,k)}{P_\phi(k_1)P_\phi(k_2)}\,. \tag{7.2}$$

The bispectrum of the potential is dominated by 3 permutations of $\langle\phi^{(1)}\phi^{(1)}\phi^{(2)}\rangle$. By using equation (7.2), we find

$$\langle\phi^{(1)}(\mathbf{k})\phi^{(1)}(\mathbf{k_1})\phi^{(2)}(\mathbf{k_2})\rangle = \frac{1}{3}(2\pi)^3\delta(\mathbf{k}-\mathbf{k_1}-\mathbf{k_2})B_\phi(k_1,k_2,k)\,. \tag{7.3}$$

The particular form of the kernel (7.2) is not unique; different kernels can yield to the same bispectrum. We can see this by noting that to find an expression for the kernel, one needs to invert equation (6.21).

In [279], they focused on the common primordial shapes. In particular, the local shape is separable since, in real space, the second-order contribution $\phi^{(2)}$ is simply the square of $\phi^{(1)}$, see (2.132). We, therefore, see here that a separable kernel greatly simplifies the computation from N^6 to N^3 because the convolution (7.1) becomes in real space a simple product, see section 2.5.1. Hence, for the local shape, they were able to compare the costly generic implementation equation (7.1) and the fast real-space calculation with a grid size 256^3. Even though the computation is mathematically equivalent, numerical effects can arise in the Fourier grid. In particular, they found that, in the case of the Fourier space computation, the power spectrum is biased by the non-vanishing second-order power spectrum $\langle\phi^{(2)}\phi^{(2)}\rangle$ which diverges at large scales. This directly comes from the particular form of the kernel given in equation (7.2).

In the following article, [280], the same team used the previous implementation to explore the scale-dependent halo bias. They used a modified version of (7.2) that yields the same bispectrum and does not suffer from the aforementioned divergence. The new kernel is now non-separable, its form was first found in [281] and reads

$$\mathcal{T}_\phi^{(2)}(k_1,k_2,k)=\frac{B_\phi(k_1,k_2,k)}{P_\phi(k)P_\phi(k_1)+P_\phi(k_1)P_\phi(k_2)+P_\phi(k)P_\phi(k_2)}\,. \tag{7.4}$$

To study the scale-dependent halo bias, they needed a larger grid but were again limited by the computational cost. They solved the problem by using two different grid sizes. The Gaussian grid was as large as the particle grid ($N=1024$) while the non-Gaussian grid was only evaluated at large scales ($N=400$). The NG grid size is a good compromise between the minimum halo size and the computation cost.

Further works have implemented PNG in NIC thanks to the property of separability, either exact or approximate [282–284]. In parallel, a novel technique has been developed based on a separable modal decomposition of the bispectrum or trispectrum [285]. The point is that the kernel (7.4) can be decomposed on a polynomial basis, such as the Legendre polynomials:

$$\mathcal{T}_\phi^{(2)}(k_1,k_2,k)=\sum_{ijk}\alpha_{ijk}q_r(k)q_j(k_1)q_k(k_2)\,, \tag{7.5}$$

where the functions q are the orthogonal polynomials and where α_{ijk} are the coefficients of the decomposition for a given bispectrum. This method was developed for the CMB bispectrum modal estimator [286]. This estimator is one of the three used in the Planck analysis [107], among which the binned bispectrum estimator that we used in the second part of this thesis. The modal estimator has also been extended to LSS studies [281] and more recently [287]. The decomposition (7.5) leads to a separable approximation of a generic kernel. It has been shown that it converges quite rapidly; the number of polynomial needed for the common templates is ~ 30.

Though this last approach is very interesting, we will use for our work a method similar to [279, 280]. The reason is that it can be easily extended to study the relativistic effects as we will see in the following subsection. We leave a modal approach extension for future work.

7.1.2 Long/short mode splitting

Let us introduce a cut-off scale k_Λ. We split $\mathcal{R}$ into two parts $\mathcal{R}=\mathcal{R}_L+\mathcal{R}_S$ such that:

$$\mathcal{R}_L(\mathbf{k})=W(k)\mathcal{R}(\mathbf{k}),\quad \mathcal{R}_S(\mathbf{k})=(1-W(k))\mathcal{R}(\mathbf{k})\,, \tag{7.6}$$

where $W(k)$ is a window function: $W(k)=1$ if $k<k_\Lambda$ and $W(k)=0$ otherwise. We replace $\mathcal{R}^{(1)}$ in equation (7.1) by the sum $\mathcal{R}_L^{(1)}+\mathcal{R}_S^{(1)}$ to get:

$$\begin{aligned}\mathcal{I}^{(2)}(\mathbf{k})=&\int\frac{d\mathbf{k_1}}{(2\pi)^3}\mathcal{T}_\mathcal{I}^{(2)}(k_1,|\mathbf{k}-\mathbf{k_1}|,k)\mathcal{R}_L^{(1)}(\mathbf{k_1})\mathcal{R}_L^{(1)}(\mathbf{k}-\mathbf{k_1})\\&+2\int\frac{d\mathbf{k_1}}{(2\pi)^3}\mathcal{T}_\mathcal{I}^{(2)}(k_1,|\mathbf{k}-\mathbf{k_1}|,k)\mathcal{R}_S^{(1)}(\mathbf{k_1})\mathcal{R}_L^{(1)}(\mathbf{k}-\mathbf{k_1})\\&+\int\frac{d\mathbf{k_1}}{(2\pi)^3}\mathcal{T}_\mathcal{I}^{(2)}(k_1,|\mathbf{k}-\mathbf{k_1}|,k)\mathcal{R}_S^{(1)}(\mathbf{k_1})\mathcal{R}_S^{(1)}(\mathbf{k}-\mathbf{k_1})\\&=\mathcal{I}_{LL}(\mathbf{k})+2\mathcal{I}_{LS}(\mathbf{k})+\mathcal{I}_{SS}(\mathbf{k})\,.\end{aligned} \tag{7.7}$$

Thanks to the cut-off, we have 3 different contributions to the second order density at point $(\mathbf{k})$. Let us review all three terms of equation (7.7):

- The first term $\mathcal{I}_{LL}$ takes into account the coupling between large scales. As we have seen in section 6.2, relativistic corrections are important at large scales, near the horizon, so that $\mathcal{I}_{LL}$ needs to be taken into account. Note that this is the only term that is computed in [280]. Its complexity scales like N_Λ^6 where N_Λ is the number of modes below the cut-off.

- To compute the second term, we have merged the two "cross" integrals SL and LS thanks to a change of variable. It accounts for the coupling between large and small scales, *i.e.* a squeezed configuration. As we have seen, the relativistic effects peak in this limit and are degenerate with local PNG, it is, therefore, crucial to compute it. The term $\mathcal{R}_L^{(1)}(\mathbf{k}-\mathbf{k_1})$ is non-zero only inside a sphere of radius k_Λ centered on $\mathbf{k}$ and zero everywhere else. On the contrary $\mathcal{R}_S^{(1)}(\mathbf{k_1})$ is filled only outside the sphere of radius k_Λ centered on 0. The number of non-zero multiplications $\mathcal{R}_S^{(1)}(\mathbf{k_1})\mathcal{R}_L^{(1)}(\mathbf{k}-\mathbf{k_1})$ can therefore not exceed N_Λ^3; this is the case where the two spheres do not intersect ($k > 2k_\Lambda$). This operation has to be repeated for each point of the total grid, the complexity is $N^3 N_\Lambda^3$.

- The last term $\mathcal{I}_{SS}$ contains the coupling between small scales. For each point $\mathbf{k}$, we now multiply two grids that are 0 only inside spheres of radius k_Λ centered on $\mathbf{k}$ and 0. Assuming that $N_\Lambda \ll N$, we roughly have N^3 operation to be repeated for all N^3 points, *i.e.* N^6. We have argued that for PNG and relativistic effects, the coupling between small modes is dominated by Newtonian non-linearities which are negligible since they scale like a^2. Note however that, like the other terms, $\mathcal{I}_{SS}(\mathbf{k})$ contributes to the power at large scales $k > k_\Lambda$. If we neglect the raw $\mathcal{I}_{SS}$, we would miss this power and bias the large scales which we want to be accurately computed. To split the large and small scale contributions, we can again apply the window function:
$$\mathcal{I}_{SS}(\mathbf{k}) = W(k)\mathcal{I}_{SS}(\mathbf{k}) + (1-W(k))\mathcal{I}_{SS}(\mathbf{k}) = \mathcal{I}_{SS}^L(\mathbf{k}) + \mathcal{I}_{SS}^S(\mathbf{k})\,. \tag{7.8}$$
This way, the $\mathcal{I}_{SS}^L$ contains all the contributions of the small-small coupling to the large scales $k < k_\Lambda$. The number of operations per point is still N^3 but we only have to compute it for $k < k_\Lambda$ since it vanishes anywhere else. Its complexity is, therefore, $N^3 N_\Lambda^3$, *i.e.* like the squeezed term. Finally, the term $\mathcal{I}_{SS}^S(\mathbf{k})$ is the one that scales like N^6 and accounts for the small-small mode coupling for the small modes. This is the term that we neglect in our analysis.

Our final approximation takes the form
$$\mathcal{I}^{(2)}(\mathbf{k}) \approx \mathcal{I}_{LL}(\mathbf{k}) + 2\mathcal{I}_{SL}(\mathbf{k}) + \mathcal{I}_{SS}^L(\mathbf{k})\,. \tag{7.9}$$
By computing $\mathcal{I}_{LL} + \mathcal{I}_{SS}^L$, we have all the possible couplings for $k < k_{min}$. This means that the computation of $\mathcal{I}^{(2)}(\mathbf{k})$ is exact if $k < k_{min}$. Hence, another way to write (7.9) is to split $\mathcal{I}_{LL}$ and $\mathcal{I}_{SL}$ in the same way as $\mathcal{I}_{SS}$ (7.8). Then, one can factorize the window function and find
$$\mathcal{I}^{(2)}(\mathbf{k}) \approx \mathcal{I}_{LL}^S(\mathbf{k}) + 2\mathcal{I}_{SL}^S(\mathbf{k}) + \mathcal{I}_{(2)}^L(\mathbf{k})\,, \tag{7.10}$$
where we have defined in the same way as (7.8) the quantities $\mathcal{I}_{LL}^S$, $\mathcal{I}_{SL}^S(\mathbf{k})$ and $\mathcal{I}_{(2)}^L(\mathbf{k})$. It appears explicitly that for $k < k_{min}$, we perform the exact computation (last term) while for $k > k_{min}$, we neglect the small-small coupling ($\mathcal{I}_{SS}^S$). The full complexity is $N_\Lambda^6 + 2N_\Lambda^3 N^3$.

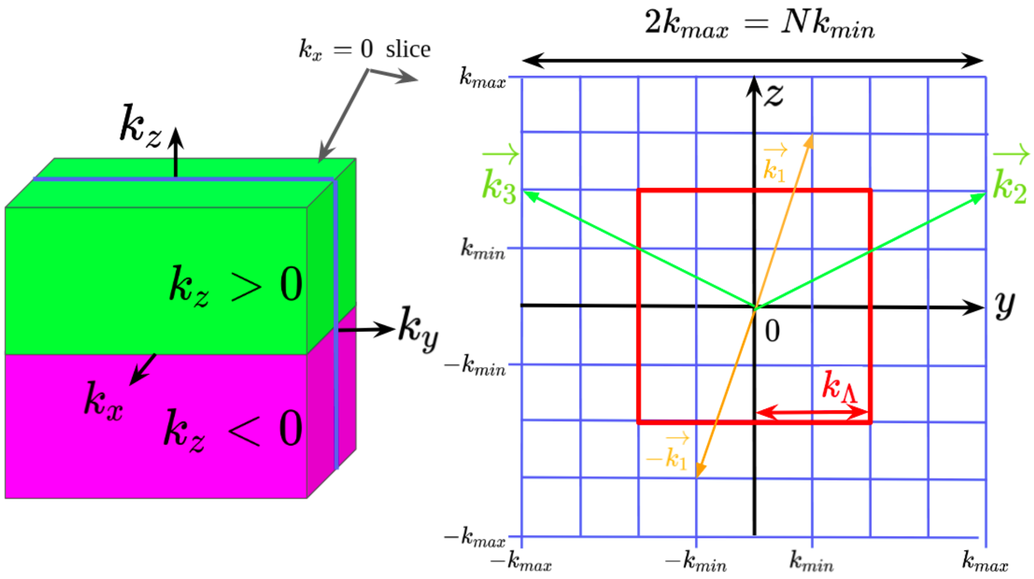

Figure 7.1: Fourier grid used in `RELIC`. On the left, the 3-dimensional grid splits into two parts: the $k_z > 0$ and $k_z < 0$ parts. The $k_x = 0$ slice is represented on the right. In the case represented we have $N = 8$ and $k_\Lambda = 2k_{min}$. In `RELIC`, the reality condition is imposed on the k_z-axis so that we have $\mathcal{I}(\mathbf{k_1}) = \mathcal{I}^\star(-\mathbf{k_1})$. This means that one of the half cubes, for instance $k_z < 0$, is redundant. Moreover, the fact that N is even in addition to the periodicity of the Fourier grids imposes $\mathcal{I}(\mathbf{k_2}) = \mathcal{I}(\mathbf{k_3})$.

7.1.3 First order implementation

We now give some details about the implementation. Let us start by describing the construction of the discrete Fourier grid.

Grid

We define the integer indices on the real space grid as l, m, n, each ranging from zero to $N-1$, such that for a system of size L we have $\mathbf{x} = (l, m, n) \times L/N$. We always work with even N in `RELIC`. In Fourier space the longest mode that fits into a system of size L has wavenumber $k_{min} = 2\pi/L$. We define the integer indices on the Fourier-space grid as u, v, w, ranging from $-N/2$ to $N/2$. The three-dimensional grid $\mathcal{G}_\mathbf{k}$ is represented on the left of figure 7.1. A two-dimensional slice is represented on the right. Hence, we have $\mathbf{k} = (u, v, w) \times k_{min}$. Discretization translates to

$$\mathcal{I}(\mathbf{k}) \to \mathcal{I}_{u,v,w} = \mathcal{I}((u, v, w) \times k_{min}) = \mathcal{I}(\hat{\mathbf{k}})\,. \tag{7.11}$$

where k_{min} is linked with the size of the real space box L by $L = 2\pi/k_{min}$. By definition, the maximum mode k_{max} is $k_{max} = k_{min}N/2$. Note that in the Fourier space, the mode 0 and all the modes with one or more components vanishing ($k_i = 0$) are part of the grid. This is very convenient because in the integral (7.1), we have to evaluate the stochastic field at $\mathbf{k} - \mathbf{k_1}$. Let us assume that $\mathbf{k}, \mathbf{k_1} \in \mathcal{G}_\mathbf{k}$. If we want $\mathbf{k} - \mathbf{k_1} \in \mathcal{G}_\mathbf{k}$, one needs $\mathbf{0} \in \mathcal{G}_\mathbf{k}$ (*i.e.* the case $\mathbf{k} = \mathbf{k_1}$), otherwise we would have to interpolate the stochastic field.

Additionally, we work with real fields in real space. We therefore impose the reality condition:

$$\mathcal{I}(\mathbf{k}) = \mathcal{I}^\star(-\mathbf{k})\,. \tag{7.12}$$

One example is represented in figure 7.1. In that sense, only half of $\mathcal{G}_{\mathbf{k}}$ matters. We arbitrarily choose to keep in memory the half corresponding to $k_z \geq 0$, *i.e.* the green upper piece in figure 7.1. Note that for the same reason only half of the plane $k_z = 0$ and half of the line $(k_z = 0, k_x = 0, k_y > 0)$ matter. Therefore, while $u, v \in [-N/2, N/2]$, we have for the z-axis: $w \in [0, N/2]$. There are $N + 1$ values in $[-N/2, N/2]$ since $0 \in [-N/2, N/2]$ while there are N values in the real space interval $[0, N-1]$. We will see when describing the first-order implementation how to deal with this.

Finally, we stress that the grid $\mathcal{G}_{\mathbf{k}}$ is periodic. This means that $\mathcal{I}(\mathbf{k}) = \mathcal{I}(\mathbf{k} + p\mathbf{N})$ where p is any integer and where $\mathbf{N}$ can be the vector $(N, 0, 0)$, $(0, N, 0)$ or $(0, 0, N)$. This property will be important when computing the second order fields.

Discretization

The whole formalism developed in this thesis works in a continuous space. However numerically, we work with discrete quantities. Let us now consider how it translates to a discrete system.

In the continuum, the Dirac distribution is defined through

$$\int d^3k' \delta(\mathbf{k} - \mathbf{k}')\mathcal{I}(\mathbf{k}') = \mathcal{I}(\mathbf{k})\,, \tag{7.13}$$

for every smooth test function $\mathcal{I}$. Discretization translates as

$$\int d^3k' \rightarrow \sum_{u',v',w'} k^3_{min}\,, \tag{7.14}$$

and

$$\delta(\mathbf{k} - \mathbf{k}') \rightarrow \frac{1}{k^3_{min}} \delta^K_{uu'} \delta^K_{vv'} \delta^K_{ww'}\,, \tag{7.15}$$

where $\delta^K_{uu'}$ is the Kronecker symbol.

Let us now consider the Fourier transform. By using (7.15), (7.11), the Fourier transform of equation (2.50) turns into:

$$\int d^3x \mathcal{I}(\mathbf{x}) e^{-i\mathbf{k}\mathbf{x}} \rightarrow \frac{(2\pi)^3}{k^3_{min} N^3} \sum_{l,m,n} \mathcal{I}_{l,m,n} \exp\left(-\frac{2\pi i}{N}\left[ul + vm + wn\right]\right). \tag{7.16}$$

Except for the normalization factor in front of the sum, this is the definition of the discrete Fourier transform provided by the `numpy` package that is used in `RELIC` to perform the inverse Fourier transform, see figure 7.2. Hence, we introduce a dimensionless Fourier field

$$\hat{\mathcal{I}}(\hat{\mathbf{k}}) = \frac{k^3_{min} N^3}{(2\pi)^3} \mathcal{I}(\hat{\mathbf{k}})\,, \tag{7.17}$$

which represents the field computed directly with the discrete Fourier transform (DFT) algorithm. In `RELIC`, we work in Fourier space in units $\hat{\mathcal{R}}(\hat{\mathbf{k}})$ so that we can perform the inverse DFT of `numpy` and get directly the right units.

First-order realization

We start by generating the first order curvature perturbation $\mathcal{R}(\mathbf{k})$. Let us first discretize the power spectrum in order to find the right units. We discretize (2.115) and use (3.36)

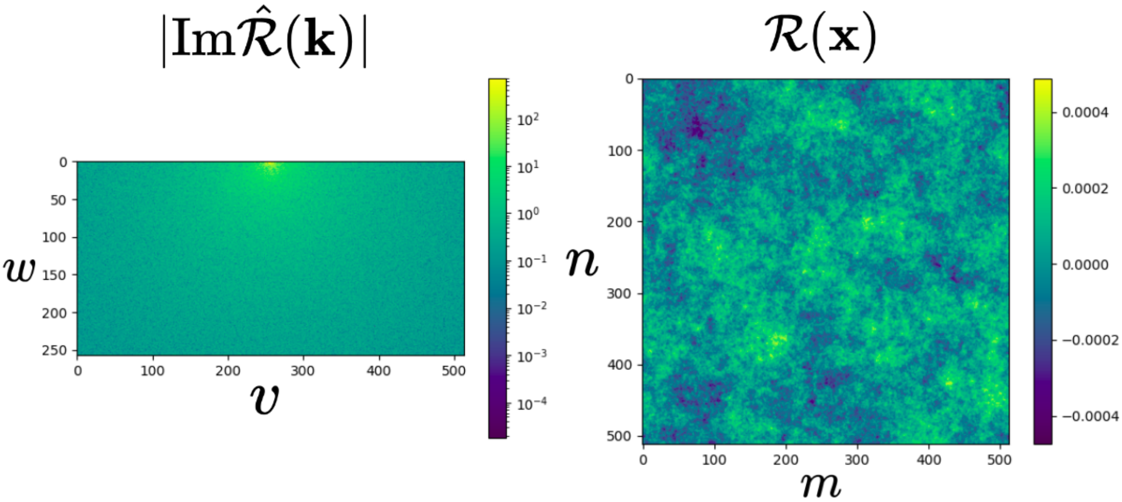

Figure 7.2: Realization of the first order curvature perturbation in the comoving gauge. On the left, a x-constant slice of the imaginary part (this choice is arbitrary) of the Fourier grid as a function of the integers v and w in units of k_{min}. On the right, the same $x-$constant slice in real space as a function of the integers n and m in units of $2\pi/k_{min}$.

to find

$$\hat{P}(\hat{k}) = \frac{N^6 k_{min}^3}{4\pi \hat{k}^3} A_s \left(\frac{\hat{k}}{k_0}\right)^{n_s-1} . \tag{7.18}$$

As explained in section 3.1.4, the power spectrum is related to the standard deviation of the Gaussian probability density function that the real and imaginary part of the field follows at first order. Thus, for each point of the grid $\mathcal{G}_\mathbf{k}$, we can randomly pick two independent numbers following the Gaussian PDF given in equation (2.112) with the standard deviation given in equations (2.119) and (7.18).

The field is real in real space. Hence, it is characterized by N^3 numbers. In Fourier space, the field is complex which means that there are 2 times more numbers. Moreover, as stressed above, the Fourier grid is larger $(N+1)$. For these reasons, in addition to the reality condition, equation (7.12), we have to impose the following constraints:

- The Fourier grid is larger than the real space grid by one unit. This means that there is twice the information needed in the boundaries. Usually, one drops the modes that verify $k_i = -k_{max}$ for one of their coordinates. In `RELIC`, *e.g.* if $k_x = k_{max}$, we impose

$$\mathcal{R}\begin{pmatrix} k_{max} \\ k_y \\ k_z \end{pmatrix} = \mathcal{R}\begin{pmatrix} -k_{max} \\ k_y \\ k_z \end{pmatrix} , \tag{7.19}$$

  and similarly if $k_y = k_{max}$. In figure 7.1, we therefore have $\mathcal{R}(\mathbf{k_2}) = \mathcal{R}(\mathbf{k_3})$.

- The case of $k_z = k_{max}$ is particular because we do not have in memory the $k_z = -k_{max}$ so that we need to impose a condition in the plane $k_z = k_{max}$. In principle we have the same as equation (7.19) but with $k_z = k_{max}$ instead of $k_x = k_{max}$. By using the reality condition (7.12) we can show that

$$\mathcal{R}\begin{pmatrix} k_x \\ k_y \\ k_{max} \end{pmatrix} = \mathcal{R}\begin{pmatrix} k_x \\ k_y \\ -k_{max} \end{pmatrix} = \mathcal{R}^\star \begin{pmatrix} -k_x \\ -k_y \\ k_{max} \end{pmatrix} , \tag{7.20}$$

where the first equality in (7.20) is similar to (7.19) and where we have used the reality condition in the second. Thus, for the plane $k_z = k_{max}$ too, only half of the numbers matter.

- Note that the combination of the reality condition (7.12), (7.19) and (7.20) implies that some particular points should be real. This is the case for the mode 0, all corners (which are in fact all equal), the center of the planes $k_i = k_{max}$ and $k_i = -k_{max}$ and for the center points of the cube edges.

Hence, given all these additional constraints, we can show that the $(N+1)^3$ free numbers reduce to N^3, as expected. A 512^3 realization is shown in figure 7.2. On the left, a x-constant slice of the imaginary part of the dimensionless curvature perturbation (7.17). As explained, we only keep in memory the $k_z \geq 0$, $k_z < 0$ can be obtained with equation (7.12). To find any field (*e.g.* $\delta^{(1)}$), we have to multiply $\mathcal{R}(\mathbf{k})$ by the transfer functions provided by `CLASS`. Then, by applying the inverse DFT, one finds the real-space curvature perturbation $\mathcal{R}(\mathbf{x})$ which is represented on the right panel of figure 7.2, or any other field if we have multiplied in Fourier space by the corresponding transfer function.

7.1.4 Second-order density field

Let us now discretize equation (7.1) and substitute all $\mathcal{R}$ by dimensionless $\hat{\mathcal{R}}$ following equation (7.17). It leads to

$$\hat{\mathcal{I}}^{(2)}(\hat{\mathbf{k}}) = \frac{1}{N^3} \sum_{u_1,v_1,w_1} \mathcal{T}_{\mathcal{I}}^{(2)}(\hat{\mathbf{k}}_1, |\hat{\mathbf{k}} - \hat{\mathbf{k}}_1|, \hat{\mathbf{k}}) \hat{\mathcal{R}}^{(1)}(\hat{\mathbf{k}}_1) \hat{\mathcal{R}}^{(1)}(\hat{\mathbf{k}} - \hat{\mathbf{k}}_1) \, . \tag{7.21}$$

The computation (7.21) is split following equation (7.10). The three pieces are computed independently. In the following, we explain the structure of the code by starting with interpolation.

`SONG` interpolation

Since we work at second order where there is mode coupling, the transfer functions depend on four variables: the conformal time τ and three moduli k_1, k_2, k, see equation (2.106). In `SONG`, the two variables k_1 and k_2 are sampled in the same way and are symmetric. There are different possibilities to sample k_1 and k_2: a linear, a logarithmic or a hybrid way called “smart”. In our code `RELIC`, we use linear sampling. In order to capture the large-scale information, the minimal k should be of the order of the step. Since the kernel is symmetric under exchange of k_1 and k_2, only half of the combinations need to be computed, that is $k_1 \geq k_2$. This symmetry is obvious by looking at the definition of the second-order transfer function (2.106), as already mentioned in section 6.1.

The third mode k is sampled so that the three moduli k_1, k_2, k satisfy the triangular inequality imposed by the δ function in the integral (2.106). Therefore we always have

$$|k_1 - k_2| \leq k \leq k_1 + k_2 \, . \tag{7.22}$$

We use the “smart” sampling for this third mode k. In combination with the linear sampling for k_1 and k_2, it works as follows. Let us call the linear grid of k_1 and k_2: $G_{\text{lin}}^{k_1,k_2}$. For a given couple $\{k_1, k_2\}$, k can take all the values of $G_{\text{lin}}^{k_1,k_2}$ that verify the triangular inequality (7.22), including the points $k_1 + k_2$ and $|k_1 - k_2|$ which, in general, are not included in $G_{\text{lin}}^{k_1,k_2}$. However, if $2k_2 < \Delta k$ where Δk is the step of the k_1 and k_2 grid and where we recall that we imposed $k_1 \geq k_2$, none of the values in the grid $G_{\text{lin}}^{k_1,k_2}$ verify the triangular inequality. In this case, `SONG` samples k linearly between $k_1 + k_2$ and $|k_1 - k_2|$ with a fixed number of points.

The `SONG` gird should not be confused with the Fourier space grid, where the fields live, described in section 7.1.3, see also figure 7.1. The `SONG` grid is also a 3-dimensional grid but as a function of the moduli of three different modes k_1, k_2, k. Therefore, we need to interpolate the kernel.

We use a multi-linear interpolation. The easiest way to linearly interpolate $\mathcal{T}_\delta^{(2)}$ is to use a linear grid. It has the advantage that it is easy to find the points surrounding the one to interpolate. In order to cover the whole range of possible modulus in our grid $\mathcal{G}_{\mathbf{k}}$, we use

$$k^s_{min} = k_{min}, \qquad k^s_{max} = 1.8\frac{N}{2}k_{min}, \qquad N^s = \frac{k^s_{max}}{k^s_{min}}\,, \tag{7.23}$$

where the subscript s stands for `SONG` . The minimum modulus possible is k_{min}. However, since our box is cubic, the maximum modulus does not correspond to k_{max}, which is the maximum value of the mode coordinates. The maximum modulus is the diagonal $\sqrt{3}k_{max}$ where we have rounded up $\sqrt{3} \approx 1.8$. Since we use a linear interpolation and because we need an accurate enough sampling of the large scales, we impose N^s such that $\Delta k^s = k_{min}$. The large scales are sampled more as needed but the computation of `SONG` is not a limitation in our case.

The multi-linear interpolation algorithm works as follows. Recall that the third mode has a different sampling w.r.t. k_1 and k_2, see (7.22) and the associated discussion. Hence, our interpolation is done in two parts. For a given triplet (k_1, k_2, k_3), we find the 4 surrounding points in the k_1 and k_2 plane:

$$k_i^n = k^s_{min} E\left(\frac{k_i - k_{min}}{\Delta k^s}\right) \leq k_i \leq k_i^{n+1} = k^s_{min} E\left(\frac{k_i - k_{min}}{\Delta k^s} + 1\right)\,, \tag{7.24}$$

where the function E is the floor function and i can be either 1 or 2. Only when we have k_i^n and k_i^{n+1}, do we know the exact sampling of the third mode for all four couples (k_1^n, k_2^n), (k_1^{n+1}, k_2^n), (k_1^n, k_2^{n+1}) and (k_1^{n+1}, k_2^{n+1}). For each of these points we can find the corresponding (k_3^n, k_3^{n+1}) similarly to (7.24) and linearly interpolate along k_3 first. Finally, we interpolate the four points in the k_1, k_2 plane.

The cut-off shape

As represented in figure 7.1, in practice, we use a cut-off on the components of the modes: $\hat{k}_x, \hat{k}_y, \hat{k}_z < k_\Lambda$. The discrete cut-off u_Λ, defined as $k_\Lambda = u_\Lambda k_{min}$, is an integer that simplifies greatly the splitting. Basically, we can work only with the indices of the grid. For example, in a `Python` code, we would write:

$$\mathcal{R}_L(\hat{\mathbf{k}_1}) \to \mathcal{R}\left[0 : u_\Lambda + 1, \frac{N}{2} - u_\Lambda : \frac{N}{2} + u_\Lambda + 1, \frac{N}{2} - u_\Lambda : \frac{N}{2} + u_\Lambda + 1\right]\,, \tag{7.25}$$

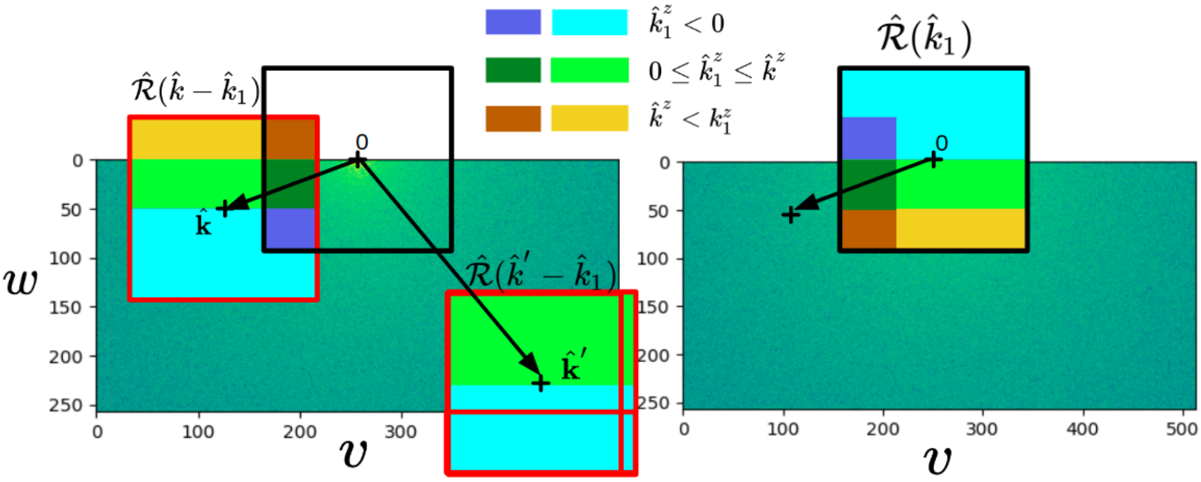

Figure 7.3: Representation of the different ensembles of pixels that have different treatments in `RELIC`. The Fourier grid represented in the background corresponds to a $x = 0$ slice of $\hat{\mathcal{R}}(\hat{\mathbf{k}}_1)$ (same as left panel of figure 7.2). Remember that solely the pixels with $k^z \geq 0$ are in memory. The cut-off is represented with a black square centered on 0. Then, we represent in the red squares of the left panel the translated grids $\hat{\mathcal{R}}(\hat{\mathbf{k}} - \hat{\mathbf{k}}_1)$ and $\hat{\mathcal{R}}(\hat{\mathbf{k}}' - \hat{\mathbf{k}}_1)$ so that the components $(\hat{\mathbf{k}} - \hat{\mathbf{k}}_1)$ and $(\hat{\mathbf{k}}' - \hat{\mathbf{k}}_1)$ are smaller that k_Λ. In the right and left panel, we represent in the black square the grid $\hat{\mathcal{R}}(\hat{\mathbf{k}}_1)$ with $\hat{k}_1^{x,y,z} \leq k_\Lambda$. The dark and light colored regions (orange green and blue) are included in both cut-offs and therefore contribute to $\mathcal{I}_{LL}$ and $\mathcal{I}_{SL}$ respectively. The different slices orange, green and blue are treated in a different ways, see the main text for the details. The colors in the left and right panels correspond to the regions that are multiplied when computing the second order value at the points $\hat{\mathbf{k}}$ and $\hat{\mathbf{k}}'$, *i.e.* $\hat{\mathcal{R}}(\hat{\mathbf{k}}_1)\hat{\mathcal{R}}(\hat{\mathbf{k}} - \hat{\mathbf{k}}_1)$ in (7.21). Note that because of the minus sign $(-\mathbf{k_1})$, the square is "rotated" by π. In the case of $\hat{\mathbf{k}}'$, the orange region does not exist because $\hat{k}'_z - \hat{k}_1^z$ is never negative inside the cut-off. Hence, the green and the orange region in the right panel should be considered as one single green region for $\hat{k}'_z$.

where $X : Y + 1$ means all values from X to Y. In a similar way, we can find $\mathcal{R}_L(\hat{\mathbf{k}} - \hat{\mathbf{k}}_1)$. Note that the first index is the z-axis for which we only have $z \geq 0$ in memory. For a cut-off on the modulus of k we would have to find all the indices that verify the conditions

$$k_{min}\left(u^2 + v^2 + w^2\right)^{1/2} \leq k_\Lambda, \qquad k_{min}\left((u - u_1)^2 + (v - v_1)^2 + (w - w_1)^2\right)^{1/2} \leq k_\Lambda\,. \tag{7.26}$$

For this, we can use masks. In addition to the fact that it takes additional memory which can be a limitation (note that the memory scales as N^6), the main problem comes from the numerical error. The conditions (7.26) would not select the same number of pixels which makes the computation much harder. For this reason, we choose to use a square cut-off (7.25). Note that the square shape of the cut-off, as far as we know, has no consequences for the computation. It can be seen as a modulus cut-off with radius $\hat{k}_\Lambda$ with additional terms, *i.e.* it takes into account slightly more terms than needed.

Implementation

The numerical implementation is based on the equation (7.10). However, for this part, we concentrate our efforts on the first two terms of equation (7.9). Once we understand how they are computed, we can easily generalize to all terms of equation (7.10) as we shall see.

In figure 7.3, we represent a two-dimensional slice ($x = 0$) of the Fourier grid $\hat{\mathcal{R}}(\hat{\mathbf{k}}_1)$ in the background of both panels. The black square is the corresponding cut-off $\hat{k}_1^{y,z} \geq k_\Lambda$ centered on zero while the red squares (in the left panel), are the cut-offs corresponding to the conditions $(\hat{k}^{y,z} - \hat{k}_1^{y,z}) \leq k_\Lambda$ and $(\hat{k}'_{y,z} - \hat{k}_1^{y,z}) \leq k_\Lambda$ respectively. They are centered on the modes $\hat{\mathbf{k}}$ and $\hat{\mathbf{k}}'$ which are the pixels of the second-order field that are computed. Basically, when we perform the sum (7.21), we multiply $\hat{\mathcal{R}}(\hat{\mathbf{k}}_1)$, represented in the right panel, with $\hat{\mathcal{R}}(\hat{\mathbf{k}} - \hat{\mathbf{k}}_1)$, represented in the left panel for two different example $\hat{\mathbf{k}}$ and $\hat{\mathbf{k}}'$. The different colored regions are pixel ensembles corresponding to the indicated conditions on the mode $\hat{\mathbf{k}}_1$ in the right and the corresponding conditions on the mode $(\hat{\mathbf{k}} - \hat{\mathbf{k}}_1)$ on the left panel, and similarly for $\hat{\mathbf{k}}'$. Let us review all regions, first for the mode $\hat{\mathbf{k}}$:

- The dark region (orange+green+blue) is the intersection of the two cut-offs. These pixels are accounted for in $\mathcal{I}_{LL}$. Indeed, let us write down $\mathcal{I}_{LL}$ explicitly:

  $$\mathcal{I}_{LL} = W(\hat{k}_1)W(|\hat{\mathbf{k}} - \hat{\mathbf{k}}_1|)\hat{\mathcal{R}}(\hat{\mathbf{k}}_1)\hat{\mathcal{R}}(\hat{\mathbf{k}} - \hat{\mathbf{k}}_1)\,. \tag{7.27}$$

  The dark region corresponds to all $\hat{\mathbf{k}}_1$ where the product $W(\hat{k}_1)W(|\hat{\mathbf{k}} - \hat{\mathbf{k}}_1|)$ does not vanish. Similarly, the light region (orange+green+blue) is the region where the product $(1 - W(\hat{k}_1))W(|\hat{\mathbf{k}} - \hat{\mathbf{k}}_1|)$ does not vanish, *i.e.* they are involved in the computation of $\mathcal{I}_{SL}$.

- The orange region is the ensemble of pixels where $\hat{k}_1^z > \hat{k}^z$ which means that $\hat{k}_1^z - \hat{k}^z$ is negative (see the left panel). Thanks to the reality condition (7.12), the product can be written

  $$\text{For } \hat{k}_1^z > \hat{k}^z\text{: } \hat{\mathcal{R}}(\hat{\mathbf{k}}_1)\hat{\mathcal{R}}^\star(\hat{\mathbf{k}}_1 - \hat{\mathbf{k}})\,. \tag{7.28}$$

- The green region corresponds to all $0 \leq \hat{k}_1^z \leq \hat{k}^z$ in the right panel. This case is the simplest since both $\hat{k}_1^z$ and $\hat{\mathbf{k}} - \hat{\mathbf{k}}_1$ are positive. The multiplication is straightforward:

  $$\text{For } 0 \leq \hat{k}^z \leq \hat{k}^z\text{: } \hat{\mathcal{R}}(\hat{\mathbf{k}}_1)\hat{\mathcal{R}}(\hat{\mathbf{k}} - \hat{\mathbf{k}}_1)\,. \tag{7.29}$$

- The blue region corresponds to $\hat{k}^z \leq 0$ represented in the right panel. This region is not in memory (again because it is redundant) so we have to use again the reality condition (7.12). The multiplication then turns into

  $$\text{For } \hat{k}^z \leq 0\text{: } \hat{\mathcal{R}}^\star(-\hat{\mathbf{k}}_1)\hat{\mathcal{R}}(\hat{\mathbf{k}} - \hat{\mathbf{k}}_1)\,. \tag{7.30}$$

Let us now focus on the mode $\hat{\mathbf{k}}'$ in figure 7.3. First, note that there are no intersections of the cut-offs centered on 0 and on $\hat{\mathbf{k}}' - \hat{\mathbf{k}}_1$. This means that the only contribution to the $\mathcal{I}^{(2)}(\hat{\mathbf{k}}')$ comes from $\mathcal{I}_{SL}$. Moreover, all the modes $\hat{\mathbf{k}}_1$ inside the cut-off centered on 0 have a smaller z-component than $\hat{\mathbf{k}}'$, *i.e.* $\hat{k}_1^z < \hat{k}'_z$. Hence, we have drawn only two colored regions: the blue corresponds, as before, to $\hat{k}_1^z < 0$ and the green one to $\hat{k}_1^z \geq 0$. They should have the same treatment discussed previously for $\hat{\mathbf{k}}$. However, we see now that some $\hat{\mathbf{k}}' - \hat{\mathbf{k}}_1$ fall outside the grid, *i.e.* $\hat{k}'_{z,y} - \hat{k}_1^{z,y} > N/2$. Recall that the Fourier grid is periodic. Hence, for the modes where $(\hat{k}'_y - \hat{k}^z_1) > N/2$ we can simply subtract N from the y coordinate. The treatment is then similar to (7.29) and (7.30).

For the case $(\hat{k}'_z - \hat{k}^z_1) > N/2$, subtracting N from the z-coordinate makes $(\hat{k}'_z - \hat{k}^z_1) < 0$. We need in addition to use the reality condition. Hence, if we note $\hat{\mathbf{N}}_z$ the vector $(0, 0, N)$, the multiplication reads

$$\text{For } (\hat{k^z}' - \hat{k^z_1}) > N/2\text{: } \hat{\mathcal{R}}^\star(-\hat{\mathbf{k}}_1)\hat{\mathcal{R}}^\star(\hat{\mathbf{N}}_z - \hat{\mathbf{k}}' + \hat{\mathbf{k}}_1)\,. \tag{7.31}$$

The treatment of the corner outside the grid, *i.e.* $(\hat{k}'_z - \hat{k}^z_1) > N/2$ and $(\hat{k}'_y - \hat{k}^y_1) > N/2$ is the combination of the two previous cases.

Structure of the code

The code `RELIC` is organized around two main functions: `I2_LL` and `I2_SL`. Both of them are accompanied by two auxiliary functions which take into account the periodicity. Here, we list the different possible inputs:

- "LL": The code calls the function `I2_LL` with the input cut-off and returns $\mathcal{I}_{LL}$, see equation (7.9). As we have seen previously, the LL contribution vanishes for $\hat{\mathbf{k}}_{x,y,z} > 2k_L$.
- "SL": The code calls the function `I2_SL` with the input cut-off and returns $\mathcal{I}_{SL}$, see equation (7.9). The only point where it vanishes is for the mode 0 which we always set to 0.
- "TT": It stands for the "total" computation (*i.e.* TT for total-total). Whatever the cut-off specified in the parameter file, it calls `I2_LL` with $k_L = k_{min}N/2$. No approximation is done there and the complexity is N^6.
- "LL+": It stands for the sum of the first and last term of (7.10). The function `I2_LL` is called twice. For the pixels inside the cut-off, it is called with $k_L = k_{min}N/2$, *i.e.* exact computation. For the pixels outside the cut-off, `I2_LL` is called with the inputted cut-off.
- "SL+": It stands for the second term of equation (7.10). It computes only for the pixels outside the cut-off the contribution to the integral "SL".
- "d3+": It computes the density given in equation (7.10), *i.e.* "LL+" + 2 "SL+".

By default, we use the `SONG` kernel for the density. It is also possible to use the analytic approximation that we have presented in (6.36) and (6.43). Moreover, we have computed in section 6.1 all the kernels as a function of the `SONG` output $(T^{(2)}_\delta)$. Hence, it is possible to compute all these quantities at second order: ψ, ψ', χ, v. Recall that these expressions are valid only in an EdS universe.

Parallelization

The code `RELIC` is written in `Python`. The main part computing the integral equation (7.21) uses the recent "just-in-time" `Python` compiler `NUMBA` . This module is specifically developed to be compatible with `Numpy` arrays which makes it extremely powerful. Basically, to compile in native machine code a specific function, we can use `NUMBA` decorators, mostly the decorator "@jit(nopython=True)". When the "nopython" mode is activated, the decorated function will be compiled at the first call and run without using any `Python` interpreter. This makes the code almost as performant as the C language.

The library `NUMBA` allows for loops threading parallelization. The integral (7.21) computed by `RELIC` basically consists of three loops: $\hat{k}_x$, $\hat{k}_y$ and $\hat{k}_z$. For each point of the grid, the sum over all pixels (u_1, v_1, w_1) is performed. We use the `NUMBA` loop parallelization to split the $\hat{k}_{x,y,z}$ loops. This is possible because the computation of each second-order grid pixel is independent of the other pixels, it just needs to keep in memory the raw first-order grid.

The threading parallelization is limited by the number of cores available in one node. To improve this, in the parameter file, there are two parameters N_{split} and i_{split}. The first parameter N_{split} indicates that the second-order Fourier grid should be split in N_{split} x-constant slices. Then, the parameter i_{split} indicates which slice has to be calculated. We can, for example, split the grid into 10 slices and run on 10 different nodes. Each slice is then also parallelized with multithread.

7.2 Second order IC for `gevolution`

As we stressed, the study of the LSS is extremely challenging because gravitational collapse is highly non-linear. In section 6.2, we discussed the analytical derivations that have been obtained, first in a Newtonian framework and then including relativistic effects. However, these derivations are only valid on large enough scales or early enough in the history of the universe so that perturbation theory still holds. Fortunately, technological advancements make possible the use of numerical simulations to study this regime. Before `gevolution`, most of the N-body simulations were based on a Newtonian gravitational law [260, 261]. It turns out that the current LSS data and the Newtonian N-body simulations studying these scales are far enough from the cosmological horizon and deep enough in matter domination (relativistic species also require a GR framework) that Newtonian laws are enough. However, the upcoming LSS surveys will probe scales closer to the horizon with a precision never achieved, see *e.g.* [204, 235, 236]. There, a fully GR framework is required.

The code `gevolution` has been developed by J. Adamek, D. Daverio, R. Durrer, and M. Kunz between 2015 and 2016 [263]. It is a fully non-perturbative relativistic N-body simulation code able to account for GR and relativistic species. It works in the Poisson gauge including vector and tensor perturbations. The dynamical equations are derived by using the weak-field expansion that we have used in section 6.2 to write down the continuity and Euler equations that are non-perturbative in $T_{\mu\nu}$.

Up to now, we have not considered the vector mode. In general, in the Poisson gauge, the vector modes are second-order quantities, which means that they are decoupled from the scalar modes up to second order. We would have to considerer vector modes only at the third order. However, to set initial conditions for `gevolution`, we have to consider the full velocity vector and hence, its curl part. Indeed, the simulation is non-perturbative so that vector modes can source important scalar modes that we would miss by setting initially the vector mode to 0. Instead of using the line element (2.20) with a vector mode, we can use a more convenient form of the Poisson gauge line element which gives simpler equations, the so-called $3+1$ decomposition:

$$ds^2 = -a^2 e^{2\phi} d\tau^2 + a^2 e^{-2\psi} \delta_{ij} \left(dx^i + \beta^i d\tau\right) \left(dx^j + \beta^j d\tau\right) \, . \tag{7.32}$$

This decomposition is commonly used in the field of numerical relativity [288]. By analogy with the line element (2.20), we see that the vector mode β^i contributes to g_{00}. As we will see, β^i is a pure second-order quantity so its contribution to g_{00} is of order 4. Then, the cross term gives

$$B_i = e^{-2\psi}\delta_{ij}\beta^j \,. \tag{7.33}$$

Recall that, from the Poisson gauge conditions, we must have $B = 0$. At second order it is enough to require that $\beta^i_{,i} = 0$ because β^i is already a second-order quantity and its covariant form only adds higher-order terms.

7.2.1 Ensemble of point particles

In this subsection, we define the canonical conjugate momentum of a point mass particle. Indeed, in `gevolution`, this is the relevant quantity that is propagated in time [263].

An N-body ensemble of point particles can be described by the action

$$\mathcal{S}_{N-\text{body}} = \sum_{p=1}^{N} \int L_p d\tau \,, \tag{7.34}$$

where the Lagrangian function of the particle particle labeled p of mass m can be written as

$$L_p = -m_p\sqrt{-g_{\mu\nu}v_p^\mu v_p^\nu} = -m_p a\sqrt{e^{2\psi} - e^{-2\phi}\delta_{ij}\left(v_p^i + \beta^i\right)\left(v_p^j + \beta^j\right)} \,, \tag{7.35}$$

where it is understood that all fields have to be evaluated at the particle positions x_p^i. Hence, the canonical momentum conjugate to x_p^i is defined as

$$q_i^p = \frac{\partial L_p}{\partial v_p^i} = a m_p \frac{e^{-2\phi}\delta_{ij}\left(v_p^j + \beta^j\right)}{\sqrt{e^{2\psi} - e^{-2\phi}\delta_{kl}\left(v_p^k + \beta^k\right)\left(v_p^l + \beta^l\right)}} \,, \tag{7.36}$$

In `gevolution`, the Euler-Lagrange equation is directly solved for q_i^p because its evolution equation takes a much simple form. As we will see, in `RELIC`, we generate the velocity initial condition and then convert into canonical momentum. For this, we expand equation (7.36) at second order to find:

$$\frac{q_i^{p,(2)}}{am} = v_i^{p,(2)} + \beta_i^{(2)} - 3\psi^{(1)}\left(v_i^{p,(1)} + \beta_i^{(1)}\right) \,. \tag{7.37}$$

From the Lagrangian (7.35), we can derive the stress-energy tensor for an ensemble of particles thanks to Noether's theorem [263]. In terms of the canonical momenta, we get

$$T^{00} = \sum_{p=1}^{N} \delta^3\left(x^i - x_p^i\right) e^{3\psi-2\phi}\frac{\sqrt{a^2m_p^2 + e^{2\psi}\delta^{ij}q_i^p q_j^p}}{a^6} \,, \tag{7.38}$$

$$T_i^0 = \sum_{p=1}^{N} \delta^3\left(x^i - x_p^i\right) \frac{e^{3\psi-\phi}q_i^p}{a^4} \,, \tag{7.39}$$

$$T_{ij} = \sum_{p=1}^{N} \delta^3\left(x^i - x_p^i\right) \frac{e^{3\phi}q_i^p q_j^p}{a^2\sqrt{a^2m_p^2 + e^{2\phi}\delta^{kl}q_k^p q_l^p}} \,. \tag{7.40}$$

The stress-energy tensor can be defined in a grid mesh x^i_{grid}. To do so, `gevolution` regularises $T_{\mu\nu}$ through a smoothing operation, which, in a particle-mesh scheme, is given by the particle-to-mesh projection. Typically, the smoothing kernel is the cloud-in-cell (CIC) weight function, noted w_{CIC} [263]. This operation is equivalent to substituting the Dirac-delta functions of (7.38), (7.39) and (7.40) by w_{CIC}. The coarse-grained density contrast of a given cell can then be defined by the projection of the stress-energy tensor on the unit normal to the equal-time hypersurface of the Poisson gauge, *i.e.* the normalized vector along the direction $\partial\tau/\partial x^\mu$. This definition is more convenient in a particle-mesh scheme since the density for a given grid cell takes the form:

$$\rho_{\mathtt{gev}}(x^i_{\mathrm{grid}}) = \bar{\rho}(1+\delta_{\mathtt{gev}}) = \sum_{p=1}^{N} w_{\mathrm{CIC}}\left(x^i_{\mathrm{grid}} - x^i_p\right) e^{3\psi}\frac{m_p}{a^3}\sqrt{1+\frac{e^{2\psi}q_p^2}{m_p^2a^2}} \tag{7.41}$$

Note that the definition of the density given in equation (7.41) differs from the usual fluid density used in this thesis and given by equation (2.49). By using our definition of the density (2.30) and the one of `gevolution` , we can link the two:

$$a^2e^{2\phi}T^{00} = \bar{\rho}(1+\delta_{\mathtt{gev}}) = a^2e^{2\phi}\bar{\rho}(1+\delta)(u^0)^2\,. \tag{7.42}$$

This leads at first order to a trivial equality $\delta^{(1)}_{\mathtt{gev}} = \delta^{(1)}$. However, at second order, they differ:

$$\delta^{(2)}_{\mathtt{gev}} = \delta^{(2)} + \left(v^{(1)}_{,i}\right)^2\,. \tag{7.43}$$

Roughly speaking, initializing the $N-$body simulation consists of finding the initial positions of each particle x^i_p such that (7.41) is satisfied. The masses of the particles are set to the same value to avoid the trivial solution of placing each particle onto each mesh point and fixing the mass to satisfy (7.41).

7.2.2 The displacement field

The displacement field is the fundamental quantity that `gevolution` uses to initialize the particle position. In [263], the derivation of the displacement field is performed at first order. Here, we first review the computation at first order and then generalize to second order in the continuum limit.

To this end, let us write

$$x^i_p = y^i_p + \xi^i(y^i_p)\,, \tag{7.44}$$

where y^i_p are the particle's coordinates on an initial homogeneous "template" and $\xi^i(y^i_p)$ is a displacement vector. If this mapping is bijective (i.e. there is no shell crossing) it can be understood as the coordinate transformation from Lagrangian to Eulerian coordinates, and we may also write

$$y^i_p = x^i_p - \xi^i(x^i_p)\,. \tag{7.45}$$

In the following, we drop the space dependence of the displacement field for simplicity. Assuming the displacement field is small, we can write equation (7.41) in the following way

$$\rho_{\mathtt{gev}}(x^i_{\mathrm{grid}}) = \sum_{p=1}^{N}\left(w_{\mathrm{CIC}}\left(x^i_{\mathrm{grid}} - y^i_p\right) - \xi^j w^{\mathrm{CIC}}_{,j}\left(x^i_{\mathrm{grid}} - y^i_p\right)\right) e^{3\psi}\frac{m_p}{a^3}\sqrt{1+\frac{e^{2\psi}q_p^2}{m_p^2a^2}} \tag{7.46}$$

The linearization of (7.46) gives

$$\rho_{\mathtt{gev}}(x^i_{\mathrm{grid}}) - \bar{\rho}(1+3\psi(x^i_{\mathrm{grid}})) = -\sum_{p=1}^{N}\xi^j w^{\mathrm{CIC}}_{,j}\left(x^i_{\mathrm{grid}} - y^i_p\right)\frac{m_p}{a^3} \tag{7.47}$$

Finally, by writing the displacement field as a gradient of a displacement potential ξ, one can solve this last equation to find the exact displacement field and therefore initialize the position of the particle.

Let us find the displacement field in the continuum limit. To do so, we can define generally the function $t^{\mu\nu}$ such that

$$T^{\mu\nu} = \sum_{n=1}^{N} \delta^3\left(x^i - x^i_p\right) \frac{m_p}{a^3} t^{\mu\nu}\left(x^i_p\right) . \tag{7.48}$$

The sum (7.48) is basically a sum over the particle masses m_p multiplied by a function $t^{\mu\nu}/a^3$. In the continuum limit, the sum over the particle masses can be understood as an integral of the constant density background over the volume in the homogeneous grid y^i_p. This means that, by using y^i_p, the continuum limit of equation (7.48) reads:

$$T^{\mu\nu} \to \bar{\rho} \int d^3y \delta^3\left(x^i - y^i - \xi^i(y^i)\right) t^{\mu\nu}\left(y^i + \xi^i(y^i)\right) . \tag{7.49}$$

Finally, we can perform a change of variables and integrate out the δ-function. We find

$$T^{\mu\nu} = \bar{\rho} \left|\frac{\partial y^j}{\partial x^k}\right| t^{\mu\nu}\left(x^i\right) , \tag{7.50}$$

where $|\partial y^j / \partial x^k|$ is the Jacobian. It can be expanded up to second order:

$$\left|\frac{\partial y^j}{\partial x^k}\right| \simeq 1 - \Delta\xi + \frac{1}{2}\left[(\Delta\xi)^2 - (\xi_{,ij})^2\right] , \tag{7.51}$$

where, similarly to the velocity in equation (2.26), we have defined the scalar part of the displacement field as $\xi^i = \xi^{,i}$. Note that the time derivative of equation (7.44) shows that the time derivative of the displacement field is the 3-velocity v^i. The vector part of ξ^i and equivalently v^i will be treated in section 7.2.3.

First order

We can now expand (7.50) for the specific case of T^0_0. Recall that this is defined as the `gevolution` density. Hence we find

$$\delta^{(1)} = 3\phi^{(1)} - \Delta\xi^{(1)} , \tag{7.52}$$

in which we recover the equation (A.2) of [263].

Second order

Now we assume that ξ is still a gradient at second order. To relate $\delta^{(2)}$ and $\xi^{(2)}$, this is accurate because the curl part of $\xi^{(2)}$ would only seed δ at third order, which we do not consider here. We consider equations (7.50) to second order and use equations (7.38) and (7.51):

$$\delta^{(2)}_{\texttt{gev}} = 3\phi^{(2)} - \Delta\xi^{(2)} + \frac{1}{2}(v^{(1)}_{,i})^2 - 3\phi^{(1)}\Delta\xi^{(1)} + \frac{9}{2}\phi^2_{(1)} + \frac{1}{2}\left((\Delta\xi^{(1)})^2 - (\xi^{(1)}_{,ij})^2\right) . \tag{7.53}$$

The second order transfer function can be written as

$$\begin{aligned}k^2\mathcal{T}_\xi^{(2)} =&\mathcal{T}_{\delta_{\texttt{gev}}}^{(2)} - 3\mathcal{T}_\phi^{(2)} - \frac{3}{2}\left(k_2^2\mathcal{T}_\phi^{(1)}(k_1)\mathcal{T}_\xi^{(1)}(k_2) + k_1^2\mathcal{T}_\phi^{(1)}(k_2)\mathcal{T}_\xi^{(1)}(k_1)\right) - \frac{9}{2}\mathcal{T}_\phi^{(1)}(k_1)\mathcal{T}_\phi^{(1)}(k_2)\\ &+ \frac{1}{2}\vec{k_1}\cdot\vec{k_2}\mathcal{T}_v^{(1)}(k_1)\mathcal{T}_v^{(1)}(k_2) - \frac{1}{2}(k_1^2k_2^2 - (\vec{k_1}\cdot\vec{k_2})^2)\mathcal{T}_\xi^{(1)}(k_1)\mathcal{T}_\xi^{(1)}(k_2)\,.\end{aligned} \tag{7.54}$$

7.2.3 The velocity

Theoretically, we can obtain the velocity by differentiating the displacement field w.r.t. time. In practice, we would have to compute the displacement field at two different times. At second order, this would involve two evaluations of the integral (7.21) at two different times and then a differentiation. However, in addition to the complexity that is multiplied by two, numerical differentiation is very noisy. We prefer to use the last Einstein equation that we did not use up to now, the $0i$ equation. Furthermore, we will also be able to estimate the vector part of the velocity.

Up to second order, if we including the vector mode, the only changed Einstein tensor component is the space-time $0i$ which becomes

$$\frac{a^2}{2}G_i^0 = e^{-\phi}\left(e^{-\phi}(\mathcal{H} - \psi')\right)_{,i} + \frac{1}{4}\Delta\beta_i\,. \tag{7.55}$$

On the other hand, the stress-energy tensor becomes

$$T_i^0 = \bar{\rho}\left(v_i^{(2)} + \beta_i^{(2)} + \delta^{(1)}v_i^{(1)} - 4\phi^{(1)}v_i^{(1)}\right)\,. \tag{7.56}$$

Therefore the $0i$ Einstein equation can be written as

$$\frac{3\mathcal{H}^2}{2}\left(v_i^{(2)} + \beta_i^{(2)} - v_i^{(1)}\Delta\xi^{(1)} - \psi^{(1)}v_i^{(1)}\right) = -\mathcal{H}\phi_{,i}^{(2)} - \psi_{,i}'^{(2)} + 2\mathcal{H}\psi^{(1)}\psi_{,i}^{(1)} + \frac{1}{4}\Delta\beta_i\,. \tag{7.57}$$

Scalar part

Let us now take the divergence of (7.57). This equation can be derived directly from equation (2.48b) since we only consider the scalar modes:

$$\frac{3\mathcal{H}^2}{2}\Delta v^{(2)} = -\mathcal{H}\Delta\phi^{(2)} - \Delta\psi'^{(2)} + \left(2\mathcal{H}\psi^{(1)}\psi_{,i}^{(1)} + 6\mathcal{H}^2v_{,i}^{(1)}\psi^{(1)} - \frac{3\mathcal{H}^2}{2}\delta^{(1)}v_{,i}^{(1)}\right)^{,i}\,, \tag{7.58}$$

which gives in Fourier space:

$$\begin{aligned}\frac{3}{2}\mathcal{T}_v^{(2)} =& -\mathcal{H}^{-1}\mathcal{T}_\phi^{(2)} - \mathcal{H}^{-2}\mathcal{T}_{\psi'}^{(2)} - \mathcal{H}^{-1}\mathcal{T}_\psi^{(1)}(k_1)\mathcal{T}_\psi^{(1)}(k_2)\\ &- \frac{3}{4k^2}\left(\vec{k}\cdot\vec{k}_2\mathcal{T}_\delta^{(1)}(k_1)\mathcal{T}_v^{(1)}(k_2) + \vec{k}\cdot\vec{k}_1\mathcal{T}_\delta^{(1)}(k_2)\mathcal{T}_v^{(1)}(k_1)\right)\,.\end{aligned} \tag{7.59}$$

We have expressed in equations (6.8) and (6.12) $T_\phi^{(2)}$ and $T_{\psi'}^{(2)}$ as a function of the second order transfer function of the density. Thus, in `RELIC`, we inject the `SONG` second-order transfer function into equation (7.59) to compute the initial conditions for the velocity field at second order.

Curl part

Taking now the curl part of (7.57), we have

$$\Delta\beta_i = 6\mathcal{H}^2\left(w_i + \beta_i - 4\phi w_i + w_i\delta\right)\,. \tag{7.60}$$

This equation is valid both at first and at second order. We now have two unknown quantities: the second-order velocity and the second-order shift-vector β_i. Hence, we need a second equation in order to solve the system. In [289], it was shown that in a perfect fluid, there is no source for the vorticity. Assuming vanishing vorticity and using the $0i$ Einstein equation, one can solve for the vector mode and the curl part of the 3-velocity.

Let us follow [289] and define the projector onto the fluid rest space $h^\mu_\nu = \delta^\mu_\nu + u^\mu u_\nu$. We then use the covariant expression for the vorticity, keeping only second-order terms,

$$\omega_{ij} = h^\alpha_{[i}h^\beta_{j]}u_{\alpha;\beta}\,, \tag{7.61}$$

where, including the vector mode, the 4-velocity of matter takes the form up to second order:

$$u_\mu = a\left(\frac{e^{-\phi}}{\sqrt{1-v^2}}, \beta_i + e^{-2\psi-\phi}w_i\right)\,. \tag{7.62}$$

The final expression reads

$$\omega_{ij} = a\left(\beta_{[i,j]} + w_{[i,j]} - 4w_{[i}\phi_{,j]} + w'_{[i}w_{j]}\right)\,. \tag{7.63}$$

We can substitute w'_i thanks to the first-order Euler equation (6.13b) whose scalar part is given in (6.16b). Then, let us substitute w_i using equation (7.60), which gives

$$\omega_{ij} = a\left(\frac{\mathcal{H}^{-2}}{6}\Delta\beta_{[i,j]} - w_{[i}\delta_{,j]} - \phi_{,[i}w_{j]}\right)\,. \tag{7.64}$$

Recall that ω_{ij} has to vanish any order according to [289]. Thus, at first order, we recover the well known result

$$\Delta\beta^{(1)}_i = 0\,, \tag{7.65}$$

and we find at second order

$$\Delta\beta^{(2)}_i = 6\mathcal{H}^2\left(w^{(1)}_i\delta^{(1)} - \phi^{(1)}w^{(1)}_i\right)\,. \tag{7.66}$$

Replacing (7.66) in equation (7.60), we find

$$w^{(2)}_i + \beta^{(2)}_i - 3v^{(1)}\phi^{(1)} = 0\,. \tag{7.67}$$

The left-hand side of (7.67) is exactly the second-order momentum with a vanishing $\beta^{(1)}$ according to equation (7.37). Hence we do not have to consider the vector part of the velocity and displacement fields.

7.3 Results

In this section, we give some preliminary results from the implementation of the code `RELIC` when writing this thesis. More definitive results have been published in [294],

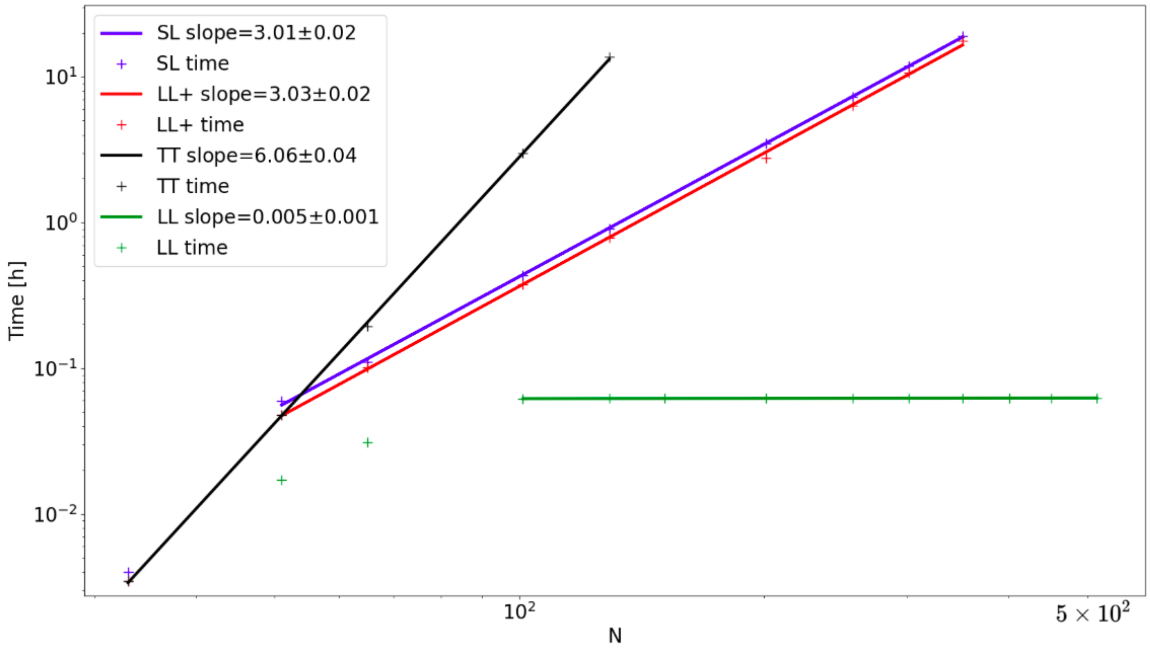

Figure 7.4: Computation time in hours as a function of the grid size N in log-scale. We show separately the $\mathcal{I}_{SL}$, $\mathcal{I}_{LL}$, $\mathcal{I}_{TT}$ and $\mathcal{I}_{LL+}$. The computation has been performed on 4 cores. The solid line shows the result of the linear fit whose slope is indicated in the legend.

but since there was no fundamental change, we will only comment on the generalizations performed in [294]. We will first show the performance of the code and then give the different consistency tests that we have performed to show how robust `RELIC` is. To finish this section, we will discuss the connections with `gevolution` and show the last consistency checks performed before writing this thesis. All power spectra and bispectra are estimated thanks to the available Python libraries for the analysis of numerical simulations `Pylians`. It provides a power spectrum and a bispectrum estimator based on [290] and on the development of [291, 292].

7.3.1 Performance

As explained in section 7.1, the main point of the long-short splitting is the complexity scaling like N^6 in general. With physical arguments, we have reduced this complexity to $N_\Lambda^3 N^3$ thanks to the approximation (7.9). In figure 7.4, we plot the computational time as a function of the grid size. The computation has been performed on 4 cores in all cases. For all curves, we have fitted only the last points that make the fit stable. Indeed, once we go to small grids, the computational time of the main part of the code can become of the same order as other residual processes which breaks the scaling. To have a proper fit, one needs to consider large enough grids so that all residual processes become negligible compared to the main integral computation.

Let us look for example at the LL curve, *i.e.* $\mathcal{I}_{LL}$ in (7.9). Theoretically, we expect a constant scaling, see section 7.1. We see that the first three points are underestimated. In this particular case, note that if we consider $N_\Lambda > N$, so that the code assumes $N = N_\Lambda$, the complexity should scales like N^6. This is also true for the other components $\mathcal{I}_{SL}$ and $\mathcal{I}_{LL+}$. For all the three curves LL, SL, and $LL+$, the scaling starts to be stable for a

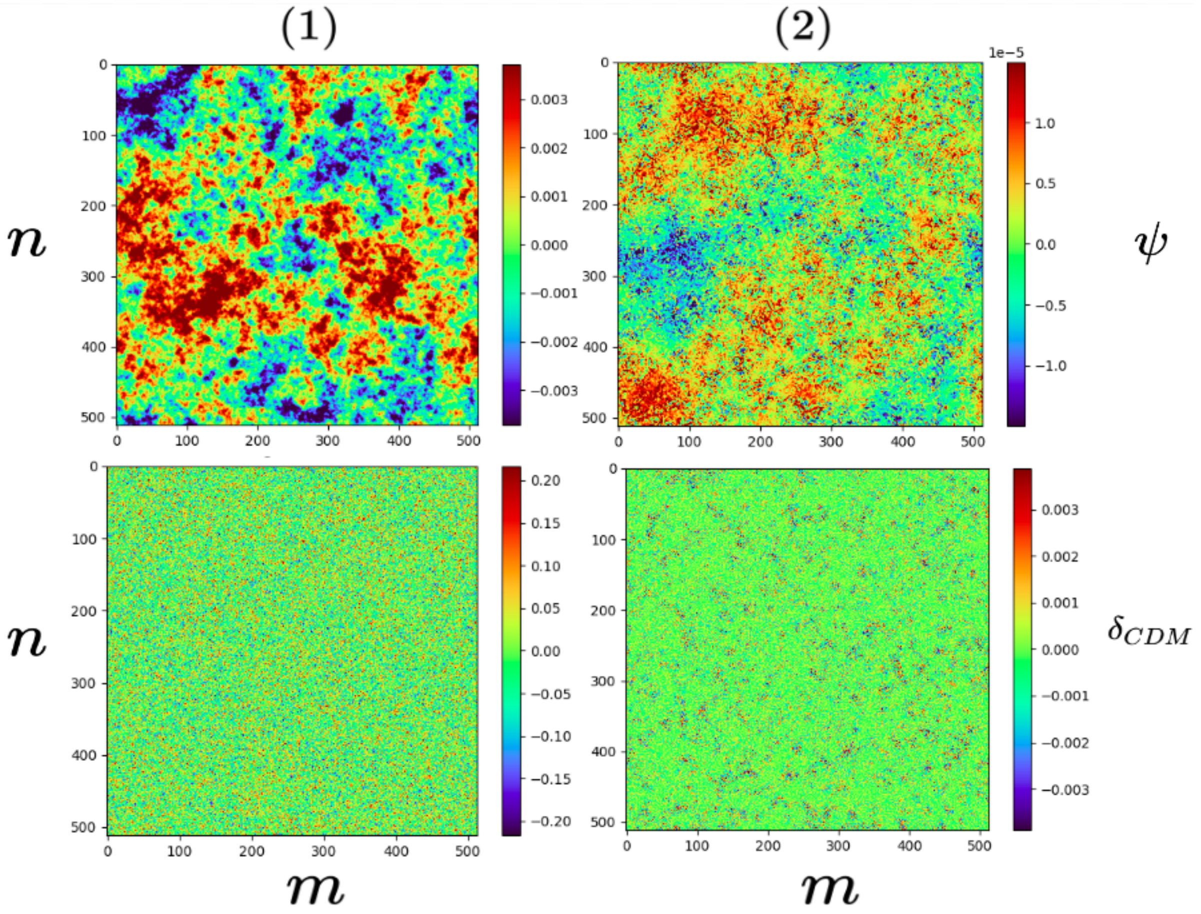

Figure 7.5: On the first(second) line, the potential(CDM density) x-constant slice field at a redshift 100 as a function of the z and y discrete indices. The first column corresponds to the first order and the second to the second order contributions. The size of the box is 512^3 with a fundamental mode $k_{min} = 2 \times 10^{-4}$ hMpc^{-1}. For the second-order field, we used $k_\Lambda = 5 \times 10^{-3}$. Note also that we used $A_s = 2.215 \times 10^{-6}$.

computational time ~ 3 minutes. Forgetting all the points where the computational time is faster than ~ 3 minutes, we find a scaling very close to the theoretical prediction, *i.e.* ~ 3 for SL and $LL+$ and a constant ~ 0 for LL, see the legend of figure 7.4.

It can also be useful to have the y-intercept parameters: $-6.5, -6.8$ for SL and $LL+$ respectively. One can then compute that for a 1024^3 grid, the computation would take ~ 0.5 day for each one on 128 cores and ~ 5 days each for a 2048^3 grid again on 128 cores.

On the other hand, we also show in figure 7.4 the total computation time. It does not have the same cut-off problem as for the previous curves, the fit is stable even for the lowest N that we consider here. As expected, it has a N^6 scaling with a y-intercept parameter -18.7. Then, we see that the next point ($N = 150$) would have taken 33 hours and $N = 200$ already more than one week (in the configuration that we choose *i.e.* 4 cores). On 128 cores, our goal of 1024^3 would take 13 years.

7.3.2 Power spectrum

We show in figure 7.5 a visual representation of the density and the potential fields at redshift 100. The computation has been performed on a 512^3 grid with a fundamental

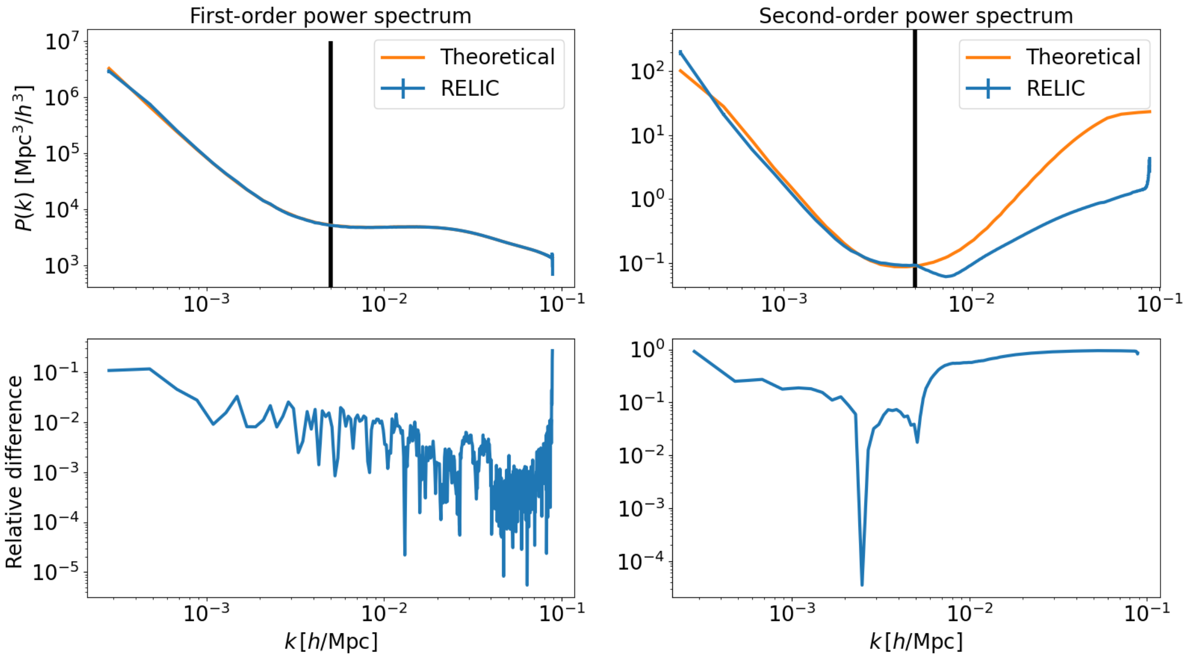

Figure 7.6: In the first row, the first- and second-order power spectra of 10 realizations with $N = 512$. In the second raw, the relative difference between the theoretical prediction and the average over the 10 realizations. The error bars are computed by dividing the standard deviation of the realizations by $\sqrt{10}$. They are very small and difficult to see. The black line indicates the cut-off scale $k_\Lambda = 0.005\ h\mathrm{Mpc}^{-1}$. The fundamental mode is $k_{min} = 0.0002\ h\mathrm{Mpc}^{-1}$.

mode $k_{min} = 2 \times 10^{-4}\ h\mathrm{Mpc}^{-1}$ and a cut-off $k_\Lambda = 5 \times 10^{-3}\ h\mathrm{Mpc}^{-1}$. To test our code, we want to boost the relativistic effects as much as possible. This is why we chose a fundamental mode larger than the horizon. For the same reason, we have boosted the initial perturbation amplitude A_s by a factor of 1000, *i.e.* we work with $A_s = 2.215 \times 10^{-6}$. We know that the variance of the bispectrum scales like $(P(k))^3$ [293] while the bispectrum scales like P^2. Hence the signal to noise scales as $\sqrt{A_s}$; multiplying A_s by 1000 increases the signal-to-noise by a factor $\sqrt{1000} \simeq 32$.

First order

In the first column of figure 7.5, we see a x-constant slice of the first order potential (on the top) and CDM density (below). These first-order quantities are obtained by multiplying the primordial curvature perturbation realizations, such as figure 7.2, by the `CLASS` transfer functions. The features observed for the potential and the density contrast are very different. For the potential, the first-order transfer function boosts the large scales which makes it smoother. For the density, however, the transfer function boosts the small scales and creates this very small noisy grain behavior. This can be understood by looking at the Poisson equation (6.2) where we see that the small scales are boosted by the Laplacian of the potential. The first-order potential standard deviation is typically of order $\sim \sqrt{A_s}$ and does not grow with time, *i.e.* the well known $\sim 10^{-5}$ with the Planck maximum likelihood $A_s = 2.215 \times 10^{-9}$. Since we have boosted A_s by a factor 1000, we have $\psi^{(1)} \sim 10^{-3}$ and $\psi^{(2)} \sim \psi^2_{(1)} \sim 10^{-6}$. We have seen in section 6.2 that, unlike the potential, the density grows like a during the matter domination era. If we neglect the growth during the radiation era (in $\ln a$), at a redshift 100 we find a growth of $z_{eq}/100 \simeq 35$ which is coherent with the order of magnitude of the perturbations observed in figure 7.5.

The first-order density power spectrum is shown in the left panel of figure 7.6. The theoretical power spectrum is computed as usual; we multiply the primordial power spectrum, given in equation (3.36), by the Poisson gauge first-order transfer function squared, *i.e.* equation (2.123) with pure ADI. The transfer functions are provided by `CLASS`. The `RELIC` power spectrum in the left panel of figure 7.6 is the mean of 10 realizations with $N = 512$. The visual representation of one of these realizations is shown in figure 7.5. The error bars are estimated by the standard deviation of the 10 realizations divided by the square root of the number of realizations, here $\sqrt{10}$.

At first order, we can claim an agreement with a relative error of 1% between $k = 10^{-3}\ h\mathrm{Mpc}^{-1}$ and $k = 10^{-3}\ h\mathrm{Mpc}^{-1}$. For small scales $k > 10^{-2}\ h\mathrm{Mpc}^{-1}$, the error is even smaller except for modes very close to k_{max} where we expect the numerical effects to become large. For the large scales $k < 10^{-3}\ h\mathrm{Mpc}^{-1}$, we observe a quite large relative error of $\sim 10\%$. This comes from two different effects. First, the cosmic variance, as explained in section 2.5, produces larger error bars at large scales. With simulations, we can reduce this error by averaging over several simulations, here 10, but the error bars remain larger for the largest scales. Moreover, at large scales, the power spectrum estimator `Pylians` generates a bias which is due to the k-binning. To avoid this bias, `Pylians` provides a routine that samples the theoretical power spectrum exactly in the same way as the power spectrum estimated from the simulations. This effect depends on the exact scaling of the power spectrum for $k \to 0$. In the case of the first- and second-order density power spectrum, the binning of the theoretical power spectra does not significantly improve the agreement.

Second order

In the second column of figure 7.5, we show a x-constant slice of one second-order potential and CDM density realization computed by `RELIC`. The CDM density is computed with the brute `SONG` second-order transfer function. For the potential, we used the kernel given in equation (6.8). The cut-off scale that we have chosen to have a reasonable computational time for a parallel computation on 256 processors with $N = 512$ is $k_\Lambda = 0.005\ h\mathrm{Mpc}^{-1}$. This corresponds in real space to a scale size $\sim 1256\ h^{-1}\mathrm{Mpc}$, *i.e.* ~ 10 times the step $2\pi/k_{max}$. The order of magnitude is consistent with first order squared since $\mathcal{I}^{(2)} \sim \mathcal{I}^2_{(1)}$.

The second-order potential figure is less smooth than at first order. We observe two distinct scales of perturbations, one quite large, similar in size to the large-scale perturbations of the potential, and one at small scales which generates a grainy feature. The large-scale perturbations are attributable to the relativistic perturbations are that important for $k < \mathcal{H}$. For the small scales, however, since we have neglected their small-scale coupling, we observe only noise for $\Delta(m, n) < 10$, *i.e.* for the scales smaller than the cut-off k_Λ.

The second-order density, which we can see in the last panel of figure 7.5, has grown by the same factor as the first order, *i.e.* like a, as predicted from the relativistic perturbation theory of chapter 6. Similarly to the first order, we do not observe perturbations at large scales. However, we observe a type of perturbation of size $\Delta(m, n) \sim 10$. They can be attributed to the cut-off. For smaller scales, we observe a noisy behavior, probably attributable to noise.

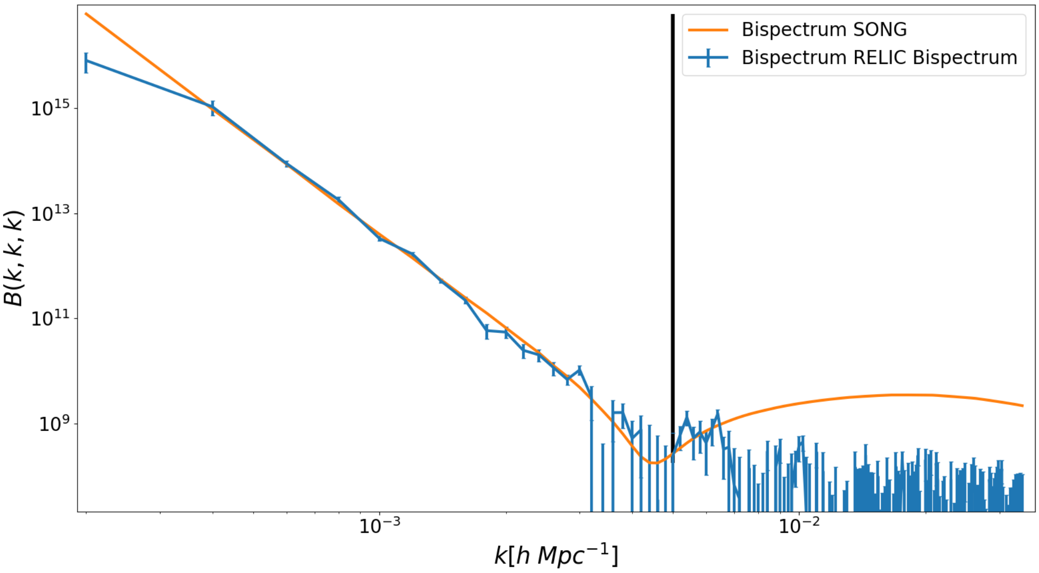

Figure 7.7: Equilateral configuration of the CDM density bispectrum. In orange, the theoretical prediction computed by injecting the `SONG` kernel in equation (6.21). In blue, the average of 14 realizations with error bars computed by dividing the standard deviation of the 14 realizations by $\sqrt{14}$. The black curve notes the cut-off scale $k_\Lambda = 0.005\ h\text{Mpc}^{-1}$. The realizations have the same specifications that indicated in the caption of figure 7.6.

In figure 7.6, we show in the second column the power spectrum of the second-order density. The orange curve is the theoretical prediction that we have computed by using equation (2.121) with vanishing PNG, *i.e.* $\mathcal{R}^{(2)} = 0$. We can integrate out the δ-function to remove one integral. Then we can replace all q_2 by $|\mathbf{k} - \mathbf{q_1}|$. Hence, all the functions that depended on q_2 now depend on the modulus of q_1 and of k and on the angle between $\mathbf{k}$ and $\mathbf{q_1}$. The integral of the third term of equation (2.121) (which is the only one that does not vanish) can be written as a two-dimensional integral:

$$P_{\delta^{(2)}}(k) = 4\pi \int \frac{q_1^2 \sin\theta dq_1 d\theta}{(2\pi)^3} \left(\mathcal{T}_\delta^{(2)}(q_1, k, \theta)\right)^2 P_{\mathcal{R}}(q_1) P_{\mathcal{R}}(q_1, k, \theta)\,. \tag{7.68}$$

The theoretical power spectrum in the right panel of figure 7.6 is obtained by numerically integrating the integral (7.68). For simplicity, we have used the analytical approximation (6.22) with $\alpha = \alpha_R$ and $\beta = \beta_R$ given in (6.36) and with $\gamma = \gamma_+$ given in (6.43). The numerical integral is slowly convergent because of an IR divergence, and the result is also dependent on the integration interval. This comes from the fact that we have chosen a very small k_{min} and, as we can see in the left panel of figure 7.6, the cut-off scale k_Λ is smaller than the matter-radiation equality scale k_{eq}, see section 6.3. This produces a lack of power. The result shown in figure 7.6 has been computed with k_{min} and k_Λ as integration interval.

On the other hand, similarly to the first-order case, the second-order `RELIC` power spectrum shown in figure 7.6 is the mean of 10 realizations with error bars computed by dividing the standard deviation of the realizations by the square root of the number of realizations. The global shape and the amplitude are well reproduced for the scales between k_{min} and k_Λ. As expected, for the small scales, when $k > k_\Lambda$, the `RELIC` power spectrum diverges from the theoretical prediction. The small-scales feature observed in the

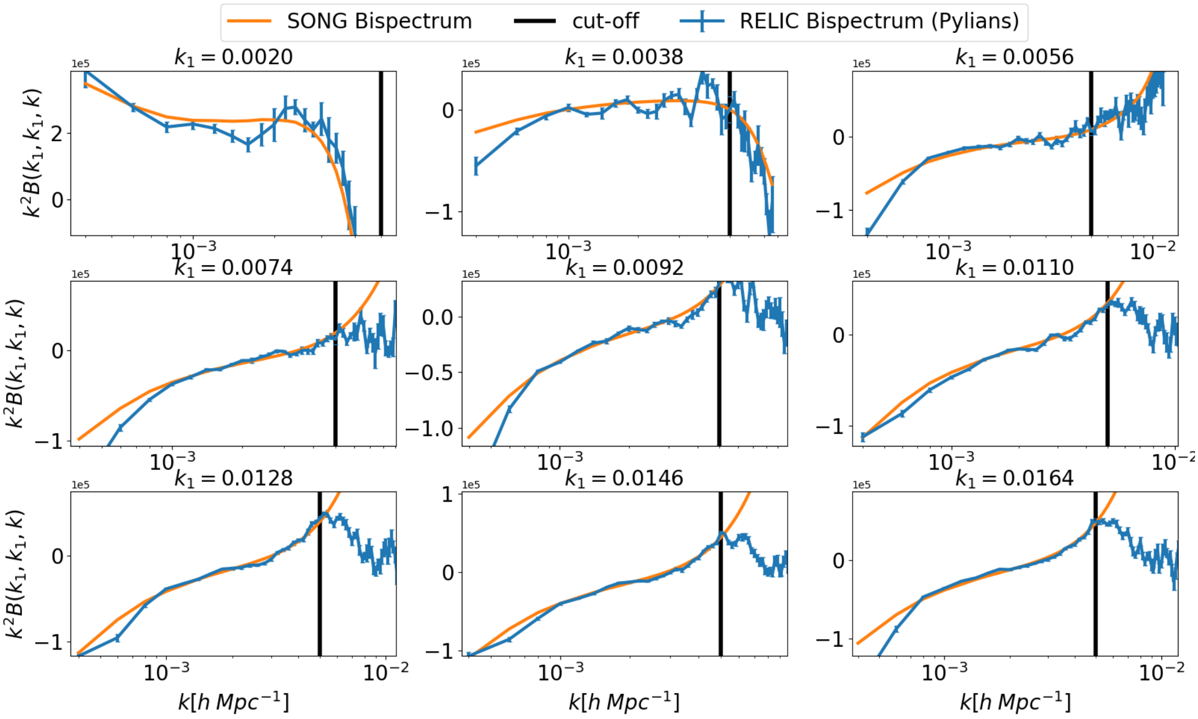

Figure 7.8: We plot for 9 squeezed configurations the CDM density bispectrum multiplied by 100; the orange curve labeled "Bispectrum Song" is the theoretical bispectrum and the blue is the measured one averaged over 14 realizations. The black vertical lines indicate the cut-off scales $k_\Lambda = 5 \times 10^{-3}\ h\mathrm{Mpc}^{-1}$. Note that for an easier visualization, we have plotted $k^2 B$. The first two arguments are fixed to k_1 whose value is indicated above each figure in $h\mathrm{Mpc}^{-1}$. We vary the third argument between k_{min} and $2k_1$ to ensure the triangular inequality. The smaller k is compared to k_1, the more squeezed the configuration is.

second-order density realization shown in figure 7.5 should only come from the noise power spectrum for the modes $k > k_\Lambda$. However, there is a discrepancy of order 10% between the theoretical and the `RELIC` power spectrum for $k < k_\Lambda$. As we will see in section 7.3.3, it is more likely that this discrepancy comes from one of the problems or approximations discussed when computing the theoretical (7.68) than from `RELIC` . Note finally that in [294], we have improved this theoretical estimation by using the different integrators (Scipy and Cuda, see [295]) and the `SONG` second-order transfer function interpolated. The conclusion is that a discrepancy remains at large scale, probably due to the IR divergence.

7.3.3 Bispectrum

In order to test our code, we have to multiply the bispectrum by an additional factor of 100. Indeed, the signal-to-noise was not enough to well observe the features of our code. This is effectively equivalent to multiplying the second-order density or the second-order transfer function by 100. As long as we only consider the density transfer function returned by `SONG`, this artificial boost is consistent. Note that the factor 100 was determined from just 4 realizations; we present here the average over 14 realizations for which this factor might be larger than needed. Effectively, given also the multiplication of multiplying A_s by a factor 10^3, the total boost of the signal-to-noise is ~ 3000.

In figure 7.7, we plot the equilateral configuration of the bispectrum. In orange, as for the power spectrum, we show the theoretical bispectrum computed from equation (2.139) with vanishing PNG or equivalently from (6.21). The output of `SONG` is exactly the second-order transfer function, hence we need to divide by the transfer function according to (6.20) to get F_2. In blue, the average of the 14 realizations with the error bars being computed in the same way as for the power spectrum. Our initial conditions generator reproduces well the theoretical bispectrum as long as we consider modes smaller than the cut-off, represented by the black vertical line, and except for the first point. The discrepancy for the first point is because the code `Pylians` includes the 0 mode in the first bin. Since this mode is zero, the absolute value of the first bin is always underestimated. For this reason, we drop this first bin in the following.

The agreement becomes difficult to see when we are close to the cut-off (but still for $k < k_\Lambda$) since the error bars include 0 already for $k < 3k_\Lambda$. However, we see that right after the cut-off, the amplitude increases again because we have chosen a cut-off similar to the horizon scale. It seems that the first points of the `RELIC` bispectrum are still compatible with the theory even though we have passed the cut-off. For modes larger than $3k_\Lambda$ however, the bispectrum falls to 0 which is expected given our approximation.

Finally, in figure 7.8, we show the main result: the squeezed limit configuration of the CDM density bispectrum. The orange and blue curves are again the theoretical and measured bispectra. For each panel, we have fixed the first two arguments of the bispectrum to a given value, called k_1. The third argument varies between k_{min} and $2k_1$ according to the triangular inequality. The smaller k is compared to k_1, the more the configuration is squeezed.

Again we observe in general a good agreement for the modes lower than the cut-off except for the first 2 points. The first panel corresponds to the lowest value of k_1. Because of this and the cosmic variance, we see large error bars for all k. Note that for the first three panels, $k_1 \lesssim k_\Lambda$, which means that in principle, we can trust the measurement even for $k > k_\Lambda$. Indeed, we have neglected the small-small coupling which means that our approximation should be accurate as long as one mode is smaller than the cut-off. We cannot see this case on the first panel since k_Λ is larger than the range of possible values for k. In the second and third panels, however, we see that the agreement continues beyond k_Λ. For all the other panels, $k_1 > k_\Lambda$ so that the bispectrum systematically falls to 0 when k also becomes larger than k_Λ.

The binning effect is expected to become important on large scale. Therefore it can explain the discrepancy of the first two points. `Pylians` does not provide a routine that bins the theoretical bispectrum in the same way as the one computed from the simulations in order to take this effect into account. An additional bias can also come from the boosting factor 100 that we used to have a measurement of the bispectrum. Indeed, the bispectrum measurement of $\delta^{(1)} + 100\delta^{(2)}$ includes $\left\langle 100\delta^{(1)}\delta^{(1)}\delta^{(2)} \right\rangle$, which is the term that we try to reproduce, and also $\left\langle 100^3\delta^{(2)}\delta^{(2)}\delta^{(2)} \right\rangle$. This higher-order term might bias our measurement. In [294], we have controlled this bias by measuring the bispectrum of $\delta^{(2)}$.

7.3.4 Consistency

The first implementation that we have performed was using the continuum limit approximations (7.52) and (7.53) to initialize the initial particle positions. However, the error generated by the continuum approximation turned out to be larger than the second-order terms. Hence was have, in principle, to solve the discrete equation (7.47). A reminder that this is only a first-order equation, which means that we would have to generalize

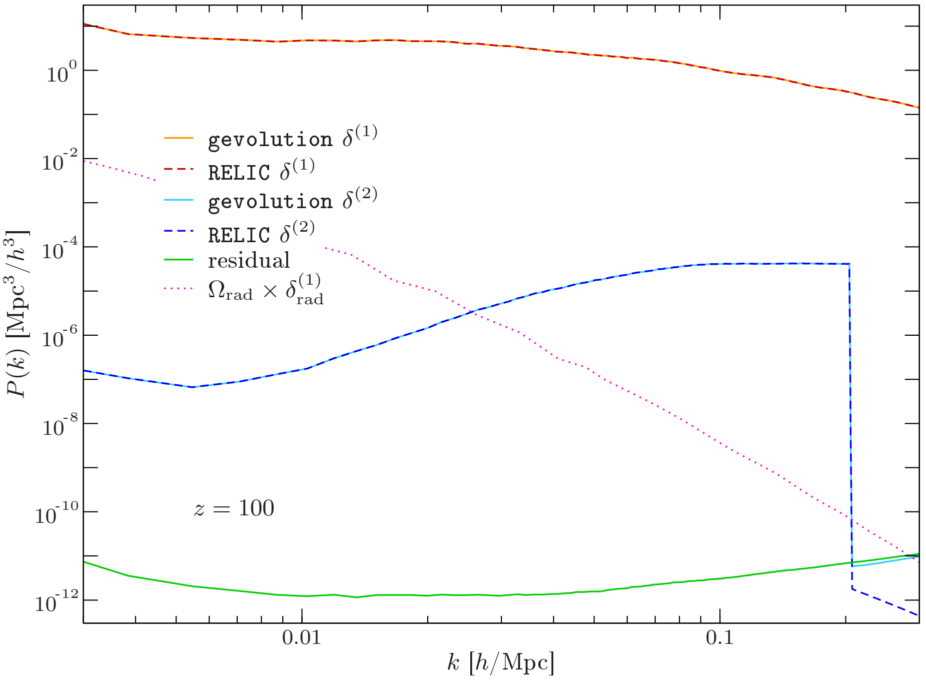

Figure 7.9: Comparison of the `RELIC` realization power spectra, in dashed lines, and, in solid lines, the power spectra after generating the point particles with `gevolution` and re-projecting on the grid. We represent in orange, the `gevolution` density power spectrum, in red the `RELIC` power spectrum, in the cyan the `gevolution` second-order power spectrum and in blue the `RELIC` second-order power spectrum. The green line is the residual of the second-order power spectrum and in pink, we represent the radiation power spectrum. All of these power spectra are computed at $z = 100$ and for a fundamental mode $k_{\rm min} = 1.6 \times 10^{-3}\ h\ \mathrm{Mpc}^{-1}$. Figure from [294].

this method at second order. Instead, we will use an iterative method that avoids this generalization and simplifies the implementation.

Let us first rewrite (7.47) by introducing the density contrast and the displacement field potential:

$$\hat{\rho}(\mathbf{x}_g) - \bar{\rho}\,(1 + 3\phi(\mathbf{x}_g)) = -\sum_{x'_{\rm grid}} \xi(\mathbf{x}'_{\rm grid}) \sum_{\rm p} \frac{m_p}{a^3} w^j_{\rm grad}(\mathbf{x}'_{\rm grid} - \mathbf{y}_p)\omega^{\rm CIC}_{,j}(\mathbf{x}'_{\rm grid} - \mathbf{y}_p)\,, \quad (7.69)$$

where the kernel $w_{\rm grad}$ is the discrete gradient kernel. This last equation is a matrix equation for an unknown N^3-dimensional vector $\xi^{(1)}(\mathbf{x}'_g)$ that is multiplied by a known $N^3 \times N^3$ matrix. This is the exact fundamental equation solved by `gevolution` in its basic implementation to initialize the particle positions. Since it is a first-order equation, even though we put in the left hand side $\delta^{(1)}_{\rm gev} - 3\phi^{(1)} + \delta^{(2)}_{\rm gev} - 3\phi^{(2)}$, the solution will be precise only at first order $\xi^{(1)}$. With this solution, one can use the fully non-linear equation (7.41) to compute the density field obtained after initialization of the particles and re-projection on the grid. We denote this density with a hat $\hat{\rho}^{(1)}_{\rm gev}$. The quantity $\hat{\rho}^{(1)}_{\rm gev}$ is not defined as a term in a series expansion but as the result of the actual projection given the particle positions obtained with the displacement field $\xi^{(1)}$. Hence, it contains quadratic, and various higher order terms, in $\xi^{(1)}$.

To be accurate at second-order, we can now expand the displacement field at second-order, *i.e.* $\xi = \xi^{(1)} + \xi^{(2)}$ and expand again (7.41). Since all the first-order, and quadratic terms are contained in $\hat{\rho}^{(1)}_{\tt gev}$ which is now known, the second order expansion can be written

$$\rho_{\tt gev}(x^i_{\rm grid}) - \rho^{(1)}_{\tt gev}(x^i_{\rm grid}) = -\sum_{x'_{\rm grid}} \xi(\mathbf{x}'_{\rm grid}) \sum_{\rm p} \frac{m_p}{a^3} w^j_{\rm grad}(\mathbf{x}'_{\rm grid} - \mathbf{y}_p)\omega^{\rm CIC}_{,j}(\mathbf{x}'_{\rm grid} - \mathbf{y}_p)\,, \quad (7.70)$$

which is the exact same equation solved by `gevolution`, see (7.69), but with a different left-hand side term. Hence, we can once again run the corresponding part in `gevolution` to get $\xi^{(2)}$ and generate the corresponding density with the non-linear equation (7.41) to have a density accurate a second order. If we need a n-order precision, the same method can be repeated n times.

In figure 7.9, we compare the power spectra of the `RELIC` density contrast with the power spectra of the density contract obtained after generating the particles, by using the displacement field obtained with the iterative method as explained above, and by re-projecting on the grid following (7.41). The orange solid line is obtained with `gevolution` while the dashed red line is obtained simply with `RELIC`. As expected, the first-order contribution dominates, and the agreement is extremely good until scale 0.3 $h\mathrm{Mpc}^{-1}$. Indeed, the discretization errors are expected to become very large for scales close to the Nyquist frequency which is why we do not show larger scales. For the same reason, we have embedded our second-order grid in a larger grid so that the larger mode considered at second order is 25% × $k_{\rm Nyquist}$. This is why we see a sharp cut-off for the second-order power spectra of the `RELIC` density contrast in dashed blue and of the particle-mesh projection in solid cyan. The residual, *i.e.* the difference between these two power spectra, is shown in green. Thanks to the iterative method, this residue is dominated by numerical precision. In [294], we also show that the agreement also holds in real space.

As a final remark, let us note that, in this third part of the thesis, we have used the Einstein-de Sitter limit for all computations. This was justified by the fact that we set the initial conditions deep in the matter domination era, here at $z = 100$. However, even though this is a good approximation at first-order, it turns out that the error made is larger than the second-order term, as shown by the radiation power spectrum represented in pink in figure 7.9. Hence, the first-order radiation contribution is as large as the second-order CDM density, which means that we need to take the radiation into account at first order. In [294], we have generalized all equations presented in section 6.1. Moreover, further works to correctly account for the baryons are planned.

7.4 Conclusion

The measurement of primordial non-Gaussianities would give us access to precious information about physics in the early universe. In particular, the measurement of a non-vanishing primordial signal in the squeezed limit of the matter density bispectrum, *i.e.* a coupling between large and small scales, would be a direct sign of the presence of at least two active primordial degrees of freedom. In the context of inflation, this means ruling out all single-field inflation models.

The current and forthcoming large-scale structure surveys are expected to reach a never achieved precision on the measurement of the amplitude of the local type of non-Gaussianities. Very optimistic forecasts in the literature gave a precision of order $f_{\rm NL} \sim 0.1$ [192, 204, 240]. To reach such a limit, the surveys have to probe the largest possible volume since the squeezed limit is a coupling between large and small scales. These very different scales make the actual measurement extremely challenging because it involves different physical effects (for instance biasing, rel effect, non-linear effects).

It is expected that the largest scales probed by the surveys will be close enough to the particle horizon that the current Newtonian theory of structure formation will not be sufficient anymore. The structure formation has to be understood in a relativistic framework. Many analytical computations have been performed over the last 30 years to account for the relativistic effects. In particular, it has been highlighted in the recent work [250] that, at second order, the relativistic effects are degenerate with the local PNG in momentum space (coupling large and small scales) and in their temporal evolution (they have the same time dependence). Hence, an accurate modelization of these effects needs to be done to disentangle them from a primordial signal.

The analytical computations are accurate when the perturbation theory still holds. In the squeezed limit, large scales influenced by the relativistic effects are mixed with the small scales where the perturbation theory completely breaks down. To study these scales, numerical simulations are a very powerful tool. Hence, the fully relativistic N-body code `gevolution` is the perfect tool to test the accuracy of analytical computations, by taking into account the small-scale non-linearities and the large-scale relativistic effects at the same time.

In its current implementation, `gevolution` uses Gaussian initial conditions, computed by linearly propagating the Gaussian primordial initial conditions. However, some second-order relativistic effects are sourced by the initial conditions of the simulation and grow like linear perturbations. We have shown that using Gaussian initial conditions for the N-body simulation is equivalent to assuming PNG that exactly cancel the relativistic non-linear effects at the initial redshift of the simulation.

Hence, in order to fully account for relativistic effects, we need to build the initial conditions of the simulation up to second order. Previous works to solve the Boltzmann equations up to second order have led to the code `SONG`. This code takes into account the relativistic effects but also the important early radiation which affects the small scales and hence the squeezed limit [100].

In this last part of the thesis, we have presented the second-order RELativistic Initial Condition generator `RELIC`. In general, generating initial conditions at second order is outside of the current numerical capacities for a reasonably large simulation. Focusing on the relativistic effects and the squeezed limit PNG contamination, we have built an approximation that consists of computing only the mode couplings that we are interested in, *i.e.* the large-large scale coupling and the squeezed limit large-small scale coupling. By doing so, we neglect the small-small scale coupling, which is dominated by the Newtonian non-linearities generated anyway by the simulation. Thanks to this approximation, the complexity of the code falls from N^6 to N^3 where N is the number of considered modes.

The code `RELIC` is written in `Python` and uses the new `Python` compiler `NUMBA`, allowing the code to reach an efficiency close to a low-level computer language. It also allows simple OpenMP parallelization which `RELIC` takes advantage of. Moreover, a higher level of parallelization is implemented, allowing the computation to be split into a given number of totally independent processes. Hence, a 1024^3 grid can be computed on 128 processors within 1 to 2 days.

The power spectrum and bispectrum measurements of the resulting CDM density field show in general a good agreement with the theoretical predictions. We have shown two limitations to the accuracy. Firstly, the theoretical prediction of the second-order power spectrum is difficult to compute because of a slowly convergent integral which, in addition, depends on the integration intervals. To solve this problem, we need to use a more physical size of the box, and to put the maximum frequency k_{max} well after the radiation-matter equality peak scale k_{eq}. The second limitation is due to the binning of the power spectrum and bispectrum estimator `Pylians`. This only affects the first two or three points. To have an accurate comparison, especially to build an $f_{\rm NL}$ estimator in the future, we need to use either a larger box than needed and then reject the first few points or to bin the theoretical prediction in the same way as the measurements. Apart from these issues, the measurements of the bispectrum in the equilateral and the squeezed limit have shown a very good agreement as long as we consider the modes lower than the cut-off (except for a few specific squeezed configurations where we could trust the measurement even beyond the cut-off).

Finally, we have presented a non-trivial consistency check of our relativistic pipeline. We have computed in two very different ways the CDM density fields. In a direct way, by using the kernel returned by `SONG`, we have computed the power spectrum of the density field as returned by `RELIC`. Then, by using an iterative method, we have computed the displacement field accurately at second-order. From this field, and with the potential and the velocity obtained by solving the Einstein equations at second order, `gevolution` generates a particle mesh grid from which it can, non-perturbatively, re-compute the density field. The comparison of the power spectrum of the two density fields has shown a strong agreement.

This new implementation would close the battery of checks and allow to have a functioning relativistic pipeline to generate relativistic IC for `gevolution` and try to measure NG in simulation output. This is exciting for the future as it allows to better model relativistic effects and its contamination for PNG. In the middle term, we will add a primordial $f_{\rm NL}$ and try to estimate it with its contaminations.

Chapter 8

Conclusion and outlook

In this thesis, we have presented two different works, both motivated by trying to improve the understanding of the early universe physics. We started with a historical review to understand the historical path that led us to build a solid understanding of our universe. In the second chapter, we introduced the perturbation theory which is one of the frameworks of modern cosmology. Cosmology is described by the perturbations around a flat, homogeneous and isotropic universe. The first-order perturbation of this theory, *i.e.* the linear order, is well measured with the current observations, while a large part of the second-order perturbation theory has not been constrained yet. Next, we briefly introduced statistical field theory which is fundamental in cosmology since we have only access to one universe. We introduced the concept of Gaussian fields described by their power spectra. We introduced the bispectrum: the function that captures the deviations from Gaussianity, *i.e.* the non-Gaussianities (NG).

To finish our introduction, we presented the main results of the paradigm of inflation. It is a period during which the universe exponentially expanded, driven by the potential energy of a scalar field called the inflaton. This early inflation can generate many features of our universe: its flatness, homogeneity, and isotropy. The simplest model of inflation is the so-called slow-roll single-field inflation with standard kinetic terms (simply referred to single-field inflation in this thesis). In addition to the aforementioned predictions, single-field inflation can predict nearly-scale invariant, adiabatic, and nearly-Gaussian perturbations that are observed in the cosmic microwave background and are the seeds of structure formation. The adiabaticity directly originates from the single active degree of freedom in the single-field inflation models. It can be broken and additional isocurvature modes can be generated in the initial conditions in the context of multi-field inflation. The second main result of single-field inflation is that it predicts an unobservable level of primordial non-Gaussianities (PNG). However, the PNG generated by multi-field inflation can lead to a particular observable signal in the so-called squeezed limit, *i.e.* for a triangle configuration with two large modes and one small. However, this signal can also be generated by the non-linear evolution of the Gaussian fluctuations after inflation.

In the second part of this thesis, we presented our first main work: a joint analysis of the CMB power spectrum and bispectrum for the isocurvature modes based on our article [205]. We first introduced the physics and the statistics of the CMB. The current best constraints on the initial conditions, provided by the Planck collaboration, show that they are compatible with purely adiabatic and Gaussian initial conditions [66, 107, 121]. The Planck collaboration also provided the best constraints on the isocurvature modes amplitudes and their correlations with the adiabatic mode by using the power spectra of the temperature and polarization anisotropies. Independently, by using the bispectra of the same anisotropies, the non-Gaussianity amplitudes of all isocurvature modes and correlations with the adiabatic modes have also been constrained. We have described the statistical analysis of Planck and, based on these methods, we have merged the information contained in the power spectrum and the bispectrum of the CMB based on the development of [113, 201]. In the case of Planck, we found that the joint analysis does not improve the constraints for the generic class of two-field inflation model but does for sub-classes of models that can be motivated by multi-field inflation. With a forecast analysis of LiteBIRD and CMB-S4, we showed that the large improvement of the polarization will also add more constraints on isocurvature modes and PNG. In an optimistic case, it can be possible to detect the neutrino density and velocity isocurvature modes and their non-Gaussian features. The main conclusion of this work can be found in section 5.6.

The measurements of the CMB temperature by Planck are now cosmic variance limited so that a significant improvement of the constraints coming from the temperature power spectrum is unlikely. The future surveys LiteBIRD and CMB-S4 will improve the polarization measurements until the cosmic variance. One way to continue to improve the constraints on the models is to perform a joint analysis of the power spectrum and the bispectrum. In principle, the same methodology can be applied to all models having a specific signature in the power spectrum and the bispectrum. For instance, this was performed for oscillatory features models in [201]. One very promising joint analysis that is expected to significantly improve the constraints on the local shape PNG is a joint analysis of the galaxy power spectrum and bispectrum for the large-scale structure of the universe, see for example [192, 235, 240]. Indeed, it is expected that a local type of PNG can generate in the power spectrum of galaxies a scale-dependent bias, which means that the PNG can be constrained also with the power spectrum, see for instance [239, 296, 297]. Note that such a joint analysis would not require assuming a specific inflation model since the same parameter is affecting the power spectrum and the bispectrum.

This led us to the third part of this thesis: the relativistic effects in the large-scale structure of the universe. These relativistic effects are of two different natures. This third part was focused on the dynamical relativistic effects. We have shown, by using an analytical approach following [269], that the relativistic effects, as well as early radiation effects, are degenerate in momentum space and in redshift space with the local shape of PNG. Recall that the specific signal of multi-field inflation is a signal in the squeezed limit of the bispectrum, *i.e.* a coupling between large and small scales. At large scales, near the horizon, the relativistic effects become important, while at small scales the early radiation needs to be accounted for. Moreover, small-scale structure formation is a highly non-linear process so that we need N-body simulations.

While most of the community devoted its effort to analytical modeling of the degeneracy of PNG with relativistic effects, in the last part of this thesis, we presented the ingredients and first steps toward a novel approach entirely based on numerical methods. It is motivated, as mentioned before, by the fact that numerical methods can give an accurate match with the observed structures in the non-linear regime. Hence, we have developed the second-order relativistic initial conditions generator `RELIC`. This code lies at the interface of two pre-existing codes: `SONG` [100] and `gevolution`[263]. The code `SONG` is a second-order Einstein-Boltzmann equations solver able to propagate the dynamical relativistic effects at second order through the cosmological history. Based on the results of `SONG`, and neglecting the coupling between the small modes, `RELIC` is able to generate initial conditions for N-body simulations. Then, using the second-order perturbation theory, we have computed the potential, the displacement field, and the velocity. These quantities define the initial conditions of the fully relativistic N-body code `gevolution`. We have presented 3 preliminary checks. The code `RELIC` seems to successfully pass all checks. The results are detailed in the main conclusion of the third part 7.4.

In [294], we have published definitive results based on the preliminary results shown in this thesis. The main difference is that we have included the radiation at first-order since, as discussed in section 7.4, it is of the same order as the second-order CDM density contrast. Moreover, we have added a test on the evolution of these initial conditions. The analytical computations predict the same scaling in redshift for the (leading order) relativistic effects and the linear perturbations. These dynamics can be verified by building the initial conditions at two different redshifts where the perturbation theory still holds, for instance, $z = 100$ and $z = 50$. Then, by running `gevolution`, it is possible to evolve the initial conditions from $z = 100$ to $z = 50$ and then compare the result with the initial conditions built directly at $z = 50$. Furthermore, this test is a strong consistency check between `SONG` and `gevolution`. This test is discussed in detail in [294].

An improvement of the power spectrum and bispectrum estimator is also needed to perform a more quantitative comparison between the theoretical prediction and the simulations. In particular, the analysis has shown that the power spectrum and bispectrum estimators, provided by `Pylians`, systematically fail for the large scales. We have justified that this comes from the binning. In order to improve this point, we should first adjust the binning (for both the power spectrum and bispectrum) so that the theoretical non-binned prediction can be reproduced in the best way given a binning specification (for instance the number of bins). Once the best binning has been found, we can bin the theoretical prediction and compute the precise errors.

All the measurements with `RELIC` and `gevolution` have been performed on a constant time hypersurface. However, in practice, the measurements of the future galaxy surveys will be performed on the light-cone. Hence, the second type of relativistic effect needs to be accounted for: the projection effects. We have briefly introduced these effects and many works are today focusing on the understanding and modelization of these effects [254–258]. As already mentioned above, the local type of PNG is expected to generate a scale-dependent bias measurable in the galaxy power spectrum at large scales. The projection and dynamical relativistic effects could also generate such a signal in the power spectrum and therefore be again degenerate with the PNG. The code `gevolution` can project the simulations on the light-cone and propagate the photons and therefore, in principle, all the ingredients are present in our analysis pipeline to allow us to precisely measure the contamination of the large-scale galactic power spectrum. The main objective would be finally to construct an f_{NL} estimator, first for the power spectrum and then for the bispectrum, and to jointly estimate the exact contamination of local PNG caused by all these relativistic effects.

Through the study of non-Gaussianities, we aim to push the limits of our knowledge of the early universe and on the most fundamental law of physics. This thesis was a small part of the exploration of these questions by elaborating two tools that will allow us to constrain or measure the primordial non-Gaussianities or the isocurvature modes with the future CMB and LSS surveys.

Bibliography

[1] William Herschel. On the Construction of the Heavens. *Philosophical Transactions of the Royal Society of London Series I*, 75:213–266, January 1785.

[2] Wilhelm Struve. Etudes d'Astronomie Stellaire. Technical report, Academie imperial des sciences, 1847.

[3] Leila Belkora. *Minding the heavens, the story of our discovery of the Milky Way.* Institute of Physics Publishing, London, 2003.

[4] Edmund Halley. Considerations on the change of the latitudes of some of the principal fixt stars. by edmund halley, r. s. sec. *Philosophical Transactions (1683-1775)*, 30:736–738, 1717. ISSN 02607085. URL `http://www.jstor.org/stable/103320`.

[5] F. W. Bessel. On the parallax of 61 Cygni. *Monthly Notices of the Royal Astronomical Society*, 4:152–161, 1838.

[6] William Huggins. Further Observations on the Spectra of Some of the Stars and Nebulae, with an Attempt to Determine Therefrom Whether These Bodies are Moving towards or from the Earth, Also Observations on the Spectra of the Sun and of Comet II. *Philosophical Transactions of the Royal Society of London*, 158:529–564, 1868.

[7] William Huggins. On the spectra of some of the nebulœ. a supplement to the paper "on the spectra of some of the fixed stars". *Royal Society*, 154, 1864. ISSN 2053-9223. doi:10.1098/1864.0013. URL `https://royalsocietypublishing.org/doi/10.1098/rstl.1864.0013`.

[8] J. C. Kapteyn. On the Mean Parallax of Stars of Determined Proper Motion and Magnitude. *Publications of the Kapteyn Astronomical Laboratory Groningen*, 8: 1–31, January 1900.

[9] Henrietta S. Leavitt and Edward C. Pickering. Periods of 25 Variable Stars in the Small Magellanic Cloud. *Harvard Obs. Circ.*, 173:1–3, 1912.

[10] Henrietta S. Leavitt. 1777 variables in the Magellanic Clouds. *Harvard Obs. Annals*, 60:87–108, 1908.

[11] Edward Pigott. Observations of a New Variable Star. *Philosophical Transactions of the Royal Society of London*, 75:127–136, 1785.

[12] Ejnar Hertzsprung. Über die räumliche Verteilung der Veränderlichen vom delta Cephei-Typus. *Astronomische Nachrichten*, 196:201, 1913.

[13] G.Fritz Benedict, Barbara E. McArthur, Michael W. Feast, Thomas G. Barnes, Thomas E. Harrison, Richard J. Patterson, John W. Menzies, Jacob L. Bean, and Wendy L. Freedman. Hubble Space Telescope Fine Guidance Sensor Parallaxes of Galactic Cepheid Variable Stars: Period-Luminosity Relations. *Astron. J.*, 133:1810–1827, 2007. doi:10.1086/511980. `http://arxiv.org/abs/astro-ph/0612465`. [Erratum: Astron.J. 133, 2980 (2007)].

[14] Harlow Shapley. Studies based on the colors and magnitudes in stellar clusters. II. Thirteeen hundred stars in the Hercules Cluster (Messier 13). *Contributions from the Mount Wilson Observatory / Carnegie Institution of Washington*, 116:1, August 1915.

[15] Harlow. Shapley. No. 152. Studies based on the colors and magnitudes in stellar clusters. Seventh paper: The distances, distribution in space, and dimensions of 69 globular clusters. *Contributions from the Mount Wilson Observatory / Carnegie Institution of Washington*, 152:1–28, January 1918.

[16] Harlow Shapley. No. 157. Studies based on the colors and magnitudes in stellar clusters. Twelfth paper: Remarks on the arrangement of the sideral universe. *Contributions from the Mount Wilson Observatory / Carnegie Institution of Washington*, 157:1–24, January 1918.

[17] Earl Of Rosse. On the Construction of Specula of Six-Feet Aperture; and a Selection from the Observations of Nebulae Made with Them. *Philosophical Transactions of the Royal Society of London Series I*, 151:681–745, January 1861.

[18] A. van Maanen. Curieux Mouvements Internes dans une Nebuleuse Immense. *L'Astronomie*, 30:365–366, January 1916.

[19] Heber D. Curtis. Novae in the Spiral Nebulae and the Island Universe Theory. *Publications of the Astronomical Society of the Pacific*, 29(171):206–207, October 1917. doi:10.1086/122632.

[20] Harlow Shapley. A Faint Nova in the Nebula of Andromeda. *Publications of the Astronomical Society of the Pacific*, 29(171):213–217, October 1917. doi:10.1086/122669.

[21] E. P. Hubble. NGC 6822, a remote stellar system. *Astrophysical Journal*, 62:409–433, December 1925. doi:10.1086/142943.

[22] E. P. Hubble. A spiral nebula as a stellar system: Messier 33. *Astrophysical Journal*, 63:236–274, May 1926. doi:10.1086/142976.

[23] E. P. Hubble. A spiral nebula as a stellar system, Messier 31. *Astrophysical Journal*, 69:103–158, March 1929. doi:10.1086/143167.

[24] James Clerk Maxwell. A dynamical theory of the electromagnetic field. *Philosophical Transactions of the Royal Society of London*, 155:459–513, 1865.

[25] Hendrik Antoon Lorentz. *Attempt of a Theory of Electrical and Optical Phenomena in Moving BodiesVersuch einer Theorie der Electrischen und Optischen Erscheinungen in Bewegten Körpern.* 1895.

[26] Henri Poincaré. La théorie de Lorentz et le principe de réaction. *Archives néerlandaises des sciences exactes et naturelles*, 5:252–278, 1900.

[27] Henri Poincaré. Les relations entre la physique expérimentale et la physique mathématique. *Revue générale des sciences pures et appliquées*, 11:1163–1175, 1900.

[28] H. A. Lorentz. Electromagnetic phenomena in a system moving with any velocity smaller than that of light. *Koninklijke Nederlandse Akademie van Wetenschappen Proceedings Series B Physical Sciences*, 6:809–831, January 1903.

[29] Henri Poincaré. Sur la dynamique de l'électron. *Comptes rendus hebdomadaires de l'Académie des sciences de Paris*, 140:1504–1508, 1905.

[30] A. Einstein. Zur Elektrodynamik bewegter Körper. *Annalen der Physik*, 322(10): 891–921, January 1905. doi:10.1002/andp.19053221004.

[31] A. Einstein and M. Grossmann. Entwurf einer verallgemeinerten relativitätstheorie und einer theorie der gravitation: Physikalischer teil von albert einstein. mathematischer teil von marcel grossmann. i.. ii. *Zeitschrift für Mathematik und Physik*, page 225–261, 1913. URL `http://www.pitt.edu/~jdnorton/teaching/GR&Grav_2007/pdf/Einstein_Entwurf_1913.pdf`.

[32] Albert Einstein. Die Feldgleichungen der Gravitation. *Sitzungsberichte der Königlich Preußischen Akademie der Wissenschaften (Berlin)*, pages 844–847, January 1915.

[33] David Hilbert. Die Grundlagen der Physik. *Konigl. Gesell. d. Wiss. Göttingen, Nachr. Math.-Phys. Kl*, pages 395–407, November 1915. URL `http://www.relativitycalculator.com/pdfs/David_Hilbert_Die_Grundlagen_der_Physik_1915.pdf`.

[34] Urbain J. Le Verrier. Theorie du mouvement de Mercure. *Annales de l'Observatoire de Paris*, 5:1, January 1859.

[35] F. W. Dyson, A. S. Eddington, and C. Davidson. A determination of the deflection of light by the sun's gravitational field, from observations made at the total eclipse of may 29, 1919. *Philosophical Transactions of the Royal Society of London. Series A, Containing Papers of a Mathematical or Physical Character*, 220:291–333, 1920. ISSN 02643952. URL `http://www.jstor.org/stable/91137`.

[36] Albert Einstein. Kosmologische Betrachtungen zur allgemeinen Relativitätstheorie. *Sitzungsberichte der Königlich Preußischen Akademie der Wissenschaften (Berlin)*, pages 142–152, January 1917.

[37] Eugenio Bianchi and Carlo Rovelli. Why all these prejudices against a constant? 2 2010. `http://arxiv.org/abs/1002.3966`.

[38] A. Einstein. Die Grundlage der allgemeinen Relativitätstheorie. *Annalen der Physik*, 354(7):769–822, January 1916. doi:10.1002/andp.19163540702.

[39] W. de Sitter. Einstein's theory of gravitation and its astronomical consequences. Third paper. *Monthly Notices of the Royal Astronomical Society*, 78:3–28, November 1917. doi:10.1093/mnras/78.1.3.

[40] G. Lemaitre. Note on de Sitter's Universe. *Publications du Laboratoire d'Astronomie et de Geodesie de l'Universite de Louvain*, 2:37–41, January 1926.

[41] G. Lemaître. Un Univers homogène de masse constante et de rayon croissant rendant compte de la vitesse radiale des nébuleuses extra-galactiques. *Annales de la Société Scientifique de Bruxelles*, 47:49–59, January 1927.

[42] A. Friedmann. Über die Krümmung des Raumes. *Zeitschrift fur Physik*, 10:377–386, January 1922. doi:10.1007/BF01332580.

[43] A. Friedmann. Über die Möglichkeit einer Welt mit konstanter negativer Krümmung des Raumes. *Zeitschrift fur Physik*, 21(1):326–332, December 1924. doi:10.1007/BF01328280.

[44] G. Stromberg. Analysis of radial velocities of globular clusters and non-galactic nebulae. *Astrophysical Journal*, 61:353–362, June 1925. doi:10.1086/142897.

[45] Edwin. Hubble. No. 324. Extra-galactic nebulae. *Contributions from the Mount Wilson Observatory / Carnegie Institution of Washington*, 324:1–49, January 1926.

[46] G. Lemaitre. L'Expansion de l'Espace. *Publications du Laboratoire d'Astronomie et de Geodesie de l'Universite de Louvain*, 8:101–120, January 1931.

[47] G. Lemaître. Expansion of the universe, The expanding universe. *Monthly Notices of the Royal Astronomical Society*, 91:490–501, March 1931. doi:10.1093/mnras/91.5.490.

[48] Georges Lemaître. L'Univers en expansion. *Annales de la Société Scientifique de Bruxelles*, 53:51, January 1933.

[49] Georges Lemaître. The beginning of the world from the point of view of quantum theory. *General Relativity and Gravitation*, 43, 10 2011. doi:10.1007/s10714-011-1214-6.

[50] Georges Lemaître. *The Primeval Atom an Essay on Cosmogony.* Van Nostrand, 1950.

[51] G. Gamow. Expanding Universe and the Origin of Elements. *Physical Review*, 70 (7-8):572–573, October 1946. doi:10.1103/PhysRev.70.572.2.

[52] Ralph A. Alpher and Robert Herman. Evolution of the Universe. *Nature*, 162(4124): 774–775, November 1948. doi:10.1038/162774b0.

[53] G. Gamow. The Evolution of the Universe. *Nature*, 162(4122):680–682, October 1948. doi:10.1038/162680a0.

[54] Jean-Pierre Luminet. *L'invention du Big Bang.* Du Seuil, 2014.

[55] A. A. Penzias and R. W. Wilson. A Measurement of Excess Antenna Temperature at 4080 Mc/s. *Astrophysical Journal*, 142:419–421, July 1965. doi:10.1086/148307.

[56] R. H. Dicke, P. J. E. Peebles, P. G. Roll, and D. T. Wilkinson. Cosmic Black-Body Radiation. 142:414–419, July 1965. doi:10.1086/148306.

[57] D. J. Fixsen, E. S. Cheng, J. M. Gales, John C. Mather, R. A. Shafer, and E. L. Wright. The Cosmic Microwave Background spectrum from the full COBE FIRAS data set. *Astrophys. J.*, 473:576, 1996. doi:10.1086/178173. `http://arxiv.org/abs/astro-ph/9605054`.

[58] Horace W. Babcock. The rotation of the Andromeda Nebula. *Lick Observatory Bulletin*, 498:41–51, January 1939. doi:10.5479/ADS/bib/1939LicOB.19.41B.

[59] J. C. Kapteyn. First Attempt at a Theory of the Arrangement and Motion of the Sidereal System. *The Astrophysical Journal*, 55:302, May 1922. doi:10.1086/142670.

[60] F. Zwicky. Die Rotverschiebung von extragalaktischen Nebeln. *Helvetica Physica Acta*, 6:110–127, January 1933.

[61] V. C. Rubin, Jr. Ford, W. K., and N. Thonnard. Rotational properties of 21 SC galaxies with a large range of luminosities and radii, from NGC 4605 (R=4kpc) to UGC 2885 (R=122kpc). *The Astrophysical Journal*, 238:471–487, June 1980. doi:10.1086/158003.

[62] W. Rindler. Visual horizons in world models. *Mon. Not. Roy. Astron. Soc.*, 116: 662, January 1956. doi:10.1093/mnras/116.6.662.

[63] Steven Weinberg. *Gravitation and Cosmology: Principles and Applications of the General Theory of Relativity.* John Wiley and Sons, New York, 1972. ISBN 978-0-471-92567-5, 978-0-471-92567-5.

[64] Dicke, Robert H. Gravitation and the universe. January 1970.

[65] Alan H. Guth. The Inflationary Universe: A Possible Solution to the Horizon and Flatness Problems. *Phys. Rev. D*, 23:347–356, 1981. doi:10.1103/PhysRevD.23.347.

[66] Planck Collaboration. Planck 2018 results. VI. Cosmological parameters. *Astron. Astrophys.*, 641:A6, 2020. doi:10.1051/0004-6361/201833910. `http://arxiv.org/abs/1807.06209`.

[67] P.J.E Peebles. *Principles of Physical Cosmology*, volume 99. Princeton University Press, 2019. ISBN 9780691209814. URL `http://www.jstor.org/stable/j.ctvxrpxvb`.

[68] C. A. Chant. Review of Publications (Relativity, Thermodynamics and Cosmology by Richard C. Tolman). *Journal of the Royal Astronomical Society of Canada*, 28: 324, September 1934.

[69] D. Kazanas. Dynamics of the universe and spontaneous symmetry breaking. *Astrophysical Journal*, 241:L59–L63, October 1980. doi:10.1086/183361.

[70] Alexei A. Starobinsky. Spectrum of relict gravitational radiation and the early state of the universe. *JETP Lett.*, 30:682–685, 1979.

[71] Bartjan Van Tent. Cosmological inflation with multiple fields and the theory of density fluctuations. 2002.

[72] A. D. Linde. A new inflationary universe scenario: A possible solution of the horizon, flatness, homogeneity, isotropy and primordial monopole problems. *Physics Letters B*, 108(6):389–393, February 1982. doi:10.1016/0370-2693(82)91219-9.

[73] A. Albrecht and P. J. Steinhardt. Cosmology for Grand Unified Theories with Radiatively Induced Symmetry Breaking. *Physics Review Letter*, 48(17):1220–1223, April 1982. doi:10.1103/PhysRevLett.48.1220.

[74] Andrei D. Linde. Chaotic Inflation. *Phys. Lett. B*, 129:177–181, 1983. doi:10.1016/0370-2693(83)90837-7.

[75] S. W. Hawking. The development of irregularities in a single bubble inflationary universe. *Physics Letters B*, 115(4):295–297, September 1982. doi:10.1016/0370-2693(82)90373-2.

[76] A. A. Starobinsky. Dynamics of phase transition in the new inflationary universe scenario and generation of perturbations. *Physics Letters B*, 117(3-4):175–178, November 1982. doi:10.1016/0370-2693(82)90541-X.

[77] Alan H. Guth and So-Young Pi. Fluctuations in the new inflationary universe. *Phys. Rev. Lett.*, 49:1110–1113, Oct 1982. doi:10.1103/PhysRevLett.49.1110. URL `https://link.aps.org/doi/10.1103/PhysRevLett.49.1110`.

[78] James M. Bardeen, Paul J. Steinhardt, and Michael S. Turner. Spontaneous Creation of Almost Scale - Free Density Perturbations in an Inflationary Universe. *Phys. Rev. D*, 28:679, 1983. doi:10.1103/PhysRevD.28.679.

[79] Viatcheslav F. Mukhanov and G. V. Chibisov. The Vacuum energy and large scale structure of the universe. *Sov. Phys. JETP*, 56:258–265, 1982.

[80] Adam G. Riess et al. Observational evidence from supernovae for an accelerating universe and a cosmological constant. *Astron. J.*, 116:1009–1038, 1998. doi:10.1086/300499. `http://arxiv.org/abs/astro-ph/9805201`.

[81] S. Perlmutter et al. Cosmology from Type Ia supernovae. *Bull. Am. Astron. Soc.*, 29:1351, 1997. `http://arxiv.org/abs/astro-ph/9812473`.

[82] D. Lovelock. The Einstein tensor and its generalizations. *J. Math. Phys.*, 12:498–501, 1971. doi:10.1063/1.1665613.

[83] D. Lovelock. The four-dimensionality of space and the einstein tensor. *J. Math. Phys.*, 13:874–876, 1972. doi:10.1063/1.1666069.

[84] Planck Collaboration. Planck 2018 results. I. Overview and the cosmological legacy of Planck. *Astron. Astrophys.*, 641:A1, 2020. doi:10.1051/0004-6361/201833880. `http://arxiv.org/abs/1807.06205`.

[85] Pierros Ntelis et al. Exploring cosmic homogeneity with the BOSS DR12 galaxy sample. *JCAP*, 06:019, 2017. doi:10.1088/1475-7516/2017/06/019. `http://arxiv.org/abs/1702.02159`.

[86] Morag Scrimgeour et al. The WiggleZ Dark Energy Survey: the transition to large-scale cosmic homogeneity. *Mon. Not. Roy. Astron. Soc.*, 425:116–134, 2012. doi:10.1111/j.1365-2966.2012.21402.x. `http://arxiv.org/abs/1205.6812`.

[87] Karim A. Malik and David Wands. Cosmological perturbations. *Phys. Rept.*, 475:1–51, 2009. doi:10.1016/j.physrep.2009.03.001. `http://arxiv.org/abs/0809.4944`.

[88] Bruce A. Bassett, Shinji Tsujikawa, and David Wands. Inflation dynamics and reheating. *Rev. Mod. Phys.*, 78:537–589, 2006. doi:10.1103/RevModPhys.78.537. `http://arxiv.org/abs/astro-ph/0507632`.

[89] Daniel Baumann. Inflation. In *Theoretical Advanced Study Institute in Elementary Particle Physics: Physics of the Large and the Small*, pages 523–686, 2011. doi:10.1142/9789814327183_0010. `http://arxiv.org/abs/0907.5424`.

[90] James M. Bardeen. Gauge-invariant cosmological perturbations. *Phys. Rev. D*, 22: 1882–1905, Oct 1980. doi:10.1103/PhysRevD.22.1882. URL `https://link.aps.org/doi/10.1103/PhysRevD.22.1882`.

[91] D. H. Lyth. Large-scale energy-density perturbations and inflation. *Phys. Rev. D*, 31:1792–1798, Apr 1985. doi:10.1103/PhysRevD.31.1792. URL `https://link.aps.org/doi/10.1103/PhysRevD.31.1792`.

[92] Jérôme Martin and Dominik J. Schwarz. The influence of cosmological transitions on the evolution of density perturbations. *Phys.Rev. D*, 57:3302, 1998. doi:10.1103/PhysRevD.57.3302. `http://arxiv.org/abs/gr-qc/9704049`.

[93] David Wands, Karim A. Malik, David H. Lyth, and Andrew R. Liddle. A New approach to the evolution of cosmological perturbations on large scales. *Phys. Rev. D*, 62:043527, 2000. doi:10.1103/PhysRevD.62.043527. `http://arxiv.org/abs/astro-ph/0003278`.

[94] F. Bernardeau, S. Colombi, E. Gaztanaga, and R. Scoccimarro. Large scale structure of the universe and cosmological perturbation theory. *Phys. Rept.*, 367:1–248, 2002. doi:10.1016/S0370-1573(02)00135-7. `http://arxiv.org/abs/astro-ph/0112551`.

[95] Viatcheslav F. Mukhanov, H. A. Feldman, and Robert H. Brandenberger. Theory of cosmological perturbations. Part 1. Classical perturbations. Part 2. Quantum theory of perturbations. Part 3. Extensions. *Phys. Rept.*, 215:203–333, 1992. doi:10.1016/0370-1573(92)90044-Z.

[96] David H. Lyth and David Wands. Conserved cosmological perturbations. *Phys. Rev. D*, 68:103515, 2003. doi:10.1103/PhysRevD.68.103515. `http://arxiv.org/abs/astro-ph/0306498`.

[97] Ruth Durrer. *The Cosmic Microwave Background*. Cambridge University Press, 12 2020. ISBN 978-1-316-47152-4, 978-1-107-13522-2. doi:10.1017/9781316471524.

[98] David Langlois. Correlated adiabatic and isocurvature perturbations from double inflation. *Phys. Rev.*, D59:123512, 1999. doi:10.1103/PhysRevD.59.123512. `http://arxiv.org/abs/astro-ph/9906080`.

[99] Patrick Peter and Jean-Philippe Uzan. *Primordial Cosmology*. Oxford Graduate Texts. Oxford University Press, 2 2013. ISBN 978-0-19-966515-0, 978-0-19-920991-0.

[100] Guido Walter Pettinari. The intrinsic bispectrum of the Cosmic Microwave Background. 9 2013. doi:10.1007/978-3-319-21882-3. `http://arxiv.org/abs/1405.2280`.

[101] Cyril Pitrou, Jean-Philippe Uzan, and Francis Bernardeau. The cosmic microwave background bispectrum from the non-linear evolution of the cosmological perturbations. *JCAP*, 07:003, 2010. doi:10.1088/1475-7516/2010/07/003. `http://arxiv.org/abs/1003.0481`.

[102] P. Coles and F. Lucchin. *Cosmology: The Origin and evolution of cosmic structure.* 1995.

[103] Athanasios Papoulis and S. Unnikrishna Pillai. *Probability, Random Variables, and Stochastic Processes.* McGraw Hill, Boston, fourth edition, 2002. URL `http://www.worldcat.org/search?qt=worldcat_org_all&q=0071226613`.

[104] Xingang Chen. Primordial Non-Gaussianities from Inflation Models. *Adv. Astron.*, 2010:638979, 2010. doi:10.1155/2010/638979. `http://arxiv.org/abs/1002.1416`.

[105] N. Bartolo, E. Komatsu, Sabino Matarrese, and A. Riotto. Non-Gaussianity from inflation: Theory and observations. *Phys. Rept.*, 402:103–266, 2004. doi:10.1016/j.physrep.2004.08.022. `http://arxiv.org/abs/astro-ph/0406398`.

[106] Sébastien Renaux-Petel. Inflation cosmologique et théorie des cordes : aspects multichamps et non-gaussianités primordiales. 2010. URL `https://tel.archives-ouvertes.fr/tel-00724157/document`.

[107] Planck Collaboration. Planck 2018 results. IX. Constraints on primordial non-Gaussianity. 2019. `http://arxiv.org/abs/1905.05697`.

[108] Planck Collaboration. Planck 2018 results. V. CMB power spectra and likelihoods. 2019. `http://arxiv.org/abs/1907.12875`.

[109] Eugene A. Lim. Advanced cosmology : Primordial non-gaussianities. 2017.

[110] Leonardo Senatore, Kendrick M. Smith, and Matias Zaldarriaga. Non-Gaussianities in Single Field Inflation and their Optimal Limits from the WMAP 5-year Data. *JCAP*, 01:028, 2010. doi:10.1088/1475-7516/2010/01/028. `http://arxiv.org/abs/0905.3746`.

[111] Daniel Babich, Paolo Creminelli, and Matias Zaldarriaga. The Shape of non-Gaussianities. *JCAP*, 08:009, 2004. doi:10.1088/1475-7516/2004/08/009. `http://arxiv.org/abs/astro-ph/0405356`.

[112] Eiichiro Komatsu and David N. Spergel. Acoustic signatures in the primary microwave background bispectrum. *Phys. Rev. D*, 63:063002, 2001. doi:10.1103/PhysRevD.63.063002. `http://arxiv.org/abs/astro-ph/0005036`.

[113] David Langlois and Bartjan van Tent. Isocurvature modes in the CMB bispectrum. *JCAP*, 1207:040, 2012. doi:10.1088/1475-7516/2012/07/040. `http://arxiv.org/abs/1204.5042`.

[114] Planck Collaboration. Planck 2013 Results. XXIV. Constraints on primordial non-Gaussianity. *Astron. Astrophys.*, 571:A24, 2014. doi:10.1051/0004-6361/201321554. `http://arxiv.org/abs/1303.5084`.

[115] Planck Collaboration. Planck 2015 results. XVII. Constraints on primordial non-Gaussianity. *Astron. Astrophys.*, 594:A17, 2016. doi:10.1051/0004-6361/201525836. `http://arxiv.org/abs/1502.01592`.

[116] David Seery and James E. Lidsey. Primordial non-Gaussianities in single field inflation. *JCAP*, 06:003, 2005. doi:10.1088/1475-7516/2005/06/003. `http://arxiv.org/abs/astro-ph/0503692`.

[117] Daniel Baumann and Liam McAllister. *Inflation and String Theory.* Cambridge Monographs on Mathematical Physics. Cambridge University Press, 5 2015. ISBN 978-1-107-08969-3, 978-1-316-23718-2. doi:10.1017/CBO9781316105733. `http://arxiv.org/abs/1404.2601`.

[118] Bartjan van Tent. Multiple-field inflation and the cmb. *Class. Quant. Grav.*, 21:349–370, 2004. doi:10.1088/0264-9381/21/2/002. `http://arxiv.org/abs/astro-ph/0307048`.

[119] Scott Dodelson. *Modern cosmology.* Academic Press, San Diego, CA, 2003. URL `https://cds.cern.ch/record/1282338`.

[120] BICEP2 Collaboration. BICEP2 / Keck Array x: Constraints on Primordial Gravitational Waves using Planck, WMAP, and New BICEP2/Keck Observations through the 2015 Season. *Phys. Rev. Lett.*, 121:221301, 2018. doi:10.1103/PhysRevLett.121.221301. `http://arxiv.org/abs/1810.05216`.

[121] Planck Collaboration. Planck 2018 results. X. Constraints on inflation. 2018. `http://arxiv.org/abs/1807.06211`.

[122] Juan Martin Maldacena. Non-Gaussian features of primordial fluctuations in single field inflationary models. *JHEP*, 05:013, 2003. doi:10.1088/1126-6708/2003/05/013. `http://arxiv.org/abs/astro-ph/0210603`.

[123] Viviana Acquaviva, Nicola Bartolo, Sabino Matarrese, and Antonio Riotto. Second order cosmological perturbations from inflation. *Nucl. Phys. B*, 667:119–148, 2003. doi:10.1016/S0550-3213(03)00550-9. `http://arxiv.org/abs/astro-ph/0209156`.

[124] N. Bartolo, S. Matarrese, and A. Riotto. Nongaussianity from inflation. *Phys. Rev. D*, 65:103505, 2002. doi:10.1103/PhysRevD.65.103505. `http://arxiv.org/abs/hep-ph/0112261`.

[125] Paolo Creminelli and Matias Zaldarriaga. Single field consistency relation for the 3-point function. *JCAP*, 10:006, 2004. doi:10.1088/1475-7516/2004/10/006. `http://arxiv.org/abs/astro-ph/0407059`.

[126] Eva-Maria Mueller et al. The clustering of galaxies in the completed SDSS-IV extended Baryon Oscillation Spectroscopic Survey: Primordial non-Gaussianity in Fourier Space. 6 2021. `http://arxiv.org/abs/2106.13725`.

[127] David H. Lyth and Antonio Riotto. Particle physics models of inflation and the cosmological density perturbation. *Phys. Rept.*, 314:1–146, 1999. doi:10.1016/S0370-1573(98)00128-8. `http://arxiv.org/abs/hep-ph/9807278`.

[128] Francis Bernardeau and Jean-Philippe Uzan. NonGaussianity in multifield inflation. *Phys. Rev. D*, 66:103506, 2002. doi:10.1103/PhysRevD.66.103506. `http://arxiv.org/abs/hep-ph/0207295`.

[129] David H. Lyth and Yeinzon Rodriguez. The Inflationary prediction for primordial non-Gaussianity. *Phys. Rev. Lett.*, 95:121302, 2005. doi:10.1103/PhysRevLett.95.121302. `http://arxiv.org/abs/astro-ph/0504045`.

[130] G.I. Rigopoulos, E.P.S. Shellard, and B.J.W. van Tent. Large non-Gaussianity in multiple-field inflation. *Phys. Rev. D*, 73:083522, 2006. doi:10.1103/PhysRevD.73.083522. `http://arxiv.org/abs/astro-ph/0506704`.

[131] G.I. Rigopoulos, E.P.S. Shellard, and B.J.W. van Tent. Quantitative bispectra from multifield inflation. *Phys. Rev. D*, 76:083512, 2007. doi:10.1103/PhysRevD.76.083512. `http://arxiv.org/abs/astro-ph/0511041`.

[132] Filippo Vernizzi and David Wands. Non-gaussianities in two-field inflation. *JCAP*, 05:019, 2006. doi:10.1088/1475-7516/2006/05/019. `http://arxiv.org/abs/astro-ph/0603799`.

[133] Eleftheria Tzavara and Bartjan van Tent. Bispectra from two-field inflation using the long-wavelength formalism. *JCAP*, 06:026, 2011. doi:10.1088/1475-7516/2011/06/026. `http://arxiv.org/abs/1012.6027`.

[134] Gabriel Jung and Bartjan van Tent. Non-Gaussianity in two-field inflation beyond the slow-roll approximation. *JCAP*, 05:019, 2017. doi:10.1088/1475-7516/2017/05/019. `http://arxiv.org/abs/1611.09233`.

[135] Christian T. Byrnes and Ki-Young Choi. Review of local non-Gaussianity from multi-field inflation. *Adv. Astron.*, 2010:724525, 2010. doi:10.1155/2010/724525. `http://arxiv.org/abs/1002.3110`.

[136] Yi Wang. Inflation, Cosmic Perturbations and Non-Gaussianities. *Commun. Theor. Phys.*, 62:109–166, 2014. doi:10.1088/0253-6102/62/1/19. `http://arxiv.org/abs/1303.1523`.

[137] Martin Bucher, Kavilan Moodley, and Neil Turok. The General primordial cosmic perturbation. *Phys. Rev.*, D62:083508, 2000. doi:10.1103/PhysRevD.62.083508. `http://arxiv.org/abs/astro-ph/9904231`.

[138] Christopher Gordon, David Wands, Bruce A. Bassett, and Roy Maartens. Adiabatic and entropy perturbations from inflation. *Phys. Rev. D*, 63:023506, 2000. doi:10.1103/PhysRevD.63.023506. `http://arxiv.org/abs/astro-ph/0009131`.

[139] S. Groot Nibbelink and B.J.W. van Tent. Scalar perturbations during multiple field slow-roll inflation. *Class. Quant. Grav.*, 19:613–640, 2002. doi:10.1088/0264-9381/19/4/302. `http://arxiv.org/abs/hep-ph/0107272`.

[140] David Wands. Multiple field inflation. *Lect. Notes Phys.*, 738:275–304, 2008. doi:10.1007/978-3-540-74353-8_8. `http://arxiv.org/abs/astro-ph/0702187`.

[141] S. Groot Nibbelink and B. J. W. van Tent. Density perturbations arising from multiple field slow roll inflation. 11 2000. `http://arxiv.org/abs/hep-ph/0011325`.

[142] Z. Lalak, D. Langlois, S. Pokorski, and K. Turzynski. Curvature and isocurvature perturbations in two-field inflation. *JCAP*, 07:014, 2007. doi:10.1088/1475-7516/2007/07/014. `http://arxiv.org/abs/0704.0212`.

[143] David Wands, Nicola Bartolo, Sabino Matarrese, and Antonio Riotto. An Observational test of two-field inflation. *Phys. Rev. D*, 66:043520, 2002. doi:10.1103/PhysRevD.66.043520. `http://arxiv.org/abs/astro-ph/0205253`.

[144] David H. Lyth and David Wands. Generating the curvature perturbation without an inflaton. *Phys. Lett. B*, 524:5–14, 2002. doi:10.1016/S0370-2693(01)01366-1. `http://arxiv.org/abs/hep-ph/0110002`.

[145] David H. Lyth, Carlo Ungarelli, and David Wands. The Primordial density perturbation in the curvaton scenario. *Phys. Rev. D*, 67:023503, 2003. doi:10.1103/PhysRevD.67.023503. `http://arxiv.org/abs/astro-ph/0208055`.

[146] David H. Lyth, Karim A. Malik, and Misao Sasaki. A General proof of the conservation of the curvature perturbation. *JCAP*, 05:004, 2005. doi:10.1088/1475-7516/2005/05/004. `http://arxiv.org/abs/astro-ph/0411220`.

[147] Misao Sasaki and Ewan D. Stewart. A General analytic formula for the spectral index of the density perturbations produced during inflation. *Prog. Theor. Phys.*, 95: 71–78, 1996. doi:10.1143/PTP.95.71. `http://arxiv.org/abs/astro-ph/9507001`.

[148] Sébastien Renaux-Petel. Primordial non-Gaussianities after Planck 2015: an introductory review. *Comptes Rendus Physique*, 16:969–985, 2015. doi:10.1016/j.crhy.2015.08.003. `http://arxiv.org/abs/1508.06740`.

[149] David Langlois and Angela Lepidi. General treatment of isocurvature perturbations and non-Gaussianities. *JCAP*, 01:008, 2011. doi:10.1088/1475-7516/2011/01/008. `http://arxiv.org/abs/1007.5498`.

[150] Planck Collaboration. Planck 2018 results. I. Overview and the cosmological legacy of Planck. *Astron. Astrophys.*, 641:A1, 2020. doi:10.1051/0004-6361/201833880. `http://arxiv.org/abs/1807.06205`.

[151] Matts Roos. *Introduction to Cosmology, Third Edition.* 2003.

[152] P. F. de Salas, D. V. Forero, C. A. Ternes, M. Tortola, and J. W. F. Valle. Status of neutrino oscillations 2018: 3σ hint for normal mass ordering and improved CP sensitivity. *Phys. Lett. B*, 782:633–640, 2018. doi:10.1016/j.physletb.2018.06.019. `http://arxiv.org/abs/1708.01186`.

[153] D. L. Helis et al. Neutrinoless Double-Beta Decay Searches with Enriched $^{116}CdWO_4$ Scintillating Bolometers. *J. Low Temp. Phys.*, 199(1-2):467–474, 2020. doi:10.1007/s10909-019-02315-2.

[154] Julien Lesgourgues. Cosmological Perturbations. In *Theoretical Advanced Study Institute in Elementary Particle Physics: Searching for New Physics at Small and Large Scales*, 2 2013. doi:10.1142/9789814525220_0002. `http://arxiv.org/abs/1302.4640`.

[155] Wayne Hu. Lecture Notes on CMB Theory: From Nucleosynthesis to Recombination. 2 2008. `http://arxiv.org/abs/0802.3688`.

[156] Xiaochun Luo and David N. Schramm. Kurtosis, Skewness, and Non-Gaussian Cosmological Density Perturbations. *The Astrophysical Journal*, 408:33, May 1993. doi:10.1086/172567.

[157] Martin Bucher, Benjamin Racine, and Bartjan van Tent. The binned bispectrum estimator: template-based and non-parametric CMB non-Gaussianity searches. *JCAP*, 1605(05):055, 2016. doi:10.1088/1475-7516/2016/05/055. `http://arxiv.org/abs/1509.08107`.

[158] Uros Seljak. A Two fluid approximation for calculating the cosmic microwave background anisotropies. *Astrophys. J. Lett.*, 435:L87–L90, 1994. doi:10.1086/187601. `http://arxiv.org/abs/astro-ph/9406050`.

[159] Wayne Hu and Naoshi Sugiyama. Small scale cosmological perturbations: An Analytic approach. *Astrophys. J.*, 471:542–570, 1996. doi:10.1086/177989. `http://arxiv.org/abs/astro-ph/9510117`.

[160] R. K. Sachs and A. M. Wolfe. Perturbations of a cosmological model and angular variations of the microwave background. *Astrophys. J.*, 147:73–90, 1967. doi:10.1007/s10714-007-0448-9.

[161] Martin J. White and Wayne Hu. The Sachs-Wolfe effect. *Astron. Astrophys.*, 321: 8–9, 1997. `http://arxiv.org/abs/astro-ph/9609105`.

[162] Joseph Silk. Cosmic Black-Body Radiation and Galaxy Formation. *The Astrophysical Journal*, 151:459, February 1968. doi:10.1086/149449.

[163] Stephon Alexander and Evan McDonough. Primordial Circular Polarization in the Cosmic Microwave Background. *Phys. Lett. B*, 0370:2693, 2018. doi:10.1016/j.physletb.2018.12.037. `http://arxiv.org/abs/1811.05953`.

[164] Lingyuan Ji, Marc Kamionkowski, and Keisuke Inomata. Standard model prediction for cosmological 21 cm circular polarization. *Phys. Rev. D*, 103(2):023516, 2021. doi:10.1103/PhysRevD.103.023516. `http://arxiv.org/abs/2005.10250`.

[165] Marc Kamionkowski, Arthur Kosowsky, and Albert Stebbins. A Probe of primordial gravity waves and vorticity. *Phys. Rev. Lett.*, 78:2058–2061, 1997. doi:10.1103/PhysRevLett.78.2058. `http://arxiv.org/abs/astro-ph/9609132`.

[166] Uros Seljak and Matias Zaldarriaga. A Line of sight integration approach to cosmic microwave background anisotropies. *Astrophys. J.*, 469:437–444, 1996. doi:10.1086/177793. `http://arxiv.org/abs/astro-ph/9603033`.

[167] Wayne Hu and Martin J. White. A CMB polarization primer. *New Astron.*, 2:323, 1997. doi:10.1016/S1384-1076(97)00022-5. `http://arxiv.org/abs/astro-ph/9706147`.

[168] L. Mousset et al. QUBIC II: Spectro-Polarimetry with Bolometric Interferometry. 10 2020. `http://arxiv.org/abs/2010.15119`.

[169] QUBIC Collaboration. QUBIC I: Overview and ScienceProgram. 11 2020. `http://arxiv.org/abs/2011.02213`.

[170] Jonathan R. Pritchard and Abraham Loeb. 21-cm cosmology. *Rept. Prog. Phys.*, 75:086901, 2012. doi:10.1088/0034-4885/75/8/086901. `http://arxiv.org/abs/1109.6012`.

[171] James E. Gunn and Bruce A. Peterson. On the Density of Neutral Hydrogen in Intergalactic Space. *Astrophysical Journal*, 142:1633–1636, November 1965. doi:10.1086/148444.

[172] Robert G. Crittenden and Neil Turok. Looking for a cosmological constant with the rees-sciama effect. *Phys. Rev. Lett.*, 76:575–578, Jan 1996. doi:10.1103/PhysRevLett.76.575. URL `https://link.aps.org/doi/10.1103/PhysRevLett.76.575`.

[173] Planck Collaboration. Planck 2018 results. VIII. Gravitational lensing. 2018. `http://arxiv.org/abs/1807.06210`.

[174] Takemi Okamoto and Wayne Hu. CMB lensing reconstruction on the full sky. *Phys. Rev.*, D67:083002, 2003. doi:10.1103/PhysRevD.67.083002. `http://arxiv.org/abs/astro-ph/0301031`.

[175] CORE Collaboration. Exploring cosmic origins with CORE: Gravitational lensing of the CMB. *JCAP*, 1804(04):018, 2018. doi:10.1088/1475-7516/2018/04/018. `http://arxiv.org/abs/1707.02259`.

[176] Antony Lewis and Anthony Challinor. Weak gravitational lensing of the CMB. *Phys. Rept.*, 429:1–65, 2006. doi:10.1016/j.physrep.2006.03.002. `http://arxiv.org/abs/astro-ph/0601594`.

[177] R. A. Sunyaev and Ya. B. Zeldovich. Small-Scale Fluctuations of Relic Radiation. *Astrophysics and Space Science*, 7(1):3–19, April 1970. doi:10.1007/BF00653471.

[178] R. A. Sunyaev and Ya. B. Zeldovich. The Observations of Relic Radiation as a Test of the Nature of X-Ray Radiation from the Clusters of Galaxies. *Comments on Astrophysics and Space Physics*, 4:173, November 1972.

[179] Planck Collaboration. Planck 2015 results. XXIV. Cosmology from Sunyaev-Zeldovich cluster counts. *Astron. Astrophys.*, 594:A24, 2016. doi:10.1051/0004-6361/201525833. `http://arxiv.org/abs/1502.01597`.

[180] Guillaume Patanchon. Analyse multi-composantes d'observations du fond diffus cosmologique. October 2003. URL `https://tel.archives-ouvertes.fr/tel-00004512`.

[181] Guilaine Lagache, Jean-Loup Puget, and Herve Dole. Dusty infrared galaxies: Sources of the cosmic infrared background. *Ann. Rev. Astron. Astrophys.*, 43:727–768, 2005. doi:10.1146/annurev.astro.43.072103.150606. `http://arxiv.org/abs/astro-ph/0507298`.

[182] Leonardo Senatore, Svetlin Tassev, and Matias Zaldarriaga. Cosmological Perturbations at Second Order and Recombination Perturbed. *JCAP*, 08:031, 2009. doi:10.1088/1475-7516/2009/08/031. `http://arxiv.org/abs/0812.3652`.

[183] Antony Lewis. The full squeezed CMB bispectrum from inflation. *JCAP*, 06:023, 2012. doi:10.1088/1475-7516/2012/06/023. `http://arxiv.org/abs/1204.5018`.

[184] Zhiqi Huang and Filippo Vernizzi. The full CMB temperature bispectrum from single-field inflation. *Phys. Rev. D*, 89(2):021302, 2014. doi:10.1103/PhysRevD.89.021302. `http://arxiv.org/abs/1311.6105`.

[185] David M. Goldberg and David N. Spergel. Microwave background bispectrum. 2. A probe of the low redshift universe. *Phys. Rev. D*, 59:103002, 1999. doi:10.1103/PhysRevD.59.103002. `http://arxiv.org/abs/astro-ph/9811251`.

[186] F. Lacasa and N. Aghanim. Optimal estimator for the amplitude of the bispectrum from infrared clustered sources. *Astron. Astrophys.*, 569:A51, 2014. doi:10.1051/0004-6361/201220751. `http://arxiv.org/abs/1211.3902`.

[187] Gabriel Jung, Benjamin Racine, and Bartjan van Tent. The bispectra of galactic CMB foregrounds and their impact on primordial non-Gaussianity estimation. *JCAP*, 11:047, 2018. doi:10.1088/1475-7516/2018/11/047. `http://arxiv.org/abs/1810.01727`.

[188] Jussi Valiviita, Matti Savelainen, Marianne Talvitie, Hannu Kurki-Suonio, and Stanislav Rusak. Constraints on scalar and tensor perturbations in phenomenological and two-field inflation models: Bayesian evidences for primordial isocurvature and tensor modes. *Astrophys. J.*, 753:151, 2012. doi:10.1088/0004-637X/753/2/151. `http://arxiv.org/abs/1202.2852`.

[189] Christopher Gordon and Antony Lewis. Observational constraints on the curvaton model of inflation. *Phys. Rev. D*, 67:123513, 2003. doi:10.1103/PhysRevD.67.123513. `http://arxiv.org/abs/astro-ph/0212248`.

[190] Masahiro Kawasaki, Toyokazu Sekiguchi, and Tomo Takahashi. Differentiating CDM and Baryon Isocurvature Models with 21 cm Fluctuations. *JCAP*, 10:028, 2011. doi:10.1088/1475-7516/2011/10/028. `http://arxiv.org/abs/1104.5591`.

[191] Chung-Pei Ma and Edmund Bertschinger. Cosmological perturbation theory in the synchronous and conformal Newtonian gauges. *Astrophys. J.*, 455:7–25, 1995. doi:10.1086/176550. `http://arxiv.org/abs/astro-ph/9506072`.

[192] Dionysios Karagiannis, Andrei Lazanu, Michele Liguori, Alvise Raccanelli, Nicola Bartolo, and Licia Verde. Constraining primordial non-Gaussianity with bispectrum and power spectrum from upcoming optical and radio surveys. *Mon. Not. Roy. Astron. Soc.*, 478(1):1341–1376, 2018. doi:10.1093/mnras/sty1029. `http://arxiv.org/abs/1801.09280`.

[193] Masahiro Kawasaki, Kazunori Nakayama, Toyokazu Sekiguchi, Teruaki Suyama, and Fuminobu Takahashi. Non-Gaussianity from isocurvature perturbations. *JCAP*, 11:019, 2008. doi:10.1088/1475-7516/2008/11/019. `http://arxiv.org/abs/0808.0009`.

[194] David Langlois, Filippo Vernizzi, and David Wands. Non-linear isocurvature perturbations and non-Gaussianities. *JCAP*, 12:004, 2008. doi:10.1088/1475-7516/2008/12/004. `http://arxiv.org/abs/0809.4646`.

[195] Masahiro Kawasaki, Kazunori Nakayama, Toyokazu Sekiguchi, Teruaki Suyama, and Fuminobu Takahashi. A General Analysis of Non-Gaussianity from Isocurvature Perturbations. *JCAP*, 01:042, 2009. doi:10.1088/1475-7516/2009/01/042. `http://arxiv.org/abs/0810.0208`.

[196] Chiaki Hikage, Kazuya Koyama, Takahiko Matsubara, Tomo Takahashi, and Masahide Yamaguchi. Limits on Isocurvature Perturbations from Non-Gaussianity in WMAP Temperature Anisotropy. *Mon. Not. Roy. Astron. Soc.*, 398:2188–2198, 2009. doi:10.1111/j.1365-2966.2009.15269.x. `http://arxiv.org/abs/0812.3500`.

[197] David Langlois and Bartjan van Tent. Hunting for Isocurvature Modes in the CMB non-Gaussianities. *Class. Quant. Grav.*, 28:222001, 2011. doi:10.1088/0264-9381/28/22/222001. `http://arxiv.org/abs/1104.2567`.

[198] Etsuko Kawakami, Masahiro Kawasaki, Koichi Miyamoto, Kazunori Nakayama, and Toyokazu Sekiguchi. Non-Gaussian isocurvature perturbations in dark radiation. *JCAP*, 07:037, 2012. doi:10.1088/1475-7516/2012/07/037. `http://arxiv.org/abs/1202.4890`.

[199] Chiaki Hikage, Masahiro Kawasaki, Toyokazu Sekiguchi, and Tomo Takahashi. CMB constraint on non-Gaussianity in isocurvature perturbations. *JCAP*, 07:007, 2013. doi:10.1088/1475-7516/2013/07/007. `http://arxiv.org/abs/1211.1095`.

[200] Chiaki Hikage, Masahiro Kawasaki, Toyokazu Sekiguchi, and Tomo Takahashi. Extended analysis of CMB constraints on non-Gaussianity in isocurvature perturbations. *JCAP*, 03:020, 2013. doi:10.1088/1475-7516/2013/03/020. `http://arxiv.org/abs/1212.6001`.

[201] P. Daniel Meerburg, Moritz Münchmeyer, and Benjamin Wandelt. Joint resonant CMB power spectrum and bispectrum estimation. *Phys. Rev.*, D93(4):043536, 2016. doi:10.1103/PhysRevD.93.043536. `http://arxiv.org/abs/1510.01756`.

[202] J.R. Fergusson, H.F. Gruetjen, E.P.S. Shellard, and B. Wallisch. Polyspectra searches for sharp oscillatory features in cosmic microwave sky data. *Phys. Rev. D*, 91(12):123506, 2015. doi:10.1103/PhysRevD.91.123506. `http://arxiv.org/abs/1412.6152`.

[203] J.R. Fergusson, H.F. Gruetjen, E.P.S. Shellard, and M. Liguori. Combining power spectrum and bispectrum measurements to detect oscillatory features. *Phys. Rev. D*, 91(2):023502, 2015. doi:10.1103/PhysRevD.91.023502. `http://arxiv.org/abs/1410.5114`.

[204] Olivier Doré et al. Cosmology with the SPHEREX All-Sky Spectral Survey. 2014. `http://arxiv.org/abs/1412.4872`.

[205] Thomas Montandon, Guillaume Patanchon, and Bartjan van Tent. Isocurvature modes: joint analysis of the CMB power spectrum and bispectrum. *JCAP*, 01:004, 2021. doi:10.1088/1475-7516/2021/01/004. `http://arxiv.org/abs/2007.05457`.

[206] Antony Lewis and Sarah Bridle. Cosmological parameters from CMB and other data: A Monte Carlo approach. *Phys. Rev.*, D66:103511, 2002. doi:10.1103/PhysRevD.66.103511. `http://arxiv.org/abs/astro-ph/0205436`. URL `https://arxiv.org/abs/astro-ph/0205436`.

[207] Antony Lewis. Efficient sampling of fast and slow cosmological parameters. *Phys. Rev.*, D87(10):103529, 2013. doi:10.1103/PhysRevD.87.103529. `http://arxiv.org/abs/1304.4473`. URL `https://arxiv.org/abs/1304.4473`.

[208] Jesus Torrado and Antony Lewis. Cobaya: Code for Bayesian Analysis of hierarchical physical models. 5 2020. `http://arxiv.org/abs/2005.05290`.

[209] Antony Lewis, Anthony Challinor, and Anthony Lasenby. Efficient computation of CMB anisotropies in closed FRW models. *Astrophys. J.*, 538:473–476, 2000. doi:10.1086/309179. `http://arxiv.org/abs/astro-ph/9911177`. URL `https://arxiv.org/abs/astro-ph/9911177`.

[210] Cullan Howlett, Antony Lewis, Alex Hall, and Anthony Challinor. CMB power spectrum parameter degeneracies in the era of precision cosmology. *JCAP*, 1204:027, 2012. doi:10.1088/1475-7516/2012/04/027. `http://arxiv.org/abs/1201.3654`. URL `https://arxiv.org/abs/1201.3654`.

[211] Antony Lewis. GetDist: a Python package for analysing Monte Carlo samples. 2019. `http://arxiv.org/abs/1910.13970`. URL `https://getdist.readthedocs.io`.

[212] Planck Collaboration. Planck 2015 results. XX. Constraints on inflation. *Astron. Astrophys.*, 594:A20, 2016. doi:10.1051/0004-6361/201525898. `http://arxiv.org/abs/1502.02114`.

[213] Planck Collaboration. Planck 2013 results. XXII. Constraints on inflation. *Astron. Astrophys.*, 571:A22, 2014. doi:10.1051/0004-6361/201321569. `http://arxiv.org/abs/1303.5082`.

[214] M. Tristram, J. F. Macias-Perez, C. Renault, and D. Santos. Xspect, estimation of the angular power spectrum by computing cross power spectra. *Mon. Not. Roy. Astron. Soc.*, 358:833, 2005. doi:10.1111/j.1365-2966.2005.08760.x. `http://arxiv.org/abs/astro-ph/0405575`.

[215] Planck Collaboration. Planck 2013 results. XV. CMB power spectra and likelihood. *Astron. Astrophys.*, 571:A15, 2014. doi:10.1051/0004-6361/201321573. `http://arxiv.org/abs/1303.5075`.

[216] Martin Bucher, Bartjan Van Tent, and Carla Sofia Carvalho. Detecting Bispectral Acoustic Oscillations from Inflation Using a New Flexible Estimator. *Mon. Not. Roy. Astron. Soc.*, 407:2193, 2010. doi:10.1111/j.1365-2966.2010.17089.x. `http://arxiv.org/abs/0911.1642`.

[217] Amit P. S. Yadav, Eiichiro Komatsu, Benjamin D. Wandelt, Michele Liguori, Frode K. Hansen, and Sabino Matarrese. Fast Estimator of Primordial Non-Gaussianity from Temperature and Polarization Anisotropies in the Cosmic Microwave Background II: Partial Sky Coverage and Inhomogeneous Noise. *Astrophys. J.*, 678:578–582, 2008. doi:10.1086/586695. `http://arxiv.org/abs/0711.4933`.

[218] Paolo Creminelli, Alberto Nicolis, Leonardo Senatore, Max Tegmark, and Matias Zaldarriaga. Limits on non-gaussianities from wmap data. *JCAP*, 05:004, 2006. doi:10.1088/1475-7516/2006/05/004. `http://arxiv.org/abs/astro-ph/0509029`.

[219] Michele Liguori and Antonio Riotto. Impact of Uncertainties in the Cosmological Parameters on the Measurement of Primordial non-Gaussianity. *Phys. Rev. D*, 78: 123004, 2008. doi:10.1103/PhysRevD.78.123004. `http://arxiv.org/abs/0808.3255`.

[220] Y. et al Sekimoto. Concept design of the LiteBIRD satellite for CMB B-mode polarization. In *Proceedings of the SPIE*, volume 10698 of *Society of Photo-Optical Instrumentation Engineers (SPIE) Conference Series*, page 106981Y, 2018. doi:10.1117/12.2313432.

[221] L. Montier et al. Overview of the Medium and High Frequency Telescopes of the LiteBIRD satellite mission. *Proc. SPIE Int. Soc. Opt. Eng.*, 11443:114432G, 2020. doi:10.1117/12.2562243. `http://arxiv.org/abs/2102.00809`.

[222] Y. Sekimoto et al. Concept Design of Low Frequency Telescope for CMB B-mode Polarization satellite LiteBIRD. *Proc. SPIE Int. Soc. Opt. Eng.*, 11453:1145310, 2020. doi:10.1117/12.2561841. `http://arxiv.org/abs/2101.06342`.

[223] M. Hazumi et al. LiteBIRD: JAXA's new strategic L-class mission for all-sky surveys of cosmic microwave background polarization. *Proc. SPIE Int. Soc. Opt. Eng.*, 11443:114432F, 2020. doi:10.1117/12.2563050. `http://arxiv.org/abs/2101.12449`.

[224] M. Hazumi et al. LiteBIRD: A Satellite for the Studies of B-Mode Polarization and Inflation from Cosmic Background Radiation Detection. *J. Low. Temp. Phys.*, 194 (5-6):443–452, 2019. doi:10.1007/s10909-019-02150-5.

[225] CORE Collaboration. Exploring cosmic origins with CORE: Cosmological parameters. *JCAP*, 1804:017, 2018. doi:10.1088/1475-7516/2018/04/017. `http://arxiv.org/abs/1612.00021`.

[226] CORE Collaboration. Exploring cosmic origins with CORE: Survey requirements and mission design. *JCAP*, 04:014, 2018. doi:10.1088/1475-7516/2018/04/014. `http://arxiv.org/abs/1706.04516`.

[227] Samira Hamimeche and Antony Lewis. Likelihood Analysis of CMB Temperature and Polarization Power Spectra. *Phys. Rev.*, D77:103013, 2008. doi:10.1103/PhysRevD.77.103013. `http://arxiv.org/abs/0801.0554`.

[228] CMB-S4 Collaboration. CMB-S4 Science Case, Reference Design, and Project Plan. 2019. `http://arxiv.org/abs/1907.04473`.

[229] CMB-S4 Collaboration. CMB-S4 Science Book, First Edition. 2016. `http://arxiv.org/abs/1610.02743`.

[230] Simons Observatory. The Simons Observatory: Science goals and forecasts. *JCAP*, 1902:056, 2019. doi:10.1088/1475-7516/2019/02/056. `http://arxiv.org/abs/1808.07445`.

[231] David J. E. Marsh. Axion Cosmology. *Phys. Rept.*, 643:1–79, 2016. doi:10.1016/j.physrep.2016.06.005. `http://arxiv.org/abs/1510.07633`.

[232] Kari Enqvist and Hannu Kurki-Suonio. Constraining isocurvature fluctuations with the Planck surveyor. *Phys. Rev. D*, 61:043002, 2000. doi:10.1103/PhysRevD.61.043002. `http://arxiv.org/abs/astro-ph/9907221`.

[233] Jan Hamann, Steen Hannestad, Georg G. Raffelt, and Yvonne Y.Y. Wong. Isocurvature forecast in the anthropic axion window. *JCAP*, 06:022, 2009. doi:10.1088/1475-7516/2009/06/022. `http://arxiv.org/abs/0904.0647`.

[234] CMBPol Collaboration. CMBPol Mission Concept Study: Probing Inflation with CMB Polarization. *AIP Conf. Proc.*, 1141(1):10–120, 2009. doi:10.1063/1.3160885. `http://arxiv.org/abs/0811.3919`.

[235] Luca Amendola et al. Cosmology and fundamental physics with the Euclid satellite. *Living Rev. Rel.*, 21(1):2, 2018. doi:10.1007/s41114-017-0010-3. `http://arxiv.org/abs/1606.00180`.

[236] Hu Zhan and J. Anthony Tyson. Cosmology with the Large Synoptic Survey Telescope: an Overview. *Rept. Prog. Phys.*, 81(6):066901, 2018. doi:10.1088/1361-6633/aab1bd. `http://arxiv.org/abs/1707.06948`.

[237] Aurel Schneider, Romain Teyssier, Doug Potter, Joachim Stadel, Julian Onions, Darren S. Reed, Robert E. Smith, Volker Springel, Frazer R. Pearce, and Roman Scoccimarro. Matter power spectrum and the challenge of percent accuracy. *JCAP*, 04:047, 2016. doi:10.1088/1475-7516/2016/04/047. `http://arxiv.org/abs/1503.05920`.

[238] Matteo Biagetti. The Hunt for Primordial Interactions in the Large Scale Structures of the Universe. *Galaxies*, 7(3):71, 2019. doi:10.3390/galaxies7030071. `http://arxiv.org/abs/1906.12244`.

[239] Vincent Desjacques, Donghui Jeong, and Fabian Schmidt. Large-Scale Galaxy Bias. *Phys. Rept.*, 733:1–193, 2018. doi:10.1016/j.physrep.2017.12.002. `http://arxiv.org/abs/1611.09787`.

[240] Dionysios Karagiannis, Anže Slosar, and Michele Liguori. Forecasts on Primordial non-Gaussianity from 21 cm Intensity Mapping experiments. *JCAP*, 11:052, 2020. doi:10.1088/1475-7516/2020/11/052. `http://arxiv.org/abs/1911.03964`.

[241] Takahiko Matsubara. On second order perturbation theories of gravitational instability in Friedmann-Lemaitre models. *Prog. Theor. Phys.*, 94:1151–1156, 1995. doi:10.1143/PTP.94.1151. `http://arxiv.org/abs/astro-ph/9510137`.

[242] Sabino Matarrese, Silvia Mollerach, and Marco Bruni. Second order perturbations of the Einstein-de Sitter universe. *Phys. Rev. D*, 58:043504, 1998. doi:10.1103/PhysRevD.58.043504. `http://arxiv.org/abs/astro-ph/9707278`.

[243] Marco Bruni, Juan Carlos Hidalgo, Nikolai Meures, and David Wands. Non-Gaussian Initial Conditions in ΛCDM: Newtonian, Relativistic, and Primordial Contributions. *Astrophys. J.*, 785:2, 2014. doi:10.1088/0004-637X/785/1/2. `http://arxiv.org/abs/1307.1478`.

[244] Lotfi Boubekeur, Paolo Creminelli, Jorge Norena, and Filippo Vernizzi. Action approach to cosmological perturbations: the 2nd order metric in matter dominance. *JCAP*, 08:028, 2008. doi:10.1088/1475-7516/2008/08/028. `http://arxiv.org/abs/0806.1016`.

[245] A. Liam Fitzpatrick, Leonardo Senatore, and Matias Zaldarriaga. Contributions to the dark matter 3-Point function from the radiation era. *JCAP*, 05:004, 2010. doi:10.1088/1475-7516/2010/05/004. `http://arxiv.org/abs/0902.2814`.

[246] Nicola Bartolo, Sabino Matarrese, Ornella Pantano, and Antonio Riotto. Second-order matter perturbations in a LambdaCDM cosmology and non-Gaussianity. *Class. Quant. Grav.*, 27:124009, 2010. doi:10.1088/0264-9381/27/12/124009. `http://arxiv.org/abs/1002.3759`.

[247] Enrico Pajer, Fabian Schmidt, and Matias Zaldarriaga. The Observed Squeezed Limit of Cosmological Three-Point Functions. *Phys. Rev. D*, 88(8):083502, 2013. doi:10.1103/PhysRevD.88.083502. `http://arxiv.org/abs/1305.0824`.

[248] Eleonora Villa, Licia Verde, and Sabino Matarrese. General relativistic corrections and non-Gaussianity in large scale structure. *Class. Quant. Grav.*, 31(23):234005, 2014. doi:10.1088/0264-9381/31/23/234005. `http://arxiv.org/abs/1409.4738`.

[249] Eleonora Villa and Cornelius Rampf. Relativistic perturbations in ΛCDM: Eulerian \& Lagrangian approaches. *JCAP*, 01:030, 2016. doi:10.1088/1475-7516/2016/01/030. `http://arxiv.org/abs/1505.04782`. [Erratum: JCAP 05, E01 (2018)].

[250] Lina Castiblanco, Radouane Gannouji, Jorge Noreña, and Clément Stahl. Relativistic cosmological large scale structures at one-loop. *JCAP*, 07:030, 2019. doi:10.1088/1475-7516/2019/07/030. `http://arxiv.org/abs/1811.05452`.

[251] Cyril Pitrou. The radiative transfer for polarized radiation at second order in cosmological perturbations. *Gen. Rel. Grav.*, 41:2587–2595, 2009. doi:10.1007/s10714-009-0782-1. `http://arxiv.org/abs/0809.3245`.

[252] Nick Kaiser. Clustering in real space and in redshift space. *Monthly Notices of the Royal Astronomical Society*, 227(1):1–21, 07 1987. ISSN 0035-8711. doi:10.1093/mnras/227.1.1. `http://arxiv.org/abs/https://academic.oup.com/mnras/article-pdf/227/1/1/18522208/mnras227-0001.pdf`.

[253] Alvise Raccanelli, Daniele Bertacca, Olivier Doré, and Roy Maartens. Large-scale 3D galaxy correlation function and non-Gaussianity. *JCAP*, 08:022, 2014. doi:10.1088/1475-7516/2014/08/022. `http://arxiv.org/abs/1306.6646`.

[254] Jaiyul Yoo, A. Liam Fitzpatrick, and Matias Zaldarriaga. A New Perspective on Galaxy Clustering as a Cosmological Probe: General Relativistic Effects. *Phys. Rev. D*, 80:083514, 2009. doi:10.1103/PhysRevD.80.083514. `http://arxiv.org/abs/0907.0707`.

[255] Camille Bonvin and Ruth Durrer. What galaxy surveys really measure. *Phys. Rev. D*, 84:063505, 2011. doi:10.1103/PhysRevD.84.063505. `http://arxiv.org/abs/1105.5280`.

[256] Jaiyul Yoo and Matias Zaldarriaga. Beyond the Linear-Order Relativistic Effect in Galaxy Clustering: Second-Order Gauge-Invariant Formalism. *Phys. Rev. D*, 90(2): 023513, 2014. doi:10.1103/PhysRevD.90.023513. `http://arxiv.org/abs/1406.4140`.

[257] Daniele Bertacca, Roy Maartens, and Chris Clarkson. Observed galaxy number counts on the lightcone up to second order: I. Main result. *JCAP*, 09:037, 2014. doi:10.1088/1475-7516/2014/09/037. `http://arxiv.org/abs/1405.4403`.

[258] Enea Di Dio, Ruth Durrer, Giovanni Marozzi, and Francesco Montanari. Galaxy number counts to second order and their bispectrum. *JCAP*, 12:017, 2014. doi:10.1088/1475-7516/2014/12/017. `http://arxiv.org/abs/1407.0376`. [Erratum: JCAP 06, E01 (2015)].

[259] Mark Vogelsberger, Federico Marinacci, Paul Torrey, and Ewald Puchwein. Cosmological Simulations of Galaxy Formation. *Nature Rev. Phys.*, 2(1):42–66, 2020. doi:10.1038/s42254-019-0127-2. `http://arxiv.org/abs/1909.07976`.

[260] Romain Teyssier. Cosmological hydrodynamics with adaptive mesh refinement: a new high resolution code called ramses. *Astron. Astrophys.*, 385:337–364, 2002. doi:10.1051/0004-6361:20011817. `http://arxiv.org/abs/astro-ph/0111367`.

[261] Volker Springel. The Cosmological simulation code GADGET-2. *Mon. Not. Roy. Astron. Soc.*, 364:1105–1134, 2005. doi:10.1111/j.1365-2966.2005.09655.x. `http://arxiv.org/abs/astro-ph/0505010`.

[262] Douglas Potter, Joachim Stadel, and Romain Teyssier. PKDGRAV3: Beyond Trillion Particle Cosmological Simulations for the Next Era of Galaxy Surveys. 9 2016. `http://arxiv.org/abs/1609.08621`.

[263] Julian Adamek, David Daverio, Ruth Durrer, and Martin Kunz. gevolution: a cosmological N-body code based on General Relativity. *JCAP*, 07:053, 2016. doi:10.1088/1475-7516/2016/07/053. `http://arxiv.org/abs/1604.06065`.

[264] Stephen R. Green and Robert M. Wald. A new framework for analyzing the effects of small scale inhomogeneities in cosmology. *Phys. Rev. D*, 83:084020, 2011. doi:10.1103/PhysRevD.83.084020. `http://arxiv.org/abs/1011.4920`.

[265] Stephen R. Green and Robert M. Wald. Newtonian and Relativistic Cosmologies. *Phys. Rev. D*, 85:063512, 2012. doi:10.1103/PhysRevD.85.063512. `http://arxiv.org/abs/1111.2997`.

[266] Bhuvnesh Jain and Edmund Bertschinger. Second order power spectrum and non-linear evolution at high redshift. *Astrophys. J.*, 431:495, 1994. doi:10.1086/174502. `http://arxiv.org/abs/astro-ph/9311070`.

[267] M. H. Goroff, B. Grinstein, S. J. Rey, and M. B. Wise. Coupling of modes of cosmological mass density fluctuations. *Astrophysical Journal*, 311:6–14, December 1986. doi:10.1086/164749.

[268] Nobuyoshi Makino, Misao Sasaki, and Yasushi Suto. Analytic approach to the perturbative expansion of nonlinear gravitational fluctuations in cosmological density and velocity fields. *Phys. Rev. D*, 46:585–602, Jul 1992. doi:10.1103/PhysRevD.46.585. URL `https://link.aps.org/doi/10.1103/PhysRevD.46.585`.

[269] Thomas Tram, Christian Fidler, Robert Crittenden, Kazuya Koyama, Guido W. Pettinari, and David Wands. The Intrinsic Matter Bispectrum in ΛCDM. *JCAP*, 05:058, 2016. doi:10.1088/1475-7516/2016/05/058. `http://arxiv.org/abs/1602.05933`.

[270] P. Meszaros. The behaviour of point masses in an expanding cosmological substratum. *Astronomy and Astrophysics*, 37(2):225–228, December 1974.

[271] Steven Weinberg. Cosmological fluctuations of short wavelength. *Astrophys. J.*, 581: 810–816, 2002. doi:10.1086/344441. `http://arxiv.org/abs/astro-ph/0207375`.

[272] Luc Voruz, Julien Lesgourgues, and Thomas Tram. The effective gravitational decoupling between dark matter and the CMB. *JCAP*, 03:004, 2014. doi:10.1088/1475-7516/2014/03/004. `http://arxiv.org/abs/1312.5301`.

[273] Nicola Bartolo, Sabino Matarrese, and Antonio Riotto. The full second-order radiation transfer function for large-scale cmb anisotropies. *JCAP*, 05:010, 2006. doi:10.1088/1475-7516/2006/05/010. `http://arxiv.org/abs/astro-ph/0512481`.

[274] Marco Bruni, Juan Carlos Hidalgo, and David Wands. Einstein's signature in cosmological large-scale structure. *Astrophys. J. Lett.*, 794(1):L11, 2014. doi:10.1088/2041-8205/794/1/L11. `http://arxiv.org/abs/1405.7006`.

[275] Matthias Bartelmann, Ivan Kostyuk, Elena Kozlikin, Robert Lilow, Carsten Littek, Felix Fabis, Celia Viermann, Lavinia Heisenberg, Sara Konrad, and Daniel Geiss. Cosmic Structure Formation with Kinetic Field Theory. *Annalen Phys.*, 531(11): 1800446, 2019. doi:10.1002/andp.201800446. `http://arxiv.org/abs/1905.01179`.

[276] Diego Blas, Julien Lesgourgues, and Thomas Tram. The Cosmic Linear Anisotropy Solving System (CLASS) II: Approximation schemes. *JCAP*, 07:034, 2011. doi:10.1088/1475-7516/2011/07/034. `http://arxiv.org/abs/1104.2933`.

[277] Christian Fidler, Kazuya Koyama, and Guido W. Pettinari. A new line-of-sight approach to the non-linear Cosmic Microwave Background. *JCAP*, 04:037, 2015. doi:10.1088/1475-7516/2015/04/037. `http://arxiv.org/abs/1409.2461`.

[278] Guido W. Pettinari, Christian Fidler, Robert Crittenden, Kazuya Koyama, and David Wands. The intrinsic bispectrum of the Cosmic Microwave Background.

JCAP, 04:003, 2013. doi:10.1088/1475-7516/2013/04/003. `http://arxiv.org/abs/1302.0832`.

[279] Christian Wagner, Licia Verde, and Lotfi Boubekeur. N-body simulations with generic non-Gaussian initial conditions I: Power Spectrum and halo mass function. *JCAP*, 10:022, 2010. doi:10.1088/1475-7516/2010/10/022. `http://arxiv.org/abs/1006.5793`.

[280] Christian Wagner and Licia Verde. N-body simulations with generic non-Gaussian initial conditions II: Halo bias. *JCAP*, 03:002, 2012. doi:10.1088/1475-7516/2012/03/002. `http://arxiv.org/abs/1102.3229`.

[281] J. R. Fergusson, D. M. Regan, and E. P. S. Shellard. Rapid Separable Analysis of Higher Order Correlators in Large Scale Structure. *Phys. Rev. D*, 86:063511, 2012. doi:10.1103/PhysRevD.86.063511. `http://arxiv.org/abs/1008.1730`.

[282] Roman Scoccimarro, Lam Hui, Marc Manera, and Kwan Chuen Chan. Large-scale Bias and Efficient Generation of Initial Conditions for Non-Local Primordial Non-Gaussianity. *Phys. Rev. D*, 85:083002, 2012. doi:10.1103/PhysRevD.85.083002. `http://arxiv.org/abs/1108.5512`.

[283] Saroj Adhikari, Sarah Shandera, and Neal Dalal. Higher moments of primordial non-Gaussianity and N-body simulations. *JCAP*, 06:052, 2014. doi:10.1088/1475-7516/2014/06/052. `http://arxiv.org/abs/1402.2336`.

[284] Kendrick M. Smith and Marilena LoVerde. Local stochastic non-Gaussianity and N-body simulations. *JCAP*, 11:009, 2011. doi:10.1088/1475-7516/2011/11/009. `http://arxiv.org/abs/1010.0055`.

[285] D. M. Regan, M. M. Schmittfull, E. P. S. Shellard, and J. R. Fergusson. Universal Non-Gaussian Initial Conditions for N-body Simulations. *Phys. Rev. D*, 86:123524, 2012. doi:10.1103/PhysRevD.86.123524. `http://arxiv.org/abs/1108.3813`.

[286] J. R. Fergusson, M. Liguori, and E. P. S. Shellard. The CMB Bispectrum. *JCAP*, 12:032, 2012. doi:10.1088/1475-7516/2012/12/032. `http://arxiv.org/abs/1006.1642`.

[287] Johnathan Hung, James R. Fergusson, and E. P. S. Shellard. Advancing the matter bispectrum estimation of large-scale structure: a comparison of dark matter codes. 2 2019. `http://arxiv.org/abs/1902.01830`.

[288] Miguel Alcubierre. *Introduction to 3+1 numerical relativity*. International series of monographs on physics. Oxford Univ. Press, Oxford, 2008. doi:10.1093/acprof:oso/9780199205677.001.0001. URL `https://cds.cern.ch/record/1138167`.

[289] Teresa Hui-Ching Lu, Kishore Ananda, Christopher Clarkson, and Roy Maartens. The cosmological background of vector modes. *JCAP*, 02:023, 2009. doi:10.1088/1475-7516/2009/02/023. `http://arxiv.org/abs/0812.1349`.

[290] Catherine A Watkinson, Suman Majumdar, Jonathan R. Pritchard, and Rajesh Mondal. A fast estimator for the bispectrum and beyond – a practical method

for measuring non-Gaussianity in 21-cm maps. *Mon. Not. Roy. Astron. Soc.*, 472 (2):2436–2446, 2017. doi:10.1093/mnras/stx2130. `http://arxiv.org/abs/1705.06284`.

[291] Emiliano Sefusatti. Probing fundamental physics with large-scale structure: From galaxy formation to inflation. December 2005. URL `https://ui.adsabs.harvard.edu/abs/2005PhDT........23S`.

[292] Emiliano Sefusatti, Martin Crocce, Roman Scoccimarro, and Hugh Couchman. Accurate Estimators of Correlation Functions in Fourier Space. *Mon. Not. Roy. Astron. Soc.*, 460(4):3624–3636, 2016. doi:10.1093/mnras/stw1229. `http://arxiv.org/abs/1512.07295`.

[293] Michele Liguori, Emiliano Sefusatti, James R. Fergusson, and E. P. S. Shellard. Primordial non-Gaussianity and Bispectrum Measurements in the Cosmic Microwave Background and Large-Scale Structure. *Adv. Astron.*, 2010:980523, 2010. doi:10.1155/2010/980523. `http://arxiv.org/abs/1001.4707`.

[294] J. Adamek, J. Calles, T. Montandon, J. Noreña, and C. Stahl. Relativistic second-order initial conditions for simulations of large-scale structure. 10 2021. `http://arxiv.org/abs/2110.11249`.

[295] T. Hahn. CUBA: A Library for multidimensional numerical integration. *Comput. Phys. Commun.*, 168:78–95, 2005. doi:10.1016/j.cpc.2005.01.010. `http://arxiv.org/abs/hep-ph/0404043`.

[296] Neal Dalal, Olivier Dore, Dragan Huterer, and Alexander Shirokov. The imprints of primordial non-gaussianities on large-scale structure: scale dependent bias and abundance of virialized objects. *Phys. Rev. D*, 77:123514, 2008. doi:10.1103/PhysRevD.77.123514. `http://arxiv.org/abs/0710.4560`.

[297] Sabino Matarrese, Licia Verde, and Raul Jimenez. The Abundance of high-redshift objects as a probe of non-Gaussian initial conditions. *Astrophys. J.*, 541:10, 2000. doi:10.1086/309412. `http://arxiv.org/abs/astro-ph/0001366`.